DEVELOPMENT OF A CRYO-ANCHORING AND RADIOFREQUENCY ABLATION CATHETER FOR PERCUTANEOUS TREATMENT OF MITRAL VALVE PROLAPSE

By

Steven Michael Boronyak

Dissertation

Submitted to the Faculty of the

Graduate School of Vanderbilt University

in partial fulfillment of the requirements

for the degree of

DOCTOR OF PHILOSOPHY

in

Biomedical Engineering

August, 2015

Nashville, Tennessee

Approved:

W. David Merryman, PhD

Brett Byram, PhD

Richard Gumina, MD, PhD

Michael Miga, PhD

Robert Webster, PhD

To my grandfather, who gave me a soldering iron and
started me on this journey

ACKNOWLEDGEMENTS

This work was funded by the Wallace H. Coulter Foundation

and the American Heart Association (13PRE16340018)

TABLE OF CONTENTS

Page

Chapter

LIST OF TABLES

LIST OF FIGURES

Figure Page

Chapter 1

INTRODUCTION

Motivation

Current treatment for moderate and severe mitral regurgitation (MR), due to degenerative mitral valve (MV) disease, is open-chest surgical repair or replacement, as there are no known pharmacologic therapies that directly affect the disease process [1, 2]. Approximately one third of MV replacements are performed in lieu of repair due to lack of expertise and not the complexity of the lesions, indicating a need for MV repair techniques that can be more broadly adopted [3]. Additionally, it is estimated that up to 50% of high-risk patients with severe symptomatic MR are not referred for surgery due to co-morbidities that may confer high perioperative risk [4]. As a result, percutaneous approaches to MV repair have received a great deal of interest. Depending on the lesions present, current MV repairs may include annuloplasty, leaflet resection, or chordal transfer or replacement. While there are several percutaneous annuloplasty and chordal repair devices currently in development [5], there are currently no percutaneous techniques to perform leaflet resection, which is used in 70-80% of all surgical MV repairs [6, 7]. Thus, there is a need for a percutaneous leaflet resection technique in the expanding MV repair armamentarium [8].

Radiofrequency (RF) ablation is a well-developed technique that has been used to treat cardiac electrophysiology abnormalities and uses electrical energy to form thermal lesions by resistive heating. The primary structural component of MV leaflets is collagen, which denatures and contracts when heated to >65°C. As a result, RF ablation can be used to reduce the size of enlarged myxomatous MV leaflets [9, 10], providing a percutaneous alternative to open-chest surgical leaflet resection (Fig. 1.1). However, application of RF ablation to MV leaflets in a dynamic hemodynamic environment is difficult without additional catheter stability. To address this, we have developed cryo-anchoring, a technique similar to cryoablation that uses pressurized nitrous oxide to provide cooling of a catheter tip [11]. The sub-freezing temperatures provide adhesion, allowing stable and reversible attachment of a catheter tip to a moving MV leaflet.

The ***objective*** of this work is to translate a combined RF ablation and cryo-anchoring (RFC) catheter for treatment of degenerative MV disease from concept to in vivo animal models. The work that follows will describe the design and development of the RFC catheter system and will evaluate the performance of the RFC catheter according to three specific aims.

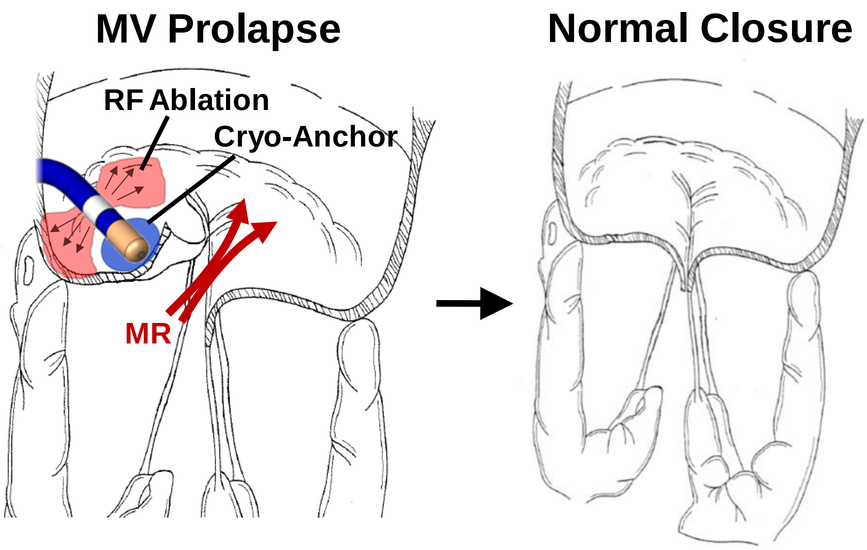

Fig. 1.1: RFC Catheter Concept
The combined radiofrequency ablation and cryo-anchoring catheter concept to treat enlarged MV leaflets percutaneously.

Specific Aims

The ***hypothesis*** of this investigation is that a combined RF ablation and cryo-anchoring catheter can reversibly adhere to MV leaflets in a beating heart environment without negatively affecting hemodynamics, and that RF ablation can be used to thermally shrink enlarged MV leaflet tissue.

1. Develop an RFC catheter prototype and assess treatment feasibility in static bench experiments. The goals of this aim are (1) to quantify the magnitude of the thermal shrinkage lesions generated by the RFC catheter and (2) to evaluate cryo-anchor effectiveness in the presence of RF ablation

2. Quantify the mechanical and morphological changes of healthy porcine mitral valve leaflets exposed to simultaneous cryo-anchoring and radiofrequency ablation in a physiologic flow environment. The goals of this aim are (1) to identify indicators of MV leaflet thermal alteration and (2) to demonstrate that combined cryo-anchoring and radiofrequency ablation effectively alters mitral valve leaflet morphology and compliance in a hemodynamic environment that mimics in vivo conditions.

3. Develop a 2D echocardiographic technique for clinically-relevant measurement of MV leaflet shrinkage and assess procedural efficacy in a porcine animal model. The goals of this aim are (1) to identify clinically measurable qualitative and quantitative indicators of MV thermal shrinkage and (2) to assess treatment efficacy in vivo.

Chapter 2

BACKGROUND AND SIGNIFICANCE

Mitral Valve Anatomy and Function

The mitral valve (MV) is a bi-leaflet heart valve which sits between the left atrium and left ventricle of the heart. The complex anatomy of the MV consists of five primary components: (1) the annulus, a fibrous ring of tissue located at the base of the atrium, (2) two leaflets, consisting of the anterior and posterior leaflets, (3) commissures, which are the sites of separation between the leaflets, (4) chordae tendineae, which act to tether the free edges of the MV leaflets to the ventricular wall, and (5) the papillary muscles, the sites of chordae tendineae attachment (Fig. 2.1). The anterior leaflet is the larger of the two leaflets, and is approximately twice the height of the posterior leaflet [12]. The posterior leaflet consists of three distinct scallops, with the central scallop being the largest in approximately 90% of normal hearts [12].

During normal functioning of the heart, the MV opens during diastole in order to allow passive filling of the left ventricle. During systole, when the heart is pumping blood to the systemic circulation of the body, the MV is closed and must resist large pressures (>120 mmHg) exerted on it to prevent reverse blood flow. Abnormalities of any of the primary components of the MV, as well as problems associated with left atrial or left ventricular dysfunction, can lead to malfunctioning of the MV [13], and the type and severity of the diseased structure determines whether surgical techniques are needed to treat the defect.

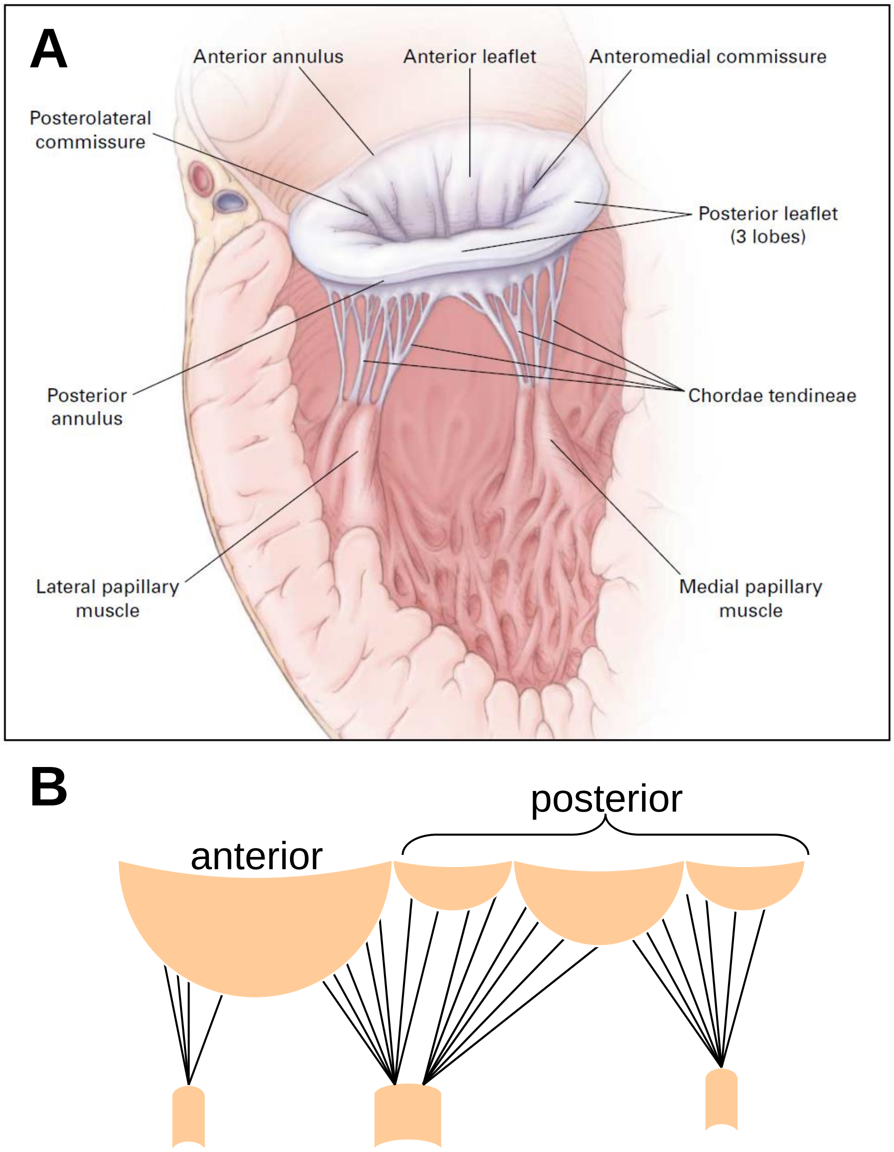

Fig. 2.1: Mitral Valve Anatomy
A: Anatomy of the mitral valve, indicating the five major structural components: the annulus, leaflets, commissures, chordae tendineae, and papillary muscles. Reproduced with permission from [1], Copyright Massachusetts Medical Society. **B:** A comparison of the larger, anterior leaflet and the three scallops that form the posterior leaflet.

Mitral Regurgitation and Mitral Valve Prolapse

Problems associated with the MV result in a "leaky" valve, in which reverse blood flow occurs across the MV during systole. This is termed mitral regurgitation (MR), and severe cases of MR can lead to left ventricular dysfunction and congestive heart failure [14]. Poor leaflet coaptation is the endpoint through which MR occurs, and one specific syndrome that may result in MR is termed mitral valve prolapse (MVP), which is found in approximately 2% of the population [15] and is defined as superior displacement greater than 2 mm of one or both leaflets into the atrium during systole [16] (Fig. 2.2). The severity and underlying cause of MR dictates the type of treatment administered, and open-chest replacement or repair is the current gold standard for treatment of moderate-to-severe and

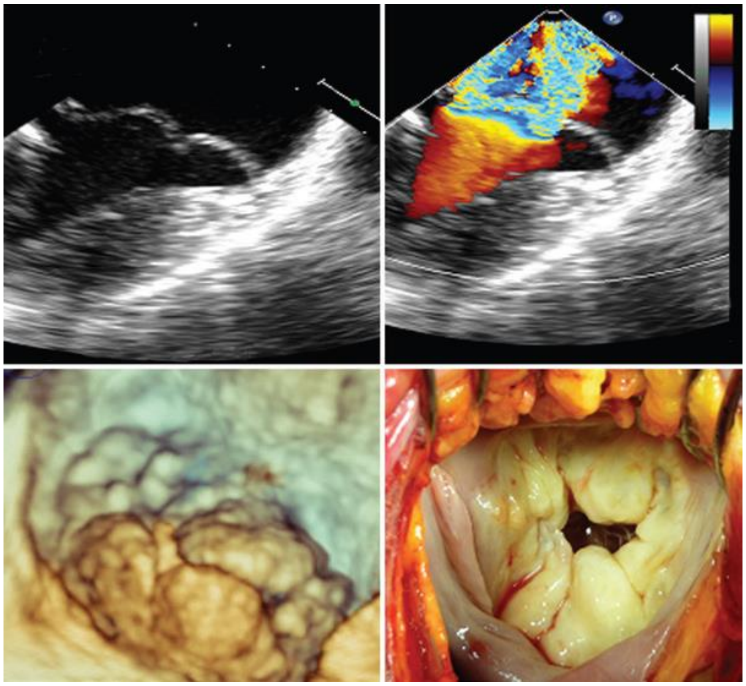

Fig. 2.2: Mitral Valve Prolapse
MV prolapse can affect one or both leaflets. Shown above is a MV with enlarged leaflet billowing into the left atrium during systole (top left) and significant MR (top right) and imaged with 2D transesophageal echocardiography. 3D transesophageal echocardiography (bottom left) and the surgical view (bottom right) further demonstrate leaflet billowing. Reproduced with permission from [17], Copyright Nature Publishing Group.

severe MR in patients with symptoms of left ventricular dysfunction [18]. This represents a significant problem in older patients who are more at-risk when undergoing invasive surgical procedures, a population that is currently growing, as the population of Americans aged 65+ is estimated to more than double – from 34 to 79 million – over the next 50 years [19].

Degenerative MV Disease: Common Characteristics

Dysfunction of the MV is classified into one of two distinct categories: (1) degenerative disease, a primary dysfunction due to abnormalities of the MV itself, and (2) functional disease, dysfunction that is secondary to diseases of the left ventricle or other areas of the heart [20]. While percutaneous MV repair devices are currently being developed to treat lesions arising from each of these sub-types, the RFC catheter is a leaflet repair device, and therefore targets lesions of degenerative disease. Degenerative disease of the MV apparatus occurs across a spectrum of conditions (Fig. 2.3), and the ends of this spectrum are termed Barlow's disease and fibroelastic deficiency. Little is known about the underlying molecular mechanisms of degenerative diseases of the MV, thus no pharmacologic therapies currently exist [2, 21].

Fibroelastic deficiency results from impaired production of connective tissue and typically presents late in life (>60 years) with only a short history of known disease. The primary lesion in fibroelastic deficiency is chordal rupture, due to the frail, thin nature of the chordae and MV leaflets [22]. Additionally, MV leaflets with fibroelastic deficiency often contain a region of thickening with excess tissue in the area of prolapse, most often present in the central segment of the posterior leaflet. Otherwise, MV leaflets with fibroelastic deficiency are typically normal in size.

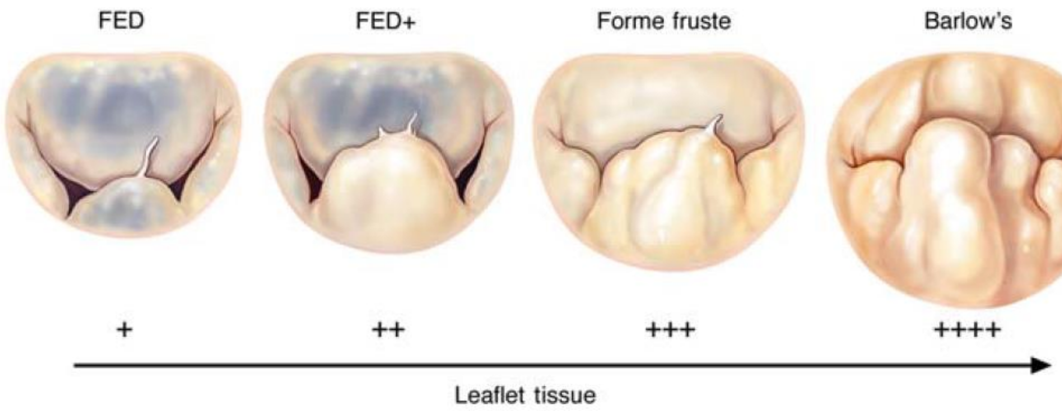

Fig. 2.3: Classification of Degenerative MV Disease
Degenerative disease of the MV occurs across a spectrum of conditions, with the ends of the spectrum termed fibroelastic deficiency (FD, or FED in above figure) and Barlow's disease. Reproduced with permission from [23]. Copyright Learned Society and Oxford University Press.

In contrast to fibroelastic deficiency, Barlow's disease presents earlier in life (<60 years) with myxoid infiltration as the primarily pathology [22]. Patients presenting with Barlow's disease may go many years before symptoms become severe enough to require treatment [24]. On echocardiography, Barlow's leaflets appear thick and voluminous, with multi-segmental prolapse [25, 26]. Surgical lesions may include excess tissue, enlarged leaflets, elongated or ruptured chords, and calcification of the chords, papillary muscles, or annulus. While myxomatous infiltration is not well characterized at the cellular and molecular levels, histological analysis of myxomatous MVs has revealed leaflets with disrupted and compromised collagen architecture and an increase in proteoglycans; chordae can be similarly affected [2]. Previous morphologic analysis of myxomatous MV leaflets demonstrated a two-fold increase in valvular surface area, due to significant increases in both anterior and posterior leaflet surface areas [27]. Additionally, mechanical testing has shown that myxomatous leaflets are twice as extensible as normal MV leaflets [28]. Similar changes in size and extensibility have been shown in MV chordae [29]. Given the variety and severity of lesions, surgical repair of Barlow's disease is generally more complex than that of fibroelastic deficiency [30].

Surgical Repair of the MV Due to Degenerative MR

The current standard in long-term treatment of MR due to degenerative disease is open-chest surgical repair or replacement, depending on the severity and structure affected. Repair of the MV is generally preferred over replacement due to lower rates of thromboembolism, resistance to endocarditis, the avoidance of a prosthetic valve and associated long-term anticoagulation therapy, as well as the excellent durability of repairs – as long as 25 years – compared to valve replacement [20]. Half of all patients undergoing MV replacement, with either a mechanical or bioprothesis, die within 10-15 years, with most deaths being valve or cardiac related [31-33]. Further, 20% of all patients receiving a MV replacement require reoperation within 20 years [31]. For comparison, MV repair using Carpentier's techniques offers a mortality rate comparable to that of the general population [34], with 6% incidence of reoperation within the first 20 years [34-36]. One benefit of MV repair is that it preserves the sub-valvular apparatus, consisting of the chords and papillary muscles, as removal of these structures has been associated with detrimental effects on left ventricular shape and performance [37-39].

The differentiation of degenerative MV disease into Barlow's and fibroelastic deficient sub-types when comparing long-term repair outcomes has only recently been made [22, 40]. One reason is that degenerative disease of the MV can frequently present in the middle of the spectrum of disease (Fig. 2.3), with lesions that are characteristic of each sub-type. Thus, when describing MV repair due to degenerative disease, the type of lesion and repair techniques are often reported without regard for disease sub-type [30].

There are a variety of surgical repair techniques employed by the cardiac surgeon, and the techniques used depend largely on the individual lesions present. Repairs of degenerative sub-types of MV disease frequently include a combination of leaflet resection and implantation of an annuloplasty ring [41]. Resection of excess leaflet tissue typically involves removal of a triangular or quadrangular section of tissue near the location of prolapse [42], while annuloplasty involves implantation of a rigid or flexible ring around the MV annulus at the base of the atrium. Implantation of annuloplasty rings are frequently used to correct an enlarged MV annulus, but their use in the normal-sized MV annulus has also been associated with improved long-term clinical outcomes [6, 43]. While it us unknown why annuloplasty usage in MVs with a normal-sized annulus improves outcomes, it is believed to be due to the progressive nature of the disease [6, 7]. Only about 70% of patients are free from MR > grade 2 (moderate) 15 years after treatment [7, 35], indicating the need for possible re-treatment in the later stages of life. In addition to leaflet resection and annuloplasty repair techniques, chordal repairs are also commonly performed and can include chordal shortening, chordal transfer, or implantation of synthetic PTFE chords [44, 45]. For an analysis of the frequency of usage for the most common repair techniques used to treat degenerative disease, see Table 2.1.

Clinical Significance of Less Invasive Techniques

In 2003, 43,000 MV valve procedures were performed in the U.S. alone, with 2,800 deaths due directly and another 6,600 due in part to MV disease [46]. Recently, less-invasive, percutaneous techniques have been in development to treat MV disease. Percutaneous techniques are often preferred over surgical procedures because they have been shown to reduce the need for blood transfusions, decrease rates of infection, and reduce recovery time [10, 47]. These benefits have the potential to reduce procedure cost and time dramatically. Additionally, approximately one third of MV replacements are performed in lieu of repair due to lack of expertise and not the complexity of the lesions, indicating a need for MV repair techniques that can be more broadly adopted [3]. Further, it is estimated that up to 50% of high-risk patients with severe symptomatic MR are not referred for surgery due to co-morbidities [4]. As a result, percutaneous approaches to MV repair have received a great deal of interest.

Due to the variety of lesions that may be present, and the multitude of techniques that may be used in surgery, attempts to percutaneously repair degenerative MVs may be best served by a combination of different repair devices, each with a specialized function. One example is the sub-optimal repair rates of the MitraClip device. Repair is sufficiently efficacious in some patients, but not in a majority [48]. There will likely be no percutaneous repair strategy that is ideal for all patients, and a combination of approaches with different percutaneous devices may best replicate the combination of repair strategies currently employed by surgeons. While there are several percutaneous annuloplasty and chordal repair devices currently in development [5, 8], there are currently no percutaneous techniques to perform leaflet resection, which is used in 70-80% of all surgical MV repairs[6, 7]. Thus, there is a need for a percutaneous leaflet resection technique in the expanding MV repair armamentarium [8].

Table 2.1: General classification of MV repairs for correction of degenerative disease.

	Flameng [6]		David [7]	
Total repairs	348		649	
Leaflet Repair				
Segmental resection	274	79%	431	66%
Other leaflet intervention	13	4%	0	0%
Chordal Repair				
Chordal shortening	22	6%	39	6%
Chordal transfer	27	8%	40	6%
Chordal replacement (PTFE)	48	14%	380	59%
Annuloplasty Rings				
Rigid ring	326	94%	96	15%
Flexible ring	11	3%	141	22%
Incomplete ring	0	0%	379	58%

Percutaneous Application of Radiofrequency Ablation to Treat MVP

One possible method to replace leaflet resection with a percutaneous technique is radiofrequency ablation (RF), an established technique for treating cardiac arrhythmias that has been around since the mid-1980s. RF ablation utilizes electrical signals at around 300-700 kHz in order to generate resistive heating for ablation of tissue. It is dependent on power, electrode-tissue interface temperature, electrode size, and contact pressure [49]. The target of RF ablation is the collagen architecture of the MV leaflets, which contributes to much of the strength and mechanical properties of the tissue [50]. Previously, the fibrillar structure of collagen has been shown to denature and contract when heated to greater than 65°C [51]. Additionally, transmission electron microscopy has shown an increase in collagen fiber diameter and a loss of cross-striations with increasing application of RF power [52]. The goal of using RF ablation to treat enlarged MV leaflets is to induce permanent changes in leaflet geometry via resistive heating of collagen and subsequent shortening.

In MV leaflets, collagen is preferentially aligned with the circumference of the MV annulus, which causes an anisotropic loading response in normal leaflets (Fig. 2.4A-B). This collagen alignment can affect the response of MV tissue to application of RF energy. Following treatment with RF ablation, collagenous tissues undergo shortening primarily in the direction of collagen alignment. Prior treatment of porcine MV leaflets with RF ablation in vitro has demonstrated directional length changes that are dependent on RF power, with the circumferential direction shortening much more than the radial direction [9].

History of RF Ablation of the MV

The history of utilizing percutaneous application of RF ablation to alter the MV apparatus is brief and began with two animal studies published in 2008. The first of these studies used the QuantumCor device, which uses a circular RF ablation probe to reduce the MV annulus diameter and is intended as a treatment for functional MR [53]. Use of the QuantumCor device in 16 sheep reduced the anterior-posterior dimension of the MV annulus by more than 20%, and these changes remained durable for the duration of the 180-day study, with

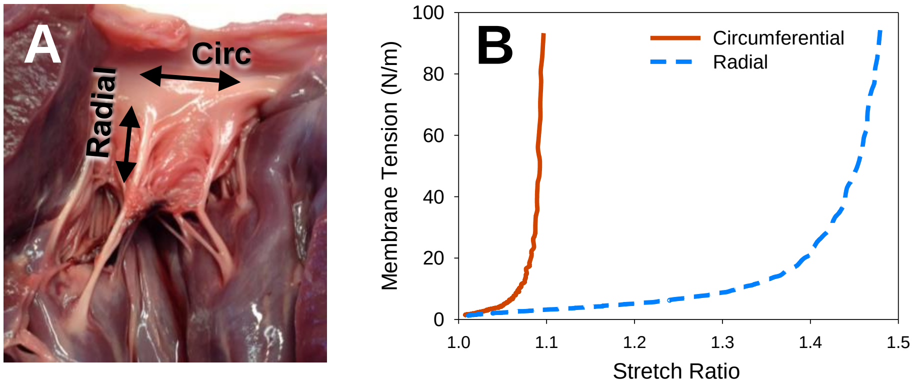

Fig. 2.4: Anisotropic Mechanical Response of MV Leaflets
A: Collagen is preferentially aligned with the circumferential (circ) direction in MV leaflets.
B: Due to this collagen alignment, MV leaflets are more stiff in the circumferential direction than the radial direction.

tissue fibrosis and necrosis present at the endpoint [54]. This study was performed in normal sheep, with little to no traces of MR at the beginning of the study.

The second study used a standard RF ablation catheter to apply RF energy directly to MV leaflets in order to reduce leaflet size and alter biomechanical properties and was performed on two separate treatment groups [10]. The first was an acute procedure performed on n=3 canines with severe MR in which RF ablation was applied under open-chest surgery. An average of 4 ablations at a power of 16 W for 40 seconds produced anywhere from 44% to 60% reduction in MR, as measured by echocardiography. An additional chronic study was performed on n=3 healthy canines, and RF ablation was applied percutaneously until structural and/or functional alteration of the MV was demonstrated by echocardiography. It took an average of 20 ablations for 60 seconds at a power of 50-60 W to induce noticeable changes, due largely to the difficulty in maintaining adequate contact between the RF ablation catheter tip and the MV leaflets. While open-chest application of RF ablation demonstrated significant reductions in post-ablation MR, the number of ablations required in the percutaneous procedure indicates that a method to stabilize catheter contact with the moving MV apparatus is clearly warranted. Further, while leaflets experience small areas of coagulation necrosis and areas of fibroblast proliferation, leaflets remained durable over 6 weeks.

Cryo-Anchoring for MV Attachment

In order to enable more reliable application of RF energy to MV leaflets, the RF electrode on the catheter device must remain in direct contact with the target tissue area. The requirements for an anchoring device are to enable reversible attachment to either the posterior or anterior MV leaflet, depending on the desired ablation target. Anchoring to the chords for RF ablation represents another potential target. Cryoablation is one technology that has been used to percutaneously treat cardiac arrhythmias since 1999 [55], which uses pressurized liquid nitrogen to cool a catheter tip to temperatures as low as -80°C. A technique termed cryo-mapping was developed for use with these cryoablation catheters, which cools the catheter tip to temperatures as low as -30°C to temporarily induce electrophysiological changes in cardiac tissues [49]. This is performed with minimal cellular damage and little effect on the structural properties of the tissue [56]. Given the negligible amount of tissue damage induced at temperatures as low as -30°C, and the temporary, reversible tissue attachment that can be created, this cryo-anchoring technique represents one potential strategy to maintain attachment to moving MV leaflets.

Potential Complications

In designing the RFC catheter treatment strategy and studying the effects of RFC catheter treatment on the MV, it is important to consider the potential complications that may arise as a result of the procedure. Potential complications of percutaneous treatment of the MV with the RFC catheter can be classified according to one of three categories, which are discussed further below: 1) complications arising as a result of RF ablation and cryo-anchoring delivery, or catheter manipulation, within the heart and vasculature generally, 2) complications arising from ablation of the MV structure specifically, and 3) complications that compromise long-term treatment efficacy, or re-dilation of the MV leaflet after treatment.

General Complications of RF Ablation and Catheter Manipulation in the Heart. Complications that may result due to administration of RF energy, cryo-anchoring, or general manipulation of a catheter within the vasculature and heart are well-known. RF ablation and cryoablation catheters have been used safely and successfully since the 1980s and 1990s [49, 55], respectively, to treat a variety of arrhythmias in the heart. A primary concern of RF ablation is tissue charring and thrombus formation due to the high temperatures produced during treatment, and the associated risk of embolization [57-59]. When ablation is performed within a cardiac chamber, thromboembolic risk is as high as 2% [57, 58]; however, the risk of cerebral embolization is much lower, around 0.1% [57]. Thromboembolic risk can be minimized by limiting RF ablation temperatures to minimize excessive charring, the use of heparin protocols, and post-procedure antithrombotic protocols [58-60]. An additional risk of RF ablation is damage to the surrounding structures, especially as thermal alterations due to RF ablation are permanent [61]. Pulmonary vein stenosis [62], coronary sinus injury or thrombus formation [63], coronary artery stenosis [64], and arrhythmogenicity of ablating critical electricity-conducting structures such as the AV node are all risks that must be considered. Cryo-anchoring was developed partly in response to this risk: the significant catheter stability provided by cryo-achoring combined with echocardiographic visualization of the RFC catheter tip minimizes the risk of off-target ablations. Additionally, cryoablation and cryo-anchoring are associated with minimal thrombus formation compared to RF ablation [65].

Specific Complications Involving the MV Following RF Ablation. A second subset of possible complications resulting from RFC catheter treatment of the MV leaflets is undesired structural damage secondary to leaflet shrinkage. MV leaflet perforation or ruptured chords are a possible concern, which may arise due to excessive heat generation (>100°C) or due to the possible frail nature of diseased tissue. There is a small body of literature on valvular lesions occurring following RF ablation of accessory atrioventricular conduction pathways in the left ventricle. These ablations are performed using a retrograde, transaortic catheter approach. A few studies have used transthoracic echocardiography to assess the incidence of valvular regurgitation following ablation of these accessory conduction pathways and found that mild MR developed in 6.7%, 5.4%, and 0.01% of cases within 24 hours in studies of 59 [66], 355 [67], and 179 patients [68], respectively. When followed long-term, findings were unchanged over 15-36 months. It is still unclear if MR results from RF energy delivery or catheter manipulation, or both [66, 67]. Two case studies of young patients undergoing routine RF ablation for treatment of Wolff-Parkinson-White syndrome provide evidence for both causes. In one, a 14 year old male developed a 3 mm by 5 mm perforation in the center of the posterior leaflet, discovered 20 months post-procedure after presentation with sudden chest pain with no other abnormal findings, suggesting catheter manipulation as the cause [69]. In another case, a 39 year old female developed severe MR 2 weeks post-procedure and was found to present with a ruptured anterior leaflet chord with surrounding reddened and thickened areas with partially necrotic tissue, suggesting excessive RF energy delivery [70]. Given the transaortic approach, any ablations near the MV annulus within the ventricle, where convective heat transfer away from the RF electrode is reduced, must be carefully monitored to avoid excessive heat generation.

Given the possibility of leaflet or chordal structural damage, RF energy delivery will have to be carefully titrated during RFC catheter treatment in order to avoid excessive tissue temperatures. Further, the proposed atrial access route of the RFC catheter, as opposed to the retrograde approach used in the ventricular ablations described above, will likely avoid many of the possible complications of ventricular access such as chordal entanglement or excessive ablation of the ventricular side of the annulus.

Long-Term Thermal Shrinkage Efficacy. A third subset of potential complications of RFC catheter treatment is the possibility of leaflet re-dilation post-treatment, which would compromise the efficacy of the procedure. The potential for thermal shrinkage lesions to re-dilate has been assessed in other tissues previously. For example, RF ablation to reduce the size of infarct area to improve left ventricular volumes found that tissue re-dilated back to baseline after 30 days [71]. However, the QuantumCor device, with is designed to thermally shrink the MV annular diameter, has been shown to produce reductions in annular diameter that remain durable 6 months post-treatment [54]. Given the disparity in the literature, the potential for MV leaflet re-dilation following RF ablation will be studied in Chapter 6 and Chapter 7.

The RFC Catheter as an Alternative to Surgical Leaflet Resection

Surgical resection of the MV leaflets is commonly used to address lesions in both fibroelastic deficiency and Barlow's disease and is a mainstay of the most commonly used methodology of degenerative MV repair: the methodology described by Carpentier [42]. Leaflet resection is just one of the repair techniques described by Carpentier, but as several of the other repair techniques were discussed earlier in this chapter and the RFC catheter is intended as a leaflet resection device, only leaflet resection will be discussed here.

The goal of the so-called French correction, which is still the most commonly used repair framework and has been shown to be highly successful [23], is to restore the MV structure to as close to normal anatomy as possible. In fibroelastic deficient valves, this often means resection of the P2 leaflet segment, since this segment is often enlarged, or contains ruptured chords, or both (Fig. 2.3, left side). In Barlow's valves, resection could be required in any of the MV segments, as leaflets are generally much enlarged with lots of billowing into the atrium (Fig. 2.3, right side). Leaflet resection, when used to treat either of these subtypes, can be carried out to varying degrees. The resection takes place in the area of leaflet enlargement, or if present, on the portion of the leaflet segment containing a ruptured chord (as on the chordal rupture and prolapsing segments seen in Fig. 2.3). Depending on the lesion and severity, leaflet resection may be triangular, quadrangular, or could be a sliding-plasty or butterfly resection (Fig. 2.5) [42, 72]. In the case of quadrangular resection, up to 30% of the leaflet area is often cut out and removed [73]. The opposing leaflet edges on either side of the resection are then sutured together using an interrupted stitch, and any cuts through the annulus are often sutured with a mattress stitch to plicate the annulus in an effort to reduce valve circumference in the case of enlarged valves.

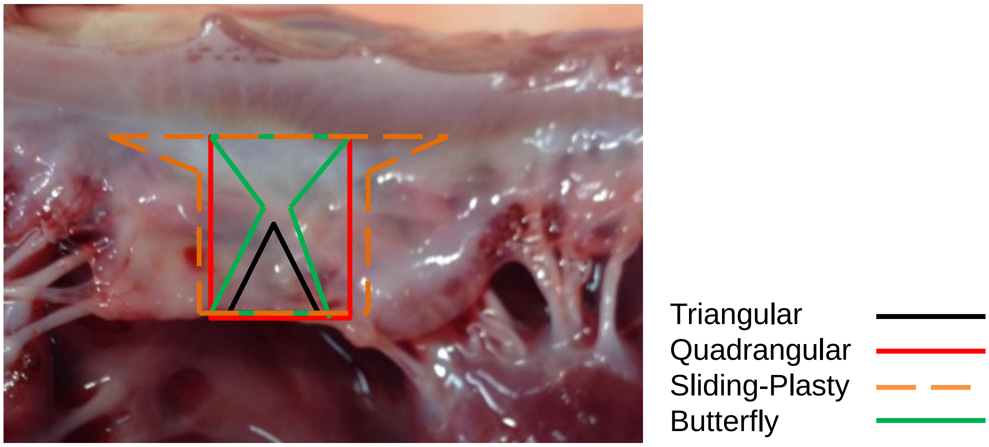

Fig. 2.5: Common Leaflet Resection Incisions
Geometric differences between the common leaflet resection techniques shown on a healthy porcine posterior leaflet.

The goal of the RFC catheter is to approximate surgical leaflet resection by thermally shrinking the prolapsing leaflet segments. Instead of physically cutting excess tissue or removing segments with detached chords, the goal is to shrink enough of the enlarged leaflet and surrounding area to replicate the results of leaflet resection. The work presented in the following chapters will show that RFC catheter treatment has to ability to reduce leaflet area by up to 40%, which is within the range of leaflet areas commonly resected surgically [73].

Chapter 3

THE STATE OF PERCUTANEOUS MV REPAIR

Text and figures for Chapter 3 taken from:
Boronyak SM, Merryman WD: "The once and future state of percutaneous mitral valve repair." Future Cardiology, Vol. 8, Issue 5, 779-93, 2012.

Introduction

Many surgical techniques exist to repair the MV and reduce MR. In any given surgical repair, a combination of techniques may be used, and thus, percutaneous MV repair is not one size fits all. In this chapter, percutaneous MV repair devices currently in use or in development will be discussed, with a focus on those through human or animal trials.

Several devices have been in development for percutaneous repair of the MV in the past decade [5]. These percutaneous techniques offer potential improvement over current, conventional surgical procedures in that they have been shown to reduce the need for blood transfusions, decrease rates of infection, and reduce hospital and recovery time significantly [10, 47]. As demonstrated by the recent enrollment in clinical trials for new percutaneous repair devices, patients are taking an interest despite the fact that long-term durability remains to be proven. Additionally, these new percutaneous approaches have the potential to greatly benefit the growing elderly population, who are more at-risk when undergoing invasive surgical procedures.

While some percutaneous techniques in development involve replicating repairs that have previously been performed surgically, such as the MitraClip edge-to-edge repair, many percutaneous devices in development alter the MV apparatus using entirely new approaches, such as direct leaflet ablation and coronary sinus (CS) annuloplasty. As a result, the long-term efficacy and durability of these repairs is unknown. Evaluation of how these devices affect the mechanics of the MV, either *in vitro* or in animal models, might offer the possibility to predict long-term efficacy. For example, analysis of the effect of various annuloplasty devices on MV leaflet strains could predict repair durability or indicate that some devices may be more suited for certain types of MV disease [74, 75]. With many leaflet repairs currently being performed in combination with annuloplasty, in the future, multiple percutaneous approaches may be combined to generate a more efficacious repair. In this review, we report on several percutaneous annuloplasty and leaflet repair devices with prior clinical or animal data, and place the results in context with hemodynamic data from *in vitro* studies.

Subtypes of Mitral Valve Disease

MV disease can be due to dysfunction of any of the components of the MV apparatus, including the annulus, leaflets, chordae, and papillary muscles, but MR can also result due to abnormalities of the left ventricle (LV) or left atrium. Most causes of MR can be classified into one of two distinct categories, degenerative (primary) and functional (secondary), and most current repair techniques target one of these subtypes [20]. In order to understand how percutaneous repairs will be required to alter the MV apparatus, degenerative MR and functional MR must first be understood in terms of how MV function and morphology is affected. For a comphrensive description of degenerative MR (DMR), see Chapter 2.

Functional MR. Another common cause of MR is functional disease due to ischemic left ventricular dysfunction or dilated cardiomyopathy. MV leaflets and chordae frequently appear normal in hearts with functional MR (FMR), but dysfunction of other components of the heart affect MV function. FMR is therefore secondary to other disease processes in the heart, frequently those that result in increased LV size. Left ventricular chamber enlargement, regional LV wall motion abnormalities, dilation of the MV annulus, and changes in LV shape may all significantly contribute to FMR [76]. Quantitative echocardiography has demonstrated an increase in the size of the MV annulus, in addition to increased papillary muscle tethering distance as a result of increased LV volume, which may contribute to MR [77]. Additionally, dyssynchrony in papillary muscle activation has also been shown to be a possible contributor to FMR [78, 79], and recently, it was found that it is the impairment of lateral shortening between the papillary muscles during systole, and not passive ventricular size, that impairs systolic valve closure in ischemic MR [80].

Annuloplasty is the dominate mode of repair for FMR, in which implantation of either a flexible or rigid ring sutured to the MV annulus reduces the MV orifice and enhances leaflet coaptation by bringing the leaflets closer together. Recently, cause-specific annuloplasty rings have been developed in order to account for morphologic differences in ischemic and dilated cardiomyopathy. Previous studies have shown that even with similar severity of MR, less enlargement of the LV and mitral annulus occurs in patients with ischemic than with dilated cardiomyopathy. Moreover, leaflet tethering tends to be symmetrical in dilated cardiomyopathy, while leaflet tethering occurs primarily on one side of the valve in ischemic cases [81]. Due to these morphologic differences between dilated and ischemic cardiomyopathy, it may be necessary to develop specialized percutaneous annuloplasty devices capable of correcting the different pathologies.

Leaflet Repair

MitraClip Edge-to-Edge Repair. The Alfieri edge-to-edge repair is one alternative surgical technique, which creates a double-orifice MV by suturing together the anterior and posterior leaflets in the central portion of the valve [82-84]. The suture point of the double-orifice MV forms a fixed coaptation point, facilitating coaptation of the remainder of the leaflet segments.

The MitraClip (Abbott Vascular) was developed in order to replicate this procedure via a percutaneous approach and is currently the most tested percutaneous MV repair technique available [18, 48, 85]. The MitraClip has been used for treatment of DMR and FMR, with reduced MR demonstrated in both subtypes. In place of the sutures used for forced leaflet coaptation, a 4-mm wide implantable, cobalt-chromium clip secures the leaflets together (Fig. 3.1A). The MitraClip system utilizes a 24-F steerable guide catheter that is introduced via transseptal access. A clip delivery catheter then passes through the guide catheter, which can be steered to the delivery site, with the MitraClip attached to the distal end. Several barbs on the center portion of the clip facilitate tissue attachment upon clip closure. One important benefit of the MitraClip device is that the clip can be opened and closed several times during delivery, in order to assess if MR is reduced and that clip attachment is secure. If the procedure cannot be completed, or MR not reduced, the MitraClip can be fully retracted and removed from the body. However, acute assessment of MitraClip efficacy can sometimes be difficult; despite device implantation, 17% of patients in a high risk study were discharged without a significant reduction in MR [48]. Further, it may be difficult to differentiate the effects of general anesthesia from the effects of MitraClip placement on MR during the procedure [85], an issue that may be common to other percutaneous devices as well.

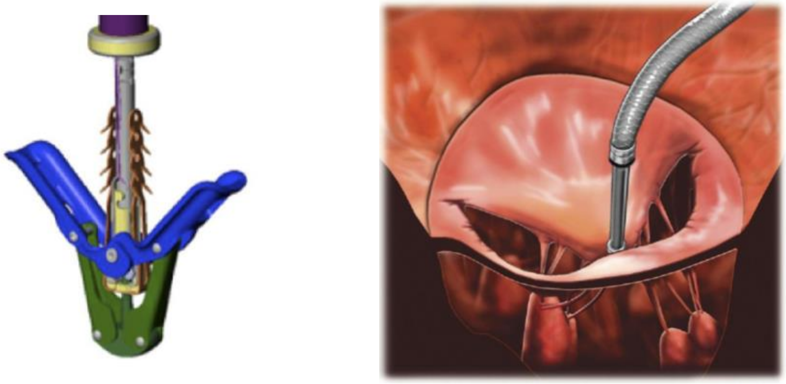

Fig. 3.1: Percutaneous Repair with the MitraClip
Detailed drawing of the MitraClip implant, showing the cobalt-chromium clip with barbs to enhance tissue attachment. Reprinted from [86]. Also depicted is MitraClip placement at the position of the A2-P2 segments of the MV. Reprinted from [87].

More clinical data exists for the MitraClip than other percutaneous leaflet repair or annuloplasty devices, and two important studies have recently been published from the EVEREST II clinical trial. Results from 12-month assessment of a randomized study comparing percutaneous MitraClip repair with conventional valve replacement or surgery identified a 55% primary end point efficacy for the MitraClip repair group and a 73% efficacy in the conventional surgery group [18]. Primary end point efficacy included freedom from death, freedom from MV surgery, and 3+ or 4+ MR at 12-months. While the MitraClip repair produced less desirable results in terms of efficacy compared with conventional surgery, the MitraClip repair was associated with enhanced safety. The rate of major adverse clinical events at 30 days was found to be 15% in those receiving the MitraClip, compared with 48% in the conventional surgery group. The superior safety results of the MitraClip and sub-optimal efficacy indicate that MitraClip treatment may be most appropriate in high-risk patients who fail to qualify for conventional surgical repair or replacement procedures.

In the EVEREST II high-risk study, 12-month survival was found to be 76% in those receiving the MitraClip device, compared with 55% of the comparator group, who either did not enroll or were anatomically ineligible for MitraClip placement [48]. Additionally, 78% of patients receiving the MitraClip with matched baseline and 12-month data had MR ≤2+. However, only 54% of all patients who received the MitraClip had MR of ≤2+ at 12-months. More recently published results from the German transcatheter mitral valve interventions registry demonstrated similar device efficacy, as 313 out of 471 (66%) patients who received MitraClip treatment had MR grade 1 or lower upon follow-up [88]. In-hospital mortality was found to be 2.5%, and post-discharge mortality was 12.5%. Results from echocardiographic assessment of patients with MitraClip implantation in the high-risk study, as well as a study involving 104 patients not amenable for surgery, are included in Table 3.1 [48, 89].

Mechanical Studies of Edge-to-Edge Repair. Several *in vitro* studies have previously been performed to analyze the effects of the edge-to-edge repair on MV mechanics and functionality, and while they have all used the conventional form of edge-to-edge repair with sutures, the results of these studies can be used to aid in prediction of long-term MitraClip efficacy. Many of these *in vitro* studies, with a focus on valve mechanics and hemodynamics, have provided insight into the use of edge-to-edge repair without annuloplasty, as prior data has suggested sub-optimal mid-term results from edge-to-edge repair alone [90]. Jimenez et al used *in vitro* testing in a left heart flow simulator to decouple the effects of MV annular area, transmitral pressure, and mitral flow rate on the force exerted on the suture (stitch force) in the edge-to-edge repair [91]. Results indicated that annular dilation negatively impacted the efficacy of edge-to-edge repair, as peak systolic stitch force increased linearly with increasing annular area, and this could lead to a reduction in long-term durability of edge-to-edge repair. Additionally, peak diastolic stitch force increased with decreasing mitral annular area. These results indicate that combined annuloplasty may be necessary in many patients to increase durability of the edge-to-edge repair by reducing annular dilation. Further study by Croft et al demonstrated that edge-to-edge repair alone can reduce, but not completely eliminate, MR due to annular dilation [92]. It was also found that edge-to-edge repair alone is ineffective at reducing MR due to papillary muscle displacement, providing evidence that in many cases, edge-to-edge repair may be secondary to annuloplasty in reduction of MR.

A more recent *in vitro* study by Bhattacharya et al demonstrated that the tension generated by the MV on the annulus is not completely restored following edge-to-edge repair in a chordal elongation model, leading to an imbalance between the inward annular tension generated by the MV apparatus and the outward force generated by the left ventricular myocardium [93]. This force imbalance at the mitral annulus could be a possible mechanism for annular dilation to occur following treatment of MR due to MV prolapse, and recurrent MR due to progressive annular dilation is a possibility that must be examined. Interestingly, echocardiographic analysis of the patients enrolled in the MitraClip EVEREST II high-risk study at 12-months showed decreases in the LV end-systolic (-10.0%) and end-diastolic volumes (-15.7%), in addition to a decrease in the septal-lateral diameter (-6.3%) of the mitral annulus (Table 3.1) [48]. These reductions are contrary to the results suggested by the *in vitro* annular tension study and suggest that MitraClip treatment may actually result in favorable remodeling of the LV following the first 12-months after treatment. Favorable LV remodeling was reported to occur in patients with FMR, as well as DMR.

Table 3.1: Assessment of Percutaneous MV Repair Devices: Data from Clinical Trials

Treatment	Study	Repair Type	Regurgitant Volume (mL)				LVESV (mL)				LVEDV (mL)				S-L Diameter Diastole (mL)				S-L Diameter Systole (mL)				Ref
			n	Pre	Post	%Δ	n	Pre	Post	%Δ	n	Pre	Post	%Δ	n	Pre	Post	%Δ	n	Pre	Post	%Δ	
Acute																							
MitraClip	EVEREST II	Leaflet Repair	68	50.7	27.4	-46.0	86	69.5	70.5	1.4	87	171	157	-8.2	-	-	-	-	-	-	-	-	[85]
Monarc	EVOLUTION I	Annuloplasty	21	40.4	31.6	-21.8	29	109.9	104.3	-5.1	29	170.1	165.1	-2.9	46	36.1	35.1	-2.8	46	36.1	35.1	-2.8	* [94]
1-month																							
MitraClip	EVEREST II	Leaflet Repair	-	-	-	-	70	80	74	-7.5	70	166	146	-12.0	64	38	38	0.0	64	32	32	0.0	[48]
Monarc	EVOLUTION I	Annuloplasty	18	37.7	31.5	-16.4	32	111.3	102.8	-7.6	32	170.6	163.3	-4.3	43	35.7	35	-2.0	43	35.7	35	-2.0	* [94]
Carillon	AMADEUS EU	Annuloplasty	28	35.1	22.6	-35.6	-	-	-	-	28	217	204	-6.0	28	42	38.1	-9.3	28	42	38.1	-9.3	* [96]
6-month																							
MitraClip	EVEREST II	Leaflet Repair	-	-	-	-	60	80	71.4	-10.8	60	166	141	-15.1	57	38	37	-2.6	57	32	31	-3.1	[48]
Monarc	EVOLUTION I	Annuloplasty	25	34.6	23.2	-32.9	34	116	111.6	-3.8	34	175.4	173.9	-0.9	35	36.1	33.6	-6.9	35	36.1	33.6	-6.9	* [94]
Carillon	AMADEUS EU	Annuloplasty	23	35.1	24.3	-30.8	-	-	-	-	24	217	192	-11.5	24	42	37.8	-10.0	24	42	37.8	-10.0	* [96]
12-month																							
MitraClip	EVEREST II	Leaflet Repair	-	-	-	-	54	80	72	-10.0	54	166	140	-15.7	52	38	36	-5.3	52	32	30	-6.3	[48]
MitraClip		Leaflet Repair	59	45	19	-57.8	63	125	102	-18.4	63	221	183	-17.2	-	-	-	-	-	-	-	-	[89]
Monarc	EVOLUTION I	Annuloplasty	19	31.8	25	-21.4	26	114.8	98.2	-14.5	26	175.4	161.9	-7.7	27	36.2	33.2	-8.3	27	36.2	33.2	-8.3	* [94]

** indicates distinction between diastolic and systolic S-L diameter was not made*

LVESV, left-ventricular end-systolic volume; LVEDV, left-ventricular end-diastolic volume; S-L Diameter, septal-lateral diameter

All data are from transthoracic echocardiography

One possible explanation that might account for some of the reduction in LV end-systolic volume, LV end-diastolic volume, and the septal-lateral diameter seen in this study is that the number of patients with matched data decreased from baseline (n = 72) to 12-months (n = 56) in the high-risk study. Additionally, when the difference between MitraClip repair and surgery was analyzed for FMR and DMR, it was found that surgery produced significantly better outcomes for DMR, while there was little difference in outcome between MitraClip repair and surgery for FMR. Therefore, while annular dilation following treatment of DMR with the MitraClip should be considered a possibility in long-term outcomes, current clinical data suggests that remodeling of the MV annulus and LV due to MitraClip therapy is favorable. Longer follow-up studies will be necessary to confirm the effects of MitraClip treatment on LV remodeling.

Annuloplasty Devices

Coronary Sinus Annuloplasty. Annuloplasty rings have been essential for surgical repair of MR due to both functional and degenerative etiologies, and several percutaneous annuloplasty approaches are currently in development. Coronary sinus (CS) annuloplasty approaches, in particular, have received a great deal of interest, due to ease of access and prior history of device implantation in the coronary vessels. As the CS sits within close proximity to the MV annulus, shortening of the CS effectively reduces the septal-lateral diameter of the annulus by forcing the posterior annulus in the anterior direction.

The Monarc device (Edwards Lifesciences) is one percutaneous approach that utilizes a nitinol implant consisting of distal and proximal self-expanding, stented anchors with an interconnecting, spring-like bridge segment that provides shortening tension (Fig. 3.2A) [94, 95]. Both distal and proximal anchors are held in place by using an anchor 2 mm to 4 mm larger in diameter than the CS. The delivery system of the Monarc device includes a 12-F guide catheter and dilator, and a 9-F delivery catheter with access via the internal jugular vein. The Monarc also contains a biodegradable element incorporated within the spring-like bridge segment, preventing complete spring tension at initial device implantation. As the biodegradable element absorbs over the first month, shortening of the device continues until full spring tension is achieved.

Safety and efficacy of the Monarc device were recently reported in the EVOLUTION I study, where device implantation was successful in 82% of patients with FMR [94]. Implantation of the device could not be completed in the remainder of study patients due to tortuosity of the CS or lack of correctly sized devices, indicating that CS devices may not be appropriate for all patients. Additionally, 81% of patients experienced a reduction in MR grade of ≥1, and average regurgitant volume was reduced by >20% and maintained for 12-months (Table 3.1). Monarc implantation also seemed to provoke favorable MV and LV remodeling, with septal-lateral diameter, LV end-systolic volume, and LV end-diastolic volume all decreasing over the 12-month study period. Despite demonstrating safety and efficacy, further study of the Monarc device has stopped due to slow patient enrollment.

The Carillon Mitral Contour System (Cardiac Dimension, Inc.) is another CS annuloplasty device that operates on a similar principle [96-98]. The implant is constructed out of nitinol wire consisting of expandable distal and proximal anchors, connected by a tensioning bridge (Fig. 3.2B). A 9-F delivery catheter is used to place the distal anchor. The delivery catheter is retracted to allow expansion of the anchor and then advanced to complete anchor expansion. Manual traction on the delivery catheter is used to provide tension on the CS and MV annulus, and the proximal anchor is then released and expanded. The result of placement of the Carillon device is that the septal-lateral diameter is reduced. Unlike the Monarc device, this septal-lateral diameter reduction occurs immediately, and no further changes in bridge tension are designed to occur. The benefit of this design is that changes in MR can be immediately assessed, and the device can be removed if no improvement occurs.

Assessment of the Carillon device in the AMADEUS EU trial resulted in successful device placement in 30 of 48 patients with FMR, with failed placement in 18 due to a combination of CS access complications, slipping of the distal anchor, vessel perforation, and insufficient reduction in FMR [96]. By 30-day follow-up, 13% of patients had experienced a major adverse event. Echocardiographic assessment of the Carillon device indicated favorable changes at 1-month and 6-month time points: regurgitant volume decreased by over 30%, and reductions in LV end-systolic volume and LV end-diastolic volume, along with a significant decrease in septal-lateral diameter, were also observed (Table 3.1). Further clinical trials are currently underway.

A percutaneous CS annuloplasty device that uses a different approach to reduce the septal-lateral diameter is the cerclage annuloplasty technique [99]. The cerclage technology uses a guide-wire that is looped around the MV annulus and LV outflow tract, which is then replaced by a suture (Fig. 3.2C). Tension exerted on the suture constricts the MV annulus, reducing the septal-lateral diameter and the annulus circumference. The guide-wire is introduced via a 9-F introducer sheath into the right jugular vein. The guide-wire then crosses through the CS, enters the proximal great cardiac vein, and then proceeds into the first septal perforator vein, where it crosses the myocardium into either the right atrium or ventricle. The guide-wire is then ensnared in the right side of the heart and exchanged for a suture and tension-fixation device. The resulting implant is a suture, tensioned to approximately 400 grams, that encircles both the MV annulus and LV outflow tract. Early results from the cerclage technology in a porcine model demonstrated septal-lateral shortening of the MV annulus without introduction of a pressure gradient across the LV outflow tract. In order to prevent compression of entrapped coronary arteries located between the CS and MV annulus, a rigid-arch protection device was developed to direct compressive forces away from the entrapped artery. The rigid-arch protection device is a nitinol implant, 1.5 mm in outer diameter, and is placed under coronary angiography. Testing of the coronary artery protection device verified that no vessel compression or significant pressure gradient was present following implantation and tensioning of the Cerlage. Successful implantation of the cerclage occurred in 14 out of 16 consecutive swine in an initial feasibility study [99]. The cerclage technology also demonstrated acute reductions in septal-lateral diameter, LV end-systolic volume, and LV end-diastolic volume in a model of ischemic cardiomyopathy (Table 3.2). The cerclage technology addresses two common issues with CS annuloplasty devices: variable vessel anatomy, which can prevent placement of a large device in theCS, and coronary artery entrapment, in which vessels between the CS and MV are compressed due to the forces generated by the annuloplasty device.

While CS annuloplasty has been shown to reduce MR, induce favorable LV remodeling, and reduce the septal-lateral diameter of the MV annulus (Table 3.1), the changes in these values are much less than those recorded with surgical annuloplasty. Surgical treatment of MR using leaflet, chordal, or papillary muscle repair in combination with an annuloplasty ring has produced reductions in the septal-lateral diameter by as much as 40-50% and reduced LV end-diastolic and end-systolic volumes by 20-30% (Table 3.3) [100]. While CS annuloplasty has yet to be used in combination with any other repair, a comparison of these results demonstrates that CS annuloplasty may not be as effective as

Table 3.2: Assessment of Percutaneous MV Repair Devices: Data from Animal Studies

Treatment	Animal	Repair Type	Method	Regurgitant Volume (mL)				LVESV (mL)				LVEDV (mL)				S-L Diameter Diastole (mL)				S-L Diameter Systole (mL)				Ref
				n	Pre	Post	%Δ	n	Pre	Post	%Δ	n	Pre	Post	%Δ	n	Pre	Post	%Δ	n	Pre	Post	%Δ	
Acute																								
Cerclage	Porcine	Annuloplasty	MRI	-	-	-	-	16	106	98	-7.5	16	172	158	-8.1	16	34	29	-14.7	16	31	25	-19.4	[99]
Direct Leaflet Ablation	Canine	Leaflet Repair	TTE	3	77	37.5	-51.5	-	-	-	-	-	-	-	-	-	-	-	-	-	-	-	-	[10]
QuantumCor	Ovine	Annuloplasty	ICE	-	-	-	-	-	-	-	-	-	-	-	-	16	-	-	-21.7	16	-	-	-21.7	* [53]
6-month																								
QuantumCor	Ovine	Annuloplasty	ICE	-	-	-	-	-	-	-	-	-	-	-	-	4	-	-	-26.4	4	-	-	-26.4	[53]

** indicates distinction between diastolic and systolic S-L diameter was not made*

LVESV, left-ventricular end-systolic volume; LVEDV, left-ventricular end-diastolic volume; S-L Diameter, septal-lateral diameter

TTE, transthoracic echocardiography; MRI, magnetic resonance imaging; ICE, intracardiac echocardiography surgically-implanted annuloplasty rings. Challenges and limitations of the various percutaneous CS annuloplasty and MV repair techniques are summarized in Table 3.4.

Anatomical and Mechanical Studies of the Coronary Sinus. One of the challenges that must be addressed in development of percutaneous CS annuloplasty devices is the variable anatomic relationship of the CS and MV annulus between patients. Prior study using multi-slice computed tomography (CT) has indicated that the CS ostium – the location of the proximal anchor in the Monarc and Carillon devices – lies at the same level as the atrioventricular groove in only 54.5% of patients at end-systole [101]. This number drops to less than 10% for locations midway between the great cardiac vein (GCV) and CS ostium. Other studies using cadaveric hearts have indicated that the CS is superior to the MV annulus in normal hearts by a mean distance of approximately 9.7 mm from the P2 scallop [102]. For maximum effectiveness, the CS should lie within the same plane as the MV annulus. As the CS is used to displace the posterior section of the MV annulus, these results indicate that efficacy of percutaneous CS annuloplasty devices could be compromised in a large group of patients. Moreover, relative positioning of the CS and MV annulus has been shown to vary based on the degree of annular dilation, LV and left atrial enlargement, and severity of MR. Multi-slice CT has shown that a shift of the CS towards the MV annulus occurs with left atrial and LV enlargement [103]. However, some studies indirectly contradict these results, indicating that increased MR severity and annular dilation leads to an increase in the CS to MV annulus distance [104, 105]. Differences in measurement techniques and the longitudinal position along the CS in which the measurement was taken could account for these differences. Assessment of CS anatomy of each patient will be important in the future to determine eligibility for device placement.

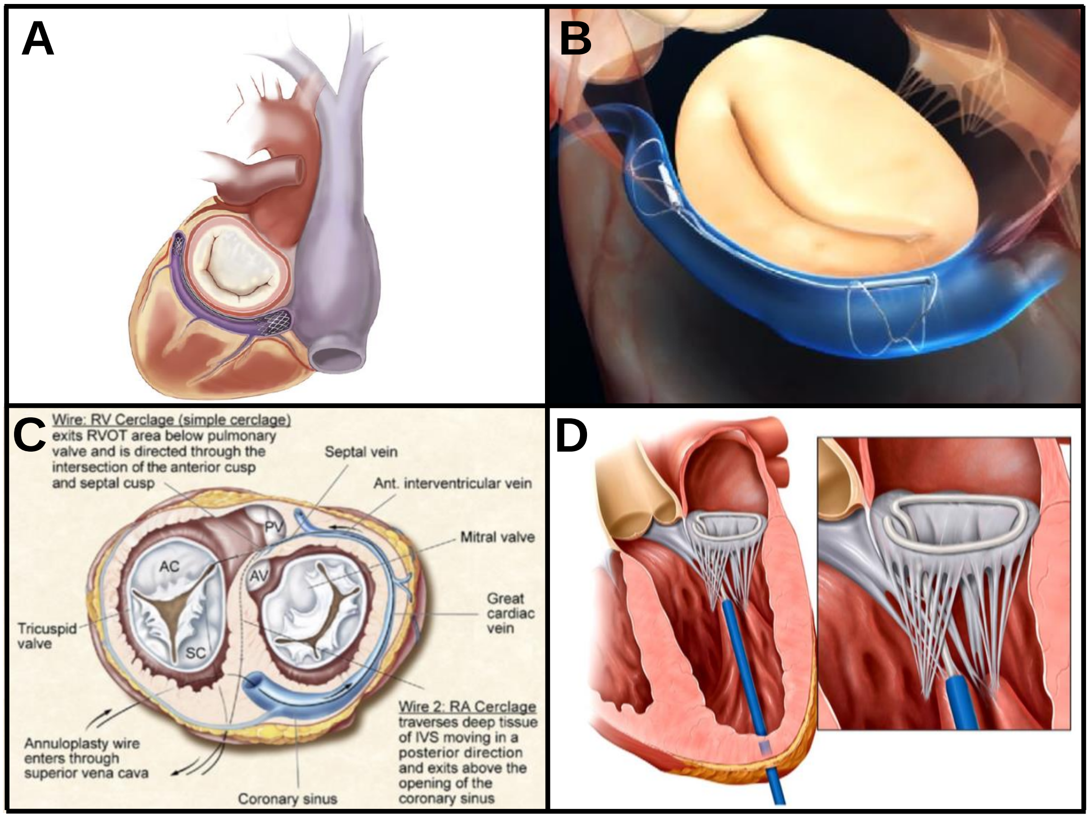

Fig. 3.2: Percutaneous Annuloplasty Devices
A: The Monarc implant located in the coronary sinus. Reprinted from [94]. The device consists of two stent-like anchors placed in the CS/GCV and CS ostium and a connecting bridge segment. **B:** The Carillon device operates on a similar principle, with two expandable anchors connected by a nitinol bridge. **C:** The cerclage system uses a wire, placed percutaneously, to encircle the MV apparatus and LV outflow tract. Reprinted from [99]. **D:** The QuantumCor device utilizes RF ablation to directly reduce the MV annulus circumference, without leaving an implant behind. Reprinted from [106].

Table 3.3: Echocardiographic Assessment of Surgical MV Repair with Annuloplasty

Treatment	LVESV (mL)				LVEDV (mL)				Avg S-L Diameter (mL)			
	n	Pre	Post	%Δ	n	Pre	Post	%Δ	n	Pre	Post	%Δ
3 months												
Carpentier-Edwards Physio ring®	23	45	48	6.7	23	138	117	-15.2	23	42.5	22.1	-48.0
Cosgrove-Edwards band®	21	45	33	-26.7	21	138	96	-30.4	21	41	24.1	-41.2
6 months												
Carpentier-Edwards Physio ring®	23	45	43	-4.4	23	138	110	-20.3	23	42.5	21.8	-48.7
Cosgrove-Edwards band®	21	45	37	-17.8	21	138	110	-20.3	21	41	23.9	-41.7

Data were acquired using real-time 3D echocardiograpy.
LVESV, left-ventricular end-systolic volume; LVEDV, left-ventricular end-diastolic volume; S-L diameter, septal-lateral diameter
Data taken from [100]

Another anatomical consideration in design of percutaneous CS annuloplasty devices is the possibility of coronary arteries traversing between the CS and MV annulus. Estimates vary, but coronary arteries have been determined to traverse between the CS and MV annulus in as many as 68-86% of patients [101, 103, 105]. Additionally, when only patients with severe MR were analyzed, the number of coronary arteries traversing the CS and MV annulus was 97% [103]. Compression of the coronary arteries due to percutaneous CS annuloplasty devices could lead to heart failure if severe enough and may exclude many patients from being eligible for device placement. The design of the cerclage device introduced a rigid-arch protection device that re-distributes the compressive forces exerted by the device on the CS, reducing coronary artery compression [99]. Future CS annuloplasty approaches may include a similar device.

As percutaneous CS annuloplasty devices exert considerable force on and around the MV apparatus, analysis of how these devices alter MV geometry and mechanics may be essential in prediction of the long-term efficacy and durability of repairs. Devices that increase leaflet strains, increase chordal elongation, or prevent annular dynamic motion may compromise long-term durability. Previous studies have tracked MV annular and/or leaflet motion in animal models using several methods, including: radiopaque, tantalum markers sutured to the annulus or leaflet surface and imaged using videofluoroscopy [107, 108], sonomicrometry using piezoelectric markers sutured to the MV annulus [109, 110], and 3-dimensional echocardiography [111, 112]. These studies have been used to determine that traditional, rigid annuloplasty rings unfavorably reduce MV annular dynamics by reducing the natural, sphincteric motion of the MV [108] and also increase excursion of the anterior leaflet, leading to higher bending stresses on the leaflet and possibly reduced repair durability [107]. Future assessment of percutaneous CS annuloplasty approaches could use these methods to enhance device design and predict long-term outcomes. Additionally, use of a technique for non-invasive assessment of MV annular dynamic motion using 3-D echocardiography was reported in an ovine model of ischemic cardiomyopathy [111]. Results demonstrated that percutaneous CS annuloplasty can reduce MV annular area without significantly reducing annular excursion, or its superior-inferior motion. The use of 3-D echocardiography to assess MV annular dynamic motion may play an important role in future assessment of percutaneous annuloplasty devices undergoing clinical trials.

In addition to the forces exerted by CS annuloplasty devices on the left heart, the CS/GCV undergoes a significant amount of motion over the course of the cardiac cycle. The dynamic motion of the CS/GCV imparts bending stresses on CS annuloplasty implants, and this may lead to degradation over time. In initial human trials with an early iteration of the Monarc device, separation of the nitinol bridge segment occurred in 3 out of 4 patients, necessitating a re-design of the device [95]. In order to better understand interactions between percutaneous CS annuloplasty devices and the CS vessel, prior study has analyzed the mechanical properties of the porcine and human CS. Pressure-inflation testing of the porcine CS demonstrated that the CS exhibited an S-shaped pressure-radius response – the CS is very distensible at low pressures (10-30 mmHg) and much stiffer at high pressures (40-80 mmHg) [113]. The CS was also found to dilate up to 88% at a pressure of 80 mmHg, and model fitting generated material parameters that can potentially be used for finite element simulations of device-tissue interactions. The biaxial mechanical properties of the CS were also quantified to compare differences between aged human, porcine, and ovine tissues, and the aged human CS was found to be significantly stiffer in both the circumferential and longitudinal directions than the porcine or ovine CS [114]. As it is generally older individuals who will receive percutaneous MV repairs, these results could have important implications in moving from animal to human clinical trials. Previously, the dynamics of the CS/GCV have been studied using CT angiography and indicated that the distance between the CS/GCV and the MV annulus can change by as much as several millimeters over the cardiac cycle, with the greatest distance occurring during end-systole [101]. The diameter of the CS/GCV also changes considerably over the cardiac cycle, and changes over 2 mm occur near the CS ostium. While motion of the CS/GCV relative to the MV annulus can be recorded, no estimates currently exist for the amount of force that may be exerted on devices within the CS. Further analysis of the dynamics between the CS/GCV and MV annulus may lead to more durable percutaneous CS annuloplasty approaches.

Direct Annuloplasty. In addition to approaches that re-shape the MV annulus via CS implants, several devices are currently in development that more directly alter the geometry of the MV annulus. These devices place an implant directly into the MV annulus in order to cinch the annulus and reduce the septal-lateral diameter. Two devices are of note, as they have demonstrated first-in-man results, although these results are yet to be published. The first of these is the Mitralign technology (Mitralign, Inc.), which places a pair of pledgets, via LV access, near each of the commissures that are then plicated and locked to reduce the septal-lateral diameter. The procedure had been performed in at least 12 patients thus far. The second device is the Accucinch Annuloplasty System (Guided Delivery Systems), also with first-in-man results. The Accucinch system uses an implant that encircles the MV annulus from one trigone to the other and uses a circumferential cinching force to restrict the annular size. Mechanical analysis of the effects of these devices on the MV structure is limited, and further study will be necessary to assess the utility of these devices in treating MR.

QuantumCor Direct Annular Ablation. One potential application for RF ablation in treatment of MR is direct annular ablation. The QuantumCor device (QuantumCor, Inc.) utilizes a circular probe that incorporates 7 RF electrodes around its radius [53, 54, 106]. The QuantumCor probe conforms to the annulus shape (Fig. 3.2D), and application of RF energy is applied directly to the annulus in order to reach electrode-tissue interface temperatures of at least 65°C. Like the MV leaflets, the annulus structure is supported by collagen, and application of RF energy to the MV annulus reduces the annulus circumference, with the intention of improving leaflet coaptation.

Acute study of the effects of RF ablation on annular size in an ovine model demonstrated a 23.8% reduction in septal-lateral diameter, with no thrombosis or damage to nearby coronary arteries, CS, or MV leaflets [53]. However, this study was performed in 16 healthy sheep with no or natural occurring MR, and the procedure was performed under cardiopulmonary bypass via access through the left atrial appendage. A 6-month follow-up study of 7 animals demonstrated that the reduction in septal-lateral diameter was durable, with a 26.4% reduction from baseline [54]. The QuantumCor device generated the largest percent reduction in septal-lateral diameter of any percutaneous device; however, the effect of this change on moderate to severe MR has not been assessed. Further study will be needed to determine device efficacy in a model of MR.

Conclusion

Percutaneous MV repair devices have received a great deal of interest in recent years, and several devices have been tested in animal models and clinical trials. Many of these devices attempt to mimic repairs that are currently performed surgically, including the MitraClip edge-to-edge repair and various percutaneous annuloplasty devices. As several of these devices alter the MV apparatus in new ways, including RF ablation treatment and CS annuloplasty, knowledge of the long-term efficacy and durability of these repairs is unknown. While it is still vitally important to analyze the effect of each device on acute MR reduction, MR recurrence rate, and mortality, engineering analysis of these devices can serve a role as a predictor of long-term outcomes. *In vitro* studies and animal testing have already led to insights into the changes that various percutaneous MV repair devices effect on the MV apparatus, but the amount of published studies in this area is still limited.

Percutaneous MV repair devices have been demonstrated to be less efficacious than surgical repair; in general, current percutaneous techniques have only been able to reduce mitral regurgitant volumes by approximately 20-40% and reduce MR by about 1 grade. Further mechanical analysis of percutaneous MV repair may be able to reveal the reasons for these sub-optimal results. For now, percutaneous MV repair devices are most suitable for high-risk patients who are ineligible for open-chest surgery. However, this is still a significantly sized group of potential patients, as a 2007 survey found that 49% of patients with severe symptomatic MR were not operated on due to old age, impaired LV function, or multiple co-morbidities [4]. Prior data has suggested that treatment with percutaneous repair produces superior outcomes in high-risk patients, and when all patients are considered, percutaneous treatment reduces the complication rate compared with open-chest repair or replacement. With safety rates in mind, several percutaneous MV repair devices may be used to treat high-risk patients in the near future; however, efficacy of these devices must be improved before widespread usage can begin. Finally, current percutaneous treatments for MR have been shown to be limited in their usage based on variability in patient anatomy and the type of lesion present. Some of these limitations are summarized in Table 3.4. As a result, no one percutaneous approach will be correct for all patients or causes of MR.

Table 3.4: Challenges and Limitations in Percutaneous MV Repair Devices

Edge-to-Edge Repair

- Limited to treatment of regurgitant jets originating from malcoaptation of the middle scallops of the anterior and posterior leaflets [48]
- Can introduce moderate stenosis in MVs with an annular area <4.0 cm^2 [48]
- Leaflet geometry must meet several requirements: coaptation length ≥2 mm, coaptation depth <11 mm, flail gap <10 mm, flail width <15 mm [18, 48]

RF Ablation (Leaflet, Chordae, and Annulus)

- Procedure cannot be reversed if too much RF energy is applied or MR is not reduced
- Introduces the potential for permanent damage to surrounding structures
- Mechanical strength of ablated tissues may be temporarily reduced [54]
- Creates detectable regions of coagulation necrosis [10, 54]

CS Annuloplasty

- Variable position and size of the CS in relation to the MV annulus between patients limits the number of patients who are anatomically eligible for device placement [101-105]
- The superior position of the CS in relation to the MV annulus reduces the cinching effect of percutaneous CS devices on the posterior annulus [102, 103]
- The CS undergoes significant motion relative to the MV annulus during the cardiac cycle, imparting strain on devices implanted in the CS [101]
- Coronary arteries frequently traverse between the CS and MV annulus and can be compressed and restricted by percutaneous CS devices [101, 103, 105]

Future Perspective

Many forms of MV repair currently utilize multiple techniques to reduce MR, especially in treatment of DMR. Leaflet resection or edge-to-edge repair is often used in combination with an annuloplasty ring in order to enhance leaflet coaptation and prevent annular dilation. Future use of percutaneous MV repair devices, several years from now, may take a similar approach by combining multiple devices to enhance the efficacy of MR reduction. As most published results of percutaneous MV repair devices typically report MR reduction by approximately 1 grade, combining multiple devices for enhanced efficacy may be likely in the future. Most percutaneous MV repair devices have gone through their first published testing in animal models, but the development of *in vitro* flow loops and other methods of bench-top analysis can permit assessment of many percutaneous repair devices before undergoing costly animal testing. *In vitro* mechanical testing and marker tracking in animal models can provide quantitative information about how current and future percutaneous repair devices alter MV mechanics and geometry, leading to insights into the durability and long-term efficacy of repairs. Additionally, more advanced quantitative imaging techniques, including multi-slice CT and 3-D echocardiography will enable better clinical assessment of patient eligibility and device function, both acutely and long-term. As it is difficult to duplicate the complex surgical repairs that are currently performed under open-heart surgery, development of future percutaneous repair devices may be very specific to the MV structure affected – including the MV annulus, leaflets, chordae, papillary muscles, and the LV. In terms of the capability of treating each of these structures, the field of percutaneous MV repair devices is relatively new, but recent developments may have the ability to treat many of these structures in the coming years.

Executive Summary

Introduction

- Current percutaneous devices have the ability to reduce MR by approximately 1 grade, which is less than that typically achieved by surgical repair or replacement of moderate-severe and severe MR
- Due to reduced rates of efficacy and increased safety compared with open-heart surgical repair and replacement, current percutaneous approaches are most suitable for high-risk patients who are ineligible for current treatments

Leaflet Repair

- The MitraClip facilitates leaflet coaptation by creating a double-orifice MV, and the EVEREST II trial has demonstrated a 55% end-point efficacy at 12-months
- RF ablation, combined with cryo-anchoring for catheter stability, can reduce leaflet size with the application of thermal energy. In vivo results are limited, and further study is needed

Annuloplasty Devices

- The Carillon and Monarc CS annuloplasty devices create septal-lateral shortening via placement of a metal implant in the CS; however, variations in patient-to-patient anatomy, including the height of the CS relative to the MV annulus and coronary arteries that may traverse between the CS and MV will limit the use of this technology
- The cerclage technology uses a suture, threaded around the MV annulus and LV outflow tract, to generate cinching, and features a rigid-arch protection device to protect against coronary artery compression

- The QuantumCor device uses RF ablation to reduce the MV annular circumference, demonstrating a >20% reduction in an initial feasibility study

Future Perspective

- In the future, percutaneous annuloplasty approaches may be used in combination with percutaneous leaflet repair techniques to increase overall efficacy and durability
- Analysis of how novel percutaneous approaches affect MV mechanics may provide insight into the long-term efficacy of repairs

Chapter 4

THE RFC CATHETER SYSTEM

RFC Catheter Design Considerations

The focal point of this work is the design and performance of the RFC catheter for thermal shrinkage of MV leaflet tissue. Throughout the development process, it has been necessary to design and build several different RFC catheter prototypes in order to execute different experiments and to iteratively improve thermal shrinkage performance. These prototypes have been designed for static bench testing (Fig. 4.1A), for bench testing in a dynamic left heart flow simulator (Fig. 4.1B), and for in vivo animal studies (Fig. 4.1C). As described in previous chapters, the RFC catheter uses an RF ablation element to produce tissue temperatures greater than 65°C for tissue shrinkage. To provide constant contact with the MV leaflets in a beating heart environment, a cryo-anchoring element is used and cooled to temperatures between -20°C and -50°C. The novelty of the RFC catheter is the combination of these two elements – resistive heating of the RF electrode and sub-freezing temperatures of the cryo-anchor – into one therapeutic device. The design goal is to place these two opposing elements on a catheter such that 1) RF electrode contact with the leaflet tissue is maximized and 2) the RF ablation and cryo-anchoring elements do not interfere with each other. As the RFC catheter is intended as a percutaneous repair device, the final design must be optimized for vascular access and maneuverability in the heart. Thus, catheter outer diameter must remain small (10 Fr or less) and the distal catheter tip segment must be steerable in at least one direction. The prototype for in vivo use described below was designed with these considerations in mind. When used percutaneously, the RFC catheter

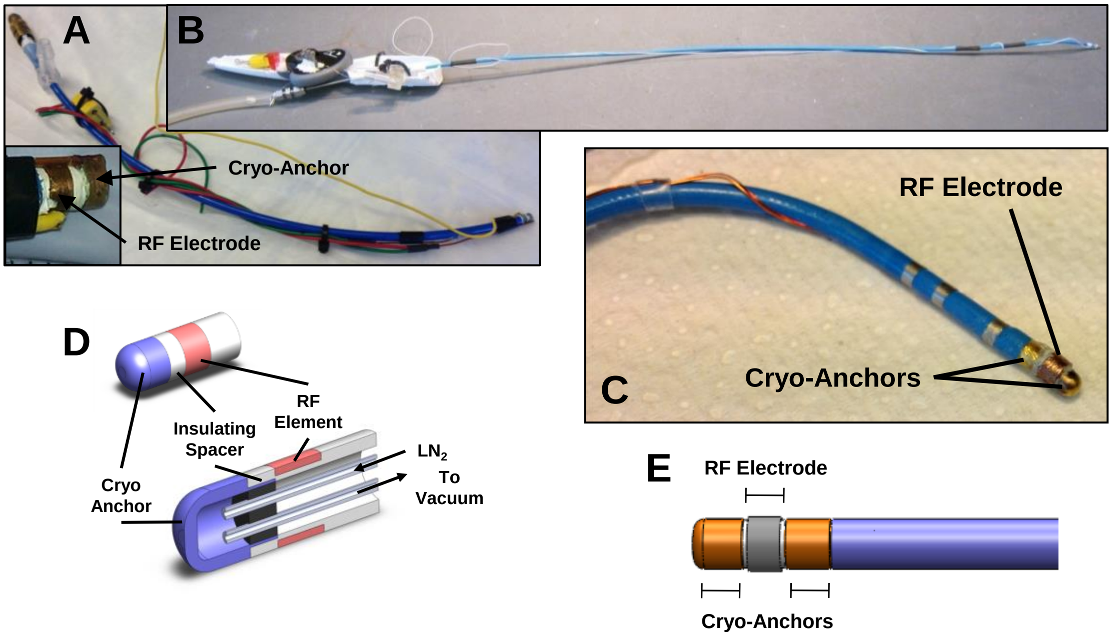

Fig. 4.1: Evolution of Catheter Prototypes

A: RFC catheter prototype for static bench experiments. **B:** RFC catheter prototype for bench studies in a left heart flow simulator. **C:** Close view of the RFC catheter prototype for non-survival animal studies. **D:** CAD drawing of the static bench prototype with liquid nitrogen or nitrous oxide delivery. **E:** CAD drawing of a prototype for non-survival animal studies showing the positions of the cryo-anchors and RF electrode.

is intended for use with a bi-directional steerable sheath via femoral access. The steerable sheath is guided up through the vena cava and into the right atrium, where a Brockenbrough needle is used to puncture the interatrial septum to pass the sheath into the left atrium. The RFC catheter is then passed through the sheath and into the left atrium, where it can be guided to the leaflets by transesophageal echocardiography and/or fluoroscopy.

Static Bench Prototype for Initial Feasibility Studies

In order to first demonstrate the feasibility of using cryo-anchoring and RF ablation together on a catheter, and to determine the geometrical and mechanical effects of RF ablation and cryo-anchoring treatment of MV leaflets, a simple prototype for static bench top experiments was developed (Fig. 4.2A). This prototype uses liquid nitrogen to cool the catheter tip, delivered through a large (0.05″ inner diameter) polyimide tube housed inside the main catheter body of Nylon 12. The 1.9 mm long cryo-anchor of the static prototype is located at the most distal point on the catheter shaft, with a 1.9 mm long RF electrode located just proximal. The outer diameters of the RF electrode and cryo-anchor are 4 mm (12 Fr). A thermocouple is used to monitor the cryo-anchor temperature and liquid nitrogen is removed from inside the catheter under vacuum.

A commercially available RF generator (Osypka) is used to deliver RF energy to the catheter (Fig. 4.2B). The cryo canister is electrically controlled in a binary fashion using an attached servo motor. Cryogen and RF energy delivery protocols were programmed on an Arduino microcontroller for repeatability. This was the first RFC catheter prototype, and it enabled the first tests of treatment feasibility to be performed on the lab bench. These experiments are described in Aim 1.

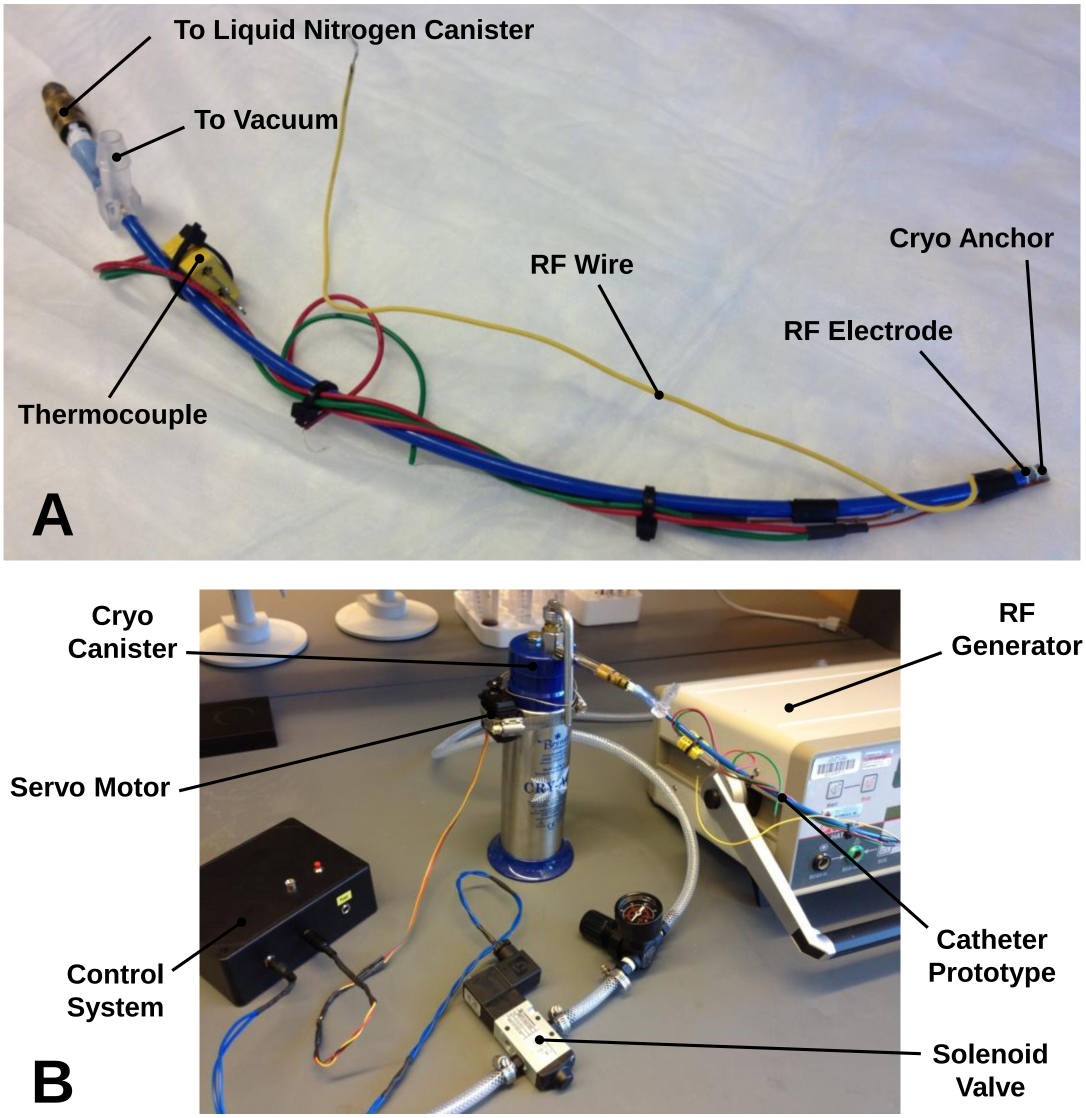

Fig. 4.2: First RFC Catheter Prototype – Static Bench Prototype
A: The RFC catheter static bench prototype. **B:** Complete static bench prototype including the RF energy and cryogen delivery systems. The compact design of the static bench prototype enables quick and easy experiments to be performed on the lab bench when steerability or extended reach are not needed.

RFC Catheter Prototype for In Vivo Studies

The current iteration of the RFC catheter is a custom device built on a steerable Freezer MAX Cardiac Cryoablation catheter (Medtronic, Minneapolis, MN). The rationale for using the Freezer MAX catheter is that components for a steerable catheter are not readily available off the shelf, and using existing components reduces cost and development time. Additionally, all cryo components are already integrated into the Freezer MAX catheter. Several non-trivial modifications were made to the Freezer MAX catheter, and a comprehensive guide to fabricating the RFC catheter can be found in the Appendix. The modifications begin with machining of the cryo applicator to provide space for the RF electrode by removing a void of material in the middle of the cryo applicator with an end mill (Fig. 4.3). The void in the cryo-anchor is then filled with epoxy to provide insulation, and a 3.0-3.3 mm (10 Fr) diameter RF electrode is placed over it. This configuration results in one cryo-anchor on either side of the RF electrode, providing maximum leaflet contact between the RF electrode and MV leaflet (Fig. 4.4A). It has been found through trial and error that cryo-anchor size does not need to be significant in comparison to the RF electrode. Cryo-anchors with outer diameter 2.3 mm (7 Fr) and 1 mm long on either side of the RF electrode are sufficient for robust leaflet cryo-anchoring.

The completed catheter tip consists of an RF electrode placed between two cryo-anchors, and the RF electrode is kept electrically insulated (Fig. 4.4A). Liquid nitrous oxide delivery to the inside of the catheter tip, which is kept under vacuum, provides the cooling power for the cryo-anchors. The catheter steering system, cryo thermocouple, and cryogen delivery tubes were retained, largely unmodified. The RF electrode wire and RF thermocouple are run outside the Freezer MAX catheter shaft and secured with clear FEP shrink tubing. All inputs and outputs to the catheter can be seen in Fig. 4.4B.

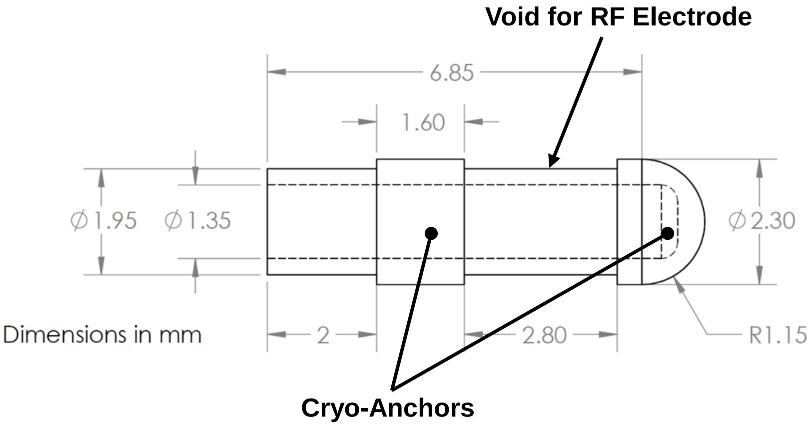

Fig. 4.3: Cryo-Anchor Dimensions
Dimensions of the cryo-anchor of the RFC catheter for in vivo use.

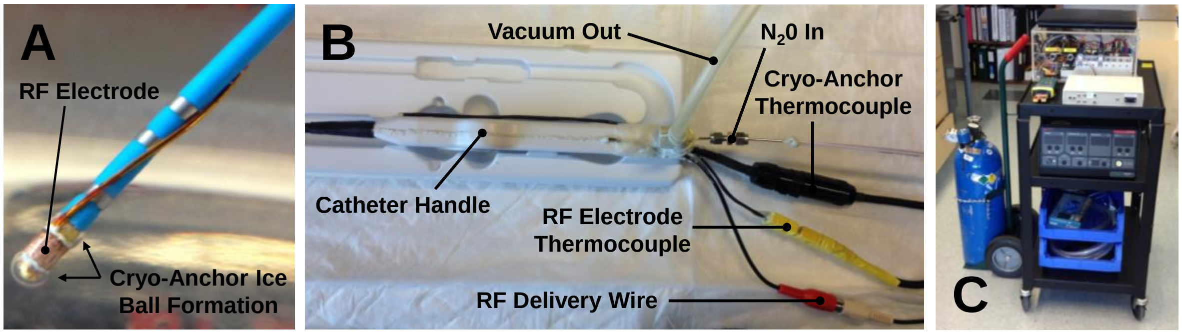

Fig. 4.4: RFC Catheter Prototype for In Vivo Use
A: RFC catheter tip showing the orientation of the RF electrode and cryo-anchors, with ice ball formation. **B:** Modified Freezer MAX catheter handle with new inputs and outputs for cryogen delivery, temperature measurement, and RF ablation. **C:** Complete RFC catheter control system with RF generator, cryogen delivery system and nitrous oxide tank, and control electronics.

To control and measure the outputs to the RFC catheter, control software and electronics were developed using LabView and the open-source Arduino platform (Fig. 4.5). The software controls nitrous oxide delivery to the catheter tip by regulating the duty cycle to a cryogenic solenoid based on the temperature desired. Once the nitrous oxide delivery lines have been primed, cryo-anchoring temperatures are achieved within 1 second after the user initiates the cryo-anchor (Fig. 4.6). RF power output to the catheter electrode is set on a commercial RF generator (EPT-1000, Boston Scientific). The control software records temperature data from the RFC catheter and uses this information to regulate the cryogenic solenoid duty cycle to modulate cryo-anchor temperature. During ablation treatment, ablation temperature is monitored and RF power is manually throttled to maintain ablation temperature within a pre-determined range. For maximum ablation effectiveness, it is desirable to use the highest ablation power that does not result in excessive tissue charring or coagulum formation [49]. As the RF electrode is in very close proximity to the cryo-anchors on the RFC catheter, RF electrode temperature, and the measurement junction, are significantly affected by the cryo-anchors. Thus, the ideal RF electrode temperature is actually many degrees cooler than the desired tissue temperature. Calibration of the desired RF electrode temperature is described in the Appendix. Control software, cryo delivery hardware, and control system electrical schematics can also be found in the Appendix.

Key to the RFC catheter treatment strategy is its ability to selectively cryo-anchor to the MV leaflets, depending on the location of leaflet enlargement or chordal rupture. In a simulated flow environment, leaflet attachment is possible to one (Fig. 4.7A-B) or both leaflets (Fig. 4.7C) at a time, depending on the placement of the catheter in relation to the leaflet free edge. Cryo-anchoring to regions closer to the free edge are more likely to result in bi-leaflet attachment, while cryo-anchoring in the leafelt belly region or closer to the annulus results in single leaflet attachment. The positions of the cryo-anchors on either side of the RF electrode encourage direct contact with the leaflets for enhanced tissue heating. The studies that follow in the remaining chapters will report RFC catheter performance according to the three specific aims discussed in Chapter 1.

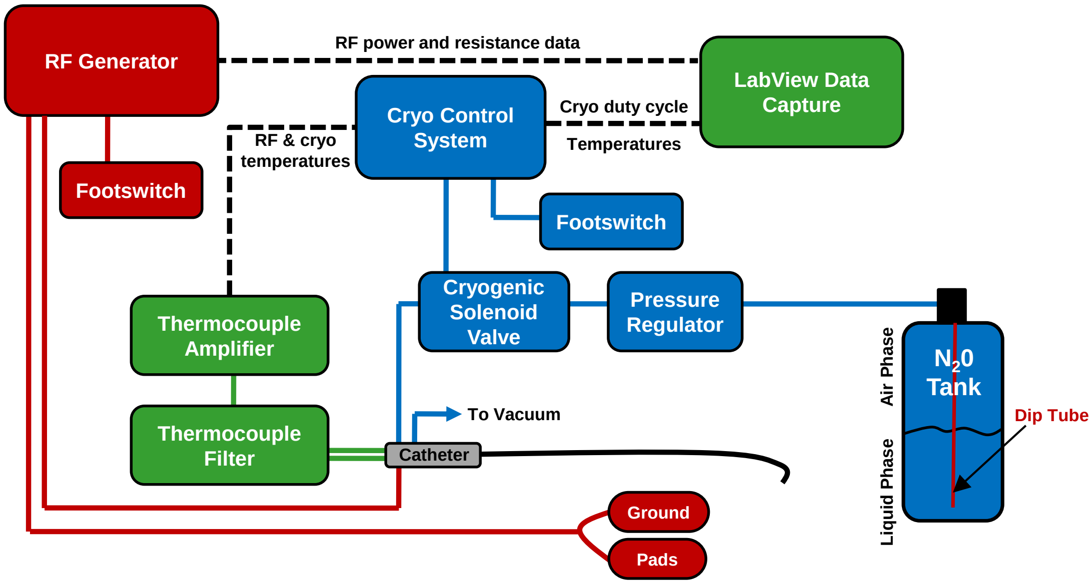

Fig. 4.5: RFC Catheter System Key Components and Data Transfer Between Systems
Schematic representation of RFC catheter system key components.

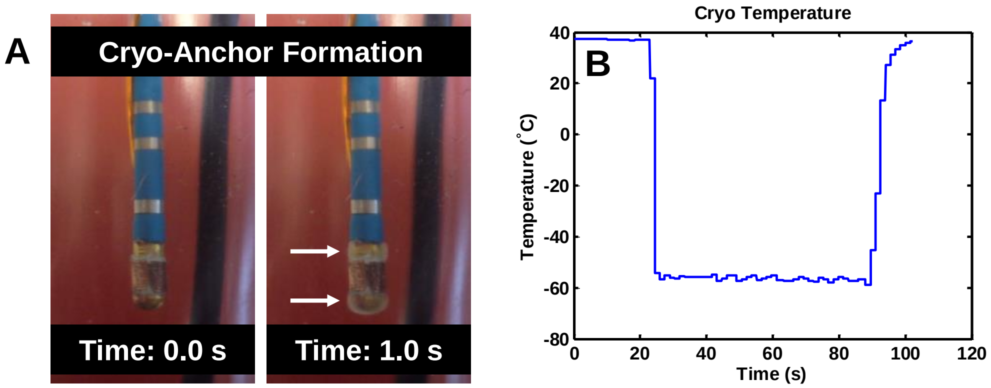

Fig. 4.6. Time to Cryo-Anchor
A: Time to cryo-anchor onset with catheter shown in a left heart flow simulator flowing at 5 L/min. Left panel: nitrous oxide flow off. Right panel: cryo-anchor temperatures have been achieved. **B:** Typical cryo-anchoring temperature measurements during in vivo use.

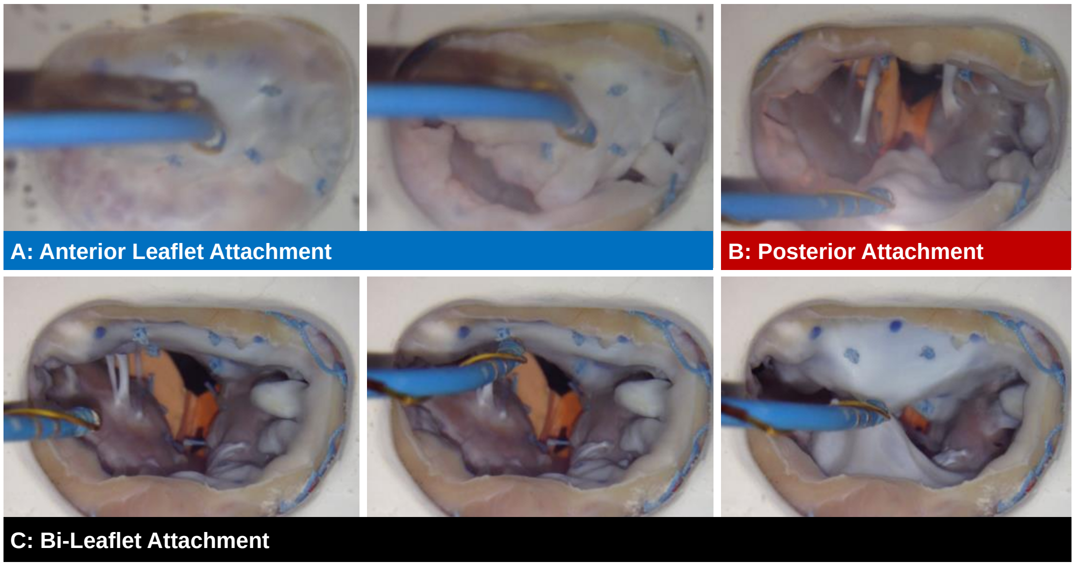

Fig. 4.7: RFC Catheter Cryo-Anchoring in a Physiologic Flow Environment
Various RFC catheter cryo-anchoring placements shown in a left heart flow simulator at physiologic flow rates and pressure. **A:** Anterior leaflet attachment in systole (left) and diastole (right). **B:** Posterior leaflet attachment in diastole. **C:** Bi-leaflet attachment, with the catheter cryo-anchors placed close to the leaflet free edge. Bi-leaflet cryo-anchoring forms a double-oriface valve, similar to that produced by an edge-to-edge repair.

Chapter 5

AIM 1 – PART 1: INITIAL RFC CATHETER DEVELOPMENT AND FEASIBILITY EXPERIMENTS

Text and figures for Chapter 5 taken from:

> *Boronyak SM, Merryman WD: "Development of a Simulataneous Cryo-Anchoring and Radiofrequency Ablation Catheter for Percutaneous Treatment of Mitral Valve Prolapse." Annals of Biomedical Engineering Vol. 40. Issue 9, 1971-81, 2012.*

Introduction

The purpose of this study was to determine the feasibility of using cryo-anchoring and RF ablation on the same catheter tip and to quantify the geometrical, biomechanical and thermodynamic effects of RF ablation on porcine MV leaflets. We hypothesized that an RF ablation catheter that utilizes a cryo-anchor will effectively adhere to and alter MV leaflet geometry and compliance, reducing MV leaflet size at maximum systolic load. To test this hypothesis, we developed a catheter prototype containing both a cryo-anchor for attachment and stability and an RF electrode for ablation. To investigate the effects of using cryogenic temperatures and resistive heating in close proximity, we quantified changes in biaxial mechanical compliance of MV leaflets and used infrared (IR) thermal imaging to discern distinct thermal regions within the tissue. We also quantified the anchor strength of the cryo-anchor both with and without RF ablation. These data support our hypothesis that simultaneous cryo-anchoring and RF ablation effectively reduces MV leaflet size, while further demonstrating that cryo-anchoring and RF ablation can function effectively in close proximity on a single catheter tip.

Materials and Methods

Catheter Prototype. A 4 mm (12 French) diameter catheter prototype was developed containing both a cryogenically cooled anchor (cryo-anchor) and an RF ablation electrode (Fig. 5.1A and Fig. 5.1B). The cryo-anchor and RF electrode reside in-line on the catheter shaft and are separated by a 1 mm spacer, with the cryo-anchor on the most distal point of the catheter. Both the cryo-anchor and RF electrode are constructed out of hollow copper rod and are approximately 1.9 mm in length. The cryo-anchor is thermally connected via a solder joint to an inner copper rod containing a lumen which allows liquid nitrogen delivery. Teflon is used to insulate the RF electrode from the cryo-anchor and inner copper rod, and a thermocouple attached to the outer surface of the cryo-anchor records the temperature at the anchor-tissue interface. RF ablation is performed with an Osypka HAT 300 generator, capable of delivering a 500 kHz electrical signal at powers of up to 50 W to the RF electrode on the catheter tip. Liquid nitrogen is contained inside a handheld canister (Cry-Ac, Brymill Cryogenic Systems) and delivered to the catheter tip under vacuum by an inner lumen housed inside the catheter.

Control of RF ablation and liquid nitrogen delivery is performed via custom built control electronics for synchronization and repeatability (Fig. 5.1C). Liquid nitrogen flow control is binary, and a servo motor is used to switch flow on and off. The sequence used for liquid nitrogen flow was developed to anchor the catheter tip to the tissue sample prior to RF ablation and to maintain anchoring throughout the ablation (Fig. 5.1D). Control of the RF generator was performed by interfacing with the footswitch port on the generator, with air flow controlled by a solenoid valve and control electronics. For each ablation, one of three RF protocols was utilized at 25, 45, or 50 W of power for 15, 20, or 30 s, respectively (Fig. 5.1D). Due to the time required for the RF generator to increase the power to the desired set-point (~3 s), the total energy output was lower than that produced by the product of time and power (Joules = W s). The final energy delivery to the tissue, as recorded by the generator for each of the 25, 45 and 50 W ablations, was 350, 850, and 1250 Joules (J), respectively.

Tissue Preparation. Healthy porcine MV leaflets were obtained from a local abattoir (Hampton Meat Processing, Hopkinsville, KY), excised on-site, and frozen in phosphate buffered saline (PBS) at -20°C until testing. Anterior leaflets were chosen for the biomechanical and thermal imaging studies due to their larger and more continuous surface area compared to posterior leaflets, although it is noted that posterior leaflets are more often affected by MVP [20]. The center portion of the leaflets were used and trimmed into rectangular sections (Fig. 5.2A) approximately 12 mm in the radial direction and 15 mm in the circumferential direction. The center portion was used as it experiences the most homogenous strains during MV closure [115]. For the anchor strength study, posterior leaflets were used for testing.

Biaxial Mechanical Testing. Biomechanical analysis was performed using a custom-designed biaxial mechanical testing device (Fig. 5.2A) [9]. Samples were loaded in each direction up to a membrane tension comparable to that experienced by the leaflet during systole (120 mmHg ≈ 90 N/m of membrane tension), and all testing was performed with samples fully submerged in PBS at 37°C. Prior to testing, each sample was pre-conditioned over ten loading cycles to 90 N/m with a 15 s rise time. Following pre-conditioning, a marker reference was recorded and used as the unloaded state. Samples were then tested for ten cycles with a 15 s rise time to 90 N/m in order to determine untreated compliance.

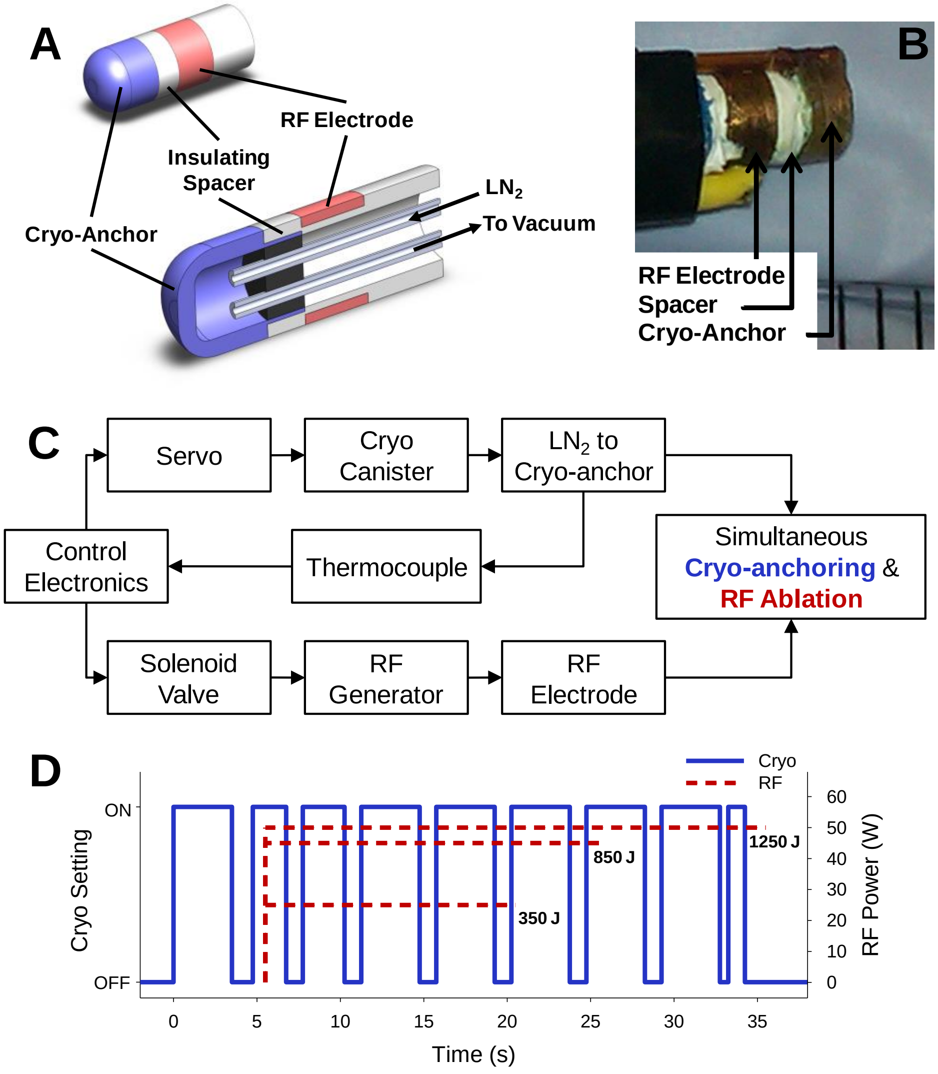

Fig. 5.1: First Prototype Design and Control Scheme
A: Solid model cut-away of the catheter prototype design, indicating the relative positions of the cryo-anchor, insulating spacer, and RF electrode. **B:** Catheter prototype tip used for all treatments of tissue (scale bar = 1/8″). **C:** Flow chart representation of the control system used to integrate and synchronize cryo-anchoring with RF ablation for treatment of tissue. **D:** Sequence programmed into the controller for performing RF ablation treatments with cryo-anchoring. Note that liquid nitrogen delivery to the catheter tip begins prior to RF ablation in order to first anchor the catheter tip to the tissue surface. RF power is represented as being applied instantaneously; however, it took ~3 s for RF power to reach target power. Final RF energy delivery (J=Joules) is indicated on the plot and represents total energy delivery of each treatment.

Stress-strain behavior has been found to be independent of loading rate for cycles with rise times of up to 15 s, thus tissues were not loaded at physiologic rates [116].

After determining leaflet biomechanical properties, samples were loaded to 10 N/m and subjected to one of the following four treatments with the catheter prototype. In order to determine the biomechanical effects of the cryo-anchor alone, samples were kept in contact with the cryo-anchor for 30 s at approximately -20 to -30°C (n = 3). To test the combined effects of cryo-anchoring and RF ablation, tissues were subjected to one of three treatment groups (n = 5) as described earlier and shown in Fig. 5.1D. During treatment, the fluid level in the bath was lowered to just below the surface of the sample in order to ensure that maximal energy transfer was through the tissue. By performing treatment such that all RF energy must pass through the sample, the amount of RF energy required to invoke the recorded biomechanical changes can be determined. The alternative is to completely submerge leaflets during treatment, but this provides a very low resistive path to ground, which bypasses the target tissue via direct conduction through the PBS bath. Four ground electrodes were placed in the bath, approximately 13 cm away from the tissue, to complete the electrical circuit for RF ablation. Following treatment, samples were returned to their unloaded state, a new marker reference was recorded to determine changes in unloaded geometry, and samples were loaded for ten cycles to 90 N/m. All data reported is from the tenth loading cycle of each experiment.

All analysis of biaxial mechanical data was performed using MATLAB (Mathworks). Marker positions recorded just prior to loading were used to determine geometric changes of the unloaded tissues due to treatment with the catheter prototype. Unloaded marker area was calculated as the area enclosed by the polygon connecting the four markers. Additionally, the percent change in the determinant of the deformation gradient tensor, **F** (% change in det(**F**)) was used to provide a quantitative assessment of the biomechanical changes of the tissue at maximum systolic load. The determinant of **F** is the ratio of the deformed marker area to the marker area of the reference state, where:

$$\boldsymbol{F} = \begin{bmatrix} F_{11} & \kappa_1 \\ \kappa_2 & F_{22} \end{bmatrix}$$

F_{11} and F_{22} represent the stretch ratios in the circumferential and radial directions, respectively, and κ_1 and κ_2 provide a measure of shear. det(***F***) was determined at 90 N/m before and after treatment, and the unloaded marker reference state recorded just after pre-conditioning was used for all calculations. Because the same marker reference state is used to determine ***F*** in both the untreated and treated conditions, % change in det(***F***) provides a direct comparison of systolic leaflet deformation before and after treatment. Therefore, we refer to % change in det(***F***) at 90 N/m as % change in areal systolic deformation. In addition to reporting changes in det(***F***) due to treatment, we also report % change in axial systolic deformations which are changes in F_{11} and F_{22} at 90 N/m. For a more complete description of the calculation of ***F*** from biaxial mechanical testing, see Humphrey [117].

Infrared Thermal Imaging. Thermal imaging of simultaneous cryo-anchoring and RF ablation was performed using an IR camera (ThermoVision A20M, FLIR Systems) with a measurement range of -20°C to 250°C and accuracy of ±2°C. Previous studies have used IR imaging to identify the lethal isotherm of RF lesions [118, 119]. Leaflets were imaged in a custom built bath, and the camera was placed below the bath for imaging of full thickness changes in temperature distribution (Fig. 5.2B). An IR window (IR Material Window, Edmund Optics Inc.) was placed at the bottom of the bath to allow imaging through the bottom surface by allowing transmission of IR wavelengths. Prior to treatment, an image

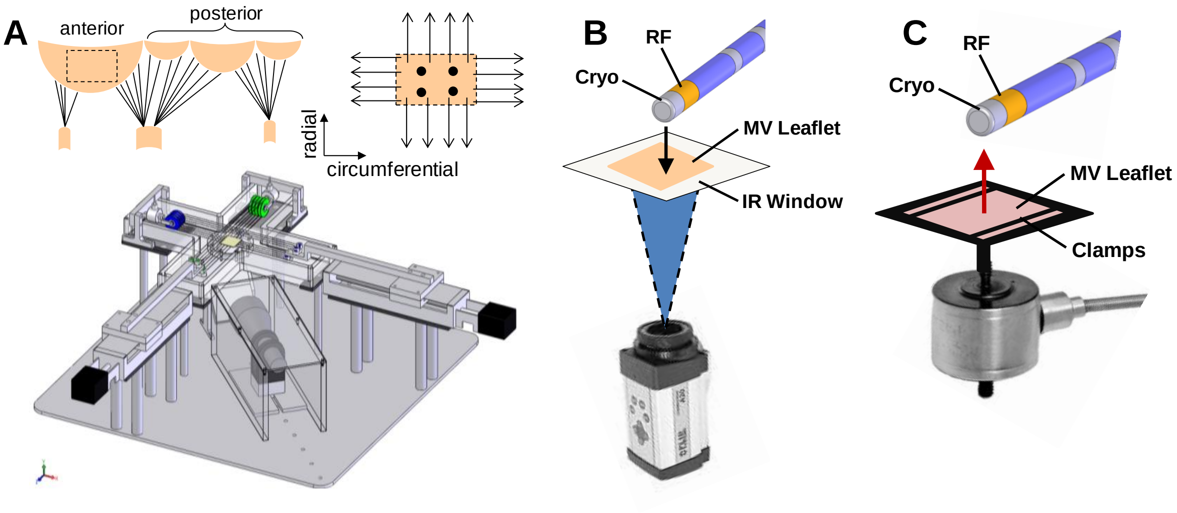

Fig. 5.2: Static Ex Vivo Experimental Set-Ups
A: Mitral valve anatomy with marker placement and biaxial testing device with leaflet tissue in place. **B:** Set-up for full thickness thermal imaging. The IR camera is placed below in order to measure the temperature distribution throughout the entire surface of the tissue. An IR window allows transmission of IR wavelengths for unimpeded temperature measurement. **C:** Set-up for measurement of anchor strength of the cryo-anchor. Leaflets are clamped into the load cell assembly, and the maximum load is recorded.

was taken of a calibration phantom to determine the x and y distance scales. Testing was performed in PBS at room temperature, and the fluid level was lowered to just below the top surface of the tissue to allow maximal energy transfer through the leaflet. Four ground electrodes were placed in the bath in a circular pattern, each approximately 13 cm from the center of the leaflet. During ablation, a non-conductive plate was placed over the leaflet in order to maintain contact of the entire leaflet surface with the IR window. This was done to ensure that the temperatures measured were of the leaflet itself and not the fluid between the leaflet and IR window. All samples were then treated using one of the ablation sequences in Fig. 5.1D (n = 3 for each of the 350, 850, and 1250 J sequences), and images of the treatment were recorded at 1 Hz beginning at the onset of RF ablation using ThermaCAM Researcher software and synchronized with the ablation sequence using the control electronics. Images were then analyzed in MATLAB to produce thermal contour plots of the tissue. Additionally, the area of tissue heated to > 65°C was quantified in order to provide a measure of the extent of thermal contracture of the extracellular matrix collagen, and the tissue area < 0°C was also quantified to provide an estimate of the attachment area of the catheter prototype.

Anchor Strength. In order to assess the anchor strength of the cryo-anchor both with and without RF ablation, a submersible load cell was used (Model 31 Mid, Honeywell). Posterior MV leaflets were clamped onto the load cell assembly and completely submersed in PBS at 37°C (Fig. 5.2). Leaflets were completely submersed during treatment in order to test the anchor strength of the cryo-anchor in an environment that more closely mimics the in vivo case. The output from the load cell was amplified using a custom built amplifier circuit and read into LabView using a data acquisition card (NI 9205, National Instruments). Anchor strength was tested at one of two protocols (n = 5 for each protocol). For the "Cryo Only" protocol, liquid nitrogen was pumped under vacuum to the catheter tip continuously for 10 s, and the catheter was then immediately pulled from the leaflet surface until separation. To determine the loss of anchor strength resulting from application of RF energy, the "RF + Cryo" protocol consisted of 5 s of continuous liquid nitrogen delivery, followed by 10 s of RF ablation at 50 W with continuous liquid nitrogen delivery. The catheter was then pulled away from the leaflet surface until separation. In both cases, the maximum load during separation was recorded. Maximum load was converted to anchor strength by dividing the load by 0.12 cm^2, the approximate area of the cryo-anchor in contact with the tissue.

Statistics. Data are presented as mean ± SE. To analyze significance of changes due to combined RF ablation and cryo-anchoring for the biomechanical and anchor strength studies, data were analyzed using a one way ANOVA (α = 0.05) for multiple pair wise comparison (Holm-Sidak method).

Results

Tissue Geometry and Compliance. Prior to treatment, leaflets displayed a typical, anisotropic mechanical response to loading [50], with the radial direction much more compliant than the circumferential direction (Fig. 5.3A and Fig. 5.3B). This is due to collagen fibers being preferentially aligned in the circumferential direction. Following 30 s of cryo-anchoring, MV leaflets experienced negligible changes in geometry and mechanical response (Fig. 5.3A). However, after 1250 J of RF ablation with cryo-anchoring, leaflets underwent significant changes. In the circumferential direction, changes in systolic deformation were attributable primarily to shrinkage of the tissue, as indicated by a large shift in stretch ratio in the unloaded state (membrane tension = 0 N/m), while the radial direction underwent a decrease in systolic deformation with little geometric changes.

There was a consistent trend of decreasing marker area with increasing RF energy (Fig. 5.3C), due primarily to decreases in length in the circumferential direction (Fig. 5.3D). Change in systolic deformation was analyzed at maximum load, 90 N/m (Fig. 5.3E and Fig. 5.3F), with all deformations referenced to the marker reference state recorded just after pre-conditioning. Similarly to geometric changes, the areal systolic deformation decreased with increasing RF energy (Fig. 5.3E), due primarily to shrinkage in the circumferential direction. Additionally, there was a consistent trend of decreasing axial systolic

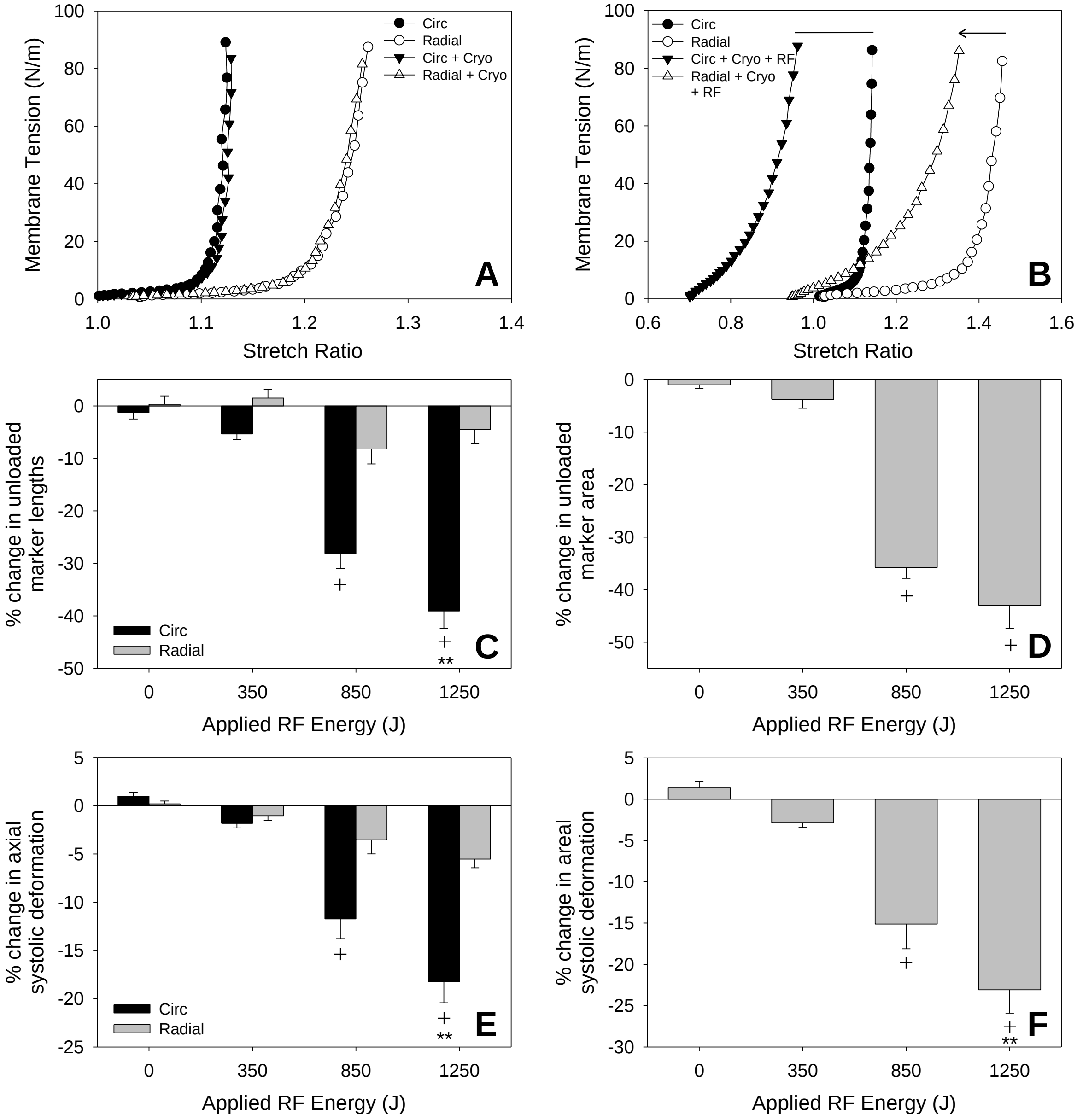

Fig. 5.3: Biaxial Mechanical Characterization of RF Ablation-Treated MV Leaflets
Biaxial, membrane tension vs. stretch ratio following 30 s of cryo-anchoring without RF ablation (**A**) and with 1250 J of RF ablation (**B**). **C:** % Change in unloaded marker area for each treatment group (0 J represents cryo-anchoring without RF ablation). % Change in unloaded marker lengths (**D**), areal systolic deformation (**E**), and axial systolic deformation (**F**) for each treatment group. $^{+}$ Significant decrease vs. 0 J ($p<0.001$) and ** significant decrease vs. 850 J ($p<0.05$).

deformation in both the circumferential and radial directions with increasing RF energy (Fig. 5.3F), although the changes in the radial direction were not significant.

Temperature Distribution. Leaflet tissue > 65°C was quantified to identify the area of the leaflet exposed to temperatures that cause thermal damage to collagen. The area > 65°C was found to increase with increasing RF energy, from 0.51 ± 0.13 cm^2 to 1.9 ± 0.13 cm^2 at energies of 350 J and 1250 J, respectively (Fig. 5.4A). The tissue area below 0°C was used to determine the degree of cryo-anchoring present during ablation and was approximately 0.14 ± 0.05 cm^2 at the end of the 1250 J ablations. For comparison, the area of the cryo-anchor in contact with the leaflet during the procedure is approximately 0.12 cm^2. Thermal contours at the end of each treatment indicate distinct regions of cryo-anchoring and tissue ablation (Fig. 5.4B). The thermal contour plots at the end of the 350 J treatment shows minimal tissue > 65°C, while the majority of the leaflet tissue is > 65°C in the 1250 J treatment.

Anchor Strength. Following cryo-anchoring for 10 s, anchor strength was found to be 1020 ± 23 kPa (Fig. 5.5). As expected, application of RF ablation at 50 W for 10 s with cryo-anchoring reduced the anchor strength significantly ($p<0.005$) to 668 ± 79 kPa; however, the adherence is still robust.

Discussion

We have previously shown that RF ablation directionally alters MV leaflet geometry and compliance [9]. The therapeutic effect of our percutaneous treatment strategy is to restore competence to diseased or prolapsed MV leaflets by reducing leaflet size, and therefore,

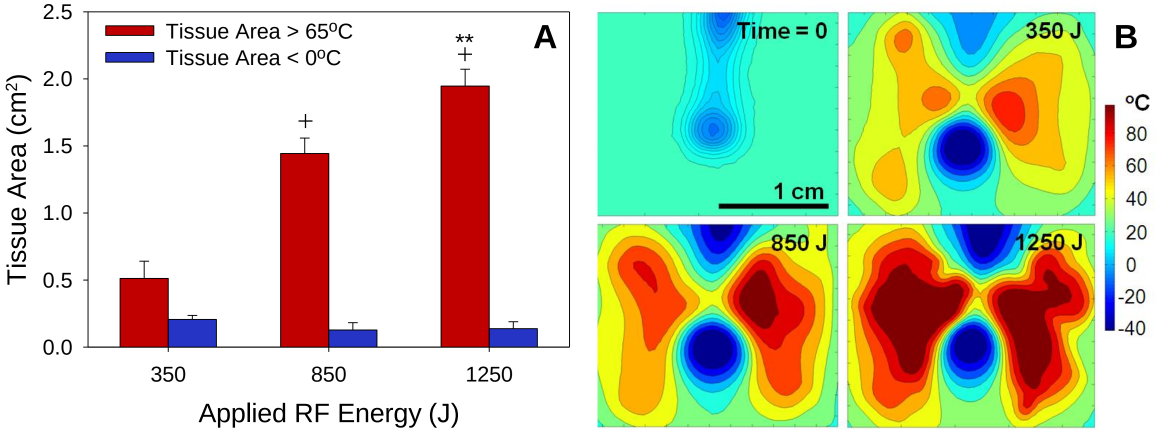

Fig. 5.4: Characteristic Thermal Contours of RFC Catheter Treatment
A: Tissue areas heated to > 65°C by RF ablation (red bars) and cooled to < 0°C by cryo-anchoring, as measured at the end of treatment. $^{+}$ Significant increase vs. 350 J ($p<0.005$) and ** significant increase vs. 850 J ($p<0.05$). **B:** Infrared thermal contour images prior to (time = 0) and following RF ablations of 350 J, 850 J, and 1250 J RF, with simultaneous cryo-anchoring.

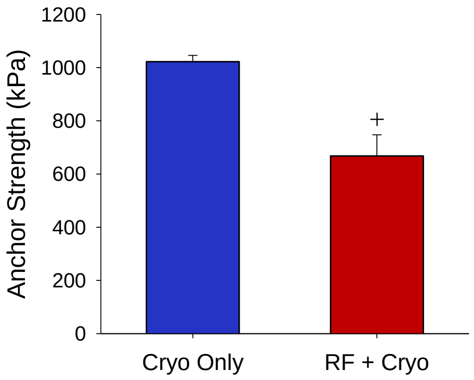

Fig. 5.5: Typical Cryo-Anchor Holding Strength
Cryo-anchor strength following 10 s of attachment (blue bar) and 10 s of cryo-anchoring with 50 W of RF ablation (red bar). $^{+}$ Significant decrease vs. cryo only ($p<0.005$).

displacement of leaflets into the atrium during systole. However, any device that aims to percutaneously treat MVP must do so in a highly dynamic mechanical environment. Additionally, due to the high rate of blood flow across the MV and the resulting potential for heat convection, application of RF energy must be performed with the RF electrode in direct contact with the target tissue. Thus, we have introduced cryo-anchoring as a means to potentially maintain direct catheter contact with a moving MV leaflet and to enhance stability during the procedure. During cryo-anchoring, tissue is cooled to < 0°C, which interferes with the resistive heating that is the therapeutic mechanism behind RF ablation. However, due to the small size of MV leaflets, cryo-anchoring must be utilized in close proximity to the RF electrode. In this study, we demonstrate the effects of using two competing energy modalities and the feasibility of RF ablation performed with cryo-anchoring.

More RF Energy Required with Cryo-Anchoring. Biaxial mechanical data following treatment with the catheter prototype demonstrates that RF ablation remains a valid therapy, even with sub-freezing temperatures on the cryo-anchor in close proximity on the MV leaflet (Fig. 5.3). To determine the extent to which cryo-anchoring reduces the biomechanical effects of RF ablation, we re-analyzed previous biaxial data from treatment with a commercially available RF catheter (7F, Blazer II, Boston Scientific) without cryo-anchoring [9], plotting the % change in areal systolic deformation alongside our data presented here (Fig. 5.6). While RF ablation with cryo-anchoring altered unloaded MV leaflet geometry and deformation at systolic loading, it took significantly more energy versus RF ablation alone to produce the same effect. Previous treatments using the commercially available RF catheter reduced areal systolic deformation by approximately

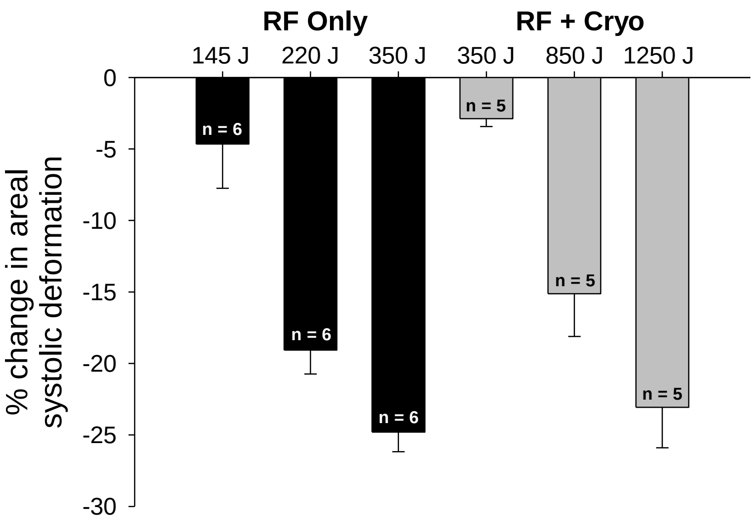

Fig. 5.6: Comparison of Shrinkage Deformations in RF Only and RF+Cryo Treatments
% change in areal systolic deformation with RF ablation alone (black bars) [9] and RF + cryo-anchoring (gray bars), demonstrating that more RF energy is needed when cryo-anchoring is utilized to produce the same therapeutic effect as RF ablation alone.

25% when 350 J of energy was applied at a power of 25 W [9]. In treatments utilizing cryo-anchoring, areal systolic deformation decreased by only 2.8 ± 0.6% under the same RF conditions. However, when 1250 J of energy was applied at a power of 50 W, our catheter prototype was able to produce changes similar to the commercially available catheter at 350 J. These results indicate that even though RF power must be increased significantly when cryo-anchoring is used, the catheter prototype can still achieve the same therapeutic effect.

Thermally-Related Collagen Contracture. RF ablation introduces both geometric and biomechanical changes in MV leaflets; specifically, changes in areal systolic deformation are primarily due to length changes in the circumferential direction (Fig. 5.3D). This shortening of the collagen fibers in the circumferential direction is due to thermal rupture of heat-sensitive bonds and uncoiling of the collagen triple helix. This uncoiling of collagen fibers and transition from a crystalline state to a random coil is responsible for collagen shortening, and transmission electron microscopy of collagenous tissues treated with RF ablation show collagen fibrils that increase in average diameter with increasing RF power [120]. Additionally, aligned collagen fibers fuse together in the orthogonal directions after treatment with RF ablation [120, 121], leading to modest changes seen in the radial direction here (Fig. 5.3D). Therefore, the use of a cryo-anchor for stability during the RF ablation procedure reduces the therapeutic effect of RF energy, but this effect can be mitigated by increasing RF power.

Heat Distribution of RF Ablation with Cryo-Anchoring. In addition to determining biomechanical changes induced by RF ablation, we have analyzed the temperature distribution resulting from combined RF ablation with cryo-anchoring. Estimates for the onset of unwinding of the collagen triple helix vary and have been determined to be approximately 60°C in the bovine joint capsule [122] and 67.1°C in the bovine mitral valve [123]. Thus, we used 65°C as a threshold for permanent collagen denaturation and determined the area of tissue heated above this temperature. IR imaging reveals that while there is a distinct region of cryo-anchoring present through the full thickness of the leaflet, which stays relatively consistent across all RF energies, heating due to RF ablation dominates the leaflet temperature distribution. As a result, full thickness temperatures $< 0°C$ are confined to an area slightly larger than the cryo-anchor attachment area. Because thermal damage to the collagen matrix forms the basis of mechanical damage, we hypothesized that the tissue area heated above 65°C would correlate with changes in areal systolic deformation (Fig. 5.7). Indeed, this correlation is evident when % change in areal systolic deformation is plotted against tissue area above 65°C, demonstrating that biomechanical changes may be directly related to the amount of thermal tissue damage.

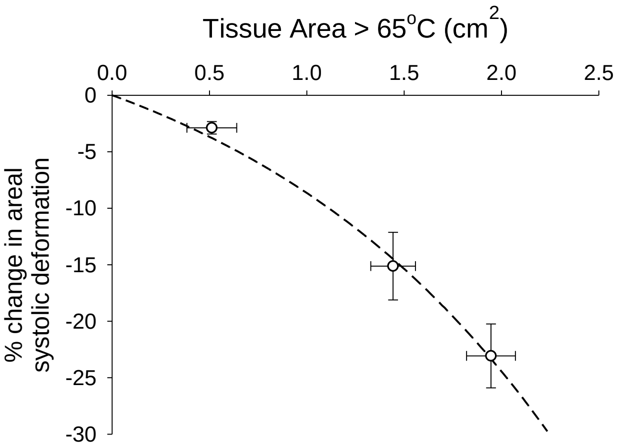

Fig. 5.7: Areal Shrinkage Deformation is Related to Area of Tissue Heating
% change in areal systolic deformation vs. tissue area > 65°C, as determined by processing of IR thermal images at the end of ablation. Model fit: % change in areal systolic deformation = $-10.54e^{0.60 * \text{tissue area}} + 10.54$

Cryo-Anchor Attachment to MV Leaflets. Testing of the anchor strength of the cryo-anchor revealed that this attachment is sufficient to maintain contact, even with RF ablation, with stationary MV leaflets. While there are currently no direct estimates for the anchor strength required to maintain attachment to the MV during the cardiac cycle, one estimate can be made based on the atrial pressure during MV opening. Because the proposed catheter treatment involves access to the MV via the left atrium, and the peak atrial pressure is a representation of the force required to open the MV, this is an estimate for the minimum attachment force required to maintain adherence. Peak atrial pressure in normally functioning hearts is typically below 20 mmHg [12], or about 2.7 kPa. Thus, even if a much higher estimate for the atrial pressure is chosen, this value is considerably lower than the approximately 668 kPa of anchor strength recorded at 10 s of the 50 W RF ablation. Additionally, we speculate that cryo-anchoring and ablation of MV leaflets will occur with the MV kept partially open, with one leaflet kept anchored and the other moving freely. This may further reduce the force required to maintain cryo-anchoring.

Study Limitations. The data presented here indicate that RF ablation performed with cryo-anchoring alters MV leaflet geometry and deformation in vitro; however, there are several limitations to this study. First, all treatments were performed on stationary leaflets in vitro. While this ensures robust delivery of RF energy, it is not realistic, particularly with regards to the anchor strength studies. Further work must be performed to verify the feasibility of cryo-anchoring on moving MV leaflets, both in vitro and in vivo. Additionally, ablations in the biomechanical and thermal imaging studies were performed on leaflets with the saline bath lowered, such that the maximum amount of RF energy would penetrate the leaflets. This provides a much more accurate measurement of the total energy delivered to the leaflet, but the in vivo environment is much more dynamic. Due to convective blood flow, in vivo treatments will require additional or prolonged RF energy delivery in order to produce the same biomechanical alterations, as demonstrated in a feasibility study utilizing a canine model [10]. Finally, these studies were performed on healthy porcine MV leaflets. It is unknown how leaflets with MVP might respond to RF ablation, due to their disorganized collagen architecture.

Design Considerations for In Vivo Translation. In light of the results from this study, and what is previously known regarding RF ablation, we have identified several design considerations for in vivo translation of our combined RF ablation and cryo-anchoring catheter. First, we demonstrated in vitro that RF energy must be increased when used in conjunction with cryo-anchoring in order to achieve a similar therapeutic effect of RF alone. Because our biaxial mechanical analysis was performed on leaflets treated while only partially submerged, heat dissipation will likely increase when treatment is performed in vivo, due to the surrounding hemodynamic environment. Thus, RF energy delivery will likely need to be increased in a similar manner and this will likely be accomplished by increasing either RF power or application time. Similarly, through placement in a dynamic hemodynamic environment and increases in application of RF energy, cryo-anchor strength may be reduced at the current liquid nitrogen delivery protocol, and liquid nitrogen delivery may need to be increased by increasing vacuum pressure and delivery time to compensate. Also, in order to decrease the amount of RF energy lost to the blood stream, RF electrode placement can be re-designed to allow for more direct delivery to the leaflets. One possible improvement is to replace the current, singular RF electrode, which encircles the entire 360º outer circumference of the catheter shaft, with three separate RF electrodes that are approximately 120º of the circumference and are insulated from each other. By having three separate electrodes, RF energy can be delivered to the electrode in direct contact with the leaflet, ensuring that the majority of RF energy enters the leaflet, as opposed to the bloodstream. These, and other potential modifications, will likely be necessary to translate this strategy into an integrated catheter that will be successful in vivo.

Conclusions

In this study, we demonstrate that RF ablation with a cryo-anchor may provide an alternative percutaneous treatment strategy for MVP. While it was previously shown that RF ablation alone reduces MV leaflet size, we have demonstrated the feasibility of cryo-anchoring as a stability technique for secure attachment of a catheter to a MV leaflet. Additionally, cryo-anchoring may have possible uses in other applications involving RF ablation or in more general percutaneous catheters as a mechanism to enhance stability and improve catheter contact in complex anatomies or hard-to-reach sites. Cryo-anchoring may be a particularly effective strategy in improving catheter stability during treatment of cardiac arrhythmias, given the dynamic environment of the heart. While we found here that cryo-anchoring reduces the effect of RF ablation, these effects can be mitigated by increasing RF power and duration. These in vitro results indicate that RF ablation with simultaneous cryo-anchoring reduces MV leaflet size and may be a viable clinical strategy for percutaneous treatment of myxomatous MVP.

Chapter 6

AIM 2 – PART 2: BIAXIAL MECHANICAL CHARACTERIZATION OF NON-UNIFORM THERMAL SHRINKAGE DEFORMATIONS

Introduction

We have shown in the previous chapter that RF ablation introduces thermal shrinkage and biomechanical changes to MV leaflets, and that thermal shrinkage of MV leaflets primarily occurs in the circumferential direction due to collagen fiber alignment. Further, cryo-anchoring was shown to significantly reduce the amount of thermal shrinkage at a given RF power. However, this study was limited in that the experimental set-up was incapable of quantifying spatial variations in leaflet shrinkage. MV leaflet tissue does not uniformly deform in response to heat. Rather, the magnitude of thermal shrinkage varies throughout the treatment zone.

One reason to quantify spatially-varying shrinkage of MV leaflet tissue in response to RFC catheter treatment is to generate data to develop patient-specific computational models of the MV, which are currently in development to aid in preoperative surgical and interventional planning [124-127]. Computational modeling of heart valves can offer the opportunity to interactively explore a repair strategy, allowing assessment of proposed structural changes to the valve [127]. Characterization of the tissue- and device-specific thermal shrinkage deformations resulting from the RFC catheter is an important first step in developing a computational model of the treatment strategy and for optimizing procedural planning. Previous studies on thermal shrinkage of collagenous tissues have used uniaxial and biaxial testing devices to characterize shrinkage deformations under a variety of loading and temperature conditions [128-132]. Moreover, previous biaxial characterization of thermally-induced deformations have used a standard 2x2 marker tracking array, which is unable to characterize non-uniform shrinkage deformations that may arise due to ablation device configuration and tissue anisotropy.

The objective of the work in this chapter was (1) to develop a biaxial mechanical testing method that more completely characterizes non-uniform tissue deformations that arise in thermal shrinkage of collagenous tissues and (2) to apply this method to characterize the shrinkage response resulting from RFC catheter treatment of MV leaflet tissue. Additionally, as mechanical loading conditions have been found to affect the thermal shrinkage response of collagenous tissues [130], we sought (3) to investigate the effect of varying preload on thermal shrinkage. Finally, pericardial tissue that has been treated with heat has been shown to dilate slightly within the first hour after treatment [128], thus we sought (4) to investigate the magnitude of post-treatment re-dilation of MV tissue. We hypothesize that tracking 16 markers on the MV leaflet surface will provide enhanced fidelity in measuring spatially-varying leaflet shrinkage induced by treatment with the RFC catheter and further, that increasing the applied preload on the MV leaflets prior to RFC catheter treatment will reduce the magnitude of thermal shrinkage.

Materials and Methods

Sample Preparation. Healthy porcine MV anterior leaflets were obtained from the local abattoir (Hampton Meats, Hopkinsville, KY). Anterior leaflets were chosen for this study due to their large and continuous surface area. The center portions of the leaflets were cut into rectangular sections and 16 markers were fixed to the atrial side of the tissue samples to allow optical tracking for strain calculations during mechanical loading. Four hooks

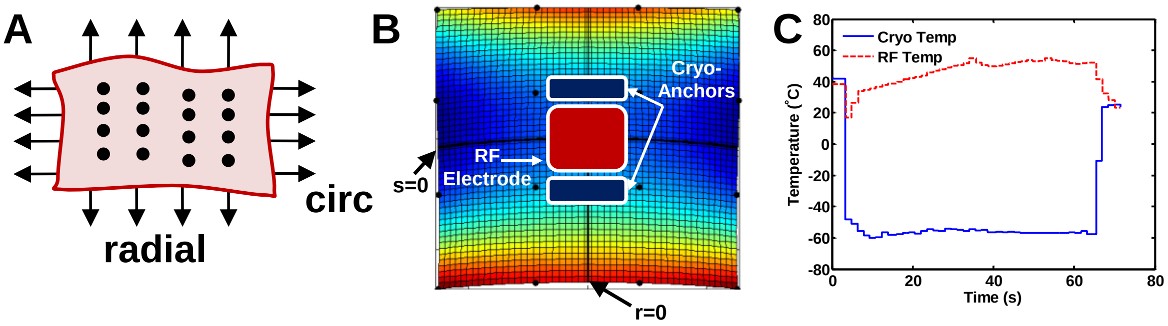

Fig. 6.1: Experimental Set-Up for 4x4 Marker Tracking
A: Relative positioning of the 4x4 marker array on the surface of a MV anterior leaflet. **B:** 4x4 marker array shown with catheter orientation and the relative sizes and positions of the RF electrode and cryo-anchors with respect to the sample. Also shown are the local coordinate axes, r=0 and s=0. **C:** Representative RFC catheter temperatures during ablation treatment in the biaxial mechanical tester showing RF electrode temperature (red dash) and cryo-anchor temperature (blue solid).

where inserted into each side of a tissue sample and attached to sutures for mechanical loading. The circumferential (direction of collagen fiber alignment) and radial leaflet directions were aligned with the loading axes (Fig. 6.1A). Samples were tested in load control mode to equibiaxial membrane tension comparable to that experienced by healthy MV leaflets during systole (120 mmHg ≈ 90 N/m). All testing and treatment was performed with samples and catheter fully submerged in phosphate buffered saline at 37°C. For more details on the biaxial mechanical testing setup, see [9].

Mechanical Testing and Catheter Treatment. Samples were initially loaded 10 times to 90 N/m of equibiaxial tension to pre-condition the tissue. Load was removed from the samples, the marker reference configuration, $\boldsymbol{X}$, was acquired, and samples were again loaded 10 times to 90 N/m of equibiaxial tension to acquire the untreated loading curves. Following acquisition of untreated mechanical loading curves, samples were treated with the RFC catheter on the ventricular side according to one of four protocols (n=5 per group) while submerged in phosphate buffered saline at a power of 50 W for 60 s (Fig. 6.1B-C). Either the samples were treated with 1) RF ablation without cryo-anchoring and no loading constraints (RF Only, No Preload), 2) RF ablation with cryo-anchoring with no loading constraints (RFC, No Preload), 3) RF ablation with cryo-anchoring with 1 N/m of equibiaxial preload (RFC, 1 N/m Preload), or 4) RF ablation with cryo-anchoring with 5 N/m of equibiaxial preload (RFC, 5 N/m Preload). For treatments with no loading constraints, it was ensured that no load was applied to the sample edges during catheter treatment. For treatments with applied preload, samples were first loaded to the specified equibiaxial preload, the loading motors were held fixed in place, and no attempt was made to control or alter the applied load during catheter treatment. Following catheter treatment, samples were pre-conditioned by loading 2-3 times to 90 N/m of equibiaxial tension, load was removed, and the treated unloaded configuration was acquired. Samples were again loaded 10 times to 90 N/m of membrane tension to acquire the treated mechanical loading curves. Pre-conditioning, unloaded marker position acquisition, and mechanical loading to 90 N/m was repeated again after one hour, during which the samples sat traction-free, to examine any possible re-dilation effects.

Deformation Characterization. Prior to analysis, the marker locations of all samples within each group were averaged together to form one average dataset per group. Additionally, radial symmetry was employed such that markers on either side of the local $r = 0$ axis were mirrored and averaged together (Fig. 6.1B).

Bilinear interpolation schemes are traditionally used to determine the deformation gradient from 2x2 marker arrays in biaxial mechanical testing of planar tissues [117, 133]. We sought a method to better characterize the non-uniform shrinkage deformations induced by catheter treatment and used 16 tracking markers in a 4x4 marker array. Briefly, bicubic interpolation, with basis functions reported from [134], was used to form an isoparametric, curved-sided quadrilateral element from the 16 marker locations, from which, a 50x50 node grid was interpolated. Bicubic interpolation has the advantage of being C^1 continuous to avoid discontinuities when determining the displacement and deformation gradients, and the curved sides enhance interpolation fidelity. The deformation gradient, $\boldsymbol{F}$, was interpolated at each nodal location within the enclosed 4x4 marker region, and directional deformations (circumferential – $F11$, radial – $F22$) and areal deformations (determinant of the deformation gradient tensor) are reported with respect to the pre-treatment, unloaded reference condition, $\boldsymbol{X}$:

$$\boldsymbol{F} = \boldsymbol{I} + \frac{\partial \boldsymbol{u}}{\partial \boldsymbol{X}}$$

Where $\boldsymbol{u}$ is the displacement gradient. In order to interpolate $\boldsymbol{F}$ everywhere between each of the markers, it is necessary to introduce a local coordinate system (r, s) that is centered about the origin and spans from -1 to 1 in each direction Fig. 6.2. The position within the element is then described in terms of the local coordinates r and s, where i is the marker number:

$$X(r,s) = \sum_{i=1}^{16} \phi_i(r,s) X_i$$

$$Y(r,s) = \sum_{i=1}^{16} \phi_i(r,s) Y_i$$

The displacements, u and v, can be interpolated similarly:

$$u(r,s) = \sum_{i=1}^{16} \phi_i(r,s) u_i$$

$$v(r,s) = \sum_{i=1}^{16} \phi_i(r,s) v_i$$

Given the marker positions (Fig. 6.2), the basis functions, ϕ_i, are:

$$\phi_{1,2,3,4} = \frac{1}{256}(9r^2-1)(r_L r+1)(9s^2-1)(s_L s+1), \{r_L = \pm 1, s_L = \pm 1\}$$

$$\phi_{5,6,9,10} = \frac{9}{256}(9s^2-1)(s_L s+1)(1-r^2)(1+9r_L r), \left\{r_L = \pm\frac{1}{3}, s_L = \pm 1\right\}$$

$$\phi_{7,8,11,12} = \frac{9}{256}(9r^2-1)(r_L r+1)(1-s^2)(1+9s_L s), \left\{r_L = \pm 1, s_L = \pm\frac{1}{3}\right\}$$

$$\phi_{13,14,15,16} = \frac{81}{256}(1-r^2)(1+9r_L r)(1-s^2)(1+9s_L s), \left\{r_L = \pm\frac{1}{3}, s_L = \pm\frac{1}{3}\right\}$$

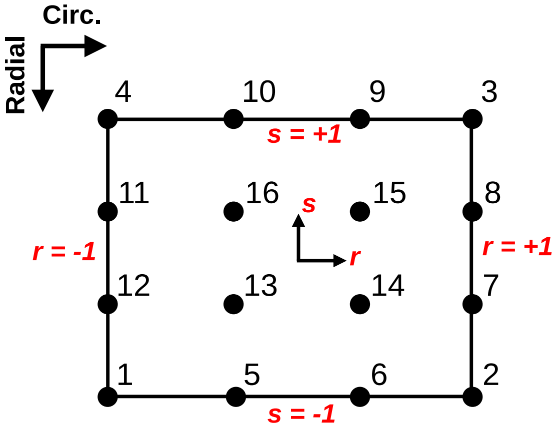

Fig. 6.2: 4x4 Marker Positions for Bicubic Interpolation Scheme

However, we’re looking to find the displacement gradient, which requires finding the derivatives of the basis functions:

$$\frac{\partial \boldsymbol{u}}{\partial \boldsymbol{X}} = \begin{bmatrix} \frac{\partial u}{\partial X} & \frac{\partial u}{\partial Y} \\ \frac{\partial v}{\partial X} & \frac{\partial v}{\partial Y} \end{bmatrix}$$

Since the displacements are now written as functions of r and s, the chain rule is needed to determine the gradient. For example:

$$\frac{\partial u}{\partial X} = \frac{\partial u}{\partial r}\frac{\partial r}{\partial X} + \frac{\partial u}{\partial s}\frac{\partial s}{\partial X}$$

In matrix form, the displacement gradient is:

$$\begin{bmatrix} \frac{\partial u}{\partial X} & \frac{\partial u}{\partial Y} \\ \frac{\partial v}{\partial X} & \frac{\partial v}{\partial Y} \end{bmatrix} = \begin{bmatrix} \frac{\partial u}{\partial r} & \frac{\partial u}{\partial s} \\ \frac{\partial v}{\partial r} & \frac{\partial v}{\partial s} \end{bmatrix} \begin{bmatrix} \frac{\partial r}{\partial X} & \frac{\partial r}{\partial Y} \\ \frac{\partial s}{\partial X} & \frac{\partial s}{\partial Y} \end{bmatrix}$$

As r and s are not explicit functions of X and Y, the last term must be inverted:

$$\begin{bmatrix} \frac{\partial r}{\partial X} & \frac{\partial r}{\partial Y} \\ \frac{\partial s}{\partial X} & \frac{\partial s}{\partial Y} \end{bmatrix} = \begin{bmatrix} \frac{\partial X}{\partial r} & \frac{\partial X}{\partial s} \\ \frac{\partial Y}{\partial r} & \frac{\partial Y}{\partial s} \end{bmatrix}^{-1} = \frac{1}{J}\boldsymbol{H}$$

Where:

$$\boldsymbol{H} = \begin{bmatrix} \frac{\partial u}{\partial r}\frac{\partial Y}{\partial s} - \frac{\partial u}{\partial s}\frac{\partial Y}{\partial r} & -\frac{\partial u}{\partial r}\frac{\partial X}{\partial s} + \frac{\partial u}{\partial s}\frac{\partial X}{\partial r} \\ \frac{\partial v}{\partial r}\frac{\partial Y}{\partial s} - \frac{\partial v}{\partial s}\frac{\partial Y}{\partial r} & -\frac{\partial v}{\partial r}\frac{\partial X}{\partial s} + \frac{\partial v}{\partial s}\frac{\partial X}{\partial r} \end{bmatrix}$$

$$J = \frac{\partial X}{\partial r}\frac{\partial Y}{\partial s} - \frac{\partial X}{\partial s}\frac{\partial Y}{\partial r}$$

The terms that compose $\boldsymbol{H}$ and J can be determined by differentiating the basis function, such as:

$$\frac{\partial X}{\partial r} = \sum_{i=1}^{16} \frac{\partial \phi_i}{\partial r} X_i$$

$$\frac{\partial X}{\partial s} = \sum_{i=1}^{16} \frac{\partial \phi_i}{\partial s} X_i$$

The derivatives of the basis functions with respect to r:

$$\frac{\partial \phi_{1,2,3,4}}{\partial r} = \frac{1}{256}(27r^2r + 18r - r_L)(9s^2 - 1)(s_Ls + 1), \{r_L = \pm 1, s_L = \pm 1\}$$

$$\frac{\partial \phi_{5,6,9,10}}{\partial r} = \frac{9}{256}(9s^2 - 1)(s_Ls + 1)(-27r^2r + 18r - r_L), \left\{r_L = \pm\frac{1}{3}, s_L = \pm 1\right\}$$

$$\frac{\partial \phi_{7,8,11,12}}{\partial r} = \frac{9}{256}(27r^2r + 18r - r_L)(1 - s^2)(1 + 9s_Ls), \left\{r_L = \pm 1, s_L = \pm\frac{1}{3}\right\}$$

$$\frac{\partial \phi_{13,14,15,16}}{\partial r} = \frac{81}{256}(-27r^2r + 18r - r_L)(1 - s^2)(1 + 9s_Ls), \left\{r_L = \pm\frac{1}{3}, s_L = \pm\frac{1}{3}\right\}$$

The derivatives of the basis functions with respect to s:

$$\frac{\partial \phi_{1,2,3,4}}{\partial r} = \frac{1}{256}(27s^2s + 18s - s_L)(9r^2 - 1)(r_Lr + 1), \{r_L = \pm 1, s_L = \pm 1\}$$

$$\frac{\partial \phi_{5,6,9,10}}{\partial r} = \frac{9}{256}(27s^2s + 18s - s_L)(1 - r^2)(1 + 9r_Lr), \left\{r_L = \pm 1, s_L = \pm\frac{1}{3}\right\}$$

$$\frac{\partial \phi_{7,8,11,12}}{\partial r} = \frac{9}{256}(9r^2 - 1)(r_Lr + 1)(-27s^2s + 18s - s_L), \left\{r_L = \pm\frac{1}{3}, s_L = \pm 1\right\}$$

$$\frac{\partial \phi_{13,14,15,16}}{\partial r} = \frac{81}{256}(-27s^2s + 18s - s_L)(1 - r^2)(1 + 9r_Lr), \left\{r_L = \pm\frac{1}{3}, s_L = \pm\frac{1}{3}\right\}$$

And substituting into $\boldsymbol{H}$ and J produces:

$$\boldsymbol{F} = \boldsymbol{I} + \frac{1}{J}\boldsymbol{H}$$

To analyze differences between treatment groups on the magnitude of thermal shrinkage deformation, the areal, circumferential, and radial deformations were averaged for each sample over all interpolated nodes in the unloaded state and at systolic loads. Differences between groups were assessed with one way ANOVA with a follow-up Holm-Sidak method for multiple pairwise t-tests at significance level α=0.05.

Results

Averaged shrinkage deformations produced by RF ablation only (left column) and RFC catheter treatment at varying levels of preload are shown in the unloaded configuration (Fig. 6.3) and at systolic loads (Fig. 6.4). The approximate center of the RF ablation electrode in this study is at position (r, s) = (0,0). In general, areal shrinkage deformations are greatest in the central RF ablation treatment region and on either side along the circumferential axis, leading to an hourglass-shaped shrinkage deformation. Cryo-anchor placement inhibits the formation of large shrinkage deformations along the border zones in the top and bottom of the radial axis. Whereas areal shrinkage deformations vary relatively uniformly around the circumference of the ablation electrode in the RF only group, cryo-anchors act to confine thermal shrinkage to the central region of the leaflet in the RFC catheter treatment groups. Interestingly, radial shrinkage magnitude is greatest in the tissue adjacent to the ablation electrode near the leaflet edges and not the leaflet tissue in direct contact with the ablation electrode. Further, as applied preload before treatment increases, the magnitude of areal shrinkage decreases and trends in directional differences between circumferential and radial deformation can be more fully appreciated.

Areal and directional shrinkages are shown plotted along the local coordinate axes $r = 0$ (Fig. 6.5A) and $s = 0$ for RFC catheter treatment at 1 N/m of preload (Fig. 6.5B). As

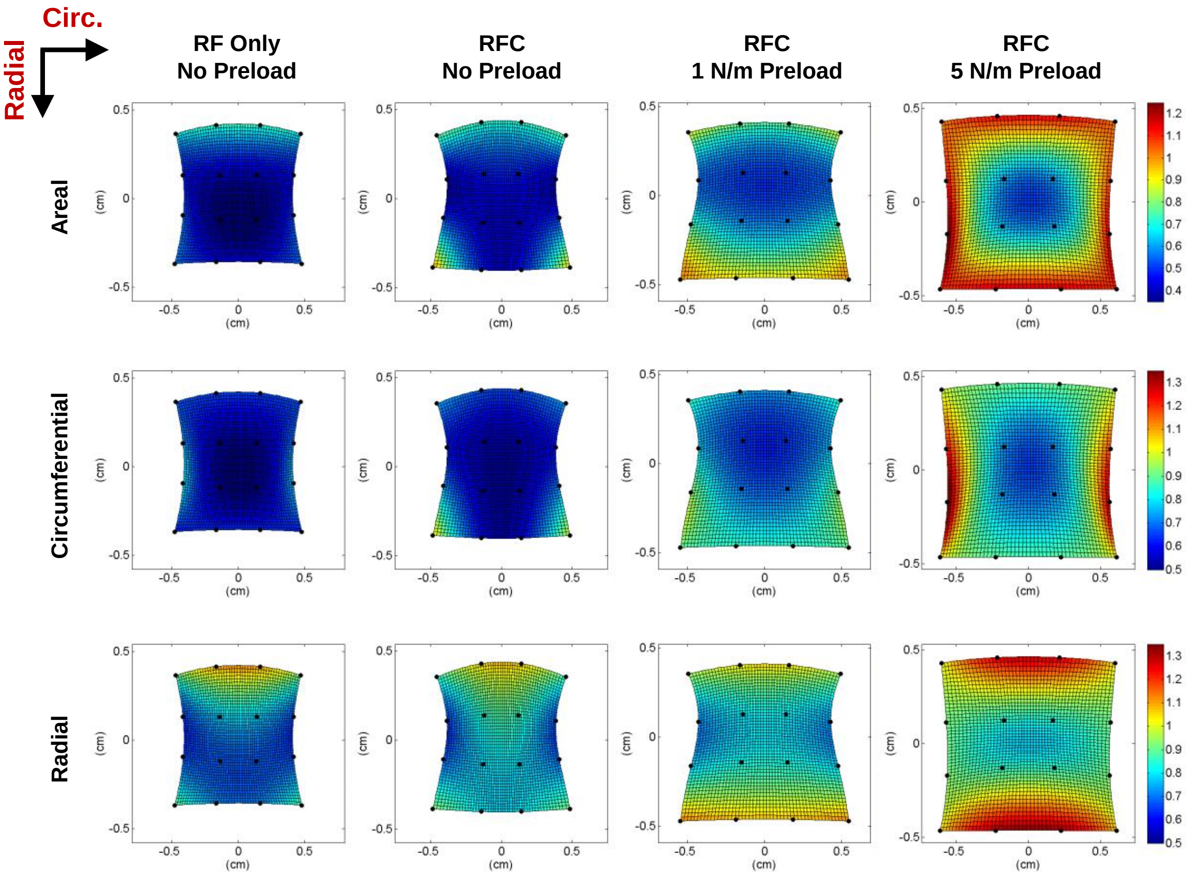

Fig. 6.3: Catheter Induced Shrinkage Deformations – Shown in the Unloaded State
Shown are areal (top row), circumferential (middle row), and radial (bottom row) deformations, in the unloaded state, induced by catheter treatment and averaged over n=5 samples with radial symmetry.

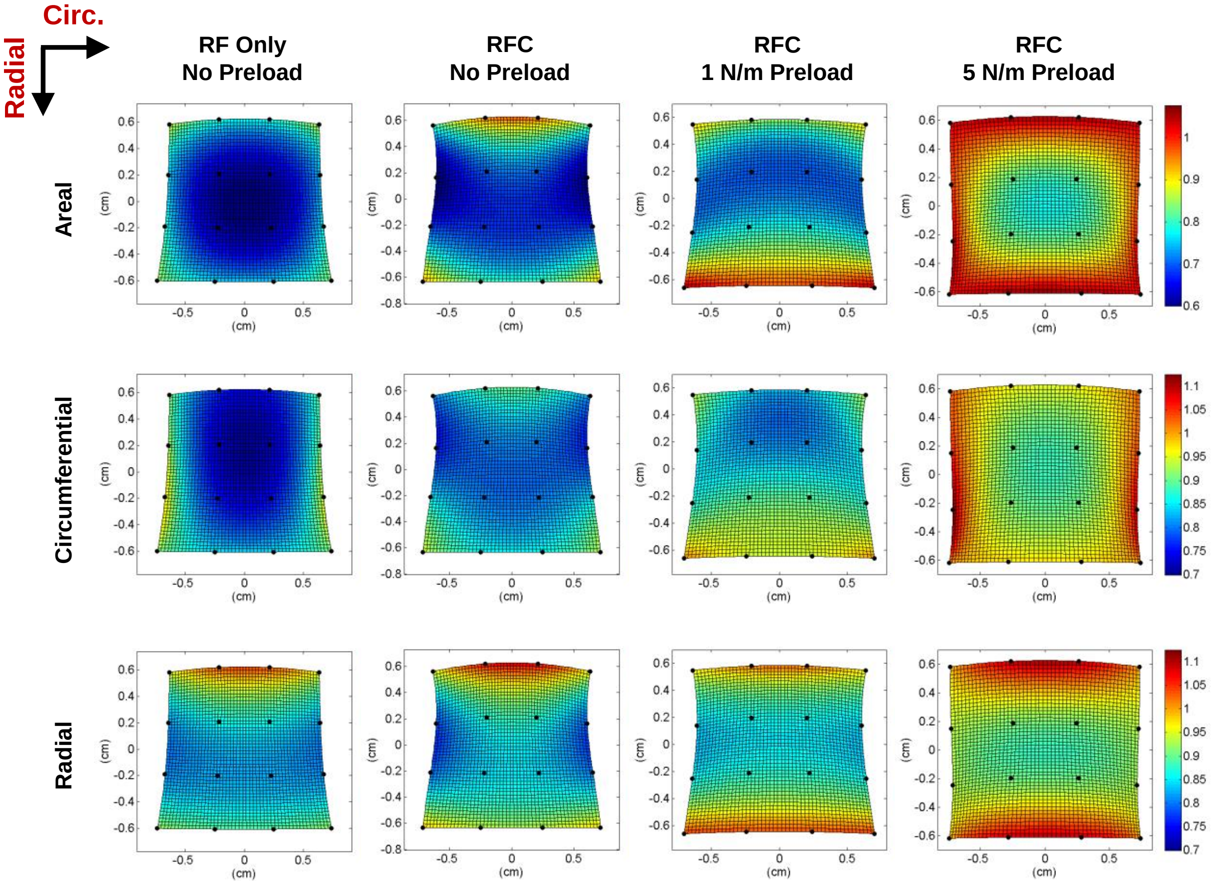

Fig. 6.4: Catheter Induced Shrinkage Deformations – Shown at Systolic Loads
Shown are areal (top row), circumferential (middle row), and radial (bottom row) deformations, shown at 90 N/m of equibiaxial load, induced by catheter treatment and averaged over n=5 samples with radial symmetry.

expected, areal and circumferential shrinkage deformation magnitude becomes smaller at locations further away from the RF ablation electrode along the circumferential and radial axes (Fig. 6.5A-B). However, radial shrinkage deformation is larger towards the edges of the leaflet than in the immediate ablation zone when plotted along the circumferential axis (Fig. 6.5A).

Thermal shrinkage deformation magnitudes were averaged over the 4x4 marker domain of each sample (Fig. 6.6). Differences in thermal shrinkage magnitude between RF ablation only and RFC catheter treatment groups with no preload were not significant. In general, preload on the MV leaflet samples significantly reduced the magnitude of shrinkage deformations. A preload of 5 N/m of membrane tension reduced shrinkage magnitude by approximately 50% compared to 1 N/m of preload (Fig. 6.6C). Additionally, shrinkage magnitude measured at systolic loading conditions was substantially lower than the shrinkage magnitude in the unloaded condition. Areal re-dilation was also measured 1 hour after treatment, with maximum re-dilation of 8.53 ± 1.99% following RFC catheter treatment at no load (Fig. 6.6D). MV leaflet samples treated in combination with preload demonstrated no significant re-dilation.

Discussion

Characteristic Shape of RFC Catheter Thermal Shrinkage Lesions. The objective of this study was to quantify spatially-varying shrinkage deformations in collagenous tissues. A 4x4 marker tracking grid on the atrial surface of the MV anterior leaflet captured the variations in tissue shrinkage that occur as a result of tissue anisotropy and ablation device geometry. The RFC catheter is a specialized tissue shrinkage device that uses two cryo-anchoring elements placed on each side of an RF electrode to enable direct electrode-tissue

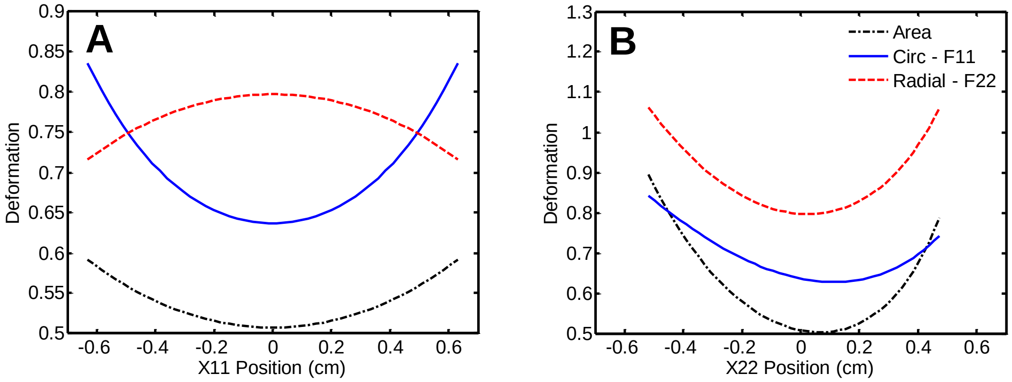

Fig. 6.5: Catheter-Induced Shrinkage Along Local Coordinate Axes

Areal, circumferential, and radial shrinkage plotted along the local coordinate axes, r=0 (A) and s=0 (B), following catheter treatment at 1 N/m of preload. Local coordinate axes are shown plotted in Fig. 6.1 and Fig. 6.2 for reference.

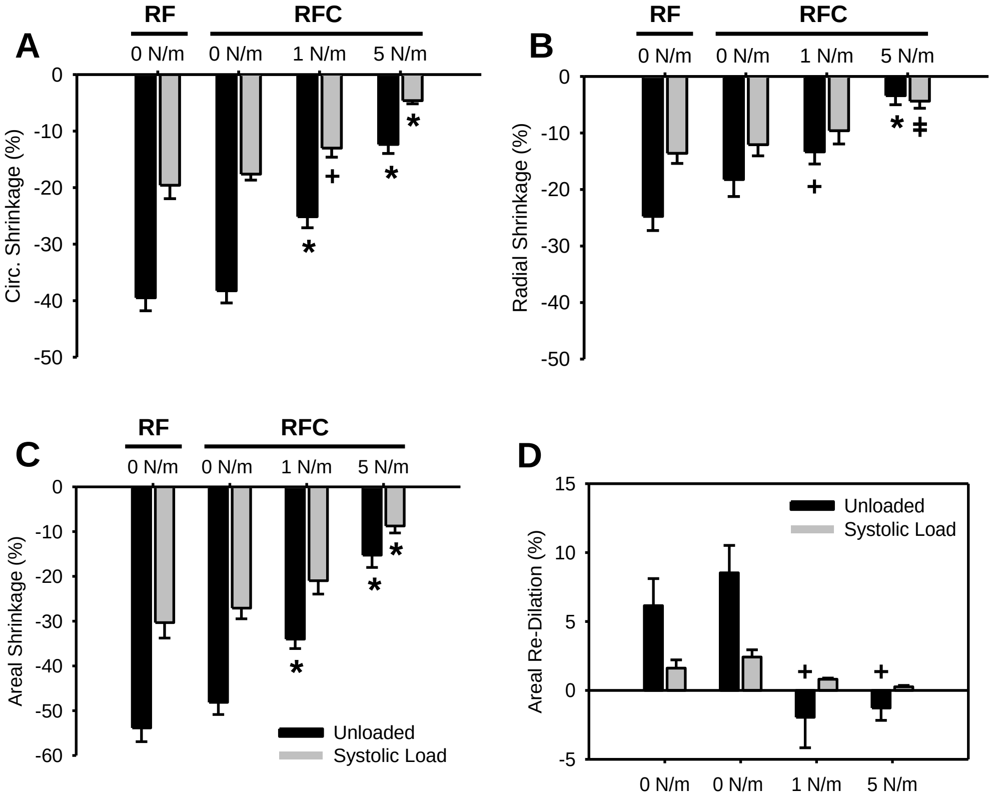

Fig. 6.6: Average Shrinkage at Varying Preloads

Circumferential (A) and radial (B) shrinkage deformation induced by catheter treatment shown in the unloaded (black) and systolic (gray) loading conditions. C: Areal shrinkage. * significant different than all other groups, + significantly different than RF only, 0 N/m and RF+Cryo 5 N/m, ‡ significantly different than RF only, 0 N/m ($p<0.05$). D: Measured areal deformation taken in the unloaded state (black) and systolic loading condition (gray) 1 hour post-treatment. + significantly different than both 0 N/m preload groups, ($p<0.05$).

contact. The result of treatment with the RFC catheter is a thermal shrinkage lesion that is affected by the cryogenic temperatures of the cryo-anchors. These sub-freezing temperatures appear to exist only on the ventricular surface, since marker positions on the atrial surface still experience shrinkage deformations with RF ablation, albeit reduced, in the areas of cryo-anchoring. Thus, cryo-anchoring reduces, but does not completely inhibit, thermal shrinkage in the vicinity. The characteristic hourglass shape of RFC catheter treatment can be fully appreciated in the no preload condition (Fig. 6.3) and is a result of collagen fiber alignment with the circumferential direction, as well as placement of the cryo-anchors relative to the RF ablation electrode.

Preload Decreases the Magnitude of Thermal Shrinkage. A further aim of this study was to examine the variation in shrinkage magnitude and directionality as a result of increased preload on the leaflet. The native MV leaflet can be thought of as a membranous tissue that is constantly in some form of tension from both the fibrous, relatively rigid trigones around the annulus and the compliant chords that connect the leaflet free edge to the papillary muscles. Recent studies have demonstrated that the native MV is always under some amount of prestrain [75, 135, 136], and the belly region of MV leaflets has been found to contract by 18% and 30% in the circumferential and radial directions, respectively, following excision [75]. While no measurements for the corresponding preload exist, the measured prestrains likely fall within the toe region of the loading curves and implies that preload likely does not exceed 5-10 N/m of tension. Thus, to simulate prestrain in this study, 1 N/m or 5 N/m of preload was applied before the start of RFC catheter treatment. At 5 N/m of preload, the shrinkage lesion was fully contained within the 4x4 marker region, unlike the shrinkage lesions of the other groups (Fig. 6.3 and Fig. 6.4). Greater applied preload seems to reduce the coverage of thermal shrinkage lesions, implying that a larger ablation electrode or more ablations are needed to thermally shrink an equivalent amount of tissue.

Acute Re-Dilation of Thermal Shrinkage Lesions is Minimal. Re-dilation of thermal shrinkage lesions in pericardial tissue is known to occur over the first hour after treatment [130, 132], thus we sought to investigate this effect in MV leaflet tissue. In treatment groups with no preload, MV leaflet tissue was found to re-dilate slightly over one hour (Fig. 6.6D). However, when RFC catheter treatment was applied with 1 or 5 N/m of preload, no re-dilation was measured. The absence of re-dilation following RFC catheter treatment with applied preload could be due to the reduced shrinkage magnitudes compared to those of the no preload groups. Regardless, the absence of re-dilation following RFC catheter treatment is beneficial to the MV repair strategy, as re-dilation will not need to be accounted for during treatment.

Study Limitations. In this study, thermal shrinkage deformations were measured and quantified in the unloaded condition and at systolic loads (90 N/m of equibiaxial tension). Future work will examine how post-treatment leaflet mechanics are affected by examining the post-treatment mechanical loading curves and determining the spatial variation of parameter estimates of a Fung-type hyperelastic constitutive model [137]. In order to cover a maximal amount of leaflet area, tracking markers were often placed near the sample edges. A further limitation of this study is occasional appearance of edge effects along the border of the 16 marker area due to the inhomogeneous strains in the vicinity of the loading attachments.

Conclusions. In this study, we developed a bicubic interpolation method to more fully characterize the non-uniform deformation response that results from the RFC catheter – a specialized ablation device that consists of an RF electrode surrounded on two sides by cryo-anchoring elements that inhibit thermal shrinkage. We found deformations that varied strongly depending on the direction of collagen fiber alignment and device alignment with the tissue. This analysis can be used to generate mechanical data for computational models to guide treatment therapy and to better understand spatially-varying tissue shrinkage dynamics.

Chapter 7

AIM 2: RFC CATHETER ASSESSMENT IN A PHYSIOLOGIC FLOW ENVIRONMENT

Text and figures for Chapter 7 taken from:

Boronyak SM, Merryman WD: "In vitro assessment of a combined radiofrequency ablation and cryo-anchoring catheter for treatment of mitral valve prolapse." Journal of Biomechanics. Vol. 47. Issue 5, 973-80, 2014.

Introduction

We have previously shown that when RF energy is applied to MV leaflets in a static environment with cryo-anchoring, leaflet size becomes significantly reduced, and infrared thermal imaging revealed that the cryo-anchor can be placed in close proximity to the RF electrode [11]. However, the effectiveness of this combined RF ablation and cryo-anchoring approach has yet to be tested in a physiologic flow environment. In particular, it is unknown whether a cryo-anchor can adhere to a moving MV leaflet and if this process negatively affects the flow and pressure across the MV.

The purpose of this study was to develop and evaluate a combined RF ablation and cryo-anchoring catheter in a left heart flow simulation environment in order to optimize catheter performance and to determine procedure feasibility. We hypothesized that our combined RF ablation and cryo-anchoring catheter would adhere to moving porcine MV leaflets in a dynamic flow environment and effectively ablate the leaflet tissue with RF energy, mimicking surgical leaflet resection. To test this hypothesis, we constructed a left heart flow loop, similar to others [138, 139], in order to simulate the flow and pressure across healthy, excised porcine MVs. The data that follow support our hypothesis that the combined catheter prototype effectively adheres to and ablates MV leaflets in a physiologic flow environment without negatively altering flow or pressure during the procedure, and that the changes induced by RF ablation remain durable over four weeks.

Materials and Methods

Left Heart Flow Loop. A left heart flow loop was developed in order to reproduce physiologic pressure and flow waveforms (Fig. 7.1A). Others have used similar flow simulators in an effort to study MV disease states and the effects of various repair strategies on MV mechanics [92, 140]. MVs were obtained from healthy pigs from a local abattoir (Hampton Meats, Hopkinsville, KY), and the entire MV apparatus was excised and kept intact. The MV annulus was sewn onto a silicone membrane, and the papillary muscles were sewn onto adjustable papillary muscle holders (Fig. 7.1B). LabView software (National Instruments, Austin, TX) was used to control the output pressure to a pump connected to the left ventricle, and an adjustable flow resistor and vessel compliance chamber were used to independently control the flow rate. Transmitral pressure and flow waveforms (Transonic Systems Inc., Ithaca, NY) were captured to assess the effect of catheter placement and cryo-anchoring on hemodynamics.

RF Ablation and Cryo-Anchoring Catheter. A steerable catheter prototype was constructed utilizing components from a Freezer MAX Cardiac Cryoablation catheter (Medtronic, Minneapolis, MN). A RF electrode was placed in between two cryo-anchors on the tip of the catheter and was electrically insulated from the cryo-anchors (Fig. 7.1C). Liquid nitrous oxide delivery to the inside of the catheter tip, which is kept under vacuum, provides the cooling power for the cryo-anchor. A deflection wire was attached to a custom steering device to allow the catheter tip to be maneuvered. A viewing window on the left heart flow

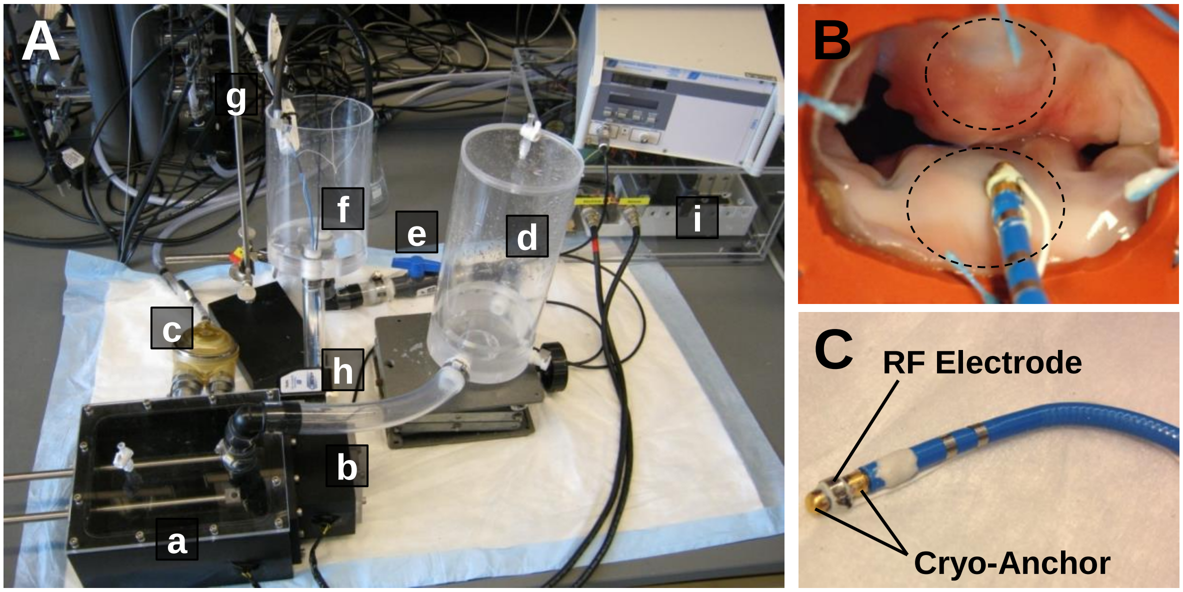

Fig. 7.1: Left Heart Flow Simulator For Simulated Testing
Left heart flow loop (**A**) used to test catheter performance consisting of, a: ventricle, b: atrium, c: Thoratec VAD bladder pump, d: compliance chamber, e: flow resistor, f: media reservoir for catheter access, g: catheter prototype, h: Transonic flow probe, and i: LabView input/output controller. **B:** A healthy MV mounted in the left heart flow loop with the catheter prototype placed on the anterior leaflet. Dotted lines represent regions targeted for cryo-anchoring and RF ablation. **C:** Catheter prototype with cryo-anchoring elements and RF electrode.

loop allowed for precise spatial localization of the catheter tip to the desired areas of the MV. The cryo-anchor temperature was controlled automatically by monitoring the temperature of the cryo-anchor and varying the duty cycle of a cryogenic solenoid.

Flow Loop Treatments. Two different treatments were tested on MVs placed in the left heart flow loop while under physiologic flow conditions. To determine the hemodynamic changes induced by cryo-anchoring, the cryo-anchoring procedure was performed without RF ablation on several locations of each MV leaflet for a total of 15 applications for 90 seconds each at a temperature of approximately -30 to -35°C. The cryo-anchoring procedure targeted the central portion of the anterior and posterior leaflets, as demonstrated in Fig. 1B. In order to assess the ability to ablate the MV leaflets, RF ablation was performed during cryo-anchoring, also in the central portion of the anterior and posterior leaflets. RF ablation was applied while cryo-anchored to the MV at a power of 50 W for 90 seconds, with 15 applications.

Parameter Fitting. Strain energy density was used to provide a quantitative measure of the extent of RF ablation, which allows post-treatment mechanical assessment of leaflets without any pre-treatment information. The strain energy density was determined by fitting post-treatment mechanical data to a three-parameter strain energy model using non-linear regression [141]. After treatment in the left heart flow loop, MV anterior leaflets were excised, tracking markers were placed on the surface of the leaflet for strain tracking, and samples were placed into a biaxial mechanical test device and loaded to 90 N/m of membrane tension in each direction. For more details, see [9, 11].

Following mechanical testing, the strain energy density was determined by fitting the membrane tension and strain data to a three-parameter strain energy model [142], in order to determine the strain energy density (W):

$$T_{ij} = \frac{\partial W}{\partial E_{ij}}$$

$$W = c[e^{Q} - 1]$$

Where:

$$Q = A_1 E_{11}^2 + A_2 E_{22}^2$$

In which c, A1, and A2, are the parameters to be fit, Eij is the Green-Lagrange strain tensor, W is a strain energy density function, and Tij is a membrane tension representation of the 2nd Piola-Kirchhoff stress tensor. Tij is a relation of membrane tension in the reference configuration to areas in the reference configuration and is defined as:

$$T_{11} = \frac{P_1}{L_2 \lambda_{11}}$$

and:

$$T_{22} = \frac{P_2}{L_1 \lambda_{22}}$$

Where P is the load in Newtons, L is the original length of the sample, and λ is the principal stretch ratio. Directions 1 and 2 correspond with the circumferential and radial directions of the MV leaflet, respectively. Experimental data was fit to the three parameter strain energy model using non-linear least squares regression with a trust-region-reflexive algorithm [143]. Boundary conditions were imposed such that all three parameters, c, A1, and A2, must be greater than zero. The results from mechanical testing, including the three parameter fits and the strain energy density, are displayed in the supplementary tables.

In order to provide a control group for comparison, biaxial mechanical data that had previously been collected on untreated MV anterior leaflets (n=100) was fit to the above three parameter model. As the distribution of the residuals from model fitting was non-normal, we used the results from parameter fitting these 100 samples to directly determine a 95% untreated confidence interval: the range that contained the middle 95 values. For additional control groups, we fit biaxial mechanical data from MV anterior leaflets treated in a static environment with 350 J, 850 J, and 1250 J of RF energy in combination with cryo-anchoring [11]. n=5 anterior leaflets were used per control group.

Picrosirius Red Staining. Collagen morphology and birefringence were assessed with picrosirius red (PSR) staining, which is specific for collagen when viewed under polarized light [144]. Leaflets were sectioned along the circumferential direction at 7 μm, stained with sirius red 0.1% in saturated picric acid (Electron Microscopy Science, Hatfield, PA) for 1 hour, and viewed between crossed polarizers at 200x magnification for morphological assessment (Eclipse E800, Nikon, Tokyo, Japan).

Collagen birefringence is an indicator of thermal damage [145], so a relative measure of birefringence was obtained by determining the average image intensity [146]. MV sections were placed between crossed polarizers and images were taken with the long-axis of each sample at 0°, 45°, and 90° relative to the polarizing axis. Average image intensity was calculated for a 250 μm x 250 μm area using images from each of the three orientations and normalized to the background light intensity. This process was repeated twice more for a total of 3 regions per MV leaflet.

Durability Study. In order to test the durability of RF ablation treatment, MV anterior leaflets were excised from porcine hearts immediately after slaughter. Leaflets were then placed in the biaxial mechanical test device, mechanically tested to 90 N/m of membrane tension, and then either treated with 1250 J of RF energy with cryo-anchoring or were left untreated (n=6 per group). After treatments, leaflets were mechanically tested, placed in a tension bioreactor (Fig. 7.2) inside of a standard incubator (37°C, 5% CO2) and stretched to 10% strain at 1 Hz. During conditioning in the stretch bioreactor, samples were submerged in DMEM containing 10% FBS and 5% antibiotic/antimicotic (ABAM) for 3 days. ABAM was then reduced to 2% following the first three days of conditioning, and all samples were stretched continuously for four weeks. After four weeks of conditioning, mechanical testing

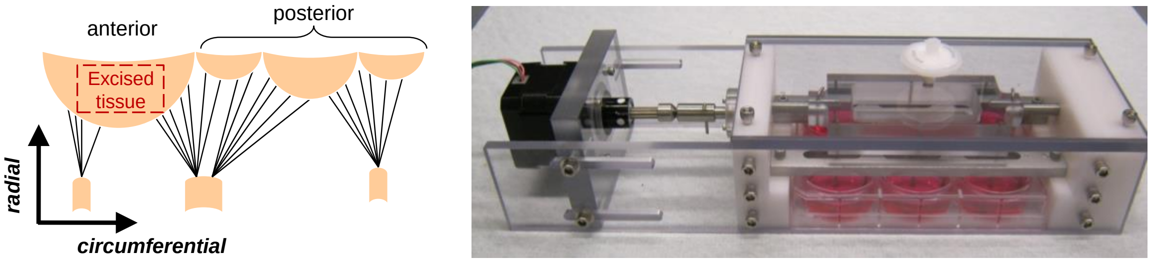

Fig. 7.2: Cyclic Stretch Bioreactor
Cyclic stretch bioreactor used for the four week durability study.

with parameter fitting and PSR staining were used to assess the state of the leaflets following four weeks of conditioning and to determine if leaflet size changes induced by RF ablation remained durable.

Statistical Methods. For analysis of average image intensity of PSR-stained sections and leaflet size in the durability study, statistical significance was determined using a student's t-test with $\alpha = 0.05$. All error bars shown indicate standard error. For comparison of the parameters determined by non-linear regression, all data was compared to the 95% confidence interval determined directly from n=100 untreated MV anterior leaflets.

Results

Hemodynamics of Cryo-Anchoring. Fluid flow and pressure across the MV were monitored before (baseline) and during the cryo-anchoring procedure, and waveforms remain largely unaltered during cryo-anchoring (Fig. 7.3A and Fig. 7.3B). When the forward cardiac output was compared between baseline and during the cryo-anchoring procedure, no significant differences were observed (inset, Fig. 7.3B). Fig. 7.3C displays typical outputs to the catheter prototype's cryo-anchor and RF ablation electrode during a combined RF

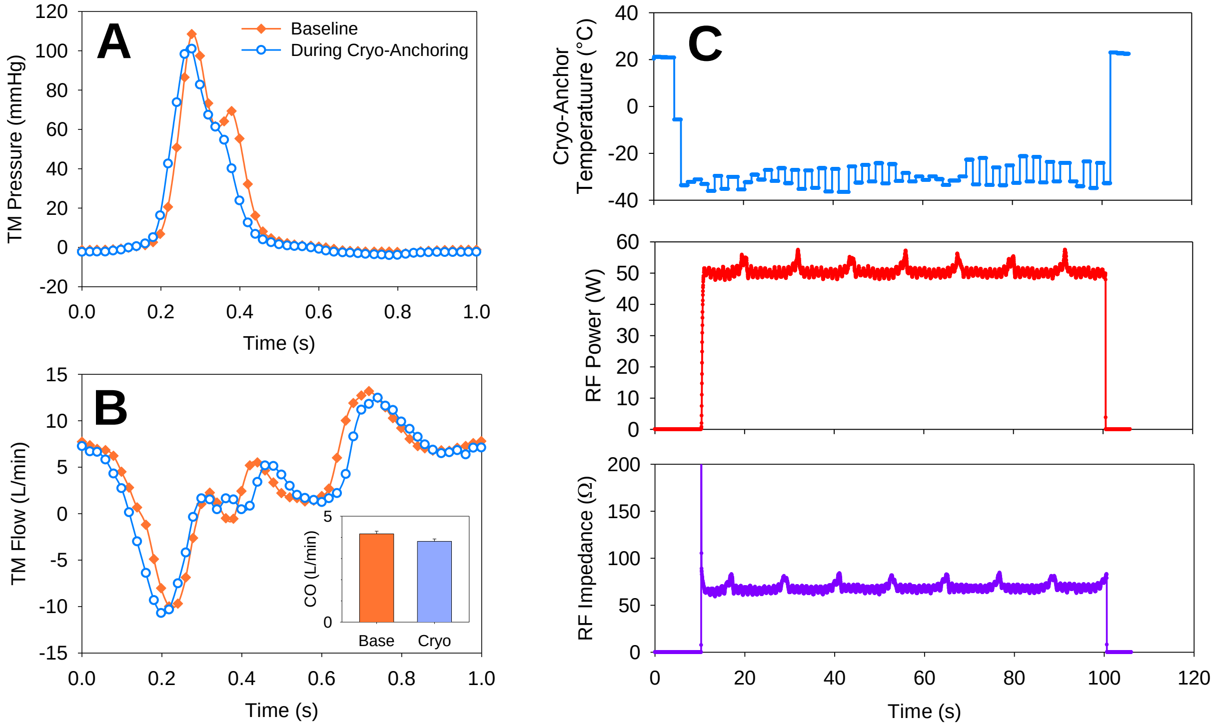

Fig. 7.3: Hemodynamics of Cryo-Anchoring and Typical Catheter Outputs
Representative transmitral pressure (**A**) and flow (**B**) waveforms for a baseline flow condition (closed diamonds) and during cryo-anchoring (open circles). Inset: average forward cardiac output during baseline and cryo-anchoring flow conditions. No significant differences between groups. **C:** Catheter outputs for one representative ablation procedure performed in the left heart flow loop.

ablation procedure with cryo-anchoring. Videos of the cryo-anchoring procedure can be found in the supplemental data (Videos S1 and S2, not shown).

Parameter Fitting. Fig. 7.4 shows a representative model fit to the biaxial mechanical data from both of the flow loop treatment groups. MV anterior leaflets treated with cryo-anchoring alone produced mechanical responses similar to those that have been reported for native, untreated MV anterior leaflets (Fig. 7.4A) [11, 50]. Qualitative differences in the shape of the loading curves can be observed between the RF ablation with cryo-anchoring group and the cryo-anchoring only group. MV leaflets treated with RF ablation lack the toe region often seen in healthy, untreated MVs, and the absence of the toe region can be seen in Fig. 4B. The shaded regions of Figs. 4A and 4B are a graphical representation of the strain energy density.

The strain energy density resulting from parameter fitting after treatment in the left heart flow loop is shown plotted alongside static controls treated with RF energy with cryo-anchoring (Fig. 7.4C). The 0 J static control group is the average of 100 untreated MV anterior leaflets that were used to determine the 95% untreated confidence interval and was found to be 4.36 N/m with a 95% confidence interval of (2.67, 7.11 N/m). The 350 J, 850 J, and 1250 J static control groups are a re-analysis of mechanical data previously presented for comparison purposes [11]. All MVs treated with RF ablation with cryo-anchoring in the flow loop have fitted parameters that fall well outside the 95% untreated confidence interval. All cryo-anchoring only MV leaflets have strain energy density similar to untreated controls, indicating that cryo-anchoring alone does not alter leaflet size or mechanical response.

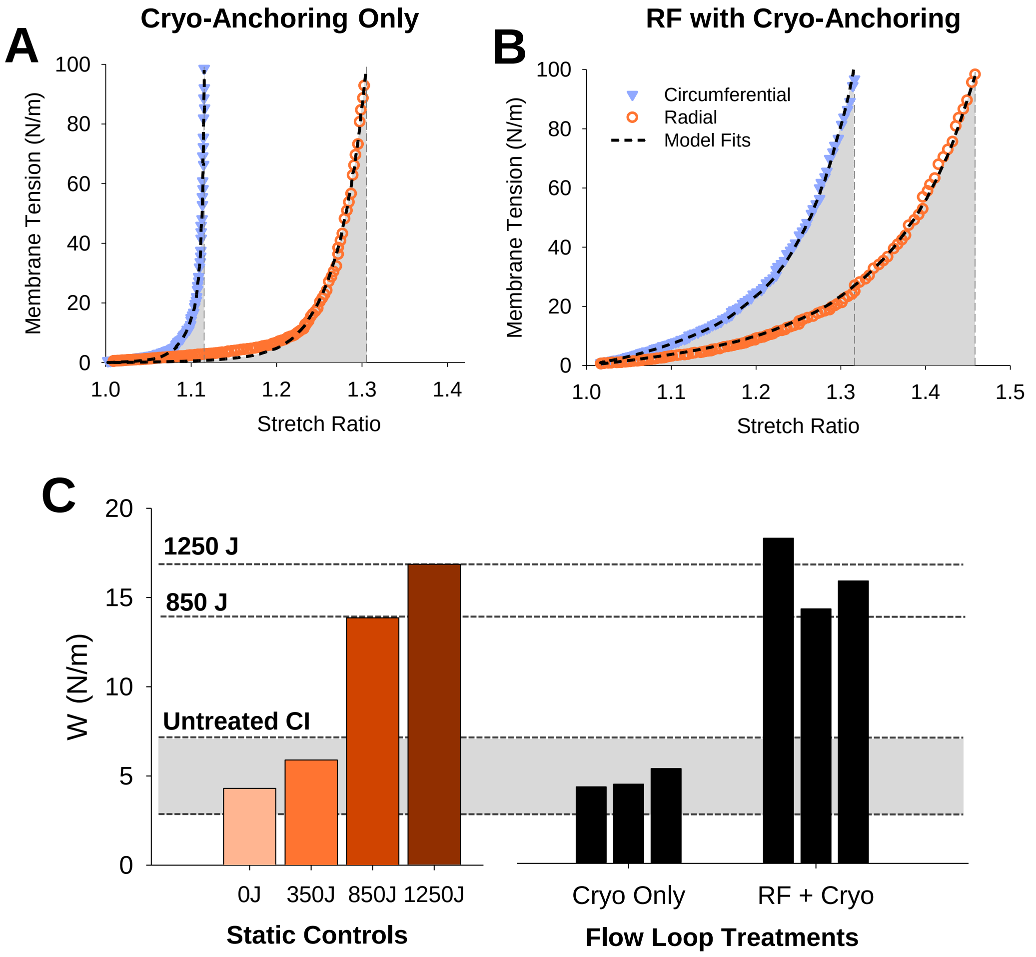

Fig. 7.4: Model Fit Results to Treated and Untreated MV Leaflets
Representative model fits to experimental mechanical data following treatment in the flow simulator following application of cryo-anchoring without RF energy (**A**) and following treatment with RF energy with cryo-anchoring (**B**). Circumferential direction, solid triangles. Radial direction, open circles. Model fits, dotted line. **C:** Strain energy density for static control leaflets and flow loop treated leaflets, an indicator of the extent of RF energy delivery. The shaded region represents the 95% untreated (0 J) confidence interval, determined from n=100 MV anterior leaflets not treated with the catheter prototype. Each of the static control leaflets (350, 850 and 1250 J) were treated with the amount of RF energy indicated combined with cryo-anchoring (n=5 per group).

Picrosirius Red Staining. Morphological analysis of MVs stained with PSR reveals the collagen crimp pattern typical of healthy MV leaflets (Fig. 7.5A). Cryo-anchoring alone does not modify collagen morphology (Fig. 7.5B); however, treatment with RF ablation denatures the collagen fibrils, and a distinct loss of collagen crimp occurs (Fig. 7.5C). Representative images of MVs treated in the left heart flow loop are also displayed in Fig. 7.5, and PSR-stained sections of flow loop treatment with cryo-anchoring only (Fig. 7.5D) demonstrates morphologies similar to untreated valves. MVs treated in the flow loop with RF ablation with cryo-anchoring (Fig. 7.5E) reveal regions of thermal damage indicated by a loss of collagen crimp. Fig. 7.5E features a distinct border between ablated tissue and normal, untreated tissue.

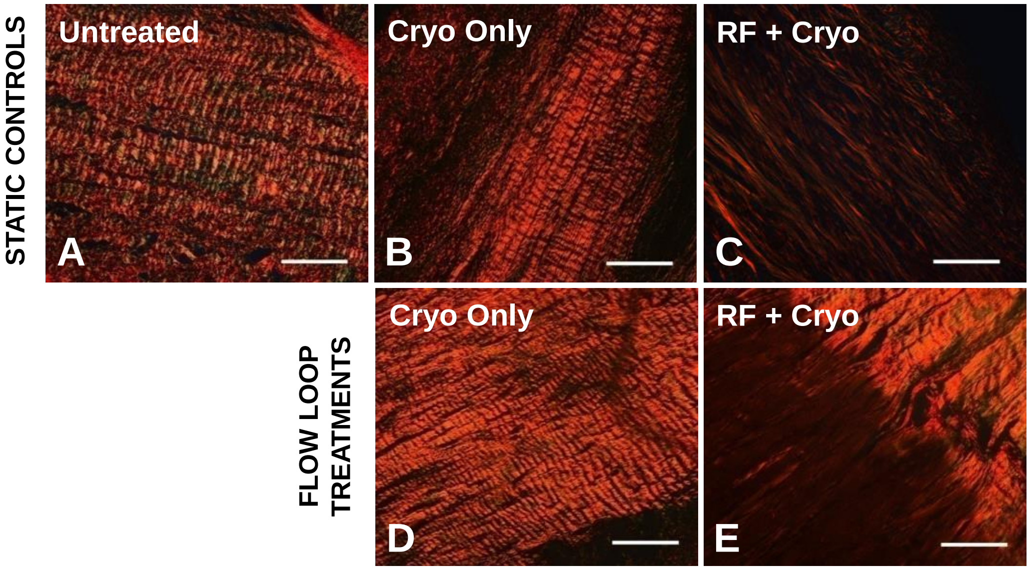

Fig. 7.5: Picrosirius Red Staining of RF Ablation-Treated MV Leaflets
Representative images of PSR-stained sections sliced with the circumferential direction and viewed between crossed polarizers. Scale bars = 100 μm. **A:** Untreated, normal MV. **B:** Statically treated with cryo-anchoring only. **C:** Statically treated with RF ablation with cryo-anchoring. **D:** Flow loop treatment with cryo-anchoring only. **E:** Flow loop treatment with RF ablation with cryo-anchoring. Note the sharp demarcation between ablated and normal tissue.

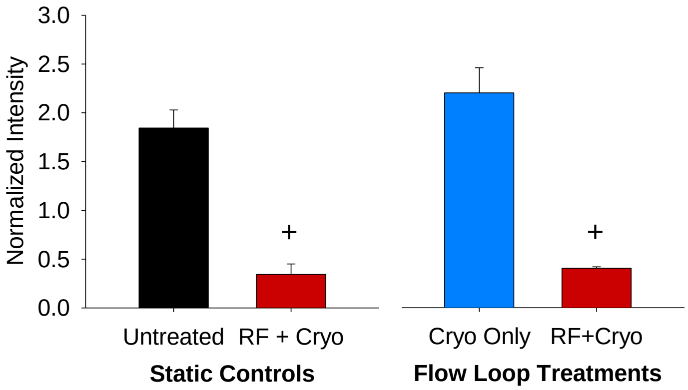

Fig. 7.6: Quantification Polarized Light Intensity of PSR-Stained MV Sections
Average normalized light intensity of PSR-stained sections viewed between crossed polarizers, a relative assessment of collagen birefringence. Average of n=3 MV anterior leaflets per group. + indicates a significant decrease ($p < 0.05$) from the static, untreated control leaflets.

Average normalized light intensity is shown for static control valves and flow loop treated MVs in Fig. 7.6. Treatment with RF ablation results in a significant reduction in average light intensity ($p < 0.05$). Consistent with morphological image analysis and parameter fitting, MVs treated with cryo-anchoring alone have a collagen birefringence similar to normal, healthy MVs, and MVs treated with RF ablation with cryo-anchoring demonstrate a significant reduction in birefringence.

Durability Study. Following static treatment of RF ablation with cryo-anchoring and four weeks in a stretch bioreactor, MV leaflets were reduced in size at all points in the loading cycle (Fig. 7.7A), similar to a typical acute post-treatment response [11]. Fig. 7.7B shows leaflet size changes, as measured at mechanical loading that mimics the systolic condition, immediately post-treatment and after four weeks of conditioning. Leaflets demonstrated size reductions in both the circumferential and radial directions that were maintained over four weeks, with no significant difference between groups. Parameter fitting indicated that strain energy density for the RF ablation-treated MV leaflets remained outside the 95% untreated confidence interval over 4 weeks (Fig. 7.7C). Untreated and treated MV leaflets stained with PSR after four weeks of conditioning in a stretch bioreactor expressed similar morphologies to healthy and RF-treated leaflets, respectively (Fig. 7.7D and Fig. 7.7E).

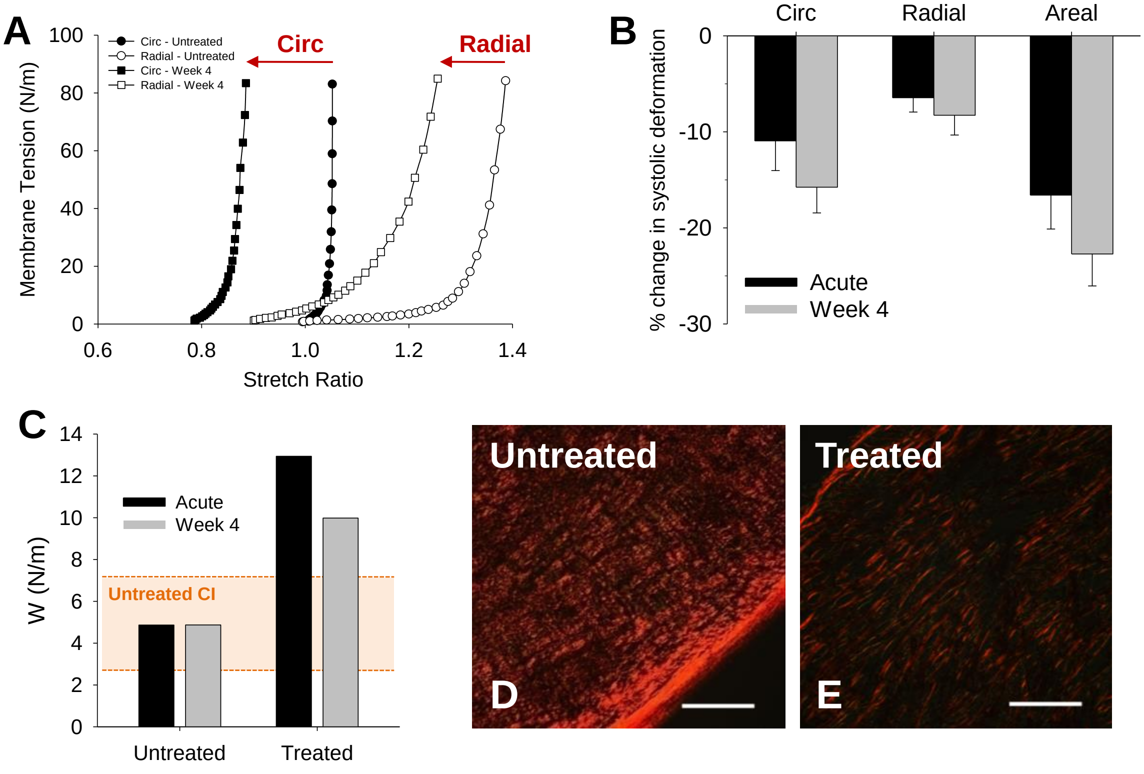

Fig. 7.7: Durability Testing of RF Ablation-Treated MV Leaflets

Representative membrane tension vs. stretch ratio for one MV leaflet treated with 1250 J of RF energy with cryo-anchoring (**A**). Shown are the pre-treatment (circles) and four week post-treatment (squares) mechanical responses with all stretch ratios referenced to the untreated, unloaded configuration. **B:** % change in areal systolic deformation (leaflet size at 90 N/m of membrane tension) immediately after treatment with 1250 J of RF energy with cryo-anchoring (black bars) and four weeks post-treatment (gray bars). No significant changes between groups ($p > 0.05$), n=6 for each group. **C:** Strain energy density for mechanical test data immediately after treatment (black bars) and four weeks post-treatment (gray bars). n=6 for each group. **D-E:** Representative images of PSR-stained sections following four weeks in a stretch bioreactor. Scale bars = 100 μm.

Discussion

Cryo-Anchoring Hemodynamics. As Video S1 (not shown) demonstrates, a steerable catheter can freely maneuver around the circumference of the MV apparatus, and placement of the catheter on or across the MV leaflet does not restrict motion. Cryo-anchoring of the catheter to the surface of the MV apparatus can be performed in a variety of locations, allowing RF energy to be distributed where desired. Video S1 demonstrates a cryo-anchoring procedure in which both the anterior and posterior leaflets are anchored simultaneously, producing leaflet movement comparable to that of an edge-to-edge repair [84]. As demonstrated, cryo-anchoring provides robust attachment to both leaflets when each of the approximately 1.75 mm long cryo-anchors of the 7 French catheter are maintained at -30 to -35°C. Cryo-anchoring can also be confined to a single leaflet, such as that shown in Video S2, in which the anterior leaflet is anchored near the MV annulus and leaflet motion is largely unaltered. Thus, cryo-anchoring can be used to target specific regions of the MV apparatus for delivery of RF energy, and cryo-anchoring can be maintained over long periods of time (90 seconds or more) at temperatures around -30°C to allow for therapeutically meaningful doses of RF energy to be delivered (Fig. 7.3C). Importantly, the cryo-anchoring procedure does not significantly alter the hemodynamics of the left side of the heart (Fig. 7.3A-B).

Assessment of RF Energy Delivery I: Strain Energy Density. As these experiments were performed on healthy MVs, flow measurements such as regurgitant volume, or geometric measurements such as the degree of leaflet prolapse, were not suitable indicators for treatment efficacy and an alternative method was necessary. In prior studies, we used biaxial mechanical testing to determine leaflet size and mechanical changes using pre- and post-treatment mechanical data and demonstrated that changes in leaflet mechanics accompanied size changes [11]. However, pre-treatment mechanical data was unattainable in this study due to the need to use the intact MV apparatus in the left heart flow loop. Thus, our strain energy density approach permits quantitative assessment of mechanical changes induced by RF energy by comparing the results from model fitting to those of untreated and treated control valves.

The robustness of strain energy density to predict alterations due to RF energy can be seen in the large differences between groups (Fig. 7.4C). The mechanical response and strain energy density of MV leaflets following cryo-anchoring are similar to the native, untreated response, confirming that cryo-anchoring does not affect leaflet mechanics. MVs treated in the flow loop with RF ablation were characterized by strain energy densities that fell well outside the 95% confidence interval, indicating that RF energy delivery to MV leaflets is still feasible in the presence of convective blood flow. As large (> 10 x 10 mm) sections of tissue are used for mechanical testing, strain energy density identifies large scale changes in the mechanics of the MV leaflets. A possible future application of this approach is for use with in vivo animal testing of the catheter prototype to verify RF energy delivery. As in vivo animal models of MV prolapse can be difficult to find, this will provide one method of testing successful delivery of RF energy in studies using healthy animals.

Assessment of RF Energy Delivery II: PSR Staining. PSR staining is another method of assessing RF energy delivery, since the primary target of both our ablation treatment and PSR is collagen. The collagen structure of normal, healthy MV leaflets is characterized by a regular crimp pattern, shown in both the untreated and cryo-anchoring only treatments (Fig. 7.5A-B and Fig. 7.5D). Studies with cryoablation on the myocardium have concluded that cryogenic temperatures, at least as low as -80°C, can be performed without structural damage to tissues [56]. MV leaflets that have been treated with RF ablation lose the collagen crimp pattern as they contract due to heat, and when stained with PSR, these same leaflets also demonstrate a significant reduction in collagen birefringence in areas of thermal damage (Fig. 7.6). In this study, we use the average light intensity of the sample as a relative measure of birefringence. The loss of birefringence manifests itself as regions of darkened tissue when viewed between crossed polarizing filters, and the difference in light intensity between ablated and untreated regions can be seen in Fig. 7.5E and Fig. 7.6.

Durability of RF Energy-Induced Changes. The in vitro durability study was performed to determine whether size changes induced by RF ablation may be temporary and whether RF-treated leaflets become mechanically compromised over time, either of which would be detrimental to this treatment strategy. Previous studies have examined the use of RF ablation to reduce left ventricular volume size in patients with congestive heart failure and found that myocardium treated with RF energy re-dilated within four weeks [51]. In this study, after static treatment with an RF ablation and cryo-anchoring catheter prototype and four weeks of conditioning in a stretch bioreactor, MV leaflets remained durable (Fig. 7.7A). Following the four weeks of bioreactor conditioning, MV leaflet size actually reduced further in each direction when measured at systolic loads (Fig. 7.7B), albeit not significantly. The mechanism for this further reduction in leaflet size is unknown, but one possible explanation is that scarring causes stiffening of the tissue and further contraction. Others have reported that the first 2-3 months following ablation is a period of remodeling in which tissue mechanics and size may be altered [147, 148]. Additionally, in vivo studies using RF ablation to shrink the MV annulus have reported that the annulus contracts to diameters below the initial shrinkage at 3- and 6-months [54], following a trend similar to our durability results. While this study on the durability of RF ablation treatment of MVs is limited in that it was performed entirely in vitro, the results are promising in that leaflet size changes are maintained.

Study Limitations. This study was somewhat limited in that healthy MVs were used, as there was not a reliable in vitro model for MV prolapse. A more precise determination of the efficacy of this percutaneous approach will be required using in vivo disease models. The procedure was also performed by direct visualization, which made accessing and treating the MV significantly easier than through echocardiographic image guidance. Lastly, ablation of the MV was confined to the leaflets, although the MV annulus and chords may also be ablated. Chordal elongation is often another target of MV repair, and further work may include ablation of the chords. However, there may be added risk of chordal rupture or of inducing arrhythmias, due to their location in the ventricle.

Conclusions

In this study, we have demonstrated that a combined RF ablation and cryo-anchoring catheter can reliably adhere to and ablate the MV in a dynamic hemodynamic environment. Cryo-anchoring provides robust, reversible attachment to the MV apparatus while RF ablation reduces MV leaflet size, effectively providing a percutaneous alternative for surgical leaflet resection. While in vitro results are promising, further study will be required to assess in vivo safety and efficacy.

Chapter 8

AIM 3: TWO-DIMENSIONAL ECHOCARDIOGRAPHIC INDICATORS OF MV LEAFLET SHRINKAGE AND ASSESSMENT OF TREATMENT EFFICACY IN VIVO

Introduction

The objective of the present work is to evaluate the efficacy of the RFC catheter to approximate surgical leaflet resection using a non-survival porcine animal model. Initially, RFC catheter treatment efficacy criteria was identified using ex vivo testing of excised porcine MVs placed in a left heart flow simulation device. The primary goal of the ex vivo study was to use quantitative leaflet length measurements, obtained on echocardiographic views of the A2-P2 imaging plane, as a predictive imaging correlate for total leaflet area reductions. Leaflet area reductions of MVs in the left heart flow simulator were measured by tracking the positions of four suture markers placed on the MV anterior leaflet (AL) surface with echocardiography in an intercommissural imaging plane to capture all markers on 2-dimensional (2D) views. Corresponding leaflet length reductions were captured in the A2-P2 imaging plane and compared to directional and areal measurements obtained in the intercommissural plane.

Following the establishment of efficacy criteria, five consecutive in vivo studies in healthy pigs were performed open-chest to test the efficacy of the RFC catheter to resect leaflet tissue. The data that follow demonstrate that RFC catheter treatment, guided by echocardiography, produces significant resection of MV leaflets without compromising hemodynamic function during treatment. Post-treatment echocardiographic images, quantification of leaflet length, as well as gross morphological, histological, and mechanical analyses provide evidence that RF ablation can produce significant reductions in MV leaflet area.

Materials and Methods

Ex Vivo Establishment of Efficacy Criteria. Intact porcine MVs were excised from hearts obtained from the local abattoir (Hampton Meats, Hopkinsville, KY) within one hour of slaughter, including the annulus, leaflets, chords, and papillary muscles (PMs). Four tracking markers (3-0 braided polyester suture with 3-4 square knot throws) were sutured to the central region of the AL on the atrial surface with approximately 1 cm spacing to track leaflet size with echocardiography. Additionally, the outer margin of the AL was marked by staining with trypan blue to provide an estimate of leaflet area pre- and post-treatment. The intact valves were then placed in a left heart flow simulator (Fig. 1A) capable of reproducing physiologic pressure and flow waveforms (average flow rate of 5 L/min, heart rate of 70 beats/min, transmitral pressure of 100-120 mmHg), as described previously [149].

Mock circulatory flow loops have been used to create models of MR and to study the hemodynamic response of MVs to various surgical treatments [150]. In this study, after a normal, baseline PM configuration was established, both PMs were displaced towards the MV annulus until significant leaflet billowing (greater than 4 mm beyond the annular line) was seen on echocardiography (Fig. 8.1). This provided an approximate simulation of bi-leaflet prolapse to more easily visualize leaflet morphologic changes following treatment with the RFC catheter.

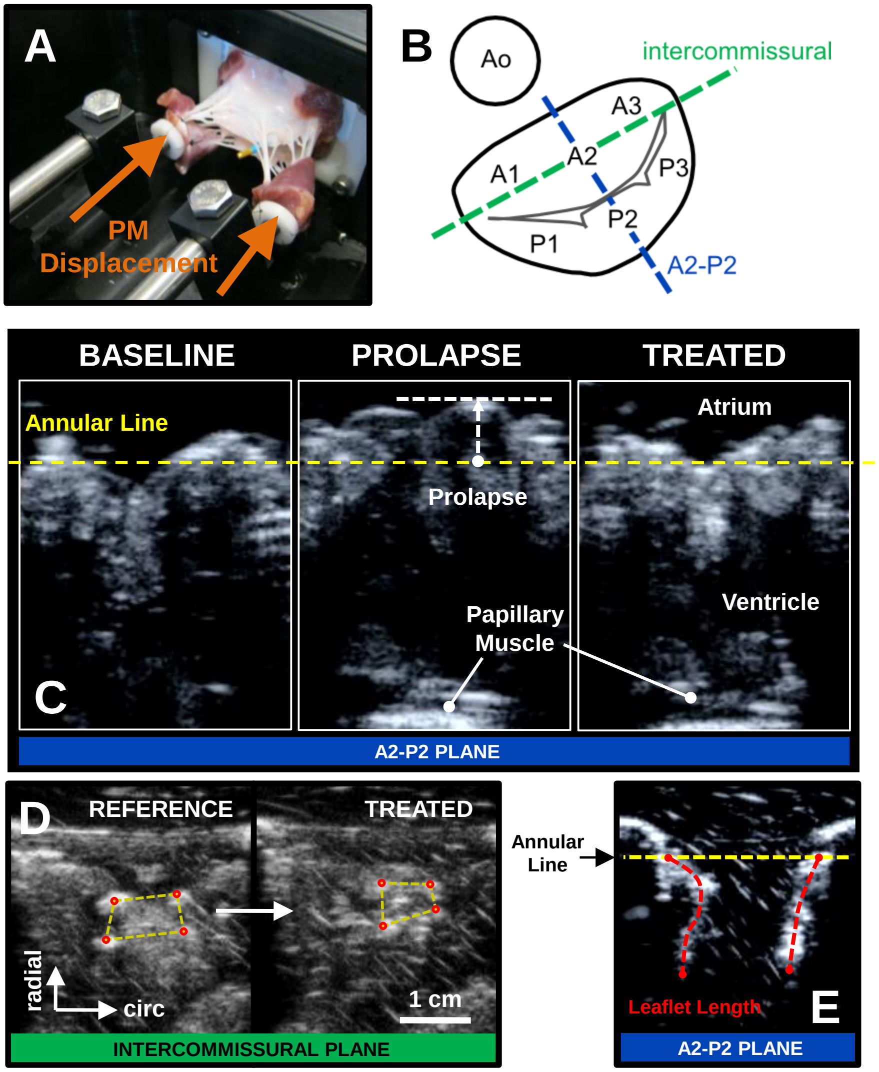

Fig. 8.1: Ex Vivo Methods
A: MV positioned into the left heart flow simulator with adjustable PM attachments (arrows). **B:** Echocardiographic imaging planes used in the ex vivo study, surgical view. **C:** Change in MV morphology following treatment with the RFC catheter, shown in the A2-P2 plane. Note the reduction of leaflet prolapse following treatment. **D:** Markers placed on the AL were tracked in the intercommissural imaging plane. **E:** Echocardiographic image of a porcine MV in the left heart flow simulator imaged in the A2-P2 plane with leaflet length measurements denoted in red.

To provide a clinically relevant assessment of RFC catheter treatment efficacy, two-dimensional (2D) echocardiography (Acuson Antares, Siemens) was used to image MVs in the left heart flow simulator. Views of the MV apparatus were captured in two imaging planes: an intercommissural plane to track the four suture markers on the surface of the AL, and an A2-P2 plane to record leaflet morphology, length, and prolapse (Fig. 8.1B). Baseline echocardiographic recordings were captured, the PMs were displaced towards the annulus, and the prolapse condition was recorded (Fig. 8.1C). The AL was then treated several times with the RFC catheter with a cryo-anchor temperature of approximately -50°C and RF ablation power of 65W for 90 seconds each. The first five ablations were performed within the area constrained by the four tracking markers, and marker positions were recorded during mid-diastole after each ablation in the intercommissural plane (Fig. 8.1D). To determine reductions in marker area, circumferential length, and radial length, the deformation gradient tensor was calculated from the four marker positions and averaged over three repeated measurements (MATLAB, MathWorks, Inc.) [11, 117]. After the first five ablations, each AL and posterior leaflet (PL) was ablated up to 10 times, and post-treatment echocardiographic recordings were captured. AL and PL lengths were measured during mid-diastole, from the base of the annulus to the leaflet free edge, and averaged over three measurements (MATLAB) (Fig. 8.1E), while corresponding leaflet prolapse measurements were taken during mid-systole (Showcase Premier, Trillium Technology) (Fig. 8.1C).

In Vivo Investigational Protocol. Five consecutive studies in healthy pigs ranging in weight from 47 to 51 kg were carried out with a Vanderbilt University approved institutional animal care and use committee protocol to evaluate RFC catheter efficacy in vivo. On the day of surgery, anesthesia was induced with ketamine (2.2 mg/kg), telazol (4.4 mg/kg), xylazine (2.2 mg/kg), and atropine (0.04 mg/kg) via intramuscular injection, and isoflurane (1-3%) with O2 was administered under endotracheal intubation for maintenance. To prevent arrhythmias, animals were treated with an intravenous bolus loading dose of 2 mg/kg of amiodarone prior to the start of surgery and 1.2 mg/kg/hr via intravenous drip for maintenance thereafter. Heart rate, rhythm, and blood pressures were monitored throughout the procedures.

A median sternotomy was performed and intervening fascial layers dissected to optimize visualization of the pericardium, heart and major blood vessels. An 18 gauge needle was utilized to cannulate the mid-to-distal anterior wall of the left ventricle through which a 0.035-inch J-wire was inserted for ventricular access. A 12 Fr short modified sheath was placed in the left ventricle (Fig. 8.2A-B) via an over-the-wire modified Seldinger technique followed by tandem removal of the wire and dilator. Sheath position on the left ventricular free wall and alignment with the MV apparatus was confirmed by direct echocardiographic guidance using an epicardial probe positioned superior to the access site on the pericardial-epicardial surface in an epicardial long-axis configuration. Fluoroscopy was available, if necessary, for sheath and catheter guidance but was used in only one animal in this study.

The RFC catheter (10 Fr) was directed through the sheath and across the MV orifice under direct echocardiographic visualization. Once the RFC catheter tip was located in the vicinity of the AL, cryo-anchoring was obtained by intra-luminal delivery of nitrous oxide to securely cryo-anchor the catheter to the leaflet surface with a temperature of -50°C (Fig. 8.2C-D). Once cryo-anchoring was achieved, RF energy was delivered to the AL for 60 seconds (Fig. 8.2E-F). RF power output was regulated to maintain the RF electrode

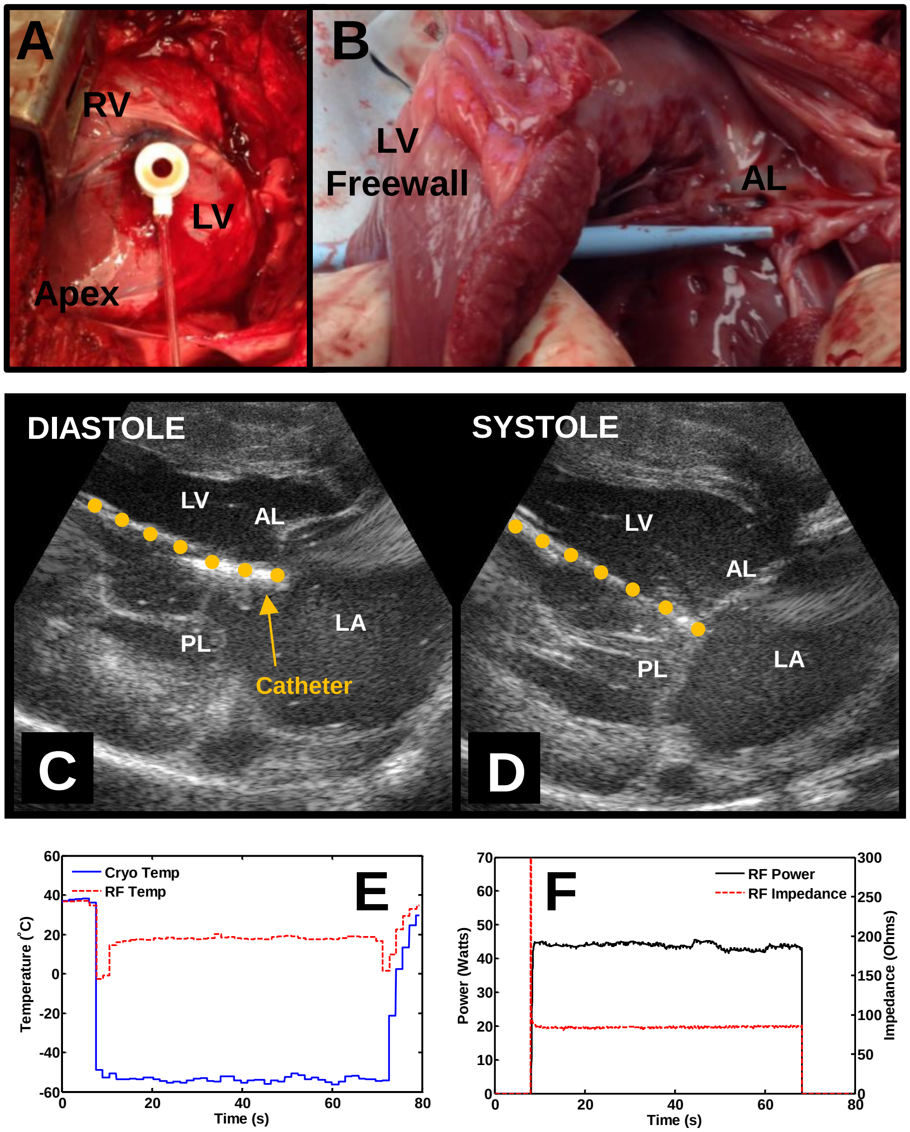

Fig. 8.2: In Vivo Methods

A: Access to the MV was gained by placing a sheath midway up the left ventricular free wall, enabling direct access to the AL, shown post-mortem (**B**). Epicardial long-axis view of the RFC catheter cryo-anchored to the AL, while the PL moves freely. The diastolic view demonstrates the free PL (**C**), while the systolic view demonstrates that leaflet mobility is maintained, allowing valve closure (**D**). Dotted yellow line indicates the catheter shaft. **E:** Representative temperatures at the RF electrode (red, dash) and cryo-anchor (blue, solid) during one ablation. **F:** Representative ablation power output (black, solid) and measured impedance (red, dashed) corresponding to temperatures measured in **E**. LV: left ventricle. RV: right ventricle.

temperature within a calibrated range that was demonstrated to produce leaflet resection without significant impedance rise. Cryo-anchoring was then ceased after 60 seconds of ablation, the RFC catheter tip was re-positioned, and the cryo-anchoring and ablation process was repeated up to 20 times for each animal.

In Vivo Study Evaluation Protocol. Echocardiographic examination of the MV and surrounding area was performed before and after RFC catheter treatment in long- and short-axis views of the heart. All echocardiographic imaging was performed epicardially using a custom-built scanner (Cephasonics, Santa Clara, CA) in B-mode with a 10 MHz linear array probe. Following catheter treatment and completion of the echocardiographic examination, each animal was euthanized according to protocol, and the heart was excised. At post-mortem, the entirety of the left heart, including the MV, ventricle, atrium and left ventricular outflow tract, was examined for signs of ablation. Gross leaflet morphology, as well as any off-target ablations, were noted. The belly region of each MV was then excised and mechanically tested to equibiaxial loads of 90 N/m in a biaxial mechanical testing device to assay for evidence of thermal alteration by fitting the mechanical loading curves to a Fung-type strain-energy model. Strain-energy measurements have previously been shown to provide a measure of thermal alteration and an estimate of resected leaflet area [130, 149]. Afterwards, leaflets were fixed in 10% formalin before histological staining with picrosirus red to assess collagen structure for characteristic markers of thermal alteration [145, 149]. Echocardiographic images of the AL in the long-axis view from pre- and post-treatment were analyzed offline to measure leaflet length (MATLAB). Leaflet length measurements were repeated three times per image frame over 3-6 different frames for a total of 9-18 measurements per leaflet and were averaged together.

Statistical Analysis. All measurements are reported as mean ± standard error. One way ANOVA was conducted to examine statistical differences between groups with a follow-up Holm-Sidak method for multiple pairwise t-tests at significance level α=0.05.

Results

Ex Vivo Assessment. Maximum areal shrinkage within the marker region of interest was achieved after 4 ablations of 50W for 90 seconds (Fig. 8.3A-B) and shrinkage was greatest in the circumferential leaflet direction (Fig. 8.3C). After 15 ablations, spread over the entirety of the AL, areal leaflet shrinkage was 38 ± 2.7%, circumferential shrinkage was 30 ± 2.3%, and radial was 12 ± 2.2% (Fig. 8.3D). For comparison, leaflet area, as measured by the area enclosed by tissue dye markers before and after experiments, was found to have shrunk by 32 ± 3.3% and 37 ± 5.9% in the AL and PL, respectively. Corresponding leaflet length reduction (9.2 ± 1.8%), measured on echocardiography in the A2-P2 imaging plane, was comparable to radial shrinkage. Overall, when leaflet length has been reduced by 9.2%, total leaflet area has decreased by 38%, which provides a quantitative target for determining leaflet resection efficacy in the in vivo study (Fig. 8.3D). PL length decreased by 12 ± 3%, and average leaflet lengths measured in the baseline, prolapse, and treated conditions are shown plotted in Fig. 8.4A-B. Leaflet prolapse decreased by 62 ± 17% and 50 ± 30% in the AL and PL, respectively (Fig. 8.4C-D).

In Vivo Efficacy. The RFC catheter was able to selectively adhere to the AL, and valve closure was minimally inhibited during cryo-anchor formation. The maximum difference in heart rate during RFC catheter treatment from baseline averaged -2 ± 3.3 beats per minute, suggesting no adverse effects on cardiac function. Cryo-anchoring was successfully

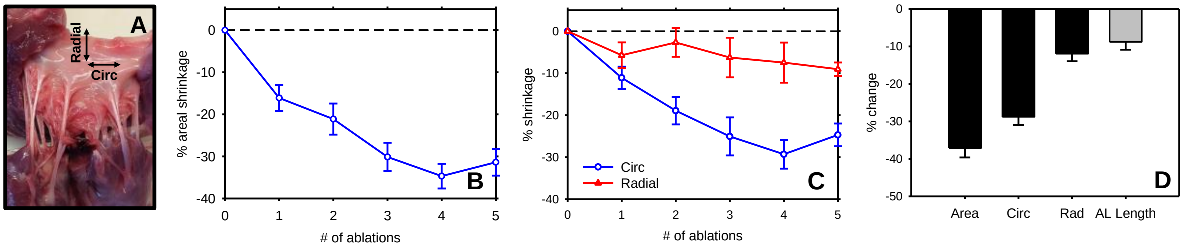

Fig. 8.3: Ex Vivo Leaflet Area Measurements

A: MV leaflet circumferential (circ) and radial directions. **B:** Areal leaflet shrinkage over the course of 5 ablations within the 2x2 marker area, n=6. **C:** Corresponding directional shrinkage measurements in the circumferential (blue circles) and radial (red triangles) directions, n=6. **D:** Average final marker size reductions recorded in the intercommissural imaging plane (black bars) and corresponding leaflet length reduction measured in the A2-P2 imaging plane (gray bar), n=9.

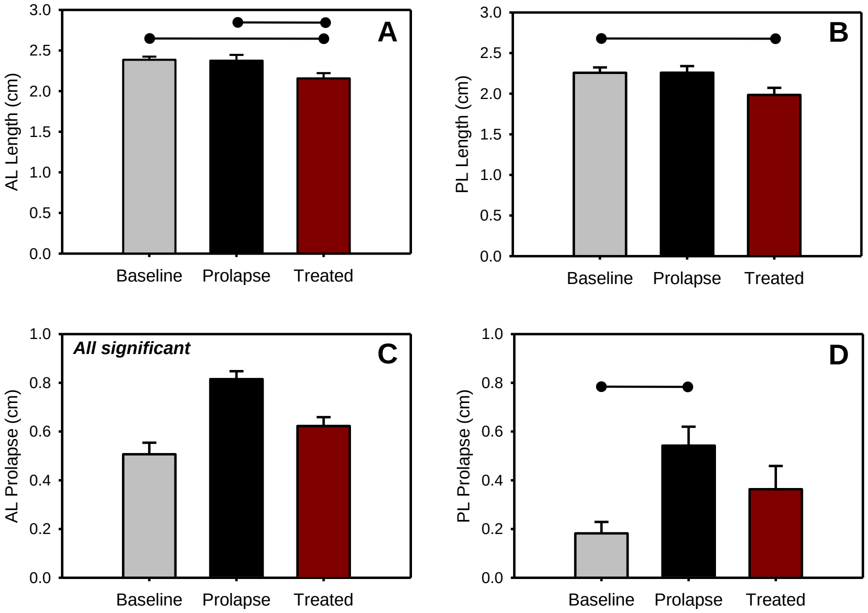

Fig. 8.4: Ex Vivo Length and Prolapse Measurements

A-B: AL and PL length measured in the baseline and prolapse configurations and following treatment with the RFC catheter. C-D: Corresponding reduction in prolapse of the AL (C) and PL (D) post-treatment. Lines above bars represent significant changes between groups ($p<0.05$). n=9 per group.

maintained throughout each ablation, and between 15-21 ablations were attempted on each animal for a target time of 60 seconds (Table 8.1). One animal (Animal #5) developed atrial fibrillation after 15 ablation attempts and was successfully cardioverted to normal rhythm. Echocardiographic images taken of the AL post-treatment demonstrated apparent leaflet thickening, shortening of leaflet length (Fig. 8.5A-B), and altered leaflet motion throughout the cardiac cycle when compared to pre-treatment images. Measurements of leaflet length on echocardiographic long-axis views indicated an average 13.3 ± 4.6% reduction in AL length following RFC catheter treatment (Fig. 8.5C).

Table 8.1: Average Ablation Output and Post-Treatment Morphological Assessment

Animal #	Ablations Attempted	Average Duration (s)	Average Power (W)	Average RF Temp. (°C)	Off-Target Ablations	Morphologic Changes
1	15	57 ± 2.5	50 ± 1.0	9.8 ± 0.4	2 – Near posteromedial commissure on ventricular wall	▪ Significant char in belly region ▪ Coagulum along annulus ▪ Thickening throughout
2	20	58 ± 1.8	50 ± 1.4	13 ± 0.6	1 - Near posteromedial commissure in atrium above annulus	▪ Small amounts of char ▪ Apparent thickening within 3-4 mm of free edge
3	21	52 ± 2.8	33 ± 2.0	14 ± 0.6	0 - None could be identified	▪ Significant char in A2 segment from annulus to leaflet free edge ▪ Coagulum along annulus ▪ Thickening throughout
4	20	58 ± 1.3	28 ± 1.5	19 ± 0.7	0 - None could be identified	▪ Moderate char, primarily in A2 segment from leaflet belly region to free edge ▪ Apparent thickening in leaflet central area
5	15	56 ± 2.8	28 ± 0.7	16 ± 0.8	2 – Near posteromedial commissure on ventricular wall	▪ Localized areas of leaflet thickening and light char on leaflet ▪ Coagulum along annulus near both commissures

ALs treated with the RFC catheter demonstrated varying levels of char formation on the leaflet surface, coagulum formation around the annulus, and apparent leaflet thickening (Fig. 8.6A; Table 8.1). Most off-target ablations were located around the posteromedial commissure in either the ventricle or atrium Ablations located on the annulus immediately above the AL were not considered off-target. Strain energy values obtained for the n=5 ALs treated in the pig study are shown plotted alongside estimates for resected leaflet area (Fig. 8.6B). Resected leaflet area estimates were obtained from previously published findings in leaflets treated in a static bench environment, and strain energy values greater than 10 N/m have been found to correlate with significant resected leaflet areas [149]. Three out of five of the leaflets positively tested for strain energy values that indicate significant leaflet resection. Additionally, picrosirius red staining confirmed that the collagen structure of the ALs had been thermally altered in four of five leaflets (Fig. 8.6C).

Discussion

Establishment of Leaflet Resection Efficacy Criteria. As healthy animals without MR were used for this study, a quantitative measurement was needed to appropriately evaluate the ability of the RFC catheter to shrink – or resect – MV leaflet tissue. Thus, we used a two-part study to identify a measurement than can be used to assess the acute success of RFC catheter treatment in healthy animals: leaflet length measured on echocardiography.

First, leaflet area and directional length measurements were taken in a physiologic ex vivo environment. These measurements were recorded in the intercommissural imaging plane (Fig. 8.1B), which cannot be sufficiently visualized without the placement of markers on the leaflet surface. Next, corresponding leaflet length measurements in the A2-P2

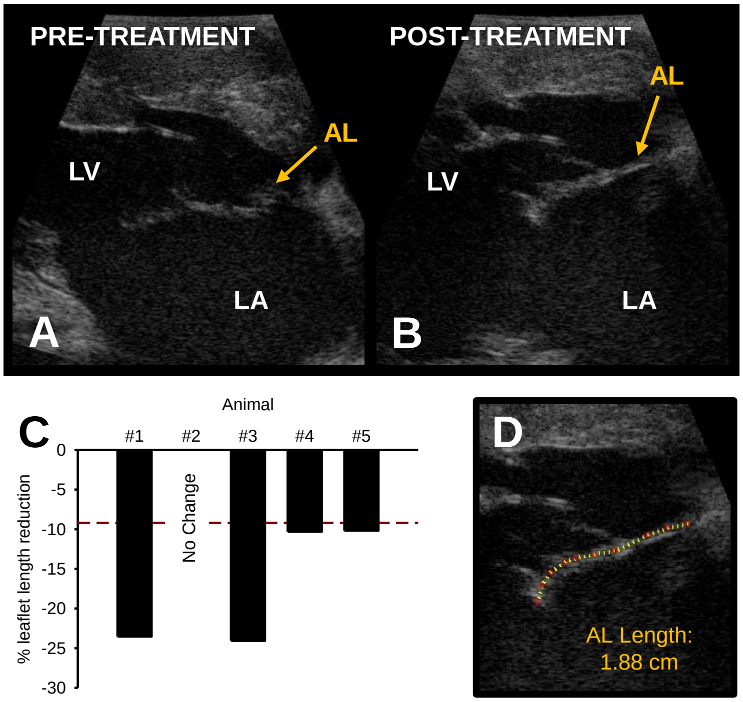

Fig. 8.5: Post-Treatment Echocardiographic AL Assessment
Long-axis view of the AL before (A) and after (B) treatment with the RFC catheter. The post-treatment AL exhibits a characteristic increase in thickness and a decrease in radial length. C: AL length reduction (% decrease) as measured on epicardial echocardiography following treatment with the RFC catheter. Dashed line indicates efficacy criteria established in the ex vivo study. D: One representative leaflet length measurement (Animal #1).

imaging plane, which is an easily obtainable measurement in vivo, were taken for comparison. As AL length (A2-P2 plane) and radial marker length (intercommissural plane) were found to agree and because the relationship between radial and circumferential shrinkage was found to remain the same across samples, leaflet length reductions measured on clinical 2D echocardiograms can be used to estimate total leaflet area shrinkage in healthy animals. Based on the ex vivo data, the target for in vivo RFC catheter treatment efficacy is approximately 10% reduction in leaflet length, which would indicate a total leaflet area reduction of approximately 40% (Fig. 8.3D). This is comparable to the average resected area of a typical PL quadrangular resection, which is 30% [73].

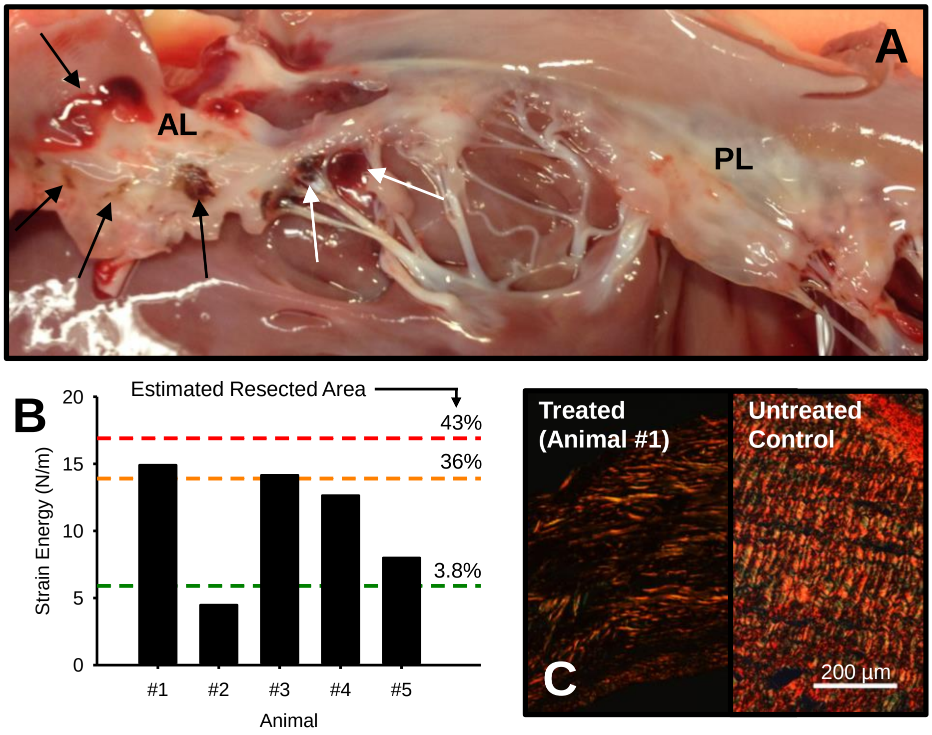

Fig. 8.6: Post-Treatment Morphological, Mechanical, and Histological Assessment
A: MV leaflets post-mortem. The AL is shown partially excised on the left and exhibits significant char and coagulum on the leaflet surface and at the base of the annulus (black arrows). Off-target ablations were seen in the posteromedial commissure (white arrows). The PL has been left untreated and is shown for comparison. B: Strain energy estimate on excised ALs following treatment with the RFC catheter. Values shown to the right are the corresponding estimates of resected leaflet area based on treated and untreated controls in a static bench environment [11, 149]. **C:** Representative picrosirius red stained section demonstrating the typical loss of collagen crimp following thermal shrinkage (Animal #1). An untreated control is shown on the right. Scale bar = 200μm.

Ex vivo testing suggests that the MV leaflet shrinks relatively linearly with the number of 65W ablations, and it takes 4 ablations to maximally shrink a 1 cm square region of tissue by approximately 40% (Fig. 8.3B). Consistent with previous studies, the majority of leaflet shrinkage occurs in the circumferential direction, the primary direction of collagen fiber alignment (Fig. 8.3A). Thus, the total leaflet length, which is aligned radially, shrinks minimally (about 10%), while the leaflet shrinks approximately 30% in the circumferential direction. The directional shrinkage response of diseased and myxomatous MV leaflets is currently unknown and warrants investigation.

A secondary component of the ex vivo study was treatment of the prolapse model, enabling large changes to MV morphology to be more easily appreciated (Fig. 8.1C). One hallmark of Barlow's disease is large, thickened, and billowing leaflets that prolapse significantly into the atrium during systole. In our ex vivo prolapse model, leaflet prolapse was reduced, on average, by over 50%. The large standard errors associated with the prolapse measurements (Fig. 8.4C-D) are likely an artifact of sample preparation (suturing of MV annulus). In some cases, leaflet prolapse was reduced by over 100% back to baseline.

RFC Catheter Treatment is Acutely Efficacious In Vivo. RFC catheter leaflet resection was acutely successful in 4 of 5 animals according to the efficacy criteria established in the ex vivo study. Additionally, minor evidence of leaflet ablation was found in the unsuccessful animal, including small amounts of char formation on the leaflet surface and collagen thermal alteration visible on histology. This is the first study to demonstrate that MV leaflet area can be significantly reduced using a catheter-based strategy in vivo.

Selective administration of thermal shrinkage to each MV leaflet is essential in the RFC catheter treatment strategy. Depending on the severity and presentation of degenerative MV disease, enlarged and myxomatous leaflet tissue could be confined to a single segment of a single leaflet or be present throughout both leaflets [20]. The AL was specifically targeted in this study due to the access route, and the AL was successfully adhered to independently of free motion of the un-targeted PL. An alternative access route, closer to the apex, was originally attempted, and it was found that the PL could be similarly targeted for cryo-anchoring (data not shown).

The ex vivo study indicates that leaflet length reductions of greater than 10% of the original length correlated with a resected area of ~40%. This benchmark was achieved in 4 of 5 animals in the present study. Echocardiographic findings showed thickened and shortened leaflets post-treatment, characteristic of thermal alteration. Gross inspection of ALs post-mortem, picrosirius red staining, and mechanical testing, each verified successful RFC catheter treatment.

Off-target ablations occurred in 3 of 5 animals. Epicardial echocardiography provides some guidance of catheter position, but probe maneuverability is limited and difficult to achieve reliably, which may have led to some of the off-target ablations observed here. Future studies will employ transesophageal echocardiography to more consistently and reliably guide catheter placement and transmitral positioning for ablation. Additionally, the catheter access route used in this study was advantageous in that it allowed direct access to the MV leaflets with little need for catheter steering, but the RFC catheter is intended to be used percutaneously, and thus approach the MV atrially through a trans-septal course. Future percutaneous studies will use the trans-septal approach with a steerable sheath and transesophageal echocardiography to more precisely target specific leaflets, which will likely reduce off-target ablations as a result

Conclusion. This study demonstrates in vivo success of a catheter-based alternative to surgical leaflet resection for repair of degenerative MV disease. RF ablation with cryo-anchoring stability can resect up to 40% of MV leaflet area. The RFC catheter cryo-anchor can selectively target each leaflet individually under echocardiographic guidance, allowing for RF delivery to specific leaflet segments. Efficacy criteria established ex vivo was used to confirm that RFC catheter treatment can be monitored on 2D echo and to confirm that treatment was efficacious in healthy pigs. While further testing of safety and efficacy remain, short-term in vivo results indicate that the RFC catheter is a potential percutaneous alternative to surgical leaflet resection.

Chapter 9

IMPACT AND FUTURE DIRECTIONS

Investigational Summary and Impact of Results

The overall goal of this research was to develop and refine a percutaneous MV repair device to provide an alternative to surgical leaflet resection and to investigate its effectiveness in reducing MV leaflet size. Several RFC catheter prototypes were designed and built throughout this investigation, and by the end of Aim 2 studies, a completed RFC catheter prototype was built for in vivo use. The current iteration of the RFC catheter is capable of controllably cryo-anchoring to MV leaflets in the beating heart, without cardiopulmonary bypass, at temperatures of -50°C, and RF ablation has been successfully delivered at powers of up to 70W in vivo. The RFC catheter interfaces with a commercially available RF generator, a custom-built nitrous oxide delivery system, and Arduino and LabView control and data acquisition software, providing a complete RFC catheter system that is ready for percutaneous studies.

We began our investigation of RFC catheter efficacy in Aim 1 by examining the thermal and mechanical effects of RF ablation and cryo-anchoring within close proximity on a catheter in a static ex vivo setup. We found that MV leaflet area could be reduced by approximately 40% or more during cryo-anchoring and demonstrated that cryo-anchoring remains robust during RF ablation, as measured on IR imaging and anchor strength testing. We also found that leaflet shrinkage magnitude varies spatially in relation to RF electrode and cryo-anchor location, and not simply according to the radial distance from the electrode, with the greatest leaflet shrinkage occurring in the direction of the circumferential axis.

In Aim 2, the RFC catheter was tested in a physiologic flow environment and it was shown that cryo-anchoring can independently adhere to moving MV leaflets while transmitral flow and pressure remain unchanged during cryo-anchoring. Additionally, we identified two techniques to assess successful delivery of RF energy to MV leaflets: mechanical model fitting and picrosirus red staining. Importantly, it was also shown that MV shrinkage deformations induced by the RFC catheter remain durable and do not re-dilate over 4 weeks.

Finally, in Aim 3, we developed echocardiographic efficacy criteria to assess RFC catheter treatment in vivo by directly measuring leaflet shrinkage before and after RFC catheter treatment and by comparing areal shrinkage measurements to measurements of leaflet length. The effectiveness of the RFC catheter to thermally shrink MV leaflets was then demonstrated in a large animal model, open-chest without cardiopulmonary bypass, by using echocardiographic efficacy criteria – leaflet length measurements – developed in the left heart flow simulator. The RFC catheter successfully reduced anterior leaflet size in four out of five animals with no compromising procedural complications. These promising results imply that the RFC catheter is a possible percutaneous alternative to surgical MV leaflet resection. With efficacy demonstrated in a small cohort of animals using an open-chest approach, further testing using a percutaneous approach is clearly justified.

The RFC catheter is not intended as a universal MV repair device. Instead, the RFC catheter is intended to be used as part of an armamentarium of percutaneous MV repair devices, with specific devices chosen to target specific lesions. Currently, percutaneous or minimally invasive approaches are in development to perform annuloplasty and chordal replacement. However, there are no devices, other than the RFC catheter, that are able to perform MV leaflet resection. In the future, the interventional cardiologist may have the tools to perform an effective MV repair without the need for cardiopulmonary bypass or general anesthesia, which will improve post-operative recovery times, decrease procedural cost, and significantly increase the percentage of patients amenable to repair [4].

Future Directions

While we have developed the RFC catheter system from concept to functioning prototype and have demonstrated its effectiveness to adhere to and resect MV leaflet tissue, there is still much testing to be done before this approach can be used in the clinic. The first step is to refine the RFC catheter treatment strategy for percutaneous delivery. The proposed percutaneous access route is to enter the right heart through the vena cava and use trans-septal puncture to access the left atrium. Trans-septal puncture is relatively common and is used in a variety of procedures such as ablation of left-sided arrhythmias and in MitraClip placement [151, 152]. Thus, there are already commercially available steerable sheaths that would enable our current RFC catheter prototypes to be used in the trans-septal approach. Transesophageal echocardiography will be needed to provide percutaneous guidance of the RFC catheter and will be available for these studies shortly. Additionally, 3D echocardiography has the potential to more completely visualize the MV leaflets and to provide a quantitative measurement of MV leaflet area, which would provide a significant improvement over 2D measurements. 3D echocardiography may also be crucial to the RFC catheter treatment strategy in the future, as it can more readily identify prolapsing leaflet segments.

Once the RFC catheter treatment strategy has been refined for percutaneous delivery and shrinkage of MV leaflets in a non-survival porcine animal model, the next step will be to treat MR in a diseased animal model and to follow the animal status for several months after treatment. Middle to small size canines commonly develop degenerative MR as they age, and thus, are an ideal pre-clinical model to test RFC catheter effectiveness [10]. With successful treatment of MR in a canine survival model, the RFC catheter will be poised for first-in-man studies of RF ablation to treat enlarged MV leaflets. By using the RFC catheter to resect prolapsing segments in degenerative MR, and by combining one of the several percutaneous annuloplasty approaches in development, a fully percutaneous and efficacious repair for degenerative MR may someday be realized.

APPENDIX

APPENDIX A: RFC CATHETER BUILD INSTRUCTIONS

A. Machine a groove in the catheter cryogen applicator:
The purpose of this part is to remove as much material as possible from the cryo applicator tip underneath where the RF electrode will sit in order to provide insulation between the cryo applicator and RF electrode. With a felt marker, mark the middle portion of the cryogen applicator where the groove will be cut. Place the catheter, wrapped in something to protect it, in a vise. Use a 1/16″ end mill to cut the groove, rotating the tip every so often and moving the catheter tip forward and back as needed to widen the groove. Place a 1/32″ end mill in a Dremel and hand cut the groove deeper, taking care to make the edges as square as possible. Use a small file to cut the edges deeper and smooth inconsistencies. Use the Dremel steel brush tool to remove sharp edges, if necessary.

Approximate groove diameter at smallest point: 1.75 mm
Approximate length of groove: 2.75 mm

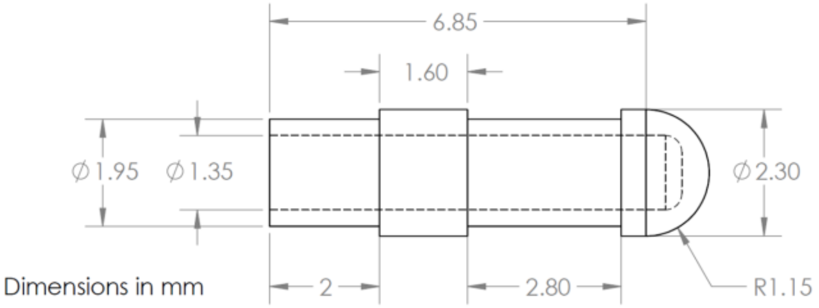

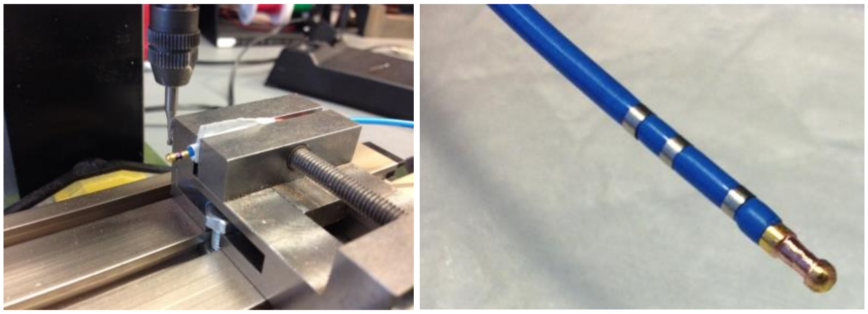

***Fig. A.1** – **Left:** Catheter in vise for machining of cryo tip. **Right:** Finished cryo tip with insulating groove for RF electrode.*

B. Remove the coaxial cryogen/vacuum connector:
Trim the connector where it meets the blue tubing, being careful to preserve as much of the tubing coming out of the catheter handle as possible. Carefully cut away the outer blue tubing lining. Near the location where the coaxial connector meets the clear vacuum tubing, there will be a strong adhesive bond between the flexible clear tubing with the outer blue tube lining.

Fig. A.2 *– Catheter with coaxial connector removed, prior to removal of blue lining.*

C. Extend the cryogen delivery tube:

First, trim some of the clear vacuum line that attaches to the catheter handle in order to expose some of the cryogen delivery tube (this is the orange, polyimide tubing). Slide a slightly larger polyimide tube (0.0159" ID/0.0179" OD) of several inches of length over the cryogen delivery tube and set with epoxy. Care should be taken to ensure there is epoxy within the inner mating surface of the larger and smaller diameter polyimide tubes, as well as a layer encapsulating the junction along the outside. Keep a 0.005" diameter wire inside the cryogen delivery tube to ensure no epoxy blocks the tube. Let this set for at least 4 hours, until it sets and is workable.

Polyimide tube: Amazon, 26 AWG, B00212Q0FY
Nitinol wire: Amazonsupply, 0.005" nitinol, B001385FJE
Epoxy: McMaster, Loctite 1C, 1813A221

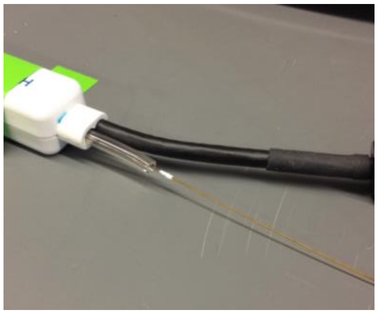

Fig. A.3 *– Large cryogen delivery tube extension epoxied to smaller cryogen delivery tube.*

D. Remove the cryo applicator tip and trim the cryogen delivery tube:

Carefully remove the cryo applicator tip from the catheter tubing by grabbing the tip with pliers and rocking back and forth. Pull the cryo applicator out just enough to expose the polyimide tube for grasping. Pull a length (6-10 cm) of the polyimide tube out of the catheter body. Some force will be needed here, and the polyimide tube may stretch significantly, especially near the distal tip. Thread the 0.005" diameter wire all the way down the cryogen delivery tube to check for any blockages. Trim the cryogen delivery tube to remove any damaged sections and to remove any blockages, leaving approximately 1 cm of tubing hanging outside of the catheter body. Carefully apply cyanoacrylate to the outside of the cryogen delivery tube, just inside of the catheter body, in order to glue it to the translucent plastic linear inside the catheter body. This helps to prevent it sliding away from the distal end of the catheter tip.

Cyanoacrylate adhesive: McMaster, Permabond 910, 7580A52

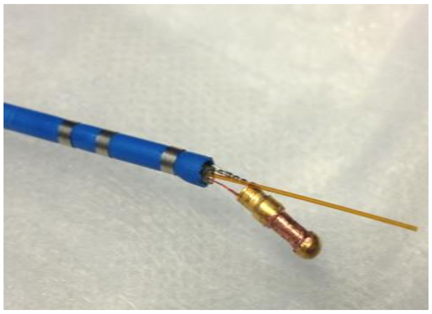

Fig. A.4 *–Cryo tip detached from catheter body with polyimide cryogen delivery tube exposed.*

E. Add a vacuum/cryogen connection to the catheter handle:

A corner barb to quick-disconnect adapter was placed in the flexible vacuum line tubing, with the polyimide tube sticking out of a hole that was 1/16″ hole that was drilled in the connector. A 1/16″ OD stainless steel tube was placed over the polyimide tube and slid into the connector for additional support. The stainless steel tube was glued with epoxy at the location where it entered the connector and where the polyimide lumen leaves the stainless steel tube. After epoxy sets, carefully trim excess polyimide tubing so that the end of the polyimide tube is approximately flush with the stainless steel tube. Add 1/16″ compression fitting components to this stainless steel tube when ready to use catheter.

Epoxy: McMaster, Loctite 1C, 1813A221
Stainless steel tube: McMaster, 0.062″ OD, 0.052″ ID, 8988K36
Quick-disconnect adapter: McMaster, polypropylene, 51545K82
Compression fitting nut: McMaster, stainless steel, 5182K672
Compression fitting front sleeve: McMaster, stainless steel, 5182K65
Compression fitting back sleeve: McMaster, stainless steel, 5182K66

Fig. A.5 *– New cryo delivery tube and vacuum connector completed with compression fitting components.*

F. Return cryo applicator tip to catheter:

Trim polyimide tube at distal end of the catheter such that approximately 4-5 mm of length remains outside of the catheter body. Carefully place polyimide tube into the cryo applicator with tweezers or other tool. Apply cyanoacrylate adhesive to the circumference of the cryo applicator – the portion that will return to the main part of the catheter. Return the cryo applicator tip to the blue catheter body. If necessary, pull back on the deflection mechanism to guide the tip back into the tube. Gently twist back and forth slightly to spread the adhesive. Let tip set overnight.

Cyanoacrylate adhesive: McMaster, Permabond 910, 7580A52

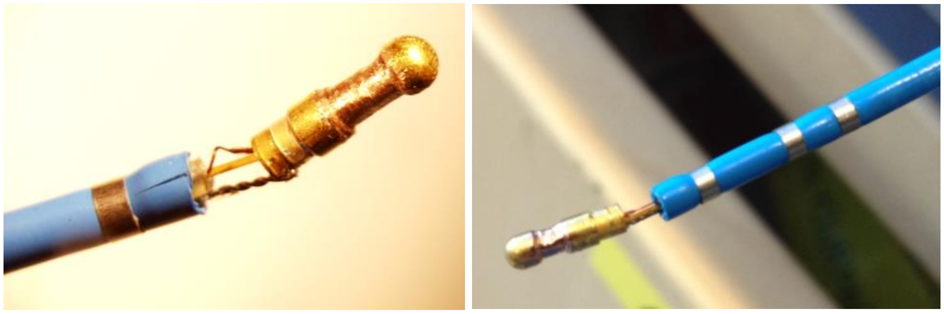

Fig. A.6 *– Catheter tip prior to being glued to the distal catheter body.*

G. Place a layer of epoxy on the cryo applicator were the metal material was machined:

Place epoxy in the space of the cryo applicator to provide additional insulation. Let set for 24 hours, at least, and remove excess with a Dremel brush or fine metal file.

Epoxy: McMaster, Loctite 1C, 1813A221

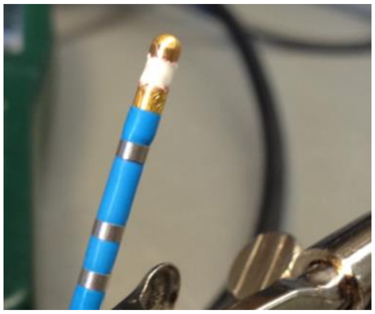

Fig. A.7 *– Thermally and electrically insulating epoxy placed on cryo applicator tip to separate RF electrode and cryo-anchor.*

H. Protect electrodes:

Drip cyanoacrylate adhesive over each of the three ring electrodes found near the distal tip of the catheter. Allow to sit for several seconds, and then remove excess with a brush or similar tool. Repeat 2-3 times. These steps are to plug any small holes which may otherwise allow nitrous oxide gas to escape during catheter operation.

Cyanoacrylate adhesive: McMaster, Permabond 910, 7580A52

Fig. A.8 – Sealing ring electrodes near tip with cyanoacrylate adhesive to prevent nitrous oxide gas leakage.

I. Fabricate the copper RF electrode:

Place a few inch length of 4 mm OD copper tube in the drill (as one would a drill bit), to create a makeshift lathe. Better yet, use a lathe if available. Turn the drill on at a moderate speed, and using a cutting blade on the Dremel, carefully thin the copper tube until the thickness of the tube is small, but great enough so as not to break under light-moderate finger pressure. Cut the copper tube into lengths that roughly match the length of the groove cut on the cryo applicator tip (approximately 2.75 mm). Use a file and/or smooth grinding wheel to remove burrs and smooth and thin the electrode. Cut the copper ring once, lengthwise, so that it can be bent open. Size the open copper ring using the cryo applicator tip. Trim any excess copper ring with wire cutters. Solder a thin enamel-coated wire (approximately two meters long, for trimming later) to the inside of the copper ring. The enamel-coated wire can be stripped by placing in a flame and then by removing the charred enamel with sandpaper.

Copper tubing: McMaster, 5/32" x 0.014,
Cutting blade: McMaster, 15/16" dia, 0.04" thick, 1257A75
Enamel-coated wire: McMaster, 32 gauge, 7588K89

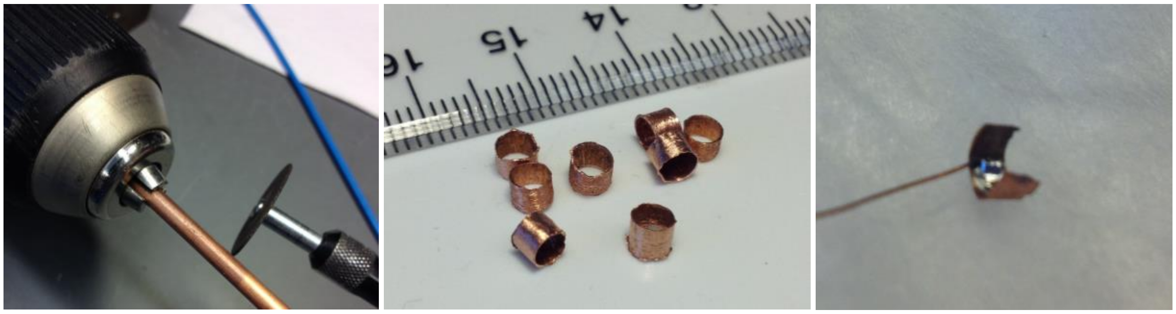

*Fig. A.9 – **Left:** Drill-Dremel lathe setup for reducing the OD of 4mm diameter hollow copper rod. **Center:** Completed RF electrodes. **Right:** RF electrode cut lengthwise with RF wire soldered.*

J. Assemble the RF thermocouple:

Use either (a) a thermocouple wire taken from the inside of another cryo catheter or (b) a small thermocouple (40 gauge wire). Strip the end, wrap wires together and solder, then place thin layer of quickset epoxy over the exposed wire leads. If using a thermocouple wire taken from the inside of a second cryo catheter, it will have to be extended. Strip both wires from the other end of the catheter thermocouple wire, as well as the two wires from the extension wire and solder to extend. Insulate with epoxy (1C). Place a thermocouple connector on the other end of the wire and check for functionality using thermocouple thermometer, Type K. Thermocouple wires taken from another cryo catheter can be stripped using sandpaper. 40 gauge thermocouple wires can be stripped with a razor blade.

+: copper colored wire (if taken from another catheter), yellow insulation (Omega 40 gauge)
-: silver colored wire (if taken from another catheter), red insulation (Omega 40 gauge)

Thermocouple wire: Omega Engineering, Type-K, TT-K-40-SLE
Epoxy: McMaster, general purpose 3-6 min, 7541A76
Epoxy: McMaster, Loctite 1C, 1813A221
Thermocouple connector: McMaster, Type-K flat-pin, 3869K35

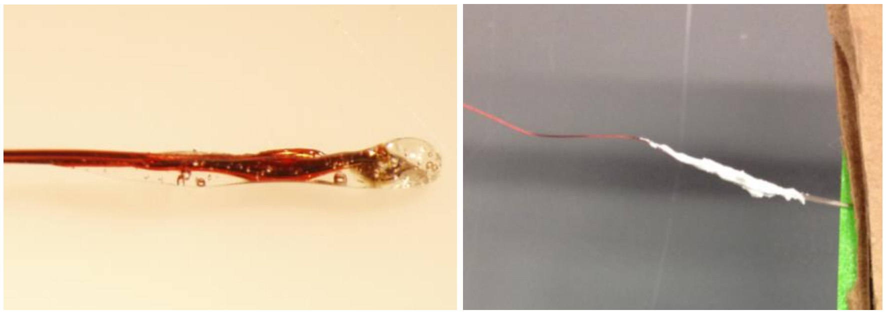

*Fig. A.10 – **Left:** Thermocouple tip with insulating epoxy at the measurement junction. **Right:** Thermocouple wire taken from a CryoCath catheter extended with a 40 gauge thermocouple extension wire.*

K. Assembly of RF components with cryo catheter:

Trim a length of heat shrink tubing that runs from the base of the catheter to just before the deflectable portion of the catheter tip. Heat shrink tubing should not cover the deflectable portion of the catheter body, as it will inhibit motion. Place RF thermocouple wire all the way down the heat shrink tubing, and leave both ends hanging out of the heat shrink tube. Place a several inch length of polyimide tube over the thermocouple wire, on the end with the measurement junction Slide RF electrode wire through the polyimide tube and through the heat shrink tubing towards the base of the catheter handle. Slide catheter down the heat shrink tube. Glue the RF thermocouple wire, with cyanoacrylate adhesive, to the inside of the RF electrode, near the RF wire solder point. Place a layer of epoxy over the dried epoxy layer already on the cryo applicator. Place RF electrode, with superglued-thermocouple wire over the epoxy layer and use pliers to secure tightly around the cryo applicator. Use a multimeter to ensure that current will not flow between the RF eletrode and cryo applicator tip. Remove any excess epoxy from the cryo applicator. Wait overnight to proceed further. Use a lighter to shrink the heat shrink tubing along the length of the catheter shaft. Once heat shrink tubing is set, use high viscosity cyanoacrylate to seal the end of the heat shrink tubing closest to the catheter tip.

Shrink wrap: McMaster, FEP, 8703K117
Polyimide tube: AmazonSupply, 0.0285” ID, B00212GAYU
Cyanoacrylate adhesive: McMaster, Permabond 910, 7580A52
Cyanoacrylate adhesive (high viscosity): McMaster, Permabond 240, 7580A85

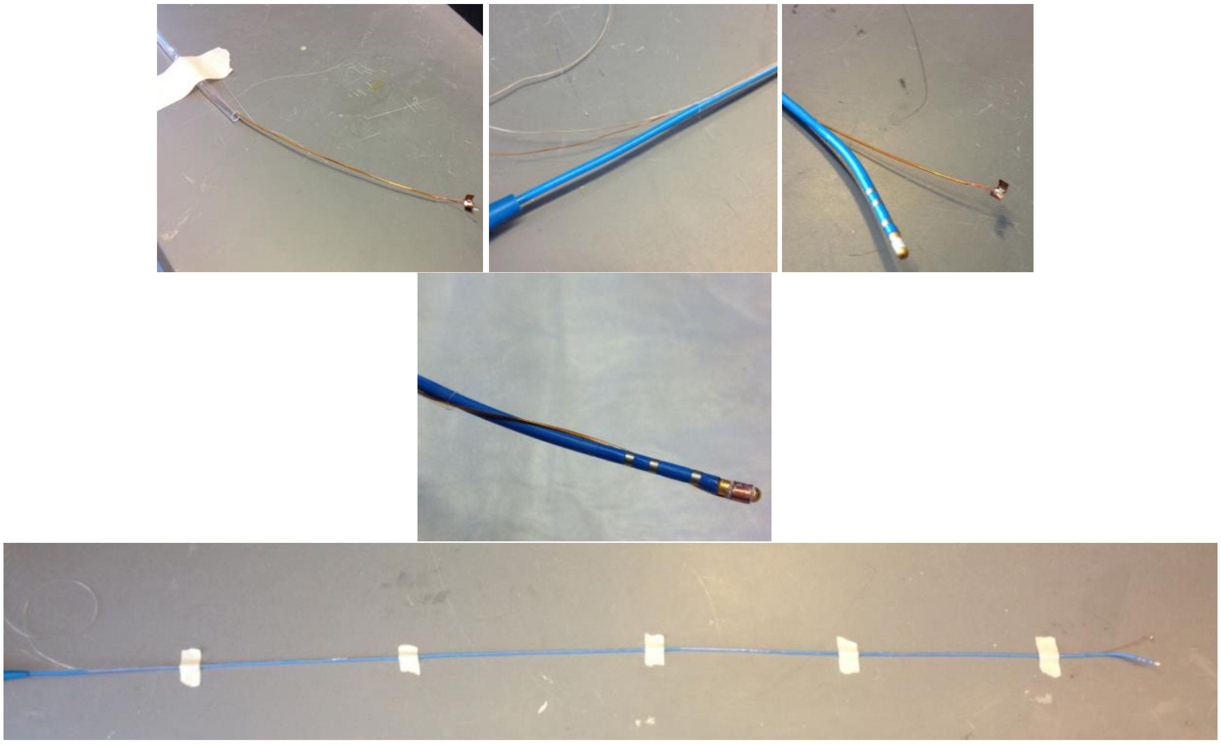

*Fig. A.11– **Top, from left:** **(1)** RF wire and RF thermocouple wire within heat shrink tubing, **(2)** Catheter body with RF electrode wire, RF thermocouple wire, and heat shrink tubing in place, **(3)** RF electrode with RF wire and RF thermocouple wire attached and ready for attachment to cryo applicator, **(4)** Polyimide tubing containing RF electrode and thermocouple wires, along with completed catheter tip. **Bottom:** Catheter with heat shrink tubing ready for RF electrode attachment.*

L. Assembly of Cryo Delivery Tube Umbilical:

Cut two 4 cm lengths of 0.062” OD stainless steel tubing. Trim polyimide tube to desired length. Bond one stainless steel tube to each end of the polyimide tubing with epoxy. Let set over night. Slide polyimide with stainless steel ends through a length of nylon tubing to protect the polyimide from kinks. Epoxy stainless steel sections to nylon tube. Add compression nut and sleeves to each stainless steel tube and a compression coupler to one.

Polyimide tube: AmazonSupply, 0.0285” ID, B00212GAYU
Epoxy: McMaster, Loctite 1C, 1813A221
Stainless steel tube: McMaster, 0.062” OD, 0.052” ID, 8988K36
Compression fitting nut: McMaster, stainless steel, 5182K672
Compression fitting front sleeve: McMaster, stainless steel, 5182K65
Compression fitting back sleeve: McMaster, stainless steel, 5182K66
Compression fitting coupler: McMaster, stainless steel, 5182K716
Tube protector: McMaster, nylon tubing, 5112K42

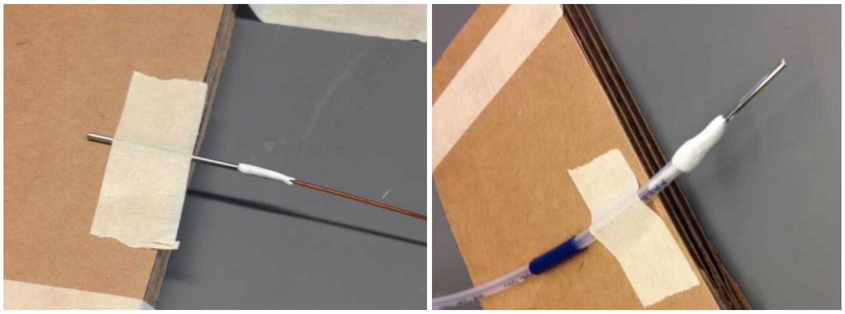

Fig. A.12– Left: *Stainless steel tube bonded to polyimide tube end.* ***Right:*** *Nylon tubing added and bonded to stainless steel tube for protection of polyimide tube.*

APPENDIX B: RF ELECTRODE TEMPERATURE CALIBRATION

RF Ablation Temperature Range

During RF ablation, it is important to maintain ablation power such that tissue temperatures are raised sufficiently to induce shrinkage (>65°C). On the other hand, charring around the RF electrode from very high ablation temperatures (>100°C) leads to a rapid impedance rise and a significant reduction in RF power delivery to the tissue. Thus, RF electrode power output must be throttled to maintain tissue temperatures between 65°C-100°C to generate significant thermal shrinkage.

Rationale for RFC Catheter Temperature Calibration

The RFC catheter contains an RF electrode that sits over cryo-anchors, and the RF electrode is separated from the cryo-anchors by only a thin layer of insulation. A thermocouple measures the RF electrode temperature and sits between the RF electrode and thin insulating layer. Thus, the measured RF electrode temperature is many degrees cooler than the RF electrode-tissue interface temperature and many degrees cooler than the surrounding tissue temperature (assuming RF ablation is currently raising the tissue temperature). This is not a significant problem when using the RFC catheter ex vivo in a flow simulator filled with saline, as there are no proteins in saline to coagulate that will char and raise the impedance (significant char of the tissue itself can occur ex vivo, but given the large heat convection due to fluid flow, the threshold of tissue charring is rarely reached). However, in vivo, blood can coagulate, char, and disrupt RF energy delivery. Therefore, the RFC catheter electrode temperature must be calibrated such that tissue temperatures of between 65°C-100°C can be generated without charring.

RFC Catheter Temperature Calibration Experiment 1: Myocardial Measurements

Calibration of the RF electrode has been performed with two different experiments. In the first experiment, small sections (very roughly: 2 cm x 2cm x 1 cm thick) of myocardium were excised from a heart and sutured to a plastic bracket (metal materials are not used as they will affect current distribution) fixed to the atrial-ventricular wall of the left heart flow simulator. A mechanical valve was placed in the atrial-ventricular wall, and the myocardial tissue was placed directly in the flow path, on the atrial side, to simulate MV flow rates. Myocardial tissue was used as the stationary nature of the tissue permits tissue temperature measurements, which is not easily performed on moving MV leaflets. A thermocouple was carefully placed approximately 1-2 mm below the myocardial surface. The left heart flow simulator was run at 5 L/min and transmitral pressures of 120 mmHg. The RFC catheter was placed on the surface of the myocardium, directly above the myocardial thermocouple placement (Fig. B.1). An indifferent electrode (wire attached to aluminum foil) was placed between the atrium and fluid reservoir of the left heart flow simulator, and its position relative to the catheter was varied to vary impedance. Three different treatments were then performed to hone in on the ideal RF electrode temperature range:

Test 1: Cryo-anchoring on, RF power of 50W, impedance high (250-300Ω)
Test 2: Cryo-anchoring on, RF power of 50W, impedance low (50-75Ω)
Test 3: Cryo-anchoring on, RF power of 80W, impedance low (50-75Ω)

Test 1 was used to demonstrate that no or minimal temperature increases may occur at high ablation powers. Test 2 and Test 3 were used to generate significant tissue temperature rises to determine the matching RF electrode temperature. Results from testing Catheter Prototype #07 on 2015-02-10 are shown below (Fig. B2).

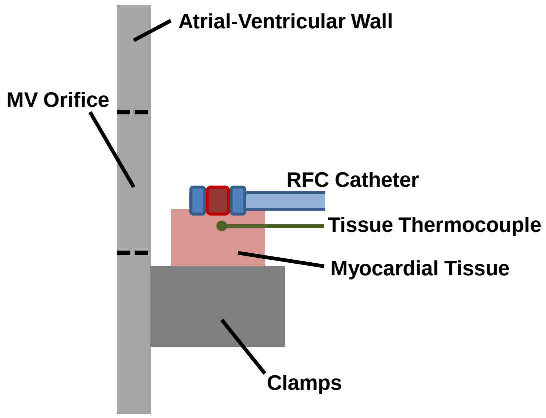

Fig. B.1. Myocardial RF Electrode Temperature Calibration Test – Experimental Set-Up

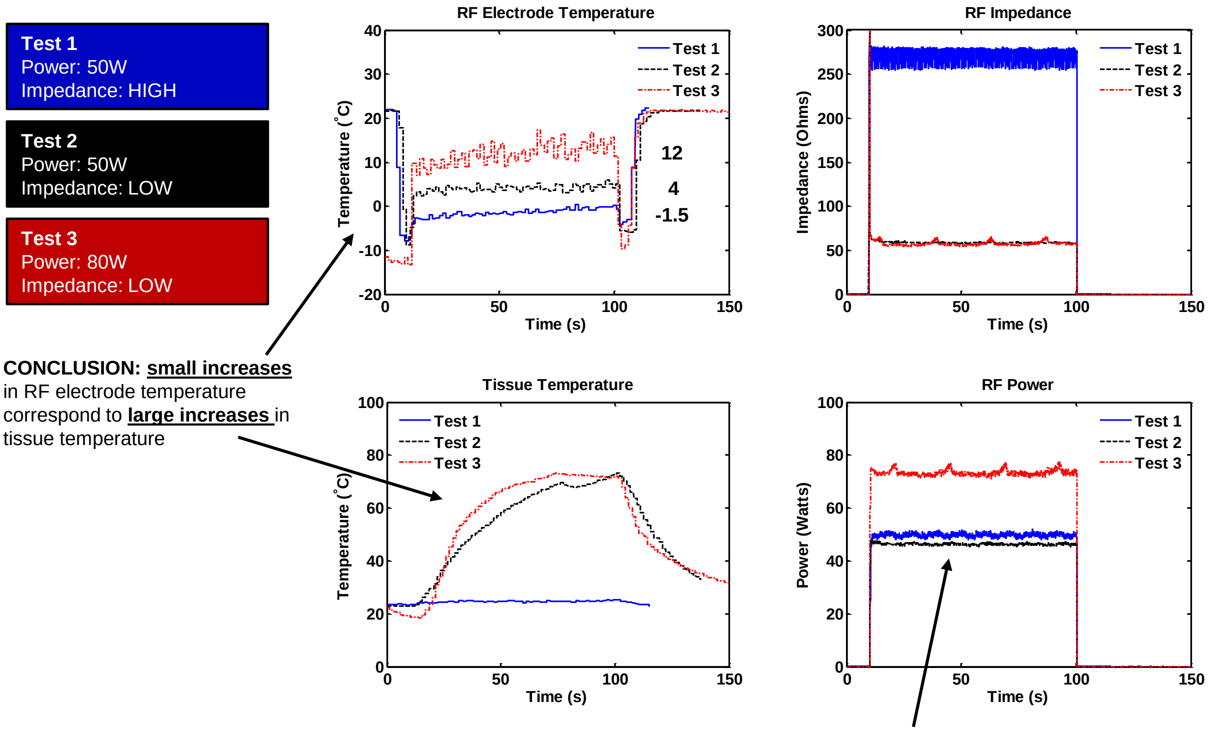

CONCLUSION: <u>**small increases**</u> in RF electrode temperature correspond to <u>**large increases**</u> in tissue temperature

Small differences in RF power output may also indicate whether ablation is occurring

Fig. B.2: Results from Myocardial Temperature Calibration Test

RF electrode calibration on Catheter Prototype #07. Recorded on 2015-02-10. During Test 3, popping of the tissue occurred, which indicated rapid boiling/expansion of the fluid contained within the myocardium.

Myocardial Temperature Calibration Test Conclusions

We conclude from the above results that RF electrode temperatures, on Catheter Prototype #07 specifically, of between 5-10°C are sufficient to generate tissue temperatures that will create tissue shrinkage. However, we can also conclude that there is a fine line between significant (tissue shrinkage causing) and insignificant (no tissue shrinkage causing) temperatures measured on the RF electrode, as temperatures below 0°C do not cause thermal shrinkage lesions. Further, RF electrode temperature must be carefully throttled to avoid excessive (>10°C) tissue temperature in this catheter prototype, as conditions were favorable for char to occur past this point.

RFC Catheter Temperature Calibration Experiment 2: Excised MV Test

The myocardial temperature calibration test above confirmed that low measured RF electrode temperatures do not necessary imply low tissue temperatures, and the test above can be used to calibrate the desired RF electrode temperature range. However, the test above takes significant time to execute. A simpler test can be performed that takes much less time, if a sewn excised MV is already available. An excised porcine MV can be placed in the left heart flow simulator with flow and pressure conditions as described above. An indifferent electrode (wire attached to aluminum foil) can be placed in the left heart flow simulator on the atrial chamber floor, which results in impedances of around 60Ω during ablation of the MV leaflets. RF electrode temperature is then measured in two different testing conditions:

Test A: Cryo-anchoring on, RF ablation at 50W, catheter positioned just in front of MV leaflets (in atrium) with no leaflet attachment

Test B: Cryo-anchoring on, RF ablation at 50W, catheter attached to MV leaflets

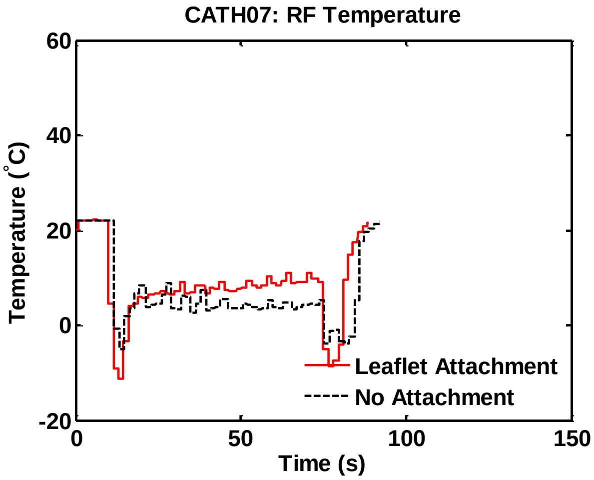

Fig. B.3. RF Electrode Calibration Test Using an Excised Porcine MV

RF electrode temperatures measured during cryo-anchoring and ablation with no leaflet attachment (black, dotted) and with direct leaflet attachment of cryo-anchor and RF electrode (red, solid). Catheter Prototype #07. Recorded on 2015-02-03.

Excised MV Calibration Test Conclusions

Assuming that MV tissue temperatures that correspond with thermal leaflet shrinkage are being generated in Test B, this test can be used to determine the RF electrode temperature target for in vivo ablations. Test A is a control test, demonstrating temperature that can be expected when RF ablation is on, but no thermal shrinkage is being produced. The difference in measured RF electrode temperature between these two tests is small (Fig. B.3): with no leaflet attachment, the averaged measured RF electrode temperature was 4.5°C and with leaflet attachment, the averaged measured RF electrode temperature was 8°C. The 8°C measured RF electrode temperature corresponds with the calibrated range in the myocardial temperature calibration test. The excised MV calibration test provides the target RF electrode temperature during RF ablation in vivo – in this case the target RF electrode temperature is 8°C – however, the excised MV calibration test will likely not provide the upper limit of RF electrode temperatures that produce charring in vivo.

Additional Conclusion

The above calibration test(s) should be performed frequently. It was found after several months during an in vivo procedure that the calibrated range for the Catheter Prototype #07 RF electrode had shifted upwards by about 10°C, to 10°C-20°C from 0°C-10°C.

RF Electrode Temperature Calibrations as of 2015-05-22

Catheter Prototype #06: -5°C to 5°C
Catheter Prototype #07: 10° C to 20°C

APPENDIX C: RFC CATHETER SYSTEM – NITROUS OXIDE DELIVERY HARDWARE

The nitrous oxide delivery system (Fig. C.1) provides the cooling power for the RFC catheter. Liquid nitrous oxide is pulled out of a nitrous oxide tank with dip tube. A pressure regulator is available to regulate the nitrous oxide pressure, if necessary, but full tank pressure (750-800psi, depending on room temperature) is used with the current iteration of the RFC catheter prototype. A solenoid valve compatible with cryogenic liquids is used to turn cryogen flow on and off. The solenoid valve is switched on when supplied with 120VAC and switched off when current is removed.

The combined weight of the nitrous oxide tank and nitrous oxide is 47lbs when full. After the tank plus nitrous oxide weight measures 35lbs or below, cryo-anchor cooling power is inconsistent and a new tank is needed.

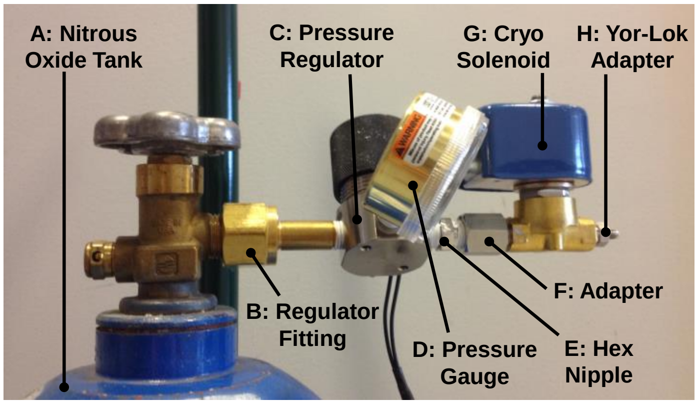

Fig. C.1: Nitrous Oxide Delivery System Hardware
Nitrous oxide delivery system hardware. Letters correspond to parts list below.

Table C.1. Nitrous Oxide Delivery System Parts List

ITEM	ITEM DESCRIPTION	SUPPLIER	PART NUMBER
A	Nitrous Oxide, 20 lbs., with Dip Tube	A-L Compressed	
B	Regulator Fitting Inlet Nipple, 1/4" NPT Male, CGA #326, 2.5" Length	McMaster	79215A673
B	Regulator Fitting Female Thread Inlet Nut, CGA #326, 0.952" Length	McMaster	79215A672
C	Pressure Regulator, Tescom BB-1 Series	Tescom	BB-13AH2KVA4
D	Pressure Gauge, 0-1200 psi	Tescom	62500-2000N
E	Hex Nipple,Precision Extreme-Pressure 316 Stainless Steel Pipe Fitting, 1/4 x 1/4 Pipe Size, 1-7/16" Length	McMaster	48805K81
F	Adapter, Precision Extreme-Pressure 316 Stainless Steel Pipe Fitting, 1/4 x 1/8 Pipe Size, Female x Male	McMaster	48805K252
G	Cryo Solenoid, Clean & Bagged Cryogenic Brass Solenoid Valve 1/8 NPT Female, 120 VAC	McMaster	50585K21
H	Yor-Lok Adapter, Type 316 Stainless Steel, Straight Adapter for 1/16" Tube OD x 1/8 NPT Male	McMaster	5182K435
	Precision Extreme-Pressure 316 Stainless Steel Pipe Fitting, 1/4 Pipe Size, Hex Head Solid Plug	McMaster	48805K28

APPENDIX D: RFC CATHETER SYSTEM – CONTROL SYSTEM CODE

The following code was developed to control the RFC catheter system using an Arduino Uno. This code reads in the temperatures of the catheter cryo-anchor and RF electrode from a serial connection to a commericially available thermocouple measurement device (EA15, Extech Instruments, Nashua, NH), and then the code throttles a cryo solenoid based upon the measured cryo-anchor temperature. If the cryo-anchor temperature is above -20°C, the cryo solenoid is set to full on. If the cryo-anchor temperature is below -20°C, the cryo-anchor is switched on/off with a duty cycle controlled by the user (default is 0.2) and a cycle period of 2 seconds. The cryo-anchor temperature, RF electrode temperature, cryo solenoid duty cycle, and cryo solenoid on/off state are then passed to LabView for data acquisition.

```
// Steve Boronyak
// July 02, 2014

/* This program also the user to manually control the duty cycle of the cryo
solenoid for
controlling the cryo cath temperature */

// DOES NOT measure RESISTANCE or RF POWER OUTPUT
// DOES NOT include temperature compensation for filter induced offsets (this is
done in LabView)

/* USB Host to PL2303-based USB Thermocouple Thermometer */
/* Extech EasyView 15 */


/* USB Host Libraries and associated code from Oleg */
/* http://www.circuitsathome.com/arduino_usb_host_shield_projects */


// DEFINE PINS /////////////////////////////////////////////////////////////////
#define cryoINPUT 2             // Cryo input switch
#define cryoIND 3               // Cryo indicator LED line
#define RFinput 4               // RF input switch
#define cryoOUTPUT 5            // Cryo output line, to 5V SSR
#define RFoutput 6              // RF output line, to TIP120 and solenoid valve
#define RFind  A0               // RF indicator LED line
#define buttUP  A1
#define buttDOWN  A2


// ADD LIBRARIES ///////////////////////////////////////////////////////////////

/* USB support */
#include <avrpins.h>
#include <max3421e.h>
#include <usbhost.h>
#include <usb_ch9.h>
#include <Usb.h>
#include <usbhub.h>
#include <avr/pgmspace.h>
#include <address.h>
```

```
/* CDC support */
#include <cdcacm.h>
#include <cdcprolific.h>

/* Debug support */
#include <printhex.h>
#include <message.h>
#include <hexdump.h>
#include <parsetools.h>


// INITILIZE VARIABLES
/////////////////////////////////////////////////////////////////////////
int count = 0;              // Count of total bytes received to the buffer
int buffer[9];              // Storage buffer for thermocouple data
int tempbuffer[9];
int sign = LOW;             // LOW means + sign, HIGH means - sign
int connection = LOW;       // HIGH means open line;
int value_CRYO = 0;         // Digital input from cryoINPUT
int PWMod = 0;              // Indicator variable: 1 if PWM pedal is active
int CRYOout = 0;            // Indicator variable: 1 if cryo solenoid out is on
int RFstate = LOW;          // Current state of the RF input switch
float cycleDELAY = 400;     // Used for switching between on and off timing
float cyclePERIOD = 2000;   // Cycle period
float DUTY = 0.2;           // Duty cycle of PWM signal to cryo solenoid
float deltaDUTY = 0;        // Duty cycle of PWM signal to cryo solenoid
float Tcryo = 25;           // Cryo temperature
float TcryoLAST = 25;       // Previously measured cryo temperature
float timeSTAMP;            // Time of temperature measurement
float deltaT = 0;           // Absolute value of change in temperature between
measurements
byte STATE = B00000000;     // Indicates the state of the cryo solenoid/RF output
boolean REC = false;        // When TRUE, thermocouple data ready to analyze
unsigned long timeZERO;     // Time of first received byte of thermocouple data
unsigned long timeF;        // Time of last received byte of thermocouple data
unsigned long OFFtime;      // Millisecond time, last time switch was off
unsigned long readTIME = 0;
unsigned long PWtimer = 0;  // Timer value: the last time the cryo solenoid was
switched on or off
unsigned long RFoff = 0;    // millisecond timer, last time RF switch was off

int valueUP = LOW;
int valueDOWN = LOW;
unsigned long buttLAST;
int duty1 = 4;



// INITLIZE USB HOST DEVICE //////////////////////////////////////////////////
class PLAsyncOper : public CDCAsyncOper
{
public:
    virtual uint8_t OnInit(ACM *pacm);
};

// Continue to initilize USB Host device, I guess
uint8_t PLAsyncOper::OnInit(ACM *pacm)
{
    uint8_t rcode;

    // Set DTR = 1 - I don't know what this means
    rcode = pacm->SetControlLineState(1);
```

```
    if (rcode) // Still don't know
    {
        ErrorMessage<uint8_t>(PSTR("SetControlLineState"), rcode);
        return rcode;
    }

    LINE_CODING lc;
    lc.dwDTERate  = 9600;   // default serial speed of unit
    lc.bCharFormat  = 0;    // i have no idea what this means
    lc.bParityType  = 0;    // default parity of the unit
    lc.bDataBits  = 8;      // number of data bits

    rcode = pacm->SetLineCoding(&lc); // Don't know

    if (rcode)      // Still don't know
        ErrorMessage<uint8_t>(PSTR("SetLineCoding"), rcode);

    return rcode;
}


// I have no idea what this does, I guess start communicating???
USB     Usb;
PLAsyncOper  AsyncOper;
PL2303       Pl(&Usb, &AsyncOper);


// SET UP CODE ////////////////////////////////////////////////////////////
void setup()
{
  // Set pin 7 HIGH for serial communication to work:
  pinMode(7, OUTPUT);              // Pin 7 must be set HIGH, active low reset
  digitalWrite(7, HIGH);           // So set Pin 7 dammit

  // Cryo and RF I/O:
  pinMode(cryoINPUT, INPUT);       // Set pin 2, as cryo input
  pinMode(cryoIND, OUTPUT);        // Cryo LED output indicator
  pinMode(cryoOUTPUT, OUTPUT);     // Cryo output line to SSR
  pinMode(RFinput, INPUT);         // RF input switch
  pinMode(RFind, OUTPUT);          // RF LED output indicator
  pinMode(RFoutput, OUTPUT);       // RF output line to TIP120 and solenoid
  pinMode(buttUP, INPUT);          // Button high increases duty cycle
  pinMode(buttDOWN, INPUT);        // Button high decreases duty cycle

  digitalWrite(cryoIND, LOW);
  digitalWrite(cryoOUTPUT, LOW);
  digitalWrite(RFind, LOW);
  digitalWrite(RFoutput, LOW);

  tempbuffer[0] = 0;
  tempbuffer[1] = 0;
  tempbuffer[2] = 0;
  tempbuffer[3] = 0;
  tempbuffer[4] = 0;
  tempbuffer[5] = 0;
  tempbuffer[6] = 0;
  tempbuffer[7] = 0;
  tempbuffer[8] = 0;


  Serial.begin(9600);              // Set baud rate of Arduino serial monitor,
must match LabView program
```

```
  if (Usb.Init() == -1)            // Error message, if USB Host fails to
initilize
      Serial.println("OSCOKIRQ failed to assert");

  delay(200);

}


void loop()
{

//////////////////////////////////////////////////////////////////////////////////
/////////
  // READ THERMOCOUPLE TEMPERATURE
//////////////////////////////////////////////////////////

//////////////////////////////////////////////////////////////////////////////////
/////////

  // INITLIZE SOME MORE VARIABLES ////////////////////////////
  REC = false;
  uint8_t rcode;      // what does the rcode do???
  uint8_t  buf[9];    // serial buffer equals Max.packet size of thermocouple
output
  uint16_t rcvd = 9;  // same as line above

  Usb.Task();

    if( Pl.isReady()) {
       /* reading the thermometer */
       rcode = Pl.RcvData(&rcvd, buf);
        if (rcode && rcode != hrNAK)
           ErrorMessage<uint8_t>(PSTR("Ret"), rcode);
            if( rcvd ) { //more than zero bytes received

              // Time stamps to check if it takes an unexpected amount of time to
get all 9 bytes
              if (count == 0){
                timeZERO = millis();
              }
              if (count == 8){
                timeF = millis();
              }

              for (uint16_t i=0; i < rcvd; i++) {

                  buffer[count] = buf[i];  // For every byte received, write to
the buffer
                  count++;                 // Increment byte count

                  if (count >= 9){         // Return byte count to zero;
                    count = 0;

                    if (timeF - timeZERO > 100){    // Check for timeout error
                      Serial.println("Timeout ERROR");
                    }

                    if (timeF - timeZERO <= 100){  // If no timeout error,
everything is good
                      REC = true;
                    }//if (timeF - timeZERO <= 100
                  }//if (count >= 9...
```

```
              }//for( uint16_t i=0; i < rcvd; i++...
            }//if( rcvd..
      tempbuffer[1] = buffer[1];
      tempbuffer[2] = buffer[2];
      tempbuffer[3] = buffer[3];
      tempbuffer[4] = buffer[4];
      tempbuffer[5] = buffer[5];
      tempbuffer[6] = buffer[6];
    }//if( Pl.isReady())..

/////////////////////////////////////////////////////////////////////////////////



/////////////////////////////////////////////////////////////////////////////////
    // DETERMINE/THROTTLE CRYO SOLENOID OUTPUT
//////////////////////////////////////

/////////////////////////////////////////////////////////////////////////////////

    value_CRYO = digitalRead(cryoINPUT);
    valueUP = digitalRead(buttUP);
    valueDOWN = digitalRead(buttDOWN);

    if (valueUP == HIGH && millis() - buttLAST > 200){
      DUTY = DUTY + 0.05;
      buttLAST = millis();
    }
    if (valueDOWN == HIGH && millis() - buttLAST > 200){
      DUTY = DUTY - 0.05;
      buttLAST = millis();
    }

    if (DUTY > 0.9){
      DUTY = 1;
    }
    if (DUTY < 0.1){
      DUTY = 0;
    }

    if (value_CRYO == HIGH && Tcryo < -15){

      if (DUTY == 1){
        if (millis() - OFFtime > 200){
          CRYOout = HIGH;
          digitalWrite(cryoIND, HIGH);
          digitalWrite(cryoOUTPUT, HIGH);
        }
      }
      if (DUTY == 0){
        CRYOout = LOW;
        digitalWrite(cryoIND, LOW);
        digitalWrite(cryoOUTPUT, LOW);
        }
      if (DUTY < 1 && DUTY > 0){
        if (CRYOout == LOW){
          cycleDELAY = (1 - DUTY)*cyclePERIOD;
        }//if (CRYOout == LOW...
        if (CRYOout == HIGH){
          cycleDELAY = DUTY*cyclePERIOD;
        }//if (CR
        if (millis() - PWtimer > cycleDELAY){
          CRYOout = !CRYOout;
```

```
          digitalWrite(cryoIND, CRYOout);
          digitalWrite(cryoOUTPUT, CRYOout);
          PWtimer = millis();
        }//if (millis() - PWtimer...
      }
    }
    else if (value_CRYO == HIGH && Tcryo >= -15){
      CRYOout = HIGH;
      digitalWrite(cryoIND, CRYOout);
      digitalWrite(cryoOUTPUT, CRYOout);
    } else {
      OFFtime = millis();
      digitalWrite(cryoIND, LOW);
      digitalWrite(cryoOUTPUT, LOW);
      CRYOout = LOW;
    }

    if (DUTY == 1){
      DUTY = 0.9;
    }
    if (DUTY == 0){
      DUTY = 0.1;
    }

    ///////////////////////////////////////////////////////////////////////////


    ///////////////////////////////////////////////////////////////////////////
    // RECORD DATA: TEMPERATURE & SOLENOID OUTPUT STATE //////////////////////
    ///////////////////////////////////////////////////////////////////////////
    if (REC == true){

      TcryoLAST = Tcryo;

      // Thermocouple CH1 - CRYO //
      // Byte 2: CH1 Status Byte
      // Bytes 3 and 4: CH1 Temperature Bytes
      connection = bitRead(buffer[1],6); // Byte 2, bit 6: OL determination
      if (connection == HIGH){
        Serial.write(255);

      }//if (connection == HIGH...

      if (connection == LOW){
        sign = bitRead(buffer[1],7);    // Byte 2, bit 7: negative sign
determination
        if (sign == LOW){               // If byte 2, bit 7 LOW: + sign
          Tcryo = (((float)buffer[2]*256) + (float)buffer[3])/10;
        }//if (sign == LOW...
        if (sign == HIGH){              // If byte 2, bit 7 HIGH: - sign
          Tcryo = -(((float)buffer[2]*256) + (float)buffer[3])/10;
        }//if (sign == HIGH...

        deltaT = Tcryo - TcryoLAST;
        timeSTAMP = (float)timeF/1000;


        bitWrite(STATE,0,value_CRYO);
        bitWrite(STATE,1,RFstate);

        duty1 = int(DUTY*100);
```

```
        //This order must stay the same for the LabView program to process
correctly
        Serial.write(128);
        Serial.write(buffer[1]);
        Serial.write(buffer[2]);
        Serial.write(buffer[3]);
        Serial.write(buffer[4]);
        Serial.write(buffer[5]);
        Serial.write(buffer[6]);
        Serial.write(STATE);
        Serial.write(duty1);
        Serial.write(255);
      }//if (connection == LOW...
      // END CH1 - Cryo //

    }//if (REC == true...

    if (REC == false){
      if (millis() - readTIME > 200){
        Serial.write(128);
        Serial.write(tempbuffer[1]);
        Serial.write(tempbuffer[2]);
        Serial.write(tempbuffer[3]);
        Serial.write(tempbuffer[4]);
        Serial.write(tempbuffer[5]);
        Serial.write(tempbuffer[6]);
        Serial.write(STATE);
        Serial.write(duty1);
        Serial.write(255);

        readTIME = millis();
      }
    }

////////////////////////////////////////////////////////////////////////////////

}
```

APPENDIX E: RFC CATHETER SYSTEM – DATA ACQUISITION CODE

All data acquisition from the RFC catheter system is done in LabView. Data is read in from the RF generator directly to a National Instruments DAQ and the catheter control system via the Arduino program in Appendix D. The front panel shown below is used to display catheter temperature, impedance, and power information during the procedure. The corresponding wire diagram is shown on the next page.

Save Waveforms 2015_05_22_Animal1

16 ID

CRYO -48.2

Cryo Duty 0.2

RF 28.3

Impedance 116

Power 28

Catheter #06
0 C
-10 C

Catheter #07
10 C
0 C

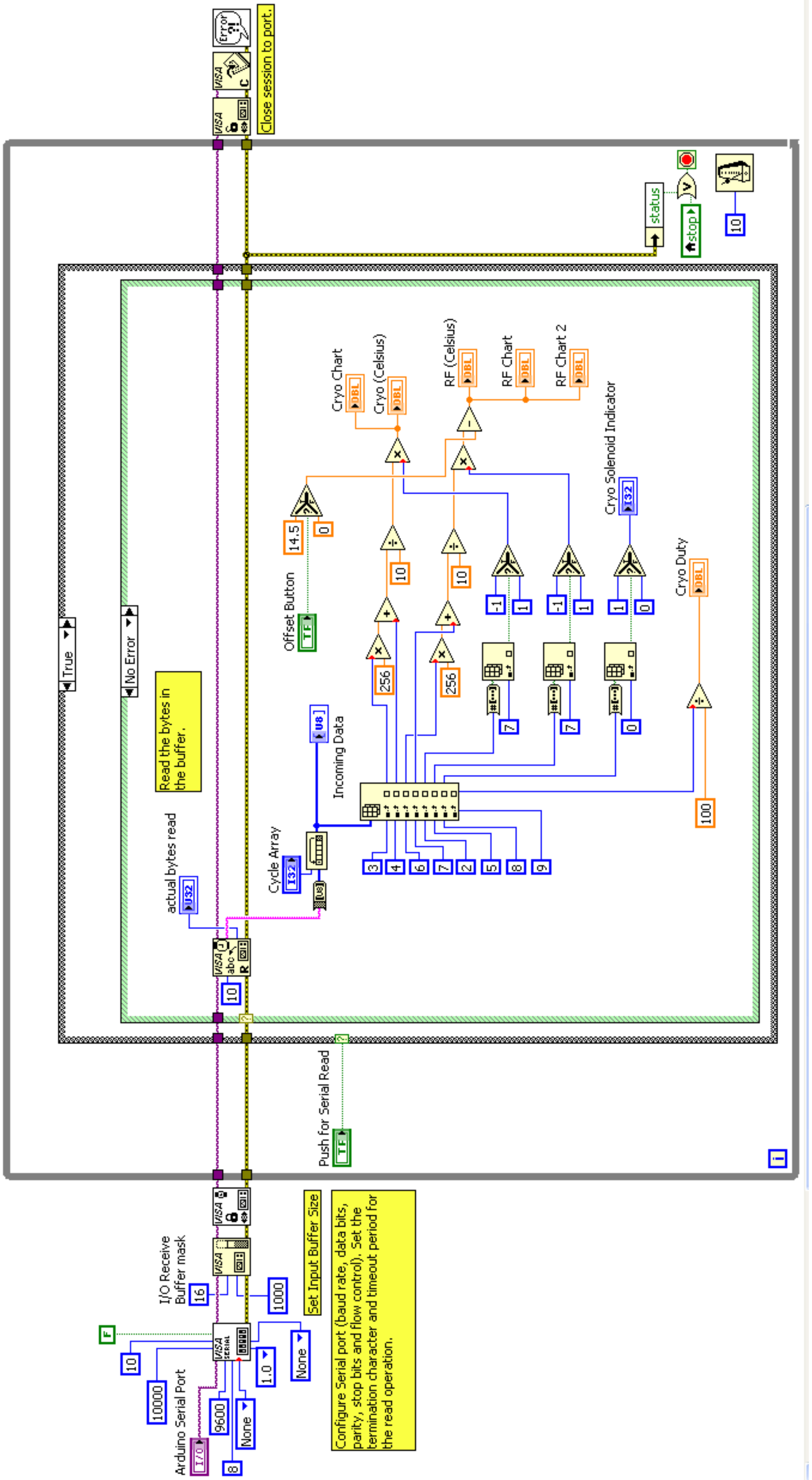

Configure Serial port (baud rate, data bits, parity, stop bits and flow control). Set the termination character and timeout period for the read operation.

Set Input Buffer Size

Read the bytes in the buffer.

Close session to port.

APPENDIX F: RFC CATHETER SYSTEM – CONTROL SYSTEM ELECTRICAL SCHEMATIC

The essential components for constructing the RFC catheter electrical control system are shown on the next page. Also of note, not indicated on the drawings, are the USB connections: 1) from the USB host shield to the EA15 thermocouple measurement device, and 2) from the Arduino Uno to the computer running the LabView data acquisition software. Non-trivial components are listed in the table below.

Table F.1. Non-Trivial Components of the RFC Catheter Control System

Description	Supplier	Cat No
USB Host Shield	Sparkfun	DEV-09947
Foot Switch with Front Pivot Steel, Maintained, SPST-NO, 6' Cord	McMaster	7717K22
Long-Life Relay 5 DC Control Voltage, 5 Amps @ 100-240V AC, G3NE-205T-US	McMaster	8192K211
ProtoBoard - Wombat (PTH)	Sparkfun	PRT-08619
Arduino Uno	Sparkfun	DEV-1102
IC REG LDO 9V 2A TO-220	DigiKey	497-6038-5-ND
BOX ABS 9.84X7.09X1.97" GREY	DigiKey	HM1099-ND

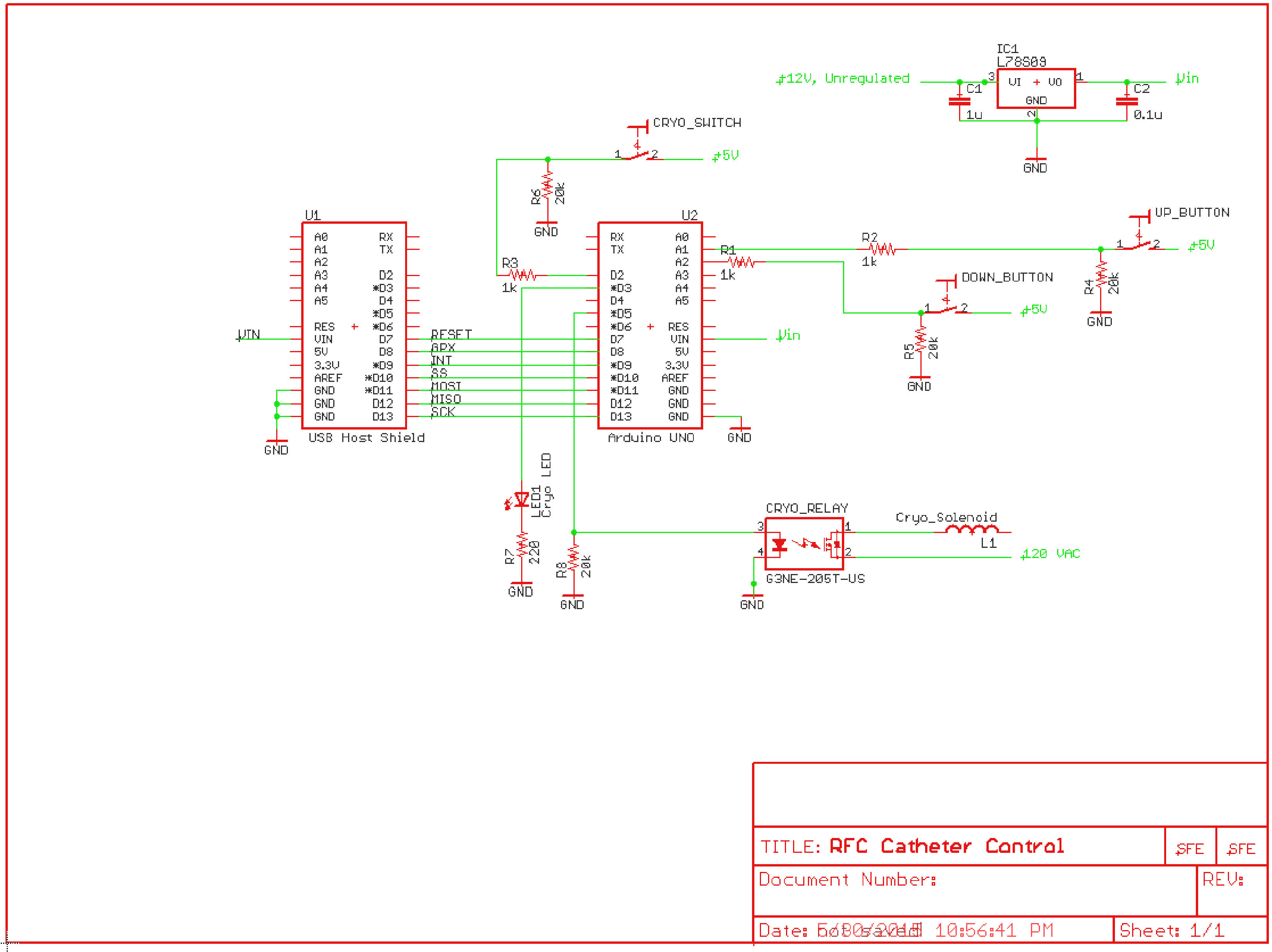
IC1
L78S09
VI + VO
GND
+12V, Unregulated
C1
1u
C2
0.1u
Vin
GND
CRYO_SWITCH
+5V
R6
20k
GND
U1
A0
A1
A2
A3
A4
A5
RES
VIN
5V
3.3V
AREF
GND
GND
GND
RX
TX
D2
*D3
D4
*D5
*D6
D7
D8
*D9
*D10
*D11
D12
D13
USB Host Shield
VIN
GND
RESET
GPX
INT
SS
MOSI
MISO
SCK
R3
1k
U2
RX
TX
D2
*D3
D4
*D5
*D6
D7
D8
*D9
*D10
*D11
D12
D13
A0
A1
A2
A3
A4
A5
RES
VIN
5V
3.3V
AREF
GND
GND
GND
Arduino UNO
GND
Vin
R1
1k
R2
1k
UP_BUTTON
+5V
R4
20k
GND
DOWN_BUTTON
+5V
R5
20k
GND
LED1
Cryo LED
R7
220
GND
R8
20k
GND
CRYO_RELAY
G3NE-205T-US
GND
Cryo_Solenoid
L1
120 VAC
TITLE: RFC Catheter Control
SFE
SFE
Document Number:
REV:
Date: 6/30/2015 10:56:41 PM
not saved!
Sheet: 1/1

APPENDIX G: RFC CATHETER SYSTEM ELECTRICAL SCHEMATIC

The RF generator (EPT-1000, Boston Scientific) measurement lines were connected to a LabView DAQ to record RF power and RF impedance during the procedure. A ground line must also be connected from the rear of the RF generator to the LabView DAQ.

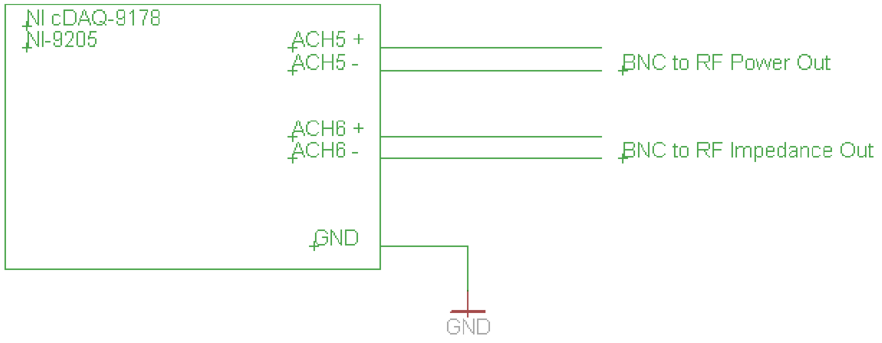

APPENDIX H: RFC CATHETER SYSTEM – THERMOCOUPLE FILTERS

Significant noise is present on the RFC catheter thermocouple measurements when RF power is actively being delivered. In order to reduce noise and obtain accurate temperature measurements, a passive low-pass filter was employed on each thermocouple (Fig. H.1 and Fig. H.2). The low-pass filters were placed just prior to the thermocouple measurement device. Ground, indicated below, is the thermocouple measurement device ground accessed in the battery compartment.

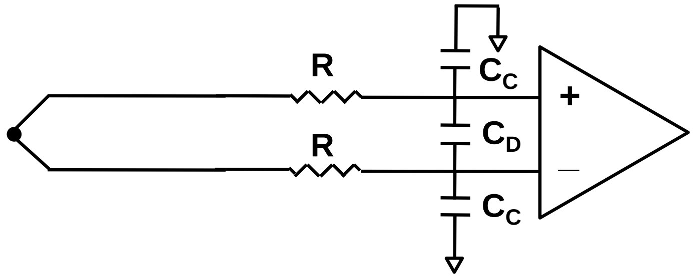

R	4.7 kΩ
C_D	1 µF
C_C	0.1 µF
f_{DIFF}	16.1 Hz
f_{CD}	339 Hz

Fig. H.1. RFC Catheter Thermocouple Filter Design
Circuit shown is adapted from the datasheet for the AD8494 instrumentation amplifier. Values selected for R, C_C, and C_D, along with the cut-off frequencies, are shown to the right.

Values for R, C_C, and C_D were selected to obtain a low cut-off frequency for differential voltage, f_{diff} , and a relatively high cut-off frequency for common mode voltage, f_{CM}:

$$f_{diff} = \frac{1}{2\pi R(2C_D + C_C)}$$

$$f_{CM} = \frac{1}{2\pi R C_C}$$

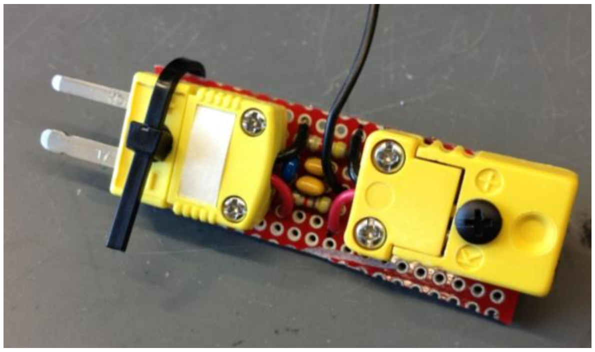

Fig. H.2. RFC Catheter Thermocouple Filter

APPENDIX I: BIAXIAL MECHANICAL TESTING ANALYSIS CODE

Basic Biaxial Mechanical Testing (2x2 Marker Grid) Analysis

The following MATLAB code was used to perform all mechanical and geometrical data analysis in Aim 1 and in the durability study in Aim 2. The program reads in data files output from the biaxial mechanical tester, which includes marker position data used to determine the deformation gradient tensor with a bilinear interpolation.

The input data files for this program must be formatted as follows, where X1q and X2q refer to marker positions in the axis 1 and axis 2 directions and q refers to the marker number:

Column #	Value
1	Time (s)
2	Load 1
3	Load 2
4	F11
5	F12
6	F21
7	F22
8	E11
9	E12
10	E22
11	X11
12	X12
13	X13
14	X14
15	X21
16	X22
17	X23
18	X24

```
% Biax Data Processing

% Steve Boronyak
% 08-16-2011

clear
clc


%% User Input %%%%%%%%%%%%%%%%%%%%%%%%%%%%%%%%%%%%%%%%%%%%%%%%%%%%%%%%%%%%%

% Sample Number
sample = 'Sample 149';

% Sample Test Date: 10-10-2012

% Sample dimensions
radial = 11.1;   % mm
circ = 11.3;     % mm

% Reference Marker Files
untreated_ref = load('Treated-4wk_ref.txt');
```

```
cryo_ref = load('Treated-4wk_ref.txt');
treated_ref = load('Treated-4wk_ref.txt');

% Load Test Data
untreated = importdata('Treated-4wk(10).txt','\t',1);
cryo = importdata('Treated-4wk(10).txt','\t',1);
treated = importdata('Treated-4wk(10).txt','\t',1);

%%%%%%%%%%%%%%%%%%%%%%%%%%%%%%%%%%%%%%%%%%%%%%%%%%%%%%%%%%%%%%%%%%%%%%%%%%%


%% Extract Data %%%%%%%%%%%%%%%%%%%%%%%%%%%%%%%%%%%%%%%%%%%%%%%%%%%%%%%%%%%

% Convert to membrane tension - units of N/m:
C_load_untreated = untreated.data(:,2).*(9.81/radial);
R_load_untreated = untreated.data(:,3).*(9.81/circ);

C_load_cryo = cryo.data(:,2).*(9.81/radial);
R_load_cryo = cryo.data(:,3).*(9.81/circ);

C_load_treated = treated.data(:,2).*(9.81/radial);
R_load_treated = treated.data(:,3).*(9.81/circ);


% Shift first data point to equal 1:
C_stretch_untreated = untreated.data(:,4) - (untreated.data(1,4)-1);
R_stretch_untreated = untreated.data(:,7) - (untreated.data(1,7)-1);

C_stretch_cryo = cryo.data(:,4) - (cryo.data(1,4)-1);
R_stretch_cryo = cryo.data(:,7) - (cryo.data(1,7)-1);

C_stretch_treated = treated.data(:,4) - (treated.data(1,4)-1);
R_stretch_treated = treated.data(:,7) - (treated.data(1,7)-1);


% Find the max load:
[n1,m1] = max(C_load_untreated);
[n2,m2] = max(R_load_untreated);

[n3,m3] = max(C_load_cryo);
[n4,m4] = max(R_load_cryo);

[n5,m5] = max(C_load_treated);
[n6,m6] = max(R_load_treated);


%% Determine Strain Differences %%%%%%%%%%%%%%%%%%%%%%%%%%%%%%%%%%%%%%%%%%%

% After data has been trimmed to include only the loading curve, find the
% data point closet to 90 N/m of membrane tension (because sometimes the
% biax overshoots this target):

[~,r1] = min( abs(90 - C_load_untreated(1:m1) ) );
max_load(1) = C_load_untreated(r1);
max_stretch(1) = C_stretch_untreated(r1);

[~,r2] = min( abs(90 - R_load_untreated(1:m2) ) );
max_load(2) = R_load_untreated(r2);
max_stretch(2) = R_stretch_untreated(r2);

[~,r3] = min( abs(90 - C_load_cryo(1:m3) ) );
max_load(3) = C_load_cryo(r3);
max_stretch(3) = C_stretch_cryo(r3);
```

```
[~,r4] = min( abs(90 - R_load_cryo(1:m4) ) );
max_load(4) = R_load_cryo(r4);
max_stretch(4) = R_stretch_cryo(r4);

[~,r5] = min( abs(90 - C_load_treated(1:m5) ) );
max_load(5) = C_load_treated(r5);
max_stretch(5) = C_stretch_treated(r5);

[~,r6] = min( abs(90 - R_load_treated(1:m6) ) );
max_load(6) = R_load_treated(r6);
max_stretch(6) = R_stretch_treated(r6);

max_strain = max_stretch - 1;

% Determine areal strain:
areal_strain_untreated = max_stretch(1)*max_stretch(2);
areal_strain_cryo = max_stretch(3)*max_stretch(4);
areal_strain_treated = max_stretch(5)*max_stretch(6);

% All change in strain data compiled into one matrix:
change_in_strain = [ (max_strain(3)-max_strain(1))/max_strain(1)*100 ...
                     (max_strain(5)-max_strain(1))/max_strain(1)*100 ...
                     (max_strain(5)-max_strain(3))/max_strain(3)*100;...
                     (max_strain(4)-max_strain(2))/max_strain(2)*100 ...
                     (max_strain(6)-max_strain(2))/max_strain(2)*100 ...
                     (max_strain(6)-max_strain(4))/max_strain(4)*100;...
                     (areal_strain_cryo -
areal_strain_untreated)/areal_strain_untreated*100 ...
                     (areal_strain_treated -
areal_strain_untreated)/areal_strain_untreated*100 ...
                     (areal_strain_treated -
areal_strain_cryo)/areal_strain_cryo*100];

% Determine % change in stretch, RFA to Untreated:
change_circ_stretch_RFA = ((max_stretch(5) - max_stretch(1))/max_stretch(1))*100;
change_rad_stretch_RFA = ((max_stretch(6) - max_stretch(2))/max_stretch(2))*100;

% Determine % change in stretch, Cryo Only to Untreated:
change_circ_stretch_cryo = ((max_stretch(3) - max_stretch(1))/max_stretch(1))*100;
change_rad_stretch_cryo = ((max_stretch(4) - max_stretch(2))/max_stretch(2))*100;

% Determine % change in stretch, RFA to Cryo Only:
change_circ_stretch_RFAcryo = ((max_stretch(5) -
max_stretch(3))/max_stretch(3))*100;
change_rad_stretch_RFAcryo = ((max_stretch(6) -
max_stretch(4))/max_stretch(4))*100;


disp('----------------------------------------------------------------------------
-')
disp('    COMPLIANCE CHANGES
')
disp('----------------------------------------------------------------------------
-')
fprintf('\n')


disp('PERCENT CHANGE IN STRETCH:')
fprintf('\n')
disp('          Cryo to Untreated        RFA to Untreated        RFA to Cryo')
```

```
fprintf('Circ         \t%+7.2f \t\t\t\t %+6.2f \t\t\t
%+7.2f',change_circ_stretch_cryo,change_circ_stretch_RFA,change_circ_stretch_RFAcr
yo)
fprintf('\n')
fprintf('Radial       \t%+7.2f \t\t\t\t %+6.2f \t\t\t %+7.2f
',change_rad_stretch_cryo,change_rad_stretch_RFA,change_rad_stretch_RFAcryo)
fprintf('\n')
fprintf('Areal           %+7.2f \t\t\t    %+7.2f \t\t\t %+7.2f
',change_in_strain(3,1),change_in_strain(3,2),change_in_strain(3,3))
fprintf('\n')
fprintf('\n')
fprintf('\n')

disp('PERCENT CHANGE IN STRAIN:')
fprintf('\n')
disp('          Cryo to Untreated        RFA to Untreated        RFA to Cryo')
fprintf('Circ         \t%+7.2f \t\t\t\t %+6.2f \t\t\t
%+7.2f',change_in_strain(1,1),change_in_strain(1,2),change_in_strain(1,3))
fprintf('\n')
fprintf('Radial       \t%+7.2f \t\t\t\t %+6.2f \t\t\t %+7.2f
',change_in_strain(2,1),change_in_strain(2,2),change_in_strain(2,3))
fprintf('\n')
fprintf('\n')
fprintf('\n')

COMPLIANCE = [change_circ_stretch_cryo change_rad_stretch_cryo
change_in_strain(3,1) 0 change_in_strain(1,1) change_in_strain(2,1);...
              change_circ_stretch_RFA change_rad_stretch_RFA change_in_strain(3,2)
0 change_in_strain(1,2) change_in_strain(2,2);...
              change_circ_stretch_RFAcryo change_rad_stretch_RFAcryo
change_in_strain(3,3) 0 change_in_strain(1,3) change_in_strain(2,3)];


%% Plot Membrance Tension v Stretch %%%%%%%%%%%%%%%%%%%%%%%%%%%%%%%%%%%%%%%

% Determine max stretch, of all samples:
total_stretch = [C_stretch_untreated(1:r1); R_stretch_untreated(1:r2);
C_stretch_cryo(1:r3);...
                 R_stretch_cryo(1:r4); C_stretch_treated(1:r5);
R_stretch_treated(1:r6)];

maximum_S = max(total_stretch);

% Set the maximum x-axis stretch on plot to 1.5 if, stretch is less than
% 1.5:
if (maximum_S > 1.5)
    % DO NOTHING
else
    maximum_S = 1.5;
end

fig1 = figure(1);
% Plot UNTREATED, CIRC and RADIAL:
plot(C_stretch_untreated(1:r1),C_load_untreated(1:r1),'ko','MarkerSize',6)
hold on
plot(R_stretch_untreated(1:r2),R_load_untreated(1:r2),'kv','MarkerSize',6)
% Plot CRYO ONLY, CIRC and RADIAL:
plot(C_stretch_cryo(1:r3),C_load_cryo(1:r3),'bo','MarkerSize',6)
plot(R_stretch_cryo(1:r4),R_load_cryo(1:r4),'bv','MarkerSize',6)
% Plot TREATED, CIRC and RADIAL:
plot(C_stretch_treated(1:r5),C_load_treated(1:r5),'ro','MarkerSize',6)
plot(R_stretch_treated(1:r6),R_load_treated(1:r6),'rv','MarkerSize',6)
grid on
```

```
axis([1 maximum_S 0 95])
xlabel('Stretch Ratio')
ylabel('Membrane Tension (N/m)')
ptitle1 = [sample,' - Membrane Tension vs. Stretch'];
title(ptitle1,'FontWeight','bold')
legend('Circ: Untreated','Radial: Untreated','Circ: Cryo','Radial: Cryo','Circ: 
Cryo + RFA','Radial: Cryo + RFA')
hold off
filename = [sample,' - Membrane Tension vs Stretch.jpg'];
saveas(fig1,filename)


%% Stretch Data Referenced to Original Untreated Marker Reference %%%%%%%%

% REFERENCE STATE, UNTREATED marker data:
X1 = untreated_ref(1,:);
X2 = untreated_ref(2,:);

% dX/dS:
dX1_dS1 = (1/4)*( X1(1) - X1(2) - X1(3) + X1(4) );
dX1_dS2 = (1/4)*( X1(1) + X1(2) - X1(3) - X1(4) );
dX2_dS1 = (1/4)*( X2(1) - X2(2) - X2(3) + X2(4) );
dX2_dS2 = (1/4)*( X2(1) + X2(2) - X2(3) - X2(4) );

% Determine which frame to use, closest to 90 N/m
if r1 > r2
    L1 = r2;
elseif r2 > r1
    L1 = r1;
else
    L1 = r2;
end

if r3 > r4
    L2 = r4;
elseif r4 > r3
    L2 = r3;
else
    L2 = r3;
end

if r5 > r6
    L3 = r6;
elseif r6 > r5
    L3 = r5;
else
    L3 = r5;
end

untreated_F11 = untreated.data(1:L1,4);
untreated_F22 = untreated.data(1:L1,7);
untreated_k1 = untreated.data(1:L1,5);
untreated_k2 = untreated.data(1:L1,6);

cryo_F11 = zeros(L2,1);
cryo_F22 = zeros(L2,1);
cryo_k1 = zeros(L2,1);
cryo_k2 = zeros(L2,1);

treated_F11 = zeros(L3,1);
treated_F22 = zeros(L3,1);
treated_k1 = zeros(L3,1);
treated_k2 = zeros(L3,1);
```

```
% CRYO ONLY F11 and F22, wrt to UNTREATED REFERENCE LOCATIONS:
for i = 1:L2

    % DEFORMED MARKER POSITIONS, frame 'i':
    xx1_treated = cryo.data(i,11:14);
    xx2_treated = cryo.data(i,15:18);

    % Displacement Field:
    u1 = xx1_treated - X1;
    u2 = xx2_treated - X2;

    % dU/dS:
    dU1_dS1 = (1/4)*( u1(1) - u1(2) - u1(3) + u1(4) );
    dU1_dS2 = (1/4)*( u1(1) + u1(2) - u1(3) - u1(4) );
    dU2_dS1 = (1/4)*( u2(1) - u2(2) - u2(3) + u2(4) );
    dU2_dS2 = (1/4)*( u2(1) + u2(2) - u2(3) - u2(4) );

    % Matrix for H:
    compH = zeros(2,2);
    compH(1,1) =  dU1_dS1 * dX2_dS2 - dU1_dS2 * dX2_dS1;
    compH(1,2) = -dU1_dS1 * dX1_dS2 + dU1_dS2 * dX1_dS1;
    compH(2,1) =  dU2_dS1 * dX2_dS2 - dU2_dS2 * dX2_dS1;
    compH(2,2) = -dU2_dS1 * dX1_dS2 + dU2_dS2 * dX1_dS1;

    % Jacobian:
    J = dX1_dS1 * dX2_dS2 - dX1_dS2 * dX2_dS1;

    % Deformation Gradient Tensor:
    F = eye(2,2) + (1/J)*compH;

    cryo_F11(i) = F(1,1);
    cryo_F22(i) = F(2,2);
    cryo_k1(i) = F(1,2);
    cryo_k2(i) = F(2,1);

end

% TREATED F11 and F22, wrt to UNTREATED REFERENCE LOCATIONS:
for i = 1:L3

    % DEFORMED MARKER POSITIONS, frame 'i':
    xx1_treated = treated.data(i,11:14);
    xx2_treated = treated.data(i,15:18);

    % Displacement Field:
    u1 = xx1_treated - X1;
    u2 = xx2_treated - X2;

    % dU/dS:
    dU1_dS1 = (1/4)*( u1(1) - u1(2) - u1(3) + u1(4) );
    dU1_dS2 = (1/4)*( u1(1) + u1(2) - u1(3) - u1(4) );
    dU2_dS1 = (1/4)*( u2(1) - u2(2) - u2(3) + u2(4) );
    dU2_dS2 = (1/4)*( u2(1) + u2(2) - u2(3) - u2(4) );

    % Matrix for H:
    compH = zeros(2,2);
    compH(1,1) =  dU1_dS1 * dX2_dS2 - dU1_dS2 * dX2_dS1;
    compH(1,2) = -dU1_dS1 * dX1_dS2 + dU1_dS2 * dX1_dS1;
    compH(2,1) =  dU2_dS1 * dX2_dS2 - dU2_dS2 * dX2_dS1;
    compH(2,2) = -dU2_dS1 * dX1_dS2 + dU2_dS2 * dX1_dS1;

    % Jacobian:
```

```
    J = dX1_dS1 * dX2_dS2 - dX1_dS2 * dX2_dS1;

    % Deformation Gradient Tensor:
    F = eye(2,2) + (1/J)*compH;

    treated_F11(i) = F(1,1);
    treated_F22(i) = F(2,2);
    treated_k1(i) = F(1,2);
    treated_k2(i) = F(2,1);

end


Jacobian_cryo = cryo_F11(L2) * cryo_F22(L2) - cryo_k1(L2 )* cryo_k2(L2);
Jacobian_RFA = treated_F11(L3) * treated_F22(L3) - treated_k1(L3) *
treated_k2(L3);
Jacobian_untreated = untreated_F11(L1) * untreated_F22(L1) - untreated_k1(L1) *
untreated_k2(L1);

% Percent change in the Jacobian (area):
Change_J_cryo = ( (Jacobian_cryo - Jacobian_untreated)/Jacobian_untreated)*100;
Change_J_RFA = ( (Jacobian_RFA - Jacobian_untreated)/Jacobian_untreated)*100;
Change_J_RFA_cryo = ( (Jacobian_RFA - Jacobian_cryo)/Jacobian_cryo)*100;

% Change in F11:
Change_F11_cryo = ( (cryo_F11(L2) - untreated_F11(L1))/untreated_F11(L1))*100;
Change_F11_RFA = ( (treated_F11(L3) - untreated_F11(L1))/untreated_F11(L1))*100;
Change_F11_RFA_cryo = ( (treated_F11(L3) - cryo_F11(L2))/cryo_F11(L2))*100;

% Change in F22:
Change_F22_cryo = ( (cryo_F22(L2) - untreated_F22(L1))/untreated_F22(L1))*100;
Change_F22_RFA = ( (treated_F22(L3) - untreated_F22(L1))/untreated_F22(L1))*100;
Change_F22_RFA_cryo = ( (treated_F22(L3) - cryo_F22(L2))/cryo_F22(L2))*100;

disp('----------------------------------------------------------------------------
-')
disp('    DEFORMATION CHANGES
')
disp('----------------------------------------------------------------------------
-')
fprintf('\n')

disp('PERCENT CHANGE:')
fprintf('\n')
disp('          Cryo to Untreated        RFA to Untreated        RFA to Cryo')
fprintf('Circ         \t%+7.2f \t\t\t\t %+6.2f \t\t\t
%+7.2f',Change_F11_cryo,Change_F11_RFA,Change_F11_RFA_cryo)
fprintf('\n')
fprintf('Radial       \t%+7.2f \t\t\t\t %+6.2f \t\t\t %+7.2f
',Change_F22_cryo,Change_F22_RFA,Change_F22_RFA_cryo)
fprintf('\n')
fprintf('Areal           %+7.2f \t\t\t    %+7.2f \t\t\t %+7.2f
',Change_J_cryo,Change_J_RFA,Change_J_RFA_cryo)
fprintf('\n')
fprintf('\n')
fprintf('\n')


DEFORMATION = [Change_F11_cryo Change_F22_cryo Change_J_cryo;...
               Change_F11_RFA Change_F22_RFA  Change_J_RFA;...
               Change_F11_RFA_cryo Change_F22_RFA_cryo Change_J_RFA_cryo];

%% Plot Membrane Tension v Stretch %%%%%%%%%%%%%%%%%%%%%%%%%%%%%%%%%%%%%%%
```

```
% Of treated data referenced to the original untreated marker reference

% Determine MAX & MIN stretch, of all samples:
total_stretch = [untreated_F11; untreated_F22; cryo_F11;...
                 cryo_F22; treated_F11; treated_F22];

maximum_S = max(total_stretch);
minimum_S = min(total_stretch);

% Set the maximum x-axis stretch on plot to 1.5 if, stretch is less than
% 1.5:
if (maximum_S > 1.5)
    % DO NOTHING
else
    maximum_S = 1.5;
end

% Set the minimum x-axis stretch on plot to 1 if, stretch is greater than
% 1:
if (minimum_S < 1)
    % DO NOTHING
else
    minimum_S = 1;
end

fig2 = figure(2);

% Plot UNTREATED, CIRC and RADIAL:
plot(untreated_F11,C_load_untreated(1:L1),'ko','MarkerSize',6)
hold on
plot(untreated_F22,R_load_untreated(1:L1),'kv','MarkerSize',6)

% Plot CRYO ONLY, CIRC and RADIAL:
plot(cryo_F11,C_load_cryo(1:L2),'bo','MarkerSize',6)
plot(cryo_F22,R_load_cryo(1:L2),'bv','MarkerSize',6)

% Plot TREATED, CIRC and RADIAL:
plot(treated_F11,C_load_treated(1:L3),'ro','MarkerSize',6)
plot(treated_F22,R_load_treated(1:L3),'rv','MarkerSize',6)

grid on
axis([minimum_S maximum_S 0 95])
xlabel('Stretch Ratio')
ylabel('Membrane Tension (N/m)')
ptitle4 = [sample,' - Tenson v Stretch - Original Reference'];
title(ptitle4,'FontWeight','bold')
legend('Circ: Untreated','Radial: Untreated','Circ: Cryo','Radial: Cryo','Circ:
Cryo + RFA','Radial: Cryo + RFA')
hold off

filename = [sample,' - Tenson v Stretch - Orig Reference.jpg'];
saveas(fig2,filename)


%% Determine GEOMETRY Changes %%%%%%%%%%%%%%%%%%%%%%%%%%%%%%%%%%%%%%%%%%%%%

untreated_ref_T = transpose(untreated_ref);
untreated_ref_T(5,1) = untreated_ref_T(1,1);
untreated_ref_T(5,2) = untreated_ref_T(1,2);

cryo_ref_T = transpose(cryo_ref);
cryo_ref_T(5,1) = cryo_ref_T(1,1);
cryo_ref_T(5,2) = cryo_ref_T(1,2);
```

```
treated_ref_T = transpose(treated_ref);
treated_ref_T(5,1) = treated_ref_T(1,1);
treated_ref_T(5,2) = treated_ref_T(1,2);


% Areal Changes:
untreated_area = polyarea(untreated_ref_T(:,1),untreated_ref_T(:,2));
cryo_area = polyarea(cryo_ref_T(:,1),cryo_ref_T(:,2));
treated_area = polyarea(treated_ref_T(:,1),treated_ref_T(:,2));

% Percent Change - Areal:
cryo_area_change = ((cryo_area - untreated_area)/untreated_area)*100;
treated_area_change = ((treated_area - untreated_area)/untreated_area)*100;
treated_cryo_area = ((treated_area - cryo_area)/cryo_area)*100;

% Circumferential & Radial Directions:
C_untreated = 0.5*(sqrt( (untreated_ref(1,1)-untreated_ref(1,2))^2 +
(untreated_ref(2,1)-untreated_ref(2,2))^2 )...
    + sqrt( (untreated_ref(1,4)-untreated_ref(1,3))^2 + (untreated_ref(2,4)-
untreated_ref(2,3))^2 ) );
R_untreated = 0.5*(sqrt( (untreated_ref(1,1)-untreated_ref(1,4))^2 +
(untreated_ref(2,1)-untreated_ref(2,4))^2 )...
    + sqrt( (untreated_ref(1,2)-untreated_ref(1,3))^2 + (untreated_ref(2,2)-
untreated_ref(2,3))^2 ) );

C_cryo = 0.5*(sqrt( (cryo_ref(1,1)-cryo_ref(1,2))^2 + (cryo_ref(2,1)-
cryo_ref(2,2))^2 )...
    + sqrt( (cryo_ref(1,4)-cryo_ref(1,3))^2 + (cryo_ref(2,4)-cryo_ref(2,3))^2 ) );
R_cryo = 0.5*(sqrt( (cryo_ref(1,1)-cryo_ref(1,4))^2 + (cryo_ref(2,1)-
cryo_ref(2,4))^2 )...
    + sqrt( (cryo_ref(1,2)-cryo_ref(1,3))^2 + (cryo_ref(2,2)-cryo_ref(2,3))^2 ) );

C_treated = 0.5*(sqrt( (treated_ref(1,1)-treated_ref(1,2))^2 + (treated_ref(2,1)-
treated_ref(2,2))^2 )...
    + sqrt( (treated_ref(1,4)-treated_ref(1,3))^2 + (treated_ref(2,4)-
treated_ref(2,3))^2 ) );
R_treated = 0.5*(sqrt( (treated_ref(1,1)-treated_ref(1,4))^2 + (treated_ref(2,1)-
treated_ref(2,4))^2 )...
    + sqrt( (treated_ref(1,2)-treated_ref(1,3))^2 + (treated_ref(2,2)-
treated_ref(2,3))^2 ) );

% Percent Change - Circ and Radial:
cryo_circ_change = (C_cryo-C_untreated)/C_untreated*100;
cryo_radial_change = (R_cryo-R_untreated)/R_untreated*100;

treated_circ_change = (C_treated-C_untreated)/C_untreated*100;
treated_radial_change = (R_treated-R_untreated)/R_untreated*100;

treated_cryo_C = (C_treated-C_cryo)/C_cryo*100;
treated_cryo_R = (R_treated-R_cryo)/R_cryo*100;

change_in_geom = [cryo_circ_change treated_circ_change treated_cryo_C;...
                  cryo_radial_change treated_radial_change treated_cryo_R;...
                  cryo_area_change treated_area_change treated_cryo_area];

disp('-----------------------------------------------------------------------------
-')
disp('    GEOMETRY CHANGES
')
disp('-----------------------------------------------------------------------------
-')
fprintf('\n')
```

```
disp('PERCENT CHANGE:')
fprintf('\n')
disp('          Cryo to Untreated        RFA to Untreated        RFA to Cryo')
fprintf('Circ         \t%+7.2f \t\t\t\t %+6.2f \t\t\t
%+7.2f',change_in_geom(1,1),change_in_geom(1,2),change_in_geom(1,3))
fprintf('\n')
fprintf('Radial       \t%+7.2f \t\t\t\t %+6.2f \t\t\t %+7.2f
',change_in_geom(2,1),change_in_geom(2,2),change_in_geom(2,3))
fprintf('\n')
fprintf('Areal           %+7.2f \t\t\t    %+7.2f \t\t\t %+7.2f
',change_in_geom(3,1),change_in_geom(3,2),change_in_geom(3,3))
fprintf('\n')
fprintf('\n')
fprintf('\n')
fprintf('\n')

GEOMETRY = [cryo_circ_change cryo_radial_change cryo_area_change;...
            treated_circ_change treated_radial_change treated_area_change;...
            treated_cryo_C treated_cryo_R treated_cryo_area];

%% Marker Geometry Plot - UNSTRAINED %%%%%%%%%%%%%%%%%%%%%%%%%%%%%%%%%%%%%%

Xdet(1:5) = untreated_ref_T(:,1);
Xdet(6:10) = treated_ref_T(:,1);
Ydet(1:5) = untreated_ref_T(:,2);
Ydet(6:10) = treated_ref_T(:,2);

min_markerX = min(Xdet);
min_markerY = min(Ydet);
max_markerX = max(Xdet);
max_markerY = max(Ydet);

figure(3)
plot(untreated_ref_T(:,1),untreated_ref_T(:,2),'ko--
','LineWidth',1,'MarkerSize',5,'MarkerFaceColor','k')
hold on
plot(cryo_ref_T(:,1),cryo_ref_T(:,2),'bo--
','LineWidth',1,'MarkerSize',5,'MarkerFaceColor','b')
plot(treated_ref_T(:,1),treated_ref_T(:,2),'ro--
','LineWidth',1,'MarkerSize',5,'MarkerFaceColor','r')
ptitle4 = [sample,' - Marker Locations - UNSTRAINED'];
title(ptitle4,'FontWeight','bold')
legend('Untreated','Cryo Only','RFA + Cryo')
axis([min_markerX-25 max_markerX+25 min_markerY-25 max_markerY+25])
hold off

%% Marker Geometry Plot - STRAINED %%%%%%%%%%%%%%%%%%%%%%%%%%%%%%%%%%%%%%%%

untreated_strained = [untreated.data(r1,11) untreated.data(r1,15);...
                      untreated.data(r1,12) untreated.data(r1,16);...
                      untreated.data(r1,13) untreated.data(r1,17);...
                      untreated.data(r1,14) untreated.data(r1,18);...
                      untreated.data(r1,11) untreated.data(r1,15)];

cryo_strained = [cryo.data(r3,11) cryo.data(r3,15);...
                 cryo.data(r3,12) cryo.data(r3,16);...
                 cryo.data(r3,13) cryo.data(r3,17);...
                 cryo.data(r3,14) cryo.data(r3,18);...
                 cryo.data(r3,11) cryo.data(r3,15)];

treated_strained = [treated.data(r5,11) treated.data(r5,15);...
                    treated.data(r5,12) treated.data(r5,16);...
                    treated.data(r5,13) treated.data(r5,17);...
```

```
                    treated.data(r5,14) treated.data(r5,18);...
                    treated.data(r5,11) treated.data(r5,15)];

Xdet(1:5) = untreated_strained(:,1);
Xdet(6:10) = treated_strained(:,1);
Ydet(1:5) = untreated_strained(:,2);
Ydet(6:10) = treated_strained(:,2);

min_markerX = min(Xdet);
min_markerY = min(Ydet);
max_markerX = max(Xdet);
max_markerY = max(Ydet);

figure(4)
plot(untreated_strained(:,1),untreated_strained(:,2),'ko--
','LineWidth',1,'MarkerSize',5,'MarkerFaceColor','k')
hold on
plot(cryo_strained(:,1),cryo_strained(:,2),'bo--
','LineWidth',1,'MarkerSize',5,'MarkerFaceColor','b')
plot(treated_strained(:,1),treated_strained(:,2),'ro--
','LineWidth',1,'MarkerSize',5,'MarkerFaceColor','r')
ptitle5 = [sample,' - Marker Locations - STRAINED'];
title(ptitle5,'FontWeight','bold')
legend('Untreated','Cryo Only','RFA + Cryo')
axis([min_markerX-25 max_markerX+25 min_markerY-25 max_markerY+25])
hold off
```

Biaxial Mechanical Testing Analysis: Fung-Type Strain Energy Model

The following MATLAB code was used to perform the fits of mechanical data to the Fung-type hyperelastic strain energy model presented in Aim 2.

```
% Parameter fitting for model of biaxial test data

% Steve Boronyak
% April 17, 2013

clear
clc
close all

%% LOAD TEST DATA %%%%%%%%%%%%%%%%%%%%%%%%%%%%%%%%%%%%%%%%%%%%%%%%%%%%%%%%%

% SAMPLE DIMENSIONS
L1 = 15;     % mm - circ
L2 = 12;   % mm - radial

test_data = importdata('Treated(10).txt','\t',1);

LOAD1 = test_data.data(:,2);    % grams
LOAD2 = test_data.data(:,3);    % grams

% MAX LOAD
[n1,m1] = max(LOAD1);
[n2,m2] = max(LOAD2);

if m1 > m2                  % Determine the length of the dataset
    length = m2;
```

```
else
    length = m1;
end

E11 = test_data.data(1:length,8);   % From Green-Lagrangian Strain Tensor
E22 = test_data.data(1:length,10);

F11 = test_data.data(1:length,4);   % From deformation gradient tensor
F22 = test_data.data(1:length,7);

LOAD1 = LOAD1(1:length);
LOAD2 = LOAD2(1:length);


%% CALCULATE S %%%%%%%%%%%%%%%%%%%%%%%%%%%%%%%%%%%%%%%%%%%%%%%%%%%%%%%%%%%%

S11 = (LOAD1.*9.81)./(L2.*F11);  % 2nd Piola-Kirchhoff Stress, without
S22 = (LOAD2.*9.81)./(L1.*F22);  % thickness


%% MODEL FITTING %%%%%%%%%%%%%%%%%%%%%%%%%%%%%%%%%%%%%%%%%%%%%%%%%%%%%%%%%%

% INITIAL GUESSES
c = 0.1;                 % N/m
A1 = 100;                % Unitless
A2 = 10;                 % Unitless
beta = [c;A1;A2];

Nfit = 3;                % Number of parameters to fit

% LOWER BOUNDS
LB = [0;0;0];            % Model makes no sense of coeffs below 0

fop = optimset('Algorithm','levenberg-marquardt');  % Doesn't use Marquardt due to
lower bounds
[betaE,RESNORM,residuals,exflag,outp,lambda,JACOBIAN] =
lsqnonlin(@biax_function_4,beta,LB,[],fop,S11,S22,E11,E22);
beta_ci = nlparci(betaE,residuals,'jacobian',JACOBIAN);


%% GENERATE FUNCTION FROM CALCULATED PARAMETERS %%%%%%%%%%%%%%%%%%%%%%%%%%%

S11_CALC = betaE(1).*( 2.*betaE(2).*E11 ).*exp( betaE(2).*E11.^2 +
betaE(3).*E22.^2 );
S22_CALC = betaE(1).*( 2.*betaE(3).*E22 ).*exp( betaE(2).*E11.^2 +
betaE(3).*E22.^2 );

W = betaE(1).*(exp( betaE(2).*E11.^2 + betaE(3).*E22.^2 ) - 1);    % Strain-energy
function
W_loading = betaE(1)*(exp( betaE(2)*E11(length)^2 + betaE(3)*E22(length)^2 ) - 1);

SStot = sum((S11 - mean(S11)).^2);
SSerr = sum((S11 - S11_CALC).^2);
R_Squared_11 = 1 - SSerr/SStot;         % R^2 of circ fit

SStot = sum((S22 - mean(S22)).^2);
SSerr = sum((S22 - S22_CALC).^2);
R_Squared_22 = 1 - SSerr/SStot;         % R^2 of radial fit


% PLOT RESIDUALS HISTOGRAM
figure(1)
hist(residuals)
```

```
% PLOT THE MODEL FIT
figure(2)
plot(F11,S11.*F11,'bo')
hold on
plot(F22,S22.*F22,'rd')
plot(F11,S11_CALC.*F11,'k-','LineWidth',2)
plot(F22,S22_CALC.*F22,'k-','LineWidth',2)
xlabel('Stretch Ratio')
ylabel('Membrane Tension (N/m)')
legend('Circ','Radial')
title('Model Fits')
hold off


%% ERROR ANALYSIS %%%%%%%%%%%%%%%%%%%%%%%%%%%%%%%%%%%%%%%%%%%%%%%%%%%%%%%%%


JACOBIAN = full(JACOBIAN);

% Sigma^2:
weight_sq = (residuals'*residuals)/(length-Nfit+1);

% Curvature matrix:
alphaS = JACOBIAN'*JACOBIAN./weight_sq;

% Covariance matrix:
covariance = inv(alphaS);

% SigmaP
sigmaP = diag(sqrt(covariance));

% Correlation matrix:
correlation = covariance ./ (sigmaP*sigmaP');
CORRELATE = det(correlation);

% Chi^2 statistic:
chisq2 = 1/weight_sq*sum(residuals.^2);
chi_critical = chi2inv(0.95,length-Nfit);


%% COMPILE DATA FOR EASY EXPORT %%%%%%%%%%%%%%%%%%%%%%%%%%%%%%%%%%%%%%%%%%%

ALL_DATA = [betaE(1);betaE(2);betaE(3);R_Squared_11;R_Squared_22;...
    W_loading;outp.iterations;chisq2;chi_critical;CORRELATE];

PLOT_DATA = [F11 S11.*F11 F22 S22.*F22 F11 S11_CALC.*F11 F22 S22_CALC.*F22];
```

```
function F = biax_function_4(beta,S11,S22,E11,E22)

F = [ S11 - beta(1).*( 2.*beta(2).*E11 ).*exp( beta(2).*E11.^2 + beta(3).*E22.^2 )
      S22 - beta(1).*( 2.*beta(3).*E22 ).*exp( beta(2).*E11.^2 + beta(3).*E22.^2 
)];
```

Basic Biaxial Mechanical Testing 16 Marker Analysis
The following MATLAB code was used to perform the Aim 1 – Part 2 studies in Chapter 6.

The data is input from a .mat file, which contains four variables: X1, X2, xx1, and xx2. X1 and X2 are the marker reference positions and xx1 and xx2 are the deformed marker positions, where 1 and 2 correspond to axis 1 and axis 2. Each variable is arranged as a 1x16 matrix, with the column number corresponding to the marker numbers shown in the code below.

```
%% BIAX 16 MARKER DEFORMATION GRADIENT AND ANALYSIS

% Steve Boronyak
% Department of Biomedical Engineering
% Vanderbilt University
% January 5, 2015

% This code only works with the AVERAGE marker positions obtained after
% using "biax_16_average_markers.m" or "biax_16_average_markersRF.m". The
% file loads in the X1, X2, xx1, and xx2 marker positions in units of cm.

% This code performs a bicubic interpolation in order to calculate the
% displacement gradient and deformation gradient within a 4x4 bicubic
% element. The spatially varying deformation gradient and maximum principal
% strain are plotted on the reference and deformed grids. The grids were
% determined using the bicubic interpolation of the 16 tracking markers.

% Marker numbering for this implementation of the bicubic interpolation
% (for X1 and X2 below):
% 04---10---09---03
% ||   ||   ||   ||
% 11---16---15---08
% ||   ||   ||   ||
% 12---13---14---07
% ||   ||   ||   ||
% 01---05---06---02

% This program loads the marker positions assuming the following
% configuration (this is the marker order of X1uo and X2uo):
% 04---03---02---01
% ||   ||   ||   ||
% 08---07---06---05
% ||   ||   ||   ||
% 12---11---10---09
% ||   ||   ||   ||
% 16---15---14---13

%%%%%%%%%%%%%%%%%%%%%%%%%%%%%%%%%%%%%%%%%%%%%%%%%%%%%%%%%%%%%%%%%%%%%%%%%%%

clear
close all
clc
colordef white              % Set figures for black background


%% USER INPUT %%%%%%%%%%%%%%%%%%%%%%%%%%%%%%%%%%%%%%%%%%%%%%%%%%%%%%%%%%%%%

% REFERENCE and DEFORMED Marker File
disp('Select DATA file');
[datafile,ImageFolder,~] = uigetfile('*.mat');
xxx = [ImageFolder datafile];
load(xxx)
```

```
%% EXTRACT DATA %%%%%%%%%%%%%%%%%%%%%%%%%%%%%%%%%%%%%%%%%%%%%%%%%%%%%%%%%%%%%

% Displacement Field:
u1 = xx1 - X1;
u2 = xx2 - X2;

% Rearrange X1/2 and xx1/2 arrays for marker outline:
jj = [1,5,6,2,7,8,3,9,10,4,11,12,1];
for i = 1:13
    X1_outline(i) = X1(jj(i));
    X2_outline(i) = X2(jj(i));
    xx1_outline(i) = xx1(jj(i));
    xx2_outline(i) = xx2(jj(i));
end

%% CALCULATE DEFORMED GRADIENT AT r=0, s=0 %%%%%%%%%%%%%%%%%%%%%%%%%%%%%%%%%%%

r = 0;
s = 0;

% Marker locations in the local (r,s) coordinate system:
rL = [-1,1,1,-1,-1/3,1/3,1,1,1/3,-1/3,-1,-1,-1/3,1/3,1/3,-1/3];
sL = [-1,-1,1,1,-1,-1,-1/3,1/3,1,1,1/3,-1/3,-1/3,-1/3,1/3,1/3];

% dX/dS:
dX1_dS1 = bicubic_derivative_r(r,s,rL,sL,X1);
dX1_dS2 = bicubic_derivative_s(r,s,rL,sL,X1);
dX2_dS1 = bicubic_derivative_r(r,s,rL,sL,X2);
dX2_dS2 = bicubic_derivative_s(r,s,rL,sL,X2);

% dU/dS:
dU1_dS1 = bicubic_derivative_r(r,s,rL,sL,u1);
dU1_dS2 = bicubic_derivative_s(r,s,rL,sL,u1);
dU2_dS1 = bicubic_derivative_r(r,s,rL,sL,u2);
dU2_dS2 = bicubic_derivative_s(r,s,rL,sL,u2);

% Matrix for H:
compH = zeros(2,2);
compH(1,1) =  dU1_dS1*dX2_dS2 - dU1_dS2*dX2_dS1;
compH(1,2) = -dU1_dS1*dX1_dS2 + dU1_dS2*dX1_dS1;
compH(2,1) =  dU2_dS1*dX2_dS2 - dU2_dS2*dX2_dS1;
compH(2,2) = -dU2_dS1*dX1_dS2 + dU2_dS2*dX1_dS1;

% Jacobian:
J = dX1_dS1*dX2_dS2 - dX1_dS2*dX2_dS1;

% Deformation Gradient Tensor:
F = eye(2,2) + (1/J)*compH;

F11 = F(1,1);
F22 = F(2,2);
k1 = F(1,2);
k2 = F(2,1);

%% GENERATE MESH GRID - DEFORMED AND UNDEFORMED %%%%%%%%%%%%%%%%%%%%%%%%%%%%%%%

node_width = 50;                            % Number of nodes in each direction
r = linspace(-1,1,node_width);              % Generate vector of points in r-space
s = linspace(-1,1,node_width);              % Generate vector of points in s-space

[rr,ss] = meshgrid(r,s);
```

```
% Generate REFERENCE and DEFORMED grids
for i = 1:node_width
    for j = 1:node_width
        X_grid(i,j) = bicubic_basis(rr(i,j),ss(i,j),rL,sL,X1);
        Y_grid(i,j) = bicubic_basis(rr(i,j),ss(i,j),rL,sL,X2);
        u_grid(i,j) =  bicubic_basis(rr(i,j),ss(i,j),rL,sL,u1);
        v_grid(i,j) = bicubic_basis(rr(i,j),ss(i,j),rL,sL,u2);
        xx_grid(i,j) = X_grid(i,j) + u_grid(i,j);
        yy_grid(i,j) = Y_grid(i,j) + v_grid(i,j);
    end
end


%% CALCULATE DEFORMATION GRADIENT EVERYWHERE %%%%%%%%%%%%%%%%%%%%%%%%%%%%%%%%%%%%%

for i = 1:node_width
    for j = 1:node_width
        % dX/dS:
        dX1_dS1 = bicubic_derivative_r(rr(i,j),ss(i,j),rL,sL,X1);
        dX1_dS2 = bicubic_derivative_s(rr(i,j),ss(i,j),rL,sL,X1);
        dX2_dS1 = bicubic_derivative_r(rr(i,j),ss(i,j),rL,sL,X2);
        dX2_dS2 = bicubic_derivative_s(rr(i,j),ss(i,j),rL,sL,X2);

        % dU/dS:
        dU1_dS1 = bicubic_derivative_r(rr(i,j),ss(i,j),rL,sL,u1);
        dU1_dS2 = bicubic_derivative_s(rr(i,j),ss(i,j),rL,sL,u1);
        dU2_dS1 = bicubic_derivative_r(rr(i,j),ss(i,j),rL,sL,u2);
        dU2_dS2 = bicubic_derivative_s(rr(i,j),ss(i,j),rL,sL,u2);

        % Matrix for H:
        compH = zeros(2,2);
        compH(1,1) =  dU1_dS1*dX2_dS2 - dU1_dS2*dX2_dS1;
        compH(1,2) = -dU1_dS1*dX1_dS2 + dU1_dS2*dX1_dS1;
        compH(2,1) =  dU2_dS1*dX2_dS2 - dU2_dS2*dX2_dS1;
        compH(2,2) = -dU2_dS1*dX1_dS2 + dU2_dS2*dX1_dS1;

        % Jacobian:
        J = dX1_dS1*dX2_dS2 - dX1_dS2*dX2_dS1;

        % Deformation Gradient Tensor:
        zF = eye(2,2) + (1/J)*compH;

        zF11(i,j) = zF(1,1);            % Axis 1 deformation
        zF22(i,j) = zF(2,2);            % Axis 2 deformation
        zFdet(i,j) = det(zF);           % Areal deformation

        E_star = 0.5*(transpose(zF)*zF - eye(2,2));
        [v,d] = eig(E_star);
        zMAXp(i,j) = min(min(d));       % Minimum principal strain
%         zMAXp(i,j) = max(max(d));       % Minimum principal strain
        zInv1(i,j) = sum(sum(d));       % 1st Invariant
    end
end

for i = 1:node_width
    % dX/dS:
    dX1_dS1 = bicubic_derivative_r(r(i),0,rL,sL,X1);
    dX1_dS2 = bicubic_derivative_s(r(i),0,rL,sL,X1);
    dX2_dS1 = bicubic_derivative_r(r(i),0,rL,sL,X2);
    dX2_dS2 = bicubic_derivative_s(r(i),0,rL,sL,X2);

    % dU/dS:
    dU1_dS1 = bicubic_derivative_r(r(i),0,rL,sL,u1);
```

```
    dU1_dS2 = bicubic_derivative_s(r(i),0,rL,sL,u1);
    dU2_dS1 = bicubic_derivative_r(r(i),0,rL,sL,u2);
    dU2_dS2 = bicubic_derivative_s(r(i),0,rL,sL,u2);

    % Matrix for H:
    compH = zeros(2,2);
    compH(1,1) =  dU1_dS1*dX2_dS2 - dU1_dS2*dX2_dS1;
    compH(1,2) = -dU1_dS1*dX1_dS2 + dU1_dS2*dX1_dS1;
    compH(2,1) =  dU2_dS1*dX2_dS2 - dU2_dS2*dX2_dS1;
    compH(2,2) = -dU2_dS1*dX1_dS2 + dU2_dS2*dX1_dS1;

    % Jacobian:
    J = dX1_dS1*dX2_dS2 - dX1_dS2*dX2_dS1;

    % Deformation Gradient Tensor:
    zF = eye(2,2) + (1/J)*compH;

    F11s0(i) = zF(1,1);            % Axis 1 deformation
    F22s0(i) = zF(2,2);            % Axis 2 deformation
    Fdets0(i) = det(zF);           % Areal deformation

    XposS0(i) = bicubic_basis(r(i),0,rL,sL,X1);
    YposS0(i) = bicubic_basis(r(i),0,rL,sL,X2);
    u_grid0(i) =  bicubic_basis(r(i),0,rL,sL,u1);
    v_grid0(i) = bicubic_basis(r(i),0,rL,sL,u2);
    xx_posS0(i) = XposS0(i) + u_grid0(i);
    yy_posS0(i) = YposS0(i) + v_grid0(i);
end

for i = 1:node_width
    % dX/dS:
    dX1_dS1 = bicubic_derivative_r(0,s(i),rL,sL,X1);
    dX1_dS2 = bicubic_derivative_s(0,s(i),rL,sL,X1);
    dX2_dS1 = bicubic_derivative_r(0,s(i),rL,sL,X2);
    dX2_dS2 = bicubic_derivative_s(0,s(i),rL,sL,X2);

    % dU/dS:
    dU1_dS1 = bicubic_derivative_r(0,s(i),rL,sL,u1);
    dU1_dS2 = bicubic_derivative_s(0,s(i),rL,sL,u1);
    dU2_dS1 = bicubic_derivative_r(0,s(i),rL,sL,u2);
    dU2_dS2 = bicubic_derivative_s(0,s(i),rL,sL,u2);

    % Matrix for H:
    compH = zeros(2,2);
    compH(1,1) =  dU1_dS1*dX2_dS2 - dU1_dS2*dX2_dS1;
    compH(1,2) = -dU1_dS1*dX1_dS2 + dU1_dS2*dX1_dS1;
    compH(2,1) =  dU2_dS1*dX2_dS2 - dU2_dS2*dX2_dS1;
    compH(2,2) = -dU2_dS1*dX1_dS2 + dU2_dS2*dX1_dS1;

    % Jacobian:
    J = dX1_dS1*dX2_dS2 - dX1_dS2*dX2_dS1;

    % Deformation Gradient Tensor:
    zF = eye(2,2) + (1/J)*compH;

    F11r0(i) = zF(1,1);            % Axis 1 deformation
    F22r0(i) = zF(2,2);            % Axis 2 deformation
    Fdetr0(i) = det(zF);           % Areal deformation

%     YposR0(i) = bicubic_basis(0,s(i),rL,sL,X2);

    XposR0(i) = bicubic_basis(0,s(i),rL,sL,X1);
    YposR0(i) = bicubic_basis(0,s(i),rL,sL,X2);
```

```
    u_grid0(i) =  bicubic_basis(0,s(i),rL,sL,u1);
    v_grid0(i) = bicubic_basis(0,s(i),rL,sL,u2);
    xx_posR0(i) = XposR0(i) + u_grid0(i);
    yy_posR0(i) = YposR0(i) + v_grid0(i);
end


%% PLOT MARKERS

% Determine boundaries of plots, so all are uniform
xMIN = min([min(min(X_grid)) min(min(xx_grid))]);
xMAX = max([max(max(X_grid)) max(max(xx_grid))]);
yMIN = min([min(min(Y_grid)) min(min(yy_grid))]);
yMAX = max([max(max(Y_grid)) max(max(yy_grid))]);

%% PLOTS OF DEFORMATION GRADIENT %%%%%%%%%%%%%%%%%%%%%%%%%%%%%%%%%%%%%%%%%%%%%%%

% Determine boundaries of plots, so all are uniform
xMIN = min([min(min(X_grid)) min(min(xx_grid))]);
xMAX = max([max(max(X_grid)) max(max(xx_grid))]);
yMIN = min([min(min(Y_grid)) min(min(yy_grid))]);
yMAX = max([max(max(Y_grid)) max(max(yy_grid))]);


fig5 = figure(5);
pcolor(xx_grid,yy_grid,zFdet)
hold on
plot(xx1,xx2,'ko','MarkerSize',5,'MarkerFaceColor','k')
% title('Areal Deformation - DEFORMED Configuration','FontSize',14)
xlim([xMIN-0.05 xMAX+0.05])
ylim([yMIN-0.05 yMAX+0.05])
colorbar
set(colorbar,'fontsize',14);
% set(gcf, 'Color', [0,0,0]);
set(gcf, 'Color', [1,1,1]);
set(gca,'FontSize',14)
% caxis([FMIN2 FMAX2])
xlabel('(cm)')
ylabel('(cm)')
hold off

fig5 = figure(8);
pcolor(xx_grid,yy_grid,zF11)
hold on
plot(xx1,xx2,'ko','MarkerSize',5,'MarkerFaceColor','k')
% title('F11 - DEFORMED Configuration','FontSize',14)
% plot(xx_posS0,yy_posS0,'k-','LineWidth',2)
% plot(xx_posR0,yy_posR0,'k-','LineWidth',2)
xlim([xMIN-0.05 xMAX+0.05])
ylim([yMIN-0.05 yMAX+0.05])
% caxis([FMIN FMAX])
colorbar
set(colorbar,'fontsize',14);
% set(gcf, 'Color', [0,0,0]);
set(gcf, 'Color', [1,1,1]);
set(gca,'FontSize',14)
xlabel('(cm)')
ylabel('(cm)')
hold off

figure(9)
pcolor(X_grid,Y_grid,zF22)
hold on
```

```
plot(X1,X2,'ko','MarkerSize',5,'MarkerFaceColor','k')
plot(XposS0,YposS0,'k-','LineWidth',2)
plot(XposR0,YposR0,'k-','LineWidth',2)
% title('F22 - REFERENCE Configuration','FontSize',14)
% caxis([FMIN FMAX])
colorbar
set(colorbar,'fontsize',14);
% set(gcf, 'Color', [0,0,0]);
set(gcf, 'Color', [1,1,1]);
set(gca,'FontSize',14)
xlabel('(cm)')
ylabel('(cm)')
hold off

fig5 = figure(10);
pcolor(xx_grid,yy_grid,zF22)
hold on
plot(xx1,xx2,'ko','MarkerSize',5,'MarkerFaceColor','k')
% title('F22 - DEFORMED Configuration','FontSize',14)
xlim([xMIN-0.05 xMAX+0.05])
ylim([yMIN-0.05 yMAX+0.05])
% plot(xx_posS0,yy_posS0,'k-','LineWidth',2)
% plot(xx_posR0,yy_posR0,'k-','LineWidth',2)
% caxis([FMIN FMAX])
colorbar
set(colorbar,'fontsize',14);
% set(gcf, 'Color', [0,0,0]);
set(gcf, 'Color', [1,1,1]);
set(gca,'FontSize',14)
xlabel('(cm)')
ylabel('(cm)')
hold off

figure(13)
plot(XposS0,Fdets0,'k-.','LineWidth',2)
hold on
set(gca,'LineWidth',2);
plot(XposS0,F11s0,'b-','LineWidth',2)
set(gca,'FontSize',14)
plot(XposS0,F22s0,'r--','LineWidth',2)
xlabel('X11 Position (cm)')
ylabel('Deformation')
legend('Areal','Circ - F11','Radial - F22')
xlim([-.7 .7])
% ylim([0.3 1.4])
hold off
```

APPENDIX J: AIM 2 SUPPLEMENTAL DATA – ESTIMATED MODEL PARAMETERS

This section of the Appendix contains the estimated model parameters for all samples analyzed in the Aim 2 study of strain energy model fits.

Table J.1. Parameter fitting results for untreated MV anterior leaflets.

Sample Number	c (N/m)	A1	A2	W (N/m)	R^2_{circ}	R^2_{rad}
92	0.10	106.67	22.48	4.56	0.995	0.996
93	0.03	89.22	35.68	3.52	0.996	0.997
94	0.01	243.43	31.78	3.03	0.995	0.993
91	0.04	607.16	21.67	3.58	0.984	0.993
83	0.04	176.96	11.32	4.49	0.992	0.989
82	0.08	54.61	8.57	5.95	0.993	0.992
86	0.06	551.91	95.91	2.64	0.980	0.987
81	0.01	50.63	23.60	3.93	0.995	0.992
80	0.03	58.24	17.52	4.31	0.993	0.992
79	0.01	244.73	13.47	3.63	0.992	0.990
78	0.10	31.05	10.71	5.11	0.987	0.988
77	0.05	57.38	21.18	4.48	0.994	0.992
76	0.05	67.95	14.41	5.06	0.992	0.991
75	0.05	62.04	6.40	6.10	0.996	0.991
74	0.05	90.93	22.04	4.36	0.995	0.994
73	0.19	110.56	36.89	4.17	0.991	0.992
72	0.07	250.95	79.96	2.68	0.995	0.992
71	0.22	89.47	55.56	4.15	0.996	0.995
70	0.06	59.32	21.74	4.47	0.994	0.992
69	0.04	152.21	14.30	4.22	0.995	0.994
68	0.02	46.74	22.24	4.19	0.994	0.992
67	0.00	71.99	24.60	3.01	0.979	0.971
66	0.09	60.70	17.16	5.25	0.996	0.996
65	0.06	187.89	30.37	3.63	0.995	0.996
64	0.06	136.58	44.86	3.48	0.995	0.995
63	0.04	131.87	17.85	3.96	0.995	0.994
62	0.07	100.49	29.29	3.98	0.995	0.995
61	0.06	87.13	16.12	4.54	0.998	0.996
60	0.04	47.42	9.43	5.37	0.993	0.990
59	0.01	58.79	39.29	3.51	0.992	0.991
58	0.11	24.26	4.09	7.11	0.990	0.982
57	0.13	155.57	12.48	4.87	0.993	0.994

56	0.09	67.37	25.05	4.44	0.994	0.992
55	0.18	75.04	6.64	6.41	0.998	0.991
54	0.07	132.86	8.85	4.86	0.994	0.983
53	0.04	74.21	14.44	4.62	0.993	0.992
52	0.05	168.59	15.23	4.31	0.994	0.992
51	0.24	285.50	48.44	3.73	0.980	0.991
49	0.05	94.55	26.80	3.97	0.995	0.996
48	0.16	65.57	16.33	5.13	0.996	0.997
45	0.12	93.19	30.80	4.16	0.998	0.997
43	0.06	184.65	17.75	4.57	0.986	0.993
42	0.05	416.00	57.58	2.82	0.993	0.996
43	0.04	168.37	48.80	2.92	0.995	0.995
95	0.07	240.39	33.54	3.55	0.997	0.994
96	0.14	67.47	9.49	6.08	0.996	0.993
97	0.04	91.43	25.24	4.07	0.995	0.992
98	0.12	69.68	17.56	4.77	0.996	0.996
99	0.10	45.97	9.15	5.47	0.995	0.992
100	0.14	162.98	36.60	3.71	0.993	0.997
101	0.21	136.42	76.56	3.58	0.995	0.995
103	0.03	154.97	33.40	3.48	0.988	0.986
104	0.20	44.04	8.52	6.64	0.992	0.983
105	0.04	258.22	38.12	3.32	0.984	0.985
106	0.33	55.40	6.79	7.38	0.994	0.977
107	0.13	186.35	24.23	3.98	0.996	0.993
108	0.14	83.86	26.39	4.41	0.995	0.993
109	0.17	152.64	53.33	3.84	0.993	0.995
110	0.15	160.30	60.48	3.54	0.991	0.994
125	0.06	114.39	16.24	4.50	0.994	0.992
127	0.14	91.13	23.50	4.67	0.998	0.996
129	0.34	61.05	8.44	7.12	0.998	0.994
145	0.17	154.65	13.03	5.87	0.996	0.995
146	0.09	230.41	39.17	3.64	0.996	0.997
147	0.02	526.90	27.44	3.39	0.990	0.990
124	0.08	82.06	17.41	4.79	0.996	0.994
126	0.15	51.12	25.01	5.09	0.997	0.997
128	0.05	158.85	47.72	2.48	0.996	0.995
142	0.03	386.66	37.21	3.15	0.955	0.982
143	0.16	146.41	13.42	5.34	0.996	0.994
144	0.06	168.88	26.36	3.91	0.996	0.995
111	0.04	146.25	61.71	3.11	0.987	0.990
112	0.00	276.11	37.01	2.43	0.975	0.985
113	0.05	32.52	9.92	5.78	0.986	0.988
114	0.05	152.65	34.42	3.66	0.995	0.995

115	0.04	419.26	56.39	2.67	0.995	0.996
116	0.04	437.05	56.27	2.68	0.995	0.996
137	0.00	118.16	22.48	3.09	0.993	0.991
138	0.01	119.28	24.53	3.57	0.992	0.991
139	0.02	76.01	26.34	3.92	0.995	0.995
140	0.01	74.87	30.87	3.52	0.994	0.992
141	0.06	58.47	18.88	4.83	0.997	0.996
87	0.01	711.96	31.84	2.82	0.982	0.984
41	0.04	168.37	48.80	2.92	0.995	0.995
40	0.19	215.39	31.59	4.20	0.991	0.994
39	0.11	161.01	18.94	4.72	0.996	0.996
38	0.08	68.82	16.56	4.79	0.998	0.995
37	0.11	104.71	16.47	4.65	0.995	0.994
36	0.05	157.64	38.10	3.61	0.995	0.994
35	0.14	95.36	62.74	3.78	0.997	0.996
33	0.02	92.65	35.68	3.23	0.994	0.995
34	0.14	64.90	21.37	4.95	0.997	0.996
31	0.17	60.90	36.08	4.71	0.995	0.994
30	0.72	17.05	3.42	10.65	0.998	0.992
29	0.14	48.10	10.11	6.12	0.995	0.993
27	0.06	64.05	19.77	4.49	0.994	0.993
26	0.13	76.28	28.52	4.54	0.998	0.997
25	0.08	65.00	18.82	4.93	0.997	0.995
24	0.11	54.21	28.00	4.71	0.996	0.997
23	0.09	57.48	11.11	5.82	0.997	0.996

Table J.2. Parameter fitting results from static control, RF-treated leaflets.

STATICALLY TREATED: 350 J

Sample Number	c (N/m)	A1	A2	W (N/m)	R^2_{circ}	R^2_{rad}
106	0.75	21.80	8.66	7.98	0.994	0.987
107	0.15	125.72	29.02	4.29	0.994	0.994
108	0.78	31.72	14.79	7.39	0.998	0.998
109	0.71	55.47	31.17	5.48	0.998	0.998
110	0.51	95.21	59.97	4.32	0.998	0.997

STATICALLY TREATED: 850 J

Sample Number	c (N/m)	A1	A2	W (N/m)	R^2_{circ}	R^2_{rad}
100	5.73	3.70	4.91	15.59	0.998	0.998
101	1.55	11.00	5.67	11.08	0.998	0.997
103	11.81	2.94	2.71	18.96	0.998	0.998
104	5.48	2.59	2.47	18.06	0.998	0.995
105	1.45	0.00	18.73	5.62	-0.838	0.980

STATICALLY TREATED: 1250 J

Sample Number	c (N/m)	A1	A2	W (N/m)	R^2_{circ}	R^2_{rad}
95	0.94	2.93	4.51	11.39	0.354	0.176
96	6.38	2.33	3.61	17.56	0.998	0.998
97	2.91	2.07	4.21	15.61	0.699	0.708
98	3.92	3.56	3.84	15.54	0.998	0.997
99	11.64	1.58	1.27	24.21	0.998	0.998

Table J.3. Parameter fitting results from flow loop treated MV leaflets.

FLOW LOOP TREATED: CRYO ONLY

Sample Number	c (N/m)	A1	A2	W (N/m)	R^2_{circ}	R^2_{rad}
157	0.14	95.21	28.11	4.29	0.999	0.998
160	0.06	74.29	23.90	4.44	0.998	0.994
163	0.08	66.10	16.89	5.31	0.997	0.993

FLOW LOOP TREATED: RF ONLY

Sample Number	c (N/m)	A1	A2	W (N/m)	R^2_{circ}	R^2_{rad}
158	3.25	5.73	4.07	14.05	0.999	0.999
161	2.50	6.00	3.62	14.28	0.999	0.998
162	2.75	11.94	8.60	11.30	0.990	0.990

FLOW LOOP TREATED: RF+CRYO

Sample Number	c (N/m)	A1	A2	W (N/m)	R^2_{circ}	R^2_{rad}
155	6.50	4.25	2.41	18.22	0.998	0.997
156	13.67	5.24	5.46	14.27	0.996	0.998
159	7.40	5.50	3.21	15.83	0.995	0.994

Table J.4. Parameter fitting results from durability study leaflets.

UNTREATED: ACUTE

Sample Number	c (N/m)	A1	A2	W (N/m)	R^2_{circ}	R^2_{rad}
125	0.06	114.39	16.24	4.50	0.994	0.992
127	0.14	91.13	23.50	4.67	0.998	0.996
129	0.34	61.05	8.44	7.12	0.998	0.994
145	0.17	154.65	13.03	5.87	0.996	0.995
146	0.09	230.41	39.17	3.64	0.996	0.997
147	0.02	526.90	27.44	3.39	0.990	0.990

UNTREATED: WEEK 4

Sample Number	c (N/m)	A1	A2	W (N/m)	R^2_{circ}	R^2_{rad}
131	0.47	81.01	31.14	5.40	0.996	0.996
133	0.31	49.23	39.41	4.87	0.998	0.998
135	0.36	57.82	13.17	6.33	0.997	0.995
149	0.13	1685.22	43.46	4.04	0.943	0.936
151	0.20	183.25	33.29	4.18	0.974	0.970
153	0.17	470.44	23.57	4.38	0.993	0.988

TREATED: ACUTE

Sample Number	c (N/m)	A1	A2	W (N/m)	R^2_{circ}	R^2_{rad}
124	10.74	3.38	2.33	18.74	0.995	0.993
126	1.93	9.17	4.92	12.39	0.995	0.997
128	3.35	11.50	5.16	12.33	0.999	0.999
142	4.26	3.03	4.36	16.00	0.972	0.980
143	1.99	14.23	4.30	11.61	0.998	0.993
144	0.43	36.18	15.34	6.54	0.993	0.989

TREATED: WEEK 4

Sample Number	c (N/m)	A1	A2	W (N/m)	R^2_{circ}	R^2_{rad}
130	3.87	13.07	7.71	11.19	0.994	0.996
132	1.51	13.18	9.88	9.35	0.996	0.995
134	3.01	19.25	11.57	8.97	0.998	0.998
148	2.87	7.44	8.53	12.06	0.982	0.989
150	2.79	21.21	4.84	11.45	0.997	0.998
152	0.95	60.30	14.16	6.88	0.998	0.996

APPENDIX K: LEFT HEART FLOW SIMULATOR

Essential accessory components for the left heart flow simulator, pinout diagrams for the LabView DAQ cards, pressure sensor calibrations, and the pneumatic system schematic are shown below. CAD drawings to reproduce the left heart flow simulator follow on the remaining pages.

Essential Components, Left Heart Flow Simulator

PART	PART NUMBER	MANUFACTURER
Proportional Pressure Regulator	PS120000-020-010	Hoerbiger
Pressure Sensors	19C003PG1L	Honeywell
Flow Meter	400 Series	Transonic
Solenoid Valve	3-Way, 8003G/H, 8202 G/H	Asco
DAQ Chassis	NI-cDAQ 9178	National Instruments
DAQ: Analog In	NI-9205	National Instruments
DAQ: Analog Out	NI-9263	National Instruments

Pinouts for DAQ Cards

NI 9205	
ACH0+	Pressure Sensor, Ventricle, OUT+
ACH0-	Pressure Sensor, Ventricle, OUT-
ACH1+	Pressure Sensor, Atrium, OUT+
ACH1-	Pressure Sensor, Atrium, OUT-
ACH3+	Flow Meter, Slot 1, Pin 1
ACH3-	GND
ACH4+	Flow Meter, Slot 1, Pin 2
ACH4-	GND
ACH5+	RF Generator, RF Power Measurement, +
ACH5-	RF Generator, RF Power Measurement, -
ACH6+	RF Generator, RF Impedance Measurement, +
ACH6-	RF Generator, RF Impedance Measurement, -
NI 9263	
AO0	Proportional Regulator, Set Value
COM	GND
AO1	Transistor to Solenoid Valve
COM	GND

Pressure Sensor Calibration: Ventricle

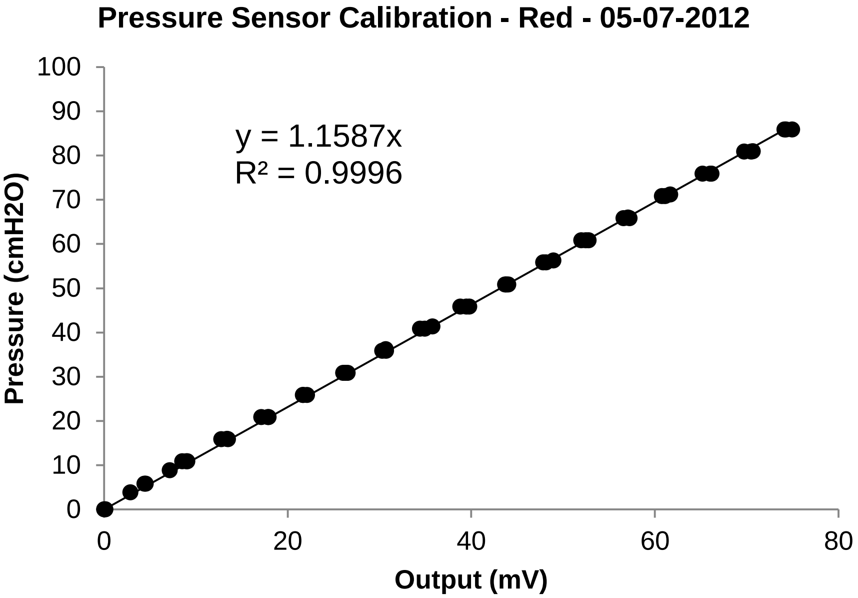

Pressure Sensor Calibration: Atrium

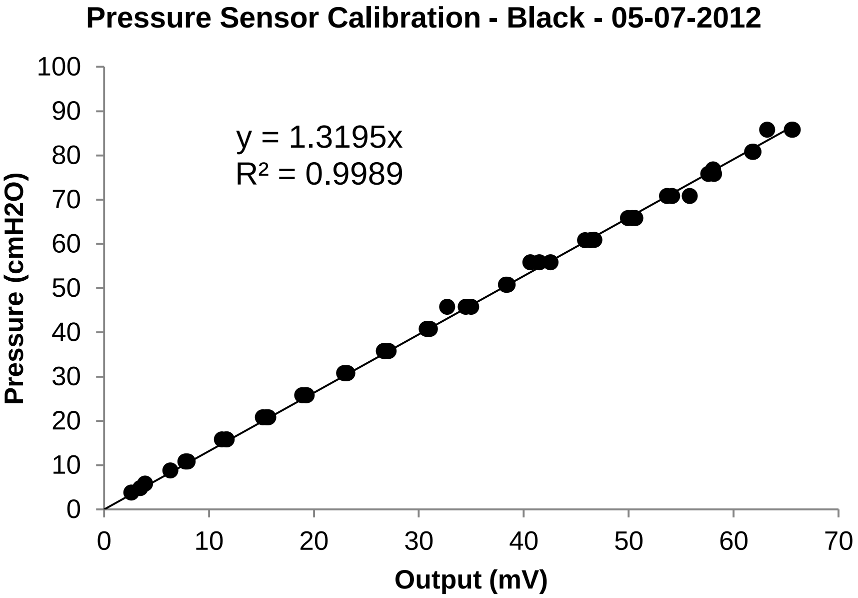

Left Heart Flow Simulator Pneumatic System Diagram

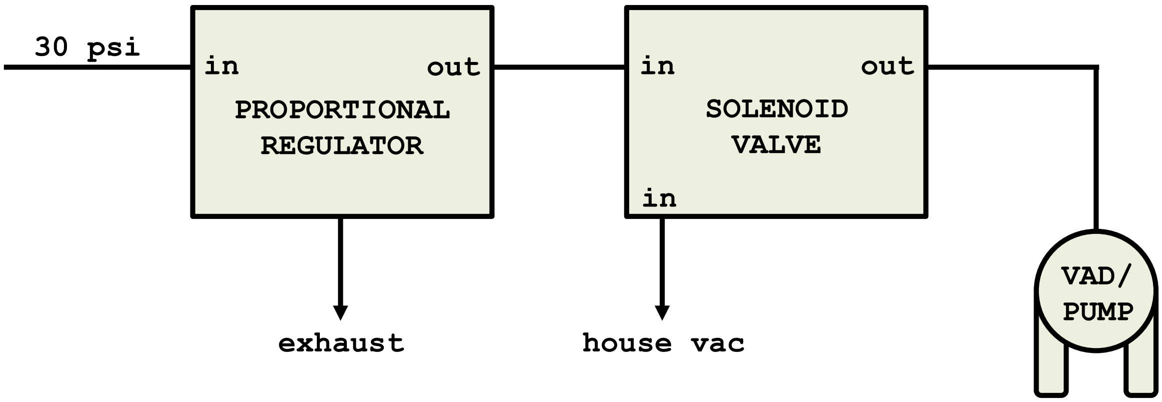

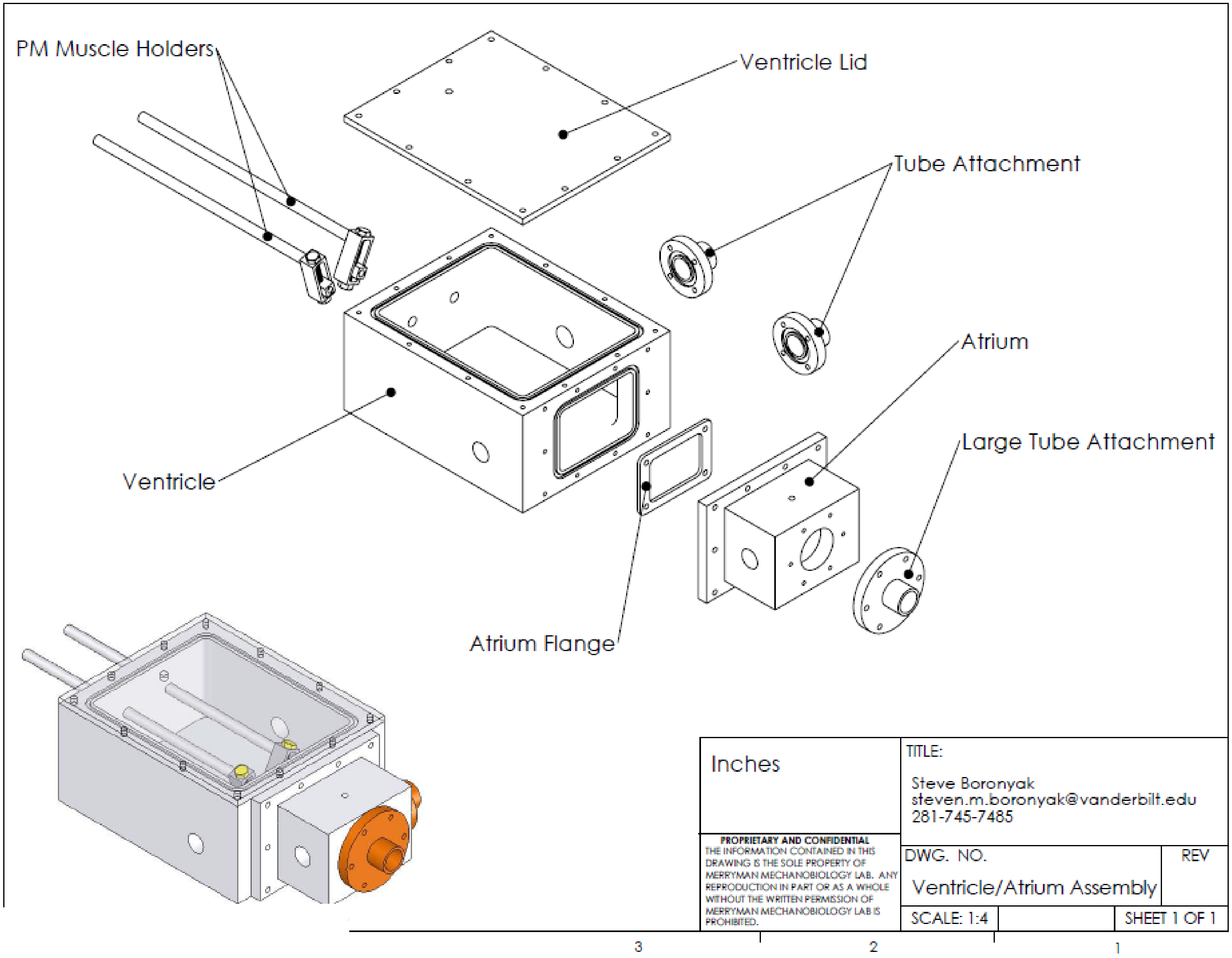
PM Muscle Holders
Ventricle Lid
Tube Attachment
Atrium
Large Tube Attachment
Ventricle
Atrium Flange
Inches
PROPRIETARY AND CONFIDENTIAL
THE INFORMATION CONTAINED IN THIS DRAWING IS THE SOLE PROPERTY OF MERRYMAN MECHANOBIOLOGY LAB. ANY REPRODUCTION IN PART OR AS A WHOLE WITHOUT THE WRITTEN PERMISSION OF MERRYMAN MECHANOBIOLOGY LAB IS PROHIBITED.
TITLE:
Steve Boronyak
steven.m.boronyak@vanderbilt.edu
281-745-7485
DWG. NO.
REV
Ventricle/Atrium Assembly
SCALE: 1:4
SHEET 1 OF 1
3
2
1

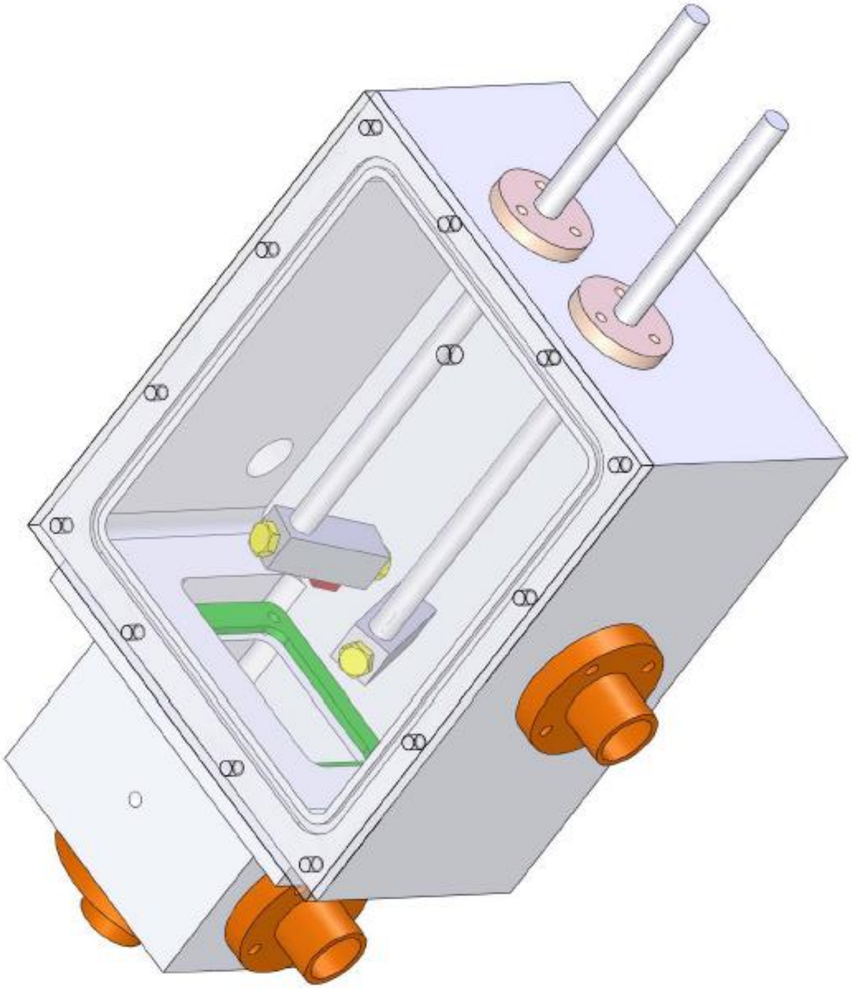

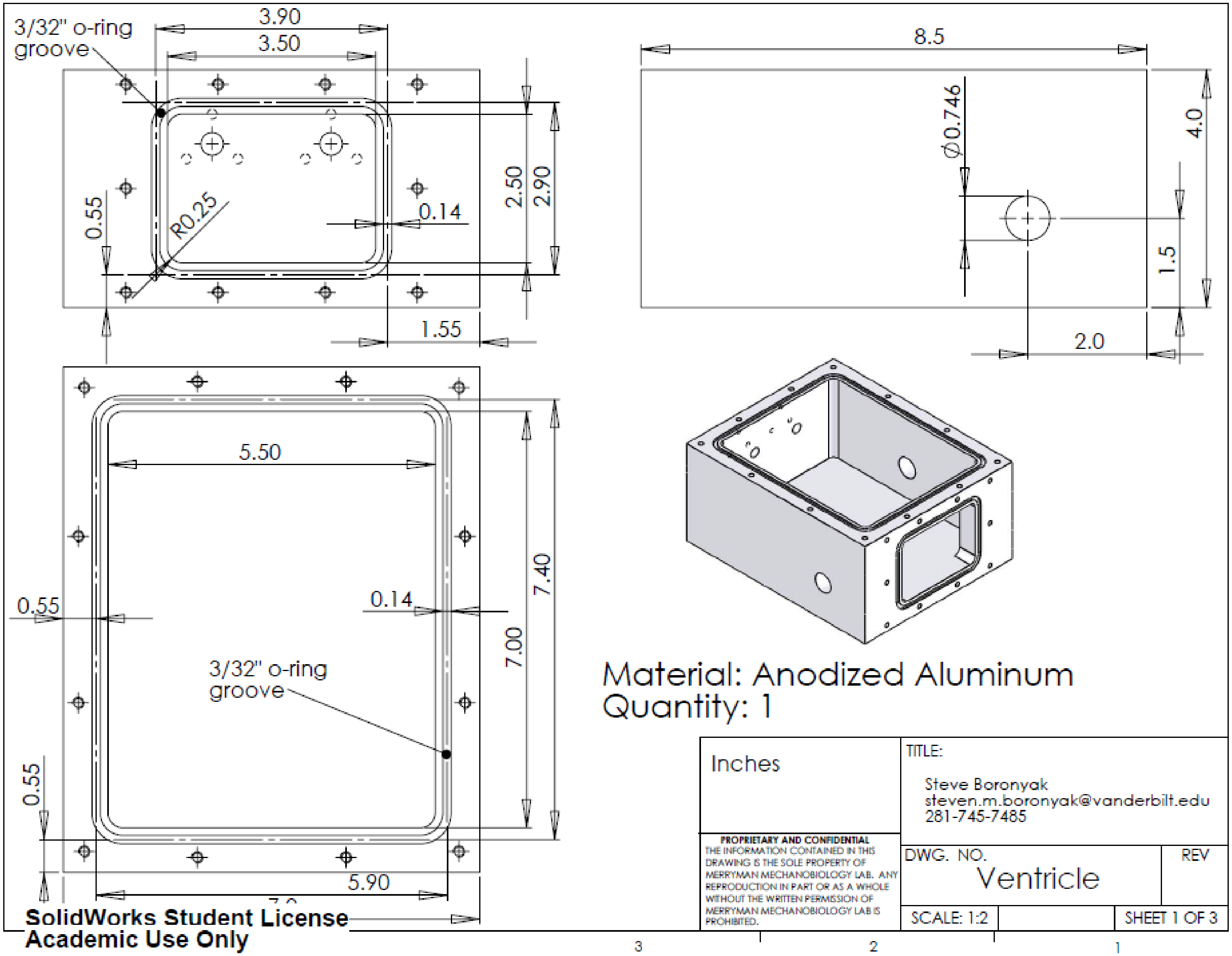
3/32" o-ring groove
3.90
3.50
0.55
R0.25
0.14
2.50
2.90
1.55
8.5
Ø0.746
4.0
1.5
2.0
5.50
0.55
0.14
7.40
7.00
3/32" o-ring groove
0.55
5.90
SolidWorks Student License
Academic Use Only
Material: Anodized Aluminum
Quantity: 1
Inches
PROPRIETARY AND CONFIDENTIAL
THE INFORMATION CONTAINED IN THIS DRAWING IS THE SOLE PROPERTY OF MERRYMAN MECHANOBIOLOGY LAB. ANY REPRODUCTION IN PART OR AS A WHOLE WITHOUT THE WRITTEN PERMISSION OF MERRYMAN MECHANOBIOLOGY LAB IS PROHIBITED.
TITLE:
Steve Boronyak
steven.m.boronyak@vanderbilt.edu
281-745-7485
DWG. NO.
Ventricle
REV
SCALE: 1:2
SHEET 1 OF 3
3
2
1

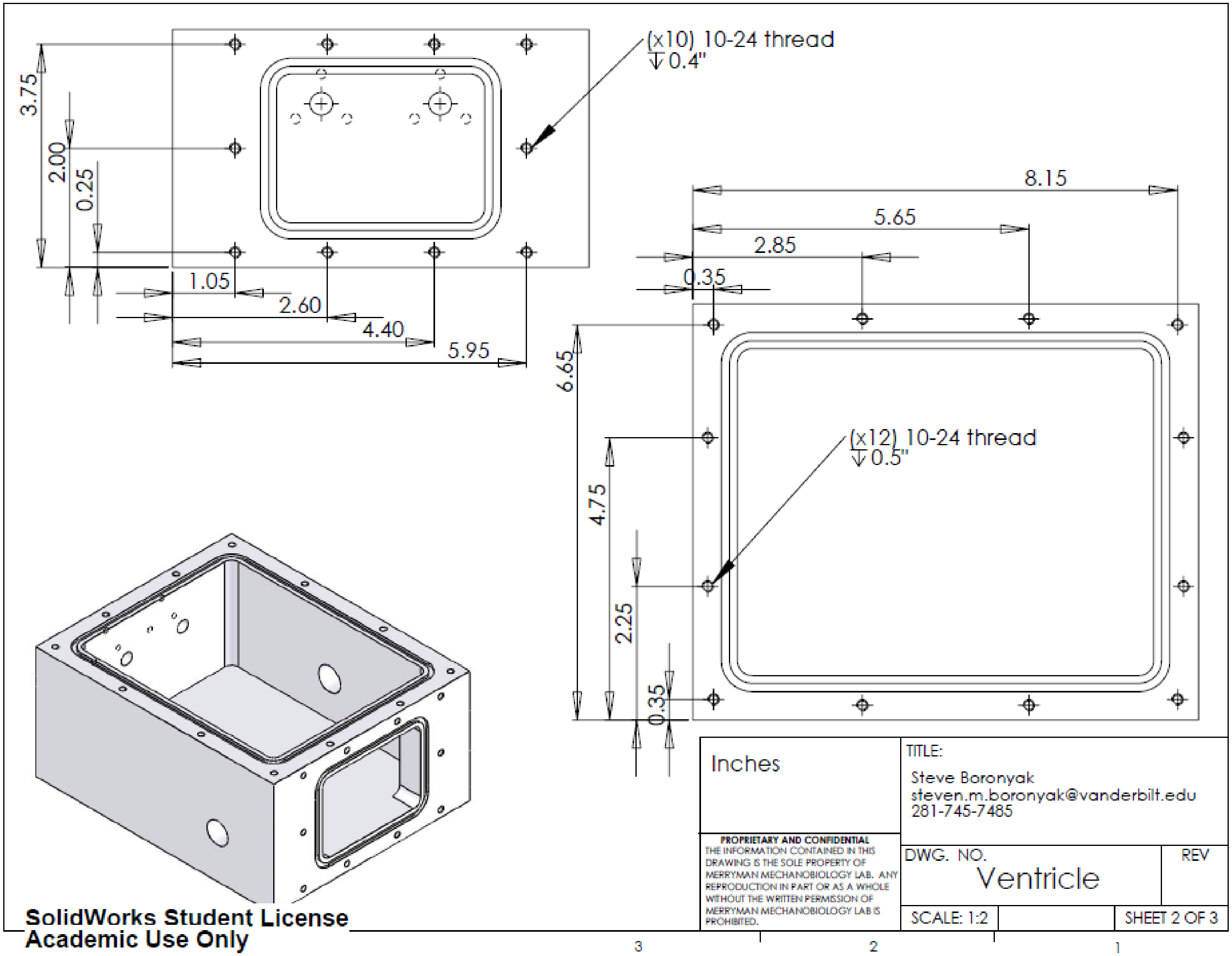
(x10) 10-24 thread
↧0.4"
3.75
2.00
0.25
1.05
2.60
4.40
5.95
8.15
5.65
2.85
0.35
6.65
(x12) 10-24 thread
↧0.5"
4.75
2.25
0.35
Inches
PROPRIETARY AND CONFIDENTIAL
THE INFORMATION CONTAINED IN THIS DRAWING IS THE SOLE PROPERTY OF MERRYMAN MECHANOBIOLOGY LAB. ANY REPRODUCTION IN PART OR AS A WHOLE WITHOUT THE WRITTEN PERMISSION OF MERRYMAN MECHANOBIOLOGY LAB IS PROHIBITED.
TITLE:
Steve Boronyak
steven.m.boronyak@vanderbilt.edu
281-745-7485
DWG. NO.
Ventricle
REV
SCALE: 1:2
SHEET 2 OF 3
3
2
1
SolidWorks Student License
Academic Use Only

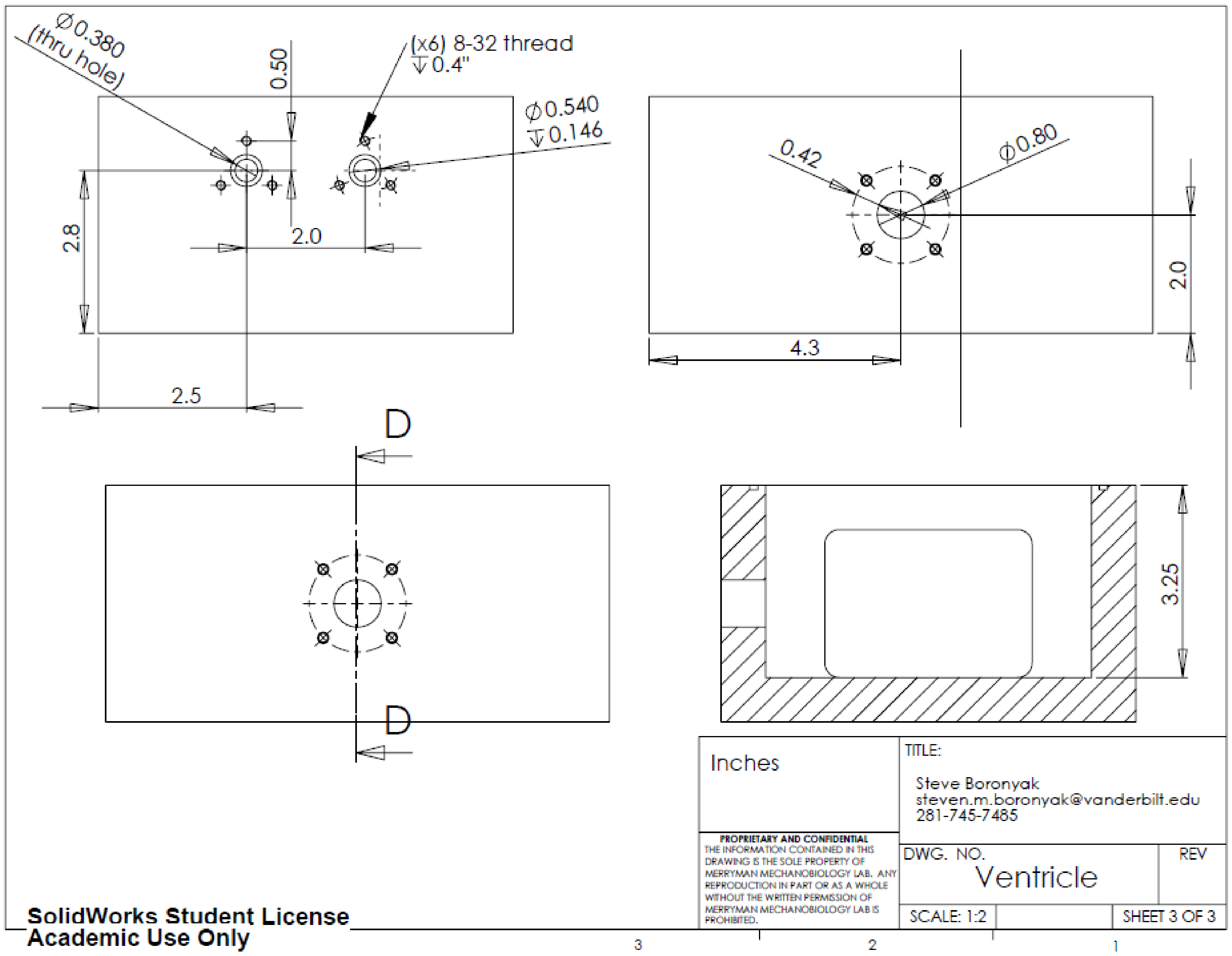
Ø0.380
(thru hole)
0.50
(x6) 8-32 thread
↧0.4"
Ø0.540
↧0.146
2.8
2.0
2.5
0.42
ϕ0.80
2.0
4.3
D
D
3.25
Inches
PROPRIETARY AND CONFIDENTIAL
THE INFORMATION CONTAINED IN THIS DRAWING IS THE SOLE PROPERTY OF MERRYMAN MECHANOBIOLOGY LAB. ANY REPRODUCTION IN PART OR AS A WHOLE WITHOUT THE WRITTEN PERMISSION OF MERRYMAN MECHANOBIOLOGY LAB IS PROHIBITED.
TITLE:
Steve Boronyak
steven.m.boronyak@vanderbilt.edu
281-745-7485
DWG. NO.
Ventricle
REV
SCALE: 1:2
SHEET 3 OF 3
3
2
1
SolidWorks Student License
Academic Use Only

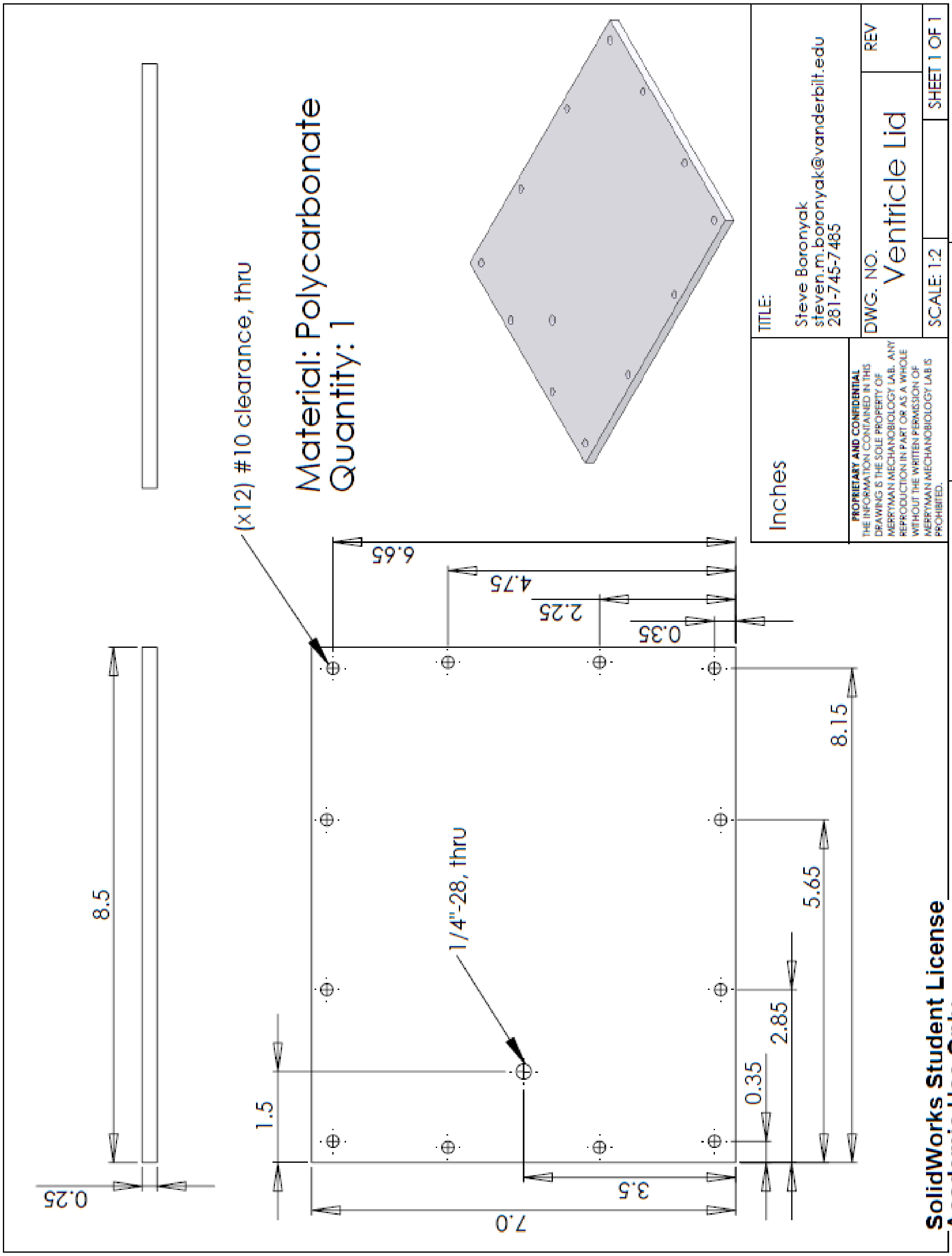
(x12) #10 clearance, thru
Material: Polycarbonate
Quantity: 1
1/4"-28, thru
8.5
0.25
1.5
3.5
7.0
0.35
2.85
5.65
8.15
6.65
4.75
2.25
0.35
Inches
PROPRIETARY AND CONFIDENTIAL
THE INFORMATION CONTAINED IN THIS DRAWING IS THE SOLE PROPERTY OF MERRYMAN MECHANOBIOLOGY LAB. ANY REPRODUCTION IN PART OR AS A WHOLE WITHOUT THE WRITTEN PERMISSION OF MERRYMAN MECHANOBIOLOGY LAB IS PROHIBITED.
TITLE:
Steve Boronyak
steven.m.boronyak@vanderbilt.edu
281-745-7485
DWG. NO.
Ventricle Lid
REV
SCALE: 1:2
SHEET 1 OF 1
1
2
3
SolidWorks Student License
Academic Use Only

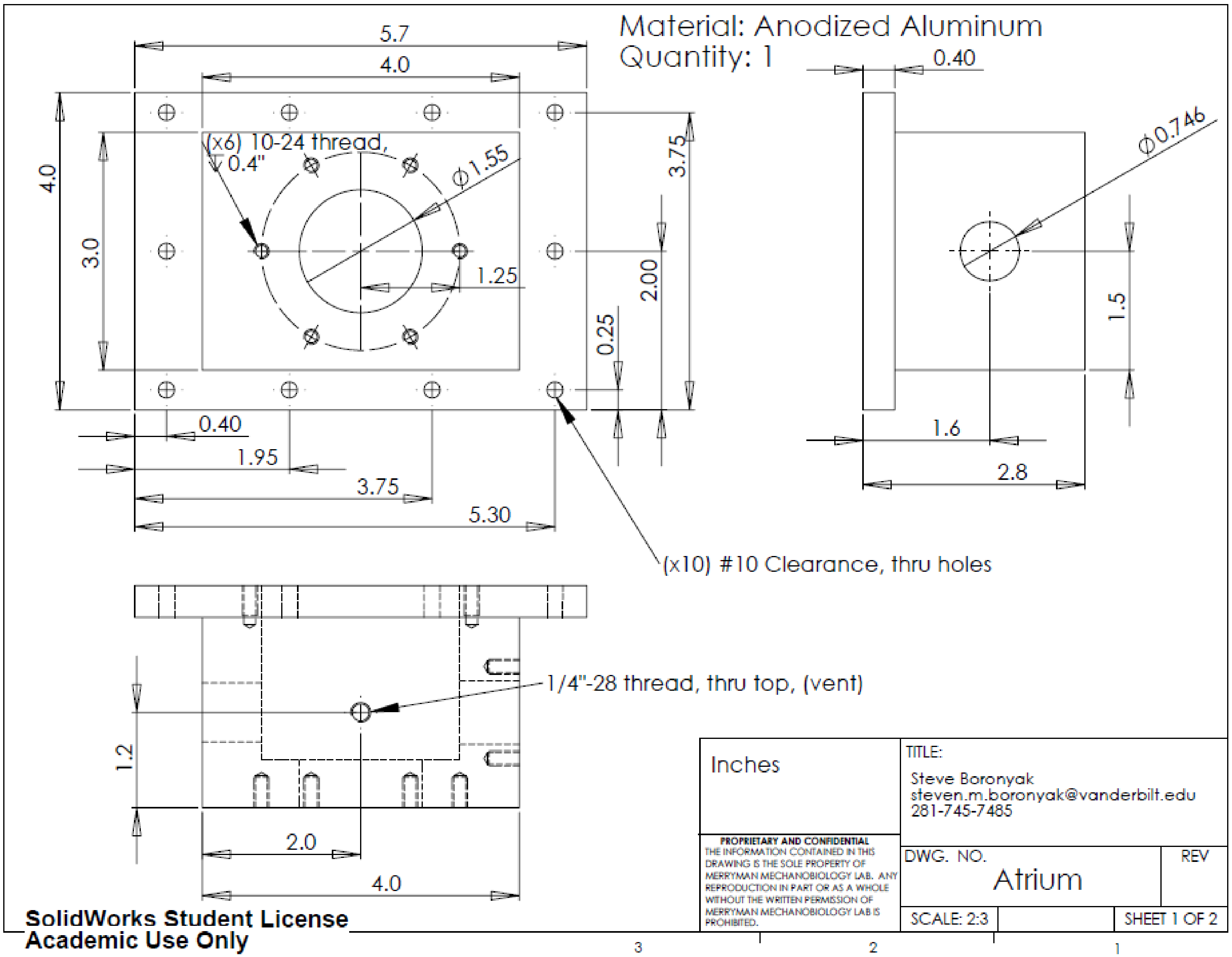
Material: Anodized Aluminum
Quantity: 1
5.7
4.0
4.0
3.0
(x6) 10-24 thread,
↧0.4"
ϕ1.55
1.25
3.75
2.00
0.25
0.40
1.95
3.75
5.30
(x10) #10 Clearance, thru holes
0.40
ϕ0.746
1.5
1.6
2.8
1/4"-28 thread, thru top, (vent)
1.2
2.0
4.0
Inches
PROPRIETARY AND CONFIDENTIAL
THE INFORMATION CONTAINED IN THIS DRAWING IS THE SOLE PROPERTY OF MERRYMAN MECHANOBIOLOGY LAB. ANY REPRODUCTION IN PART OR AS A WHOLE WITHOUT THE WRITTEN PERMISSION OF MERRYMAN MECHANOBIOLOGY LAB IS PROHIBITED.
TITLE:
Steve Boronyak
steven.m.boronyak@vanderbilt.edu
281-745-7485
DWG. NO.
Atrium
REV
SCALE: 2:3
SHEET 1 OF 2
SolidWorks Student License
Academic Use Only
3
2
1

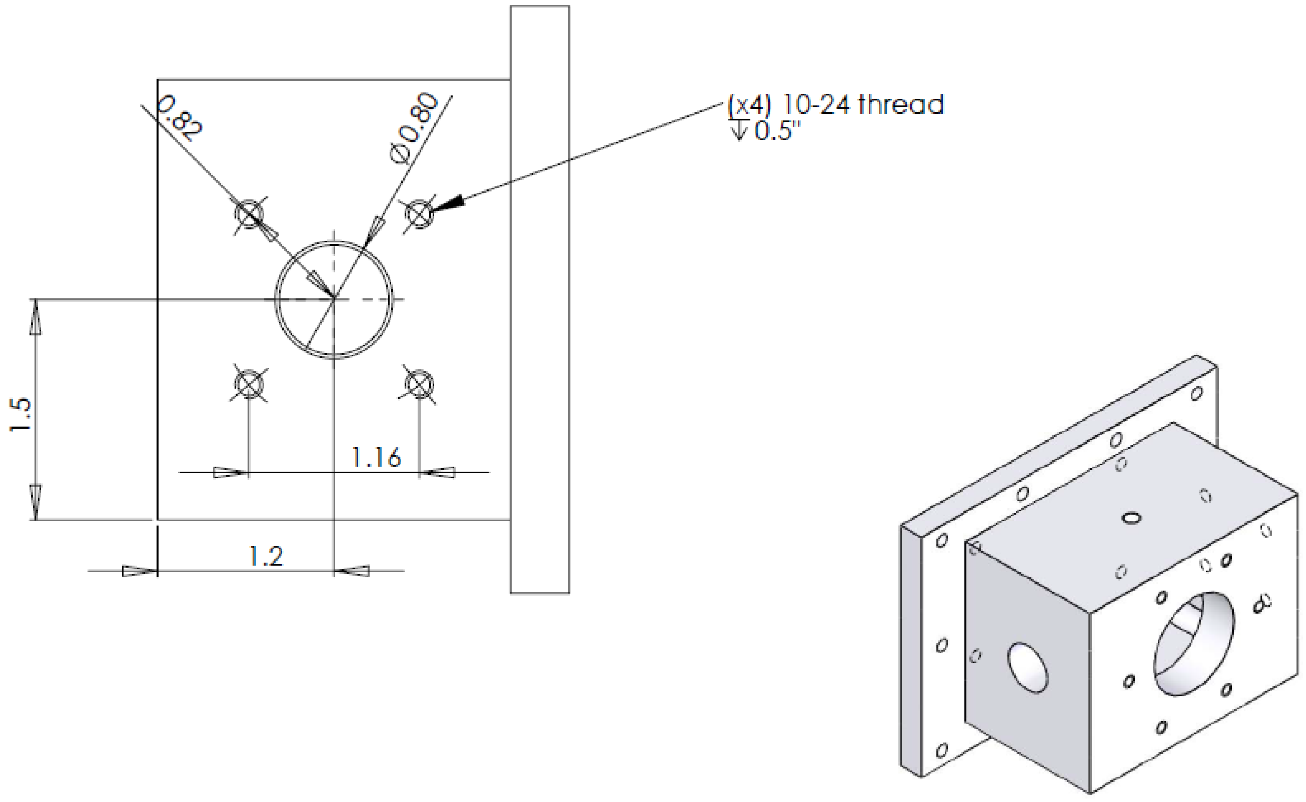

Inches

PROPRIETARY AND CONFIDENTIAL
THE INFORMATION CONTAINED IN THIS DRAWING IS THE SOLE PROPERTY OF MERRYMAN MECHANOBIOLOGY LAB. ANY REPRODUCTION IN PART OR AS A WHOLE WITHOUT THE WRITTEN PERMISSION OF MERRYMAN MECHANOBIOLOGY LAB IS PROHIBITED.

TITLE:

Steve Boronyak
steven.m.boronyak@vanderbilt.edu
281-745-7485

DWG. NO. Atrium

REV

SCALE: 1:2

SHEET 2 OF 2

3 2 1

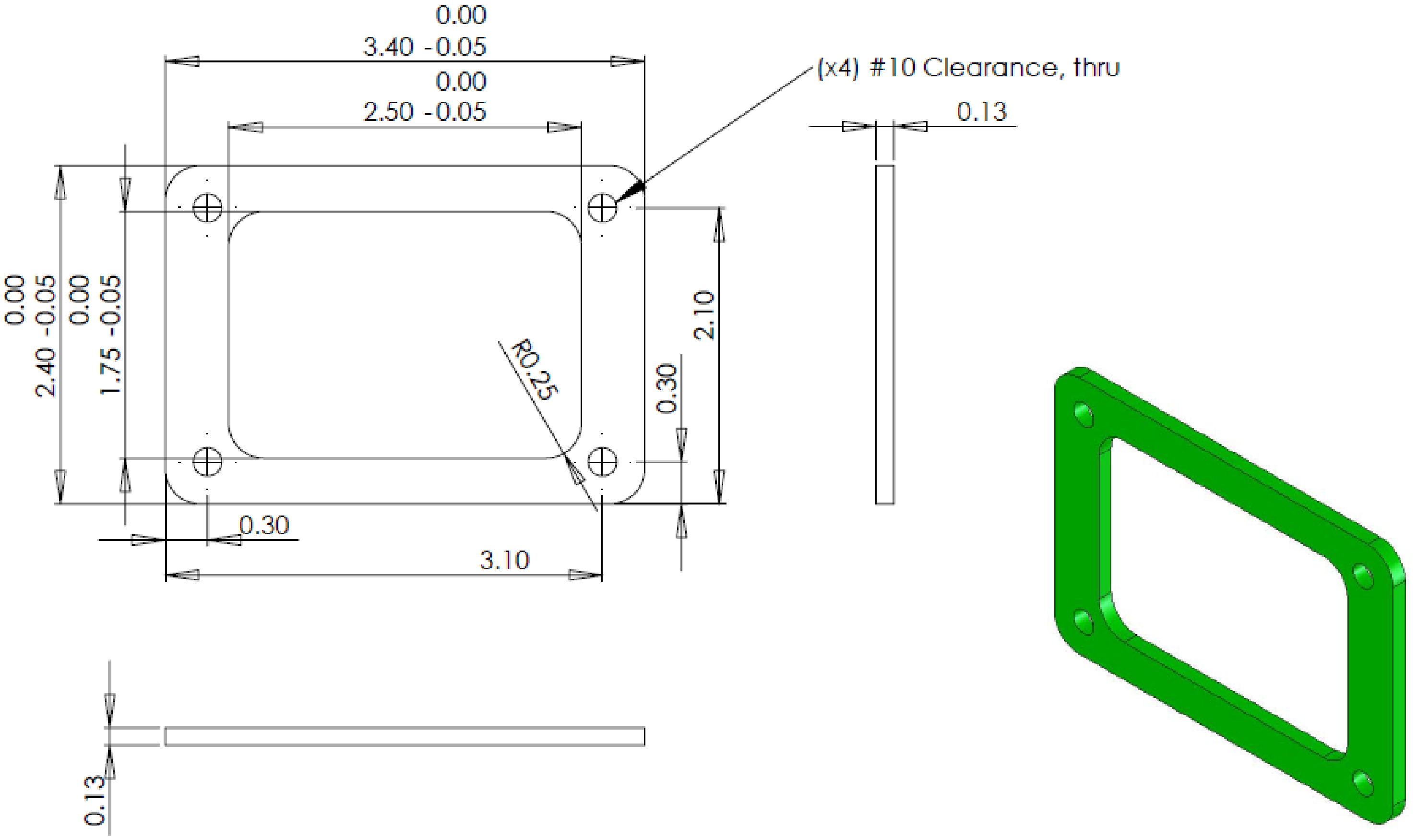

Material: 1/8" Delrin
Quantity: 1

Inches

PROPRIETARY AND CONFIDENTIAL
THE INFORMATION CONTAINED IN THIS DRAWING IS THE SOLE PROPERTY OF MERRYMAN MECHANOBIOLOGY LAB. ANY REPRODUCTION IN PART OR AS A WHOLE WITHOUT THE WRITTEN PERMISSION OF MERRYMAN MECHANOBIOLOGY LAB IS PROHIBITED.

TITLE:
Steve Boronyak
steven.m.boronyak@vanderbilt.edu
281-745-7485

DWG. NO.
Atrium Flange

REV

SCALE: 1:1

SHEET 1 OF 1

3
2
1

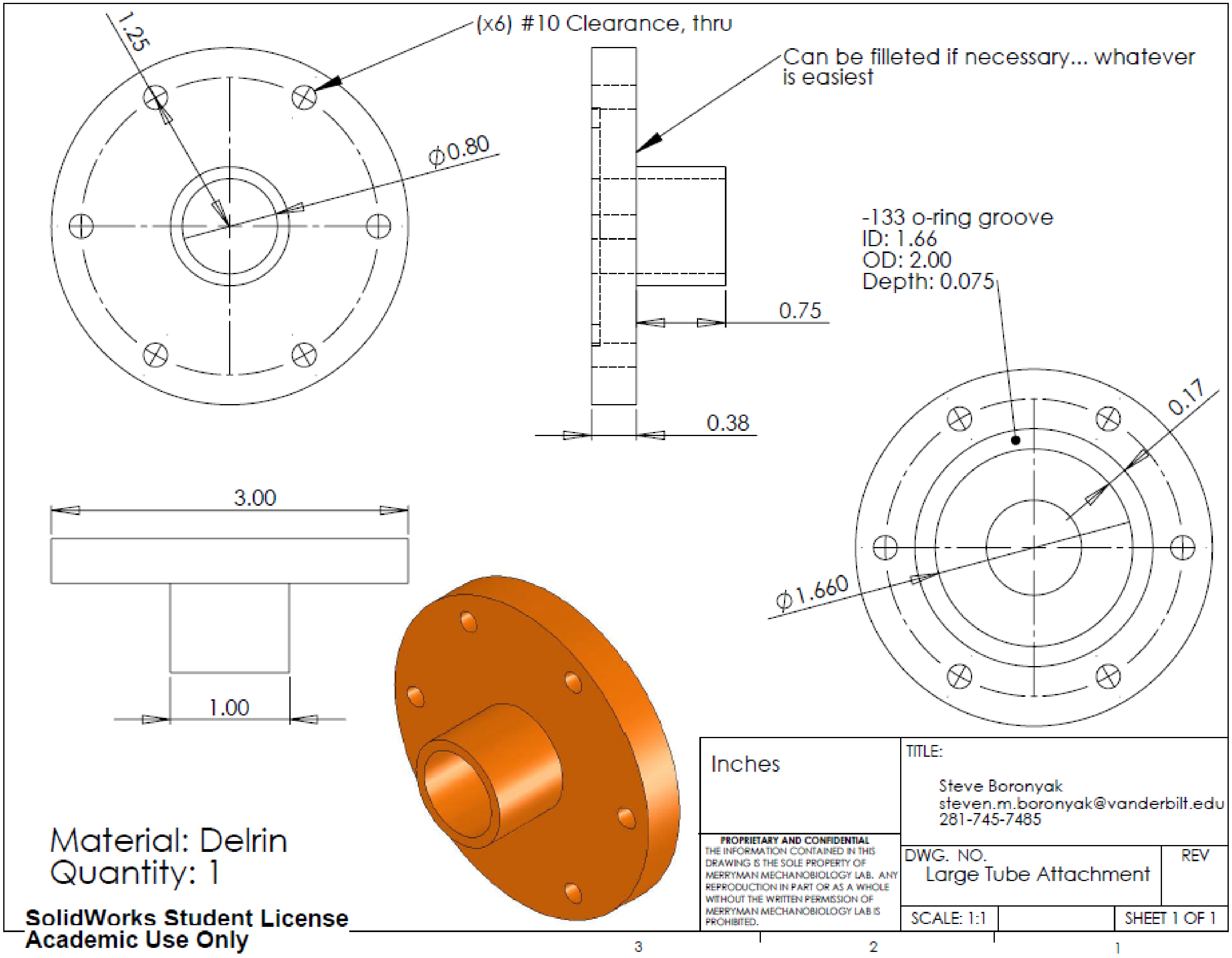
(x6) #10 Clearance, thru
1.25
ϕ0.80
Can be filleted if necessary... whatever is easiest
0.75
0.38
-133 o-ring groove
ID: 1.66
OD: 2.00
Depth: 0.075
0.17
ϕ1.660
3.00
1.00
Material: Delrin
Quantity: 1
SolidWorks Student License
Academic Use Only
Inches
PROPRIETARY AND CONFIDENTIAL
THE INFORMATION CONTAINED IN THIS DRAWING IS THE SOLE PROPERTY OF MERRYMAN MECHANOBIOLOGY LAB. ANY REPRODUCTION IN PART OR AS A WHOLE WITHOUT THE WRITTEN PERMISSION OF MERRYMAN MECHANOBIOLOGY LAB IS PROHIBITED.
TITLE:
Steve Boronyak
steven.m.boronyak@vanderbilt.edu
281-745-7485
DWG. NO.
Large Tube Attachment
REV
SCALE: 1:1
SHEET 1 OF 1
3
2
1

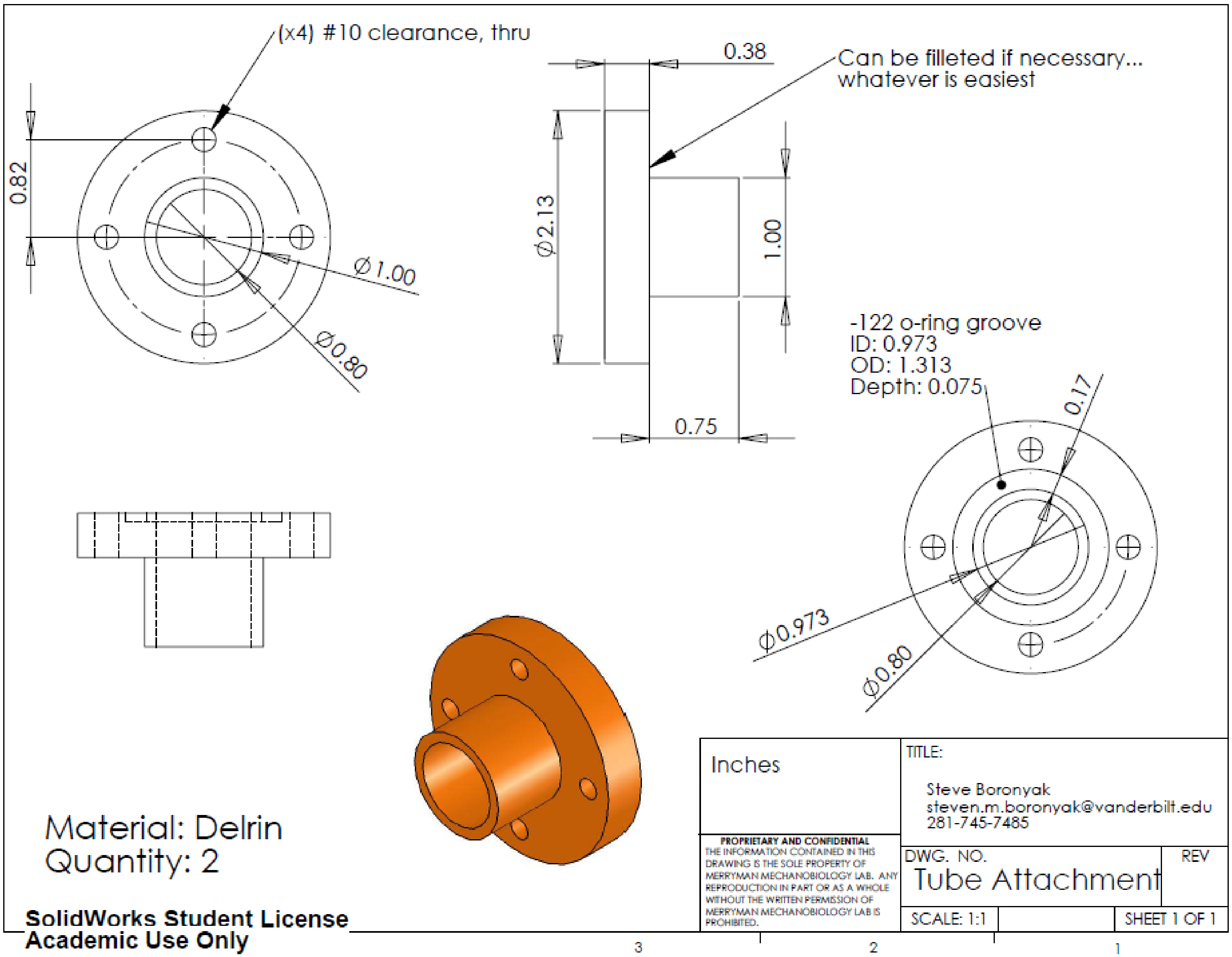
(x4) #10 clearance, thru
0.82
∅1.00
∅0.80
0.38
∅2.13
1.00
0.75
Can be filleted if necessary...
whatever is easiest
-122 o-ring groove
ID: 0.973
OD: 1.313
Depth: 0.075
0.17
∅0.973
∅0.80
Material: Delrin
Quantity: 2
SolidWorks Student License
Academic Use Only
Inches
PROPRIETARY AND CONFIDENTIAL
THE INFORMATION CONTAINED IN THIS DRAWING IS THE SOLE PROPERTY OF MERRYMAN MECHANOBIOLOGY LAB. ANY REPRODUCTION IN PART OR AS A WHOLE WITHOUT THE WRITTEN PERMISSION OF MERRYMAN MECHANOBIOLOGY LAB IS PROHIBITED.
TITLE:
Steve Boronyak
steven.m.boronyak@vanderbilt.edu
281-745-7485
DWG. NO.
Tube Attachment
REV
SCALE: 1:1
SHEET 1 OF 1
3
2
1

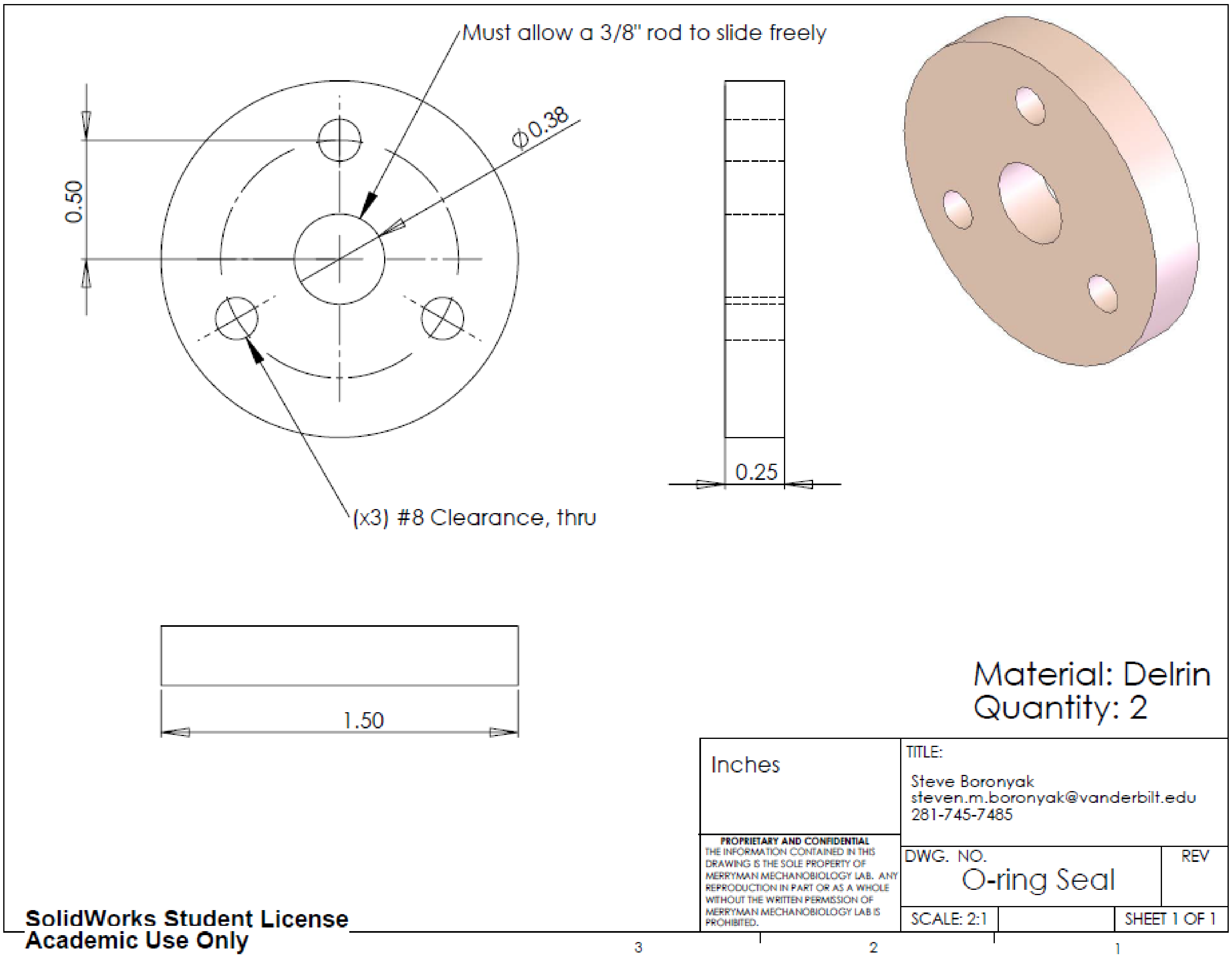
Must allow a 3/8" rod to slide freely
Ø0.38
0.50
(x3) #8 Clearance, thru
0.25
1.50
Material: Delrin
Quantity: 2
Inches
PROPRIETARY AND CONFIDENTIAL
THE INFORMATION CONTAINED IN THIS DRAWING IS THE SOLE PROPERTY OF MERRYMAN MECHANOBIOLOGY LAB. ANY REPRODUCTION IN PART OR AS A WHOLE WITHOUT THE WRITTEN PERMISSION OF MERRYMAN MECHANOBIOLOGY LAB IS PROHIBITED.
TITLE:
Steve Boronyak
steven.m.boronyak@vanderbilt.edu
281-745-7485
DWG. NO.
O-ring Seal
REV
SCALE: 2:1
SHEET 1 OF 1
SolidWorks Student License
Academic Use Only
3
2
1

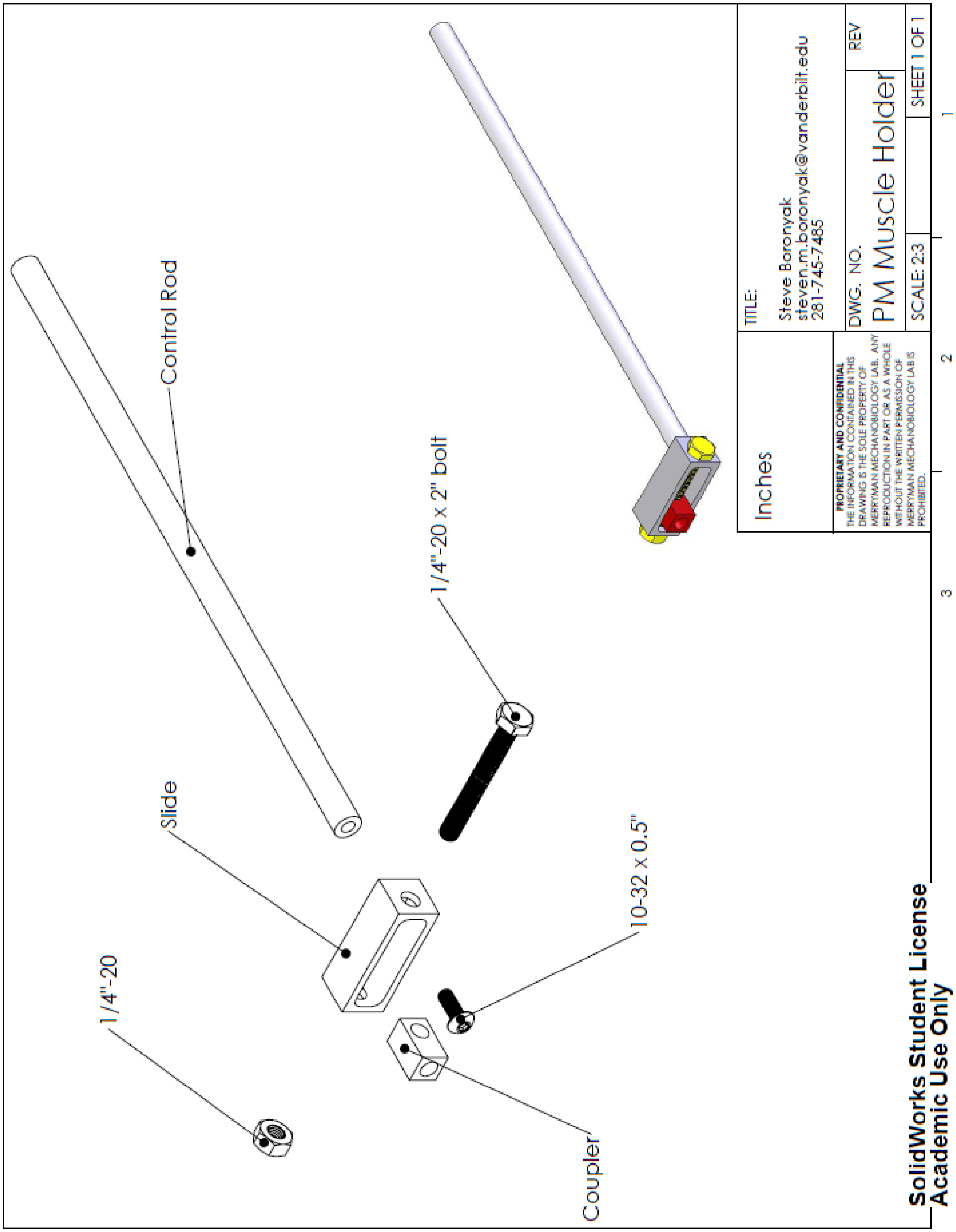
Coupler
1/4"-20
Slide
10-32 x 0.5"
Control Rod
1/4"-20 x 2" bolt
Inches
TITLE:
Steve Boronyak
steven.m.boronyak@vanderbilt.edu
281-745-7485
PROPRIETARY AND CONFIDENTIAL
THE INFORMATION CONTAINED IN THIS DRAWING IS THE SOLE PROPERTY OF MERRYMAN MECHANOBIOLOGY LAB. ANY REPRODUCTION IN PART OR AS A WHOLE WITHOUT THE WRITTEN PERMISSION OF MERRYMAN MECHANOBIOLOGY LAB IS PROHIBITED.
DWG. NO.
PM Muscle Holder
REV
SCALE: 2:3
SHEET 1 OF 1
3
2
1
SolidWorks Student License
Academic Use Only

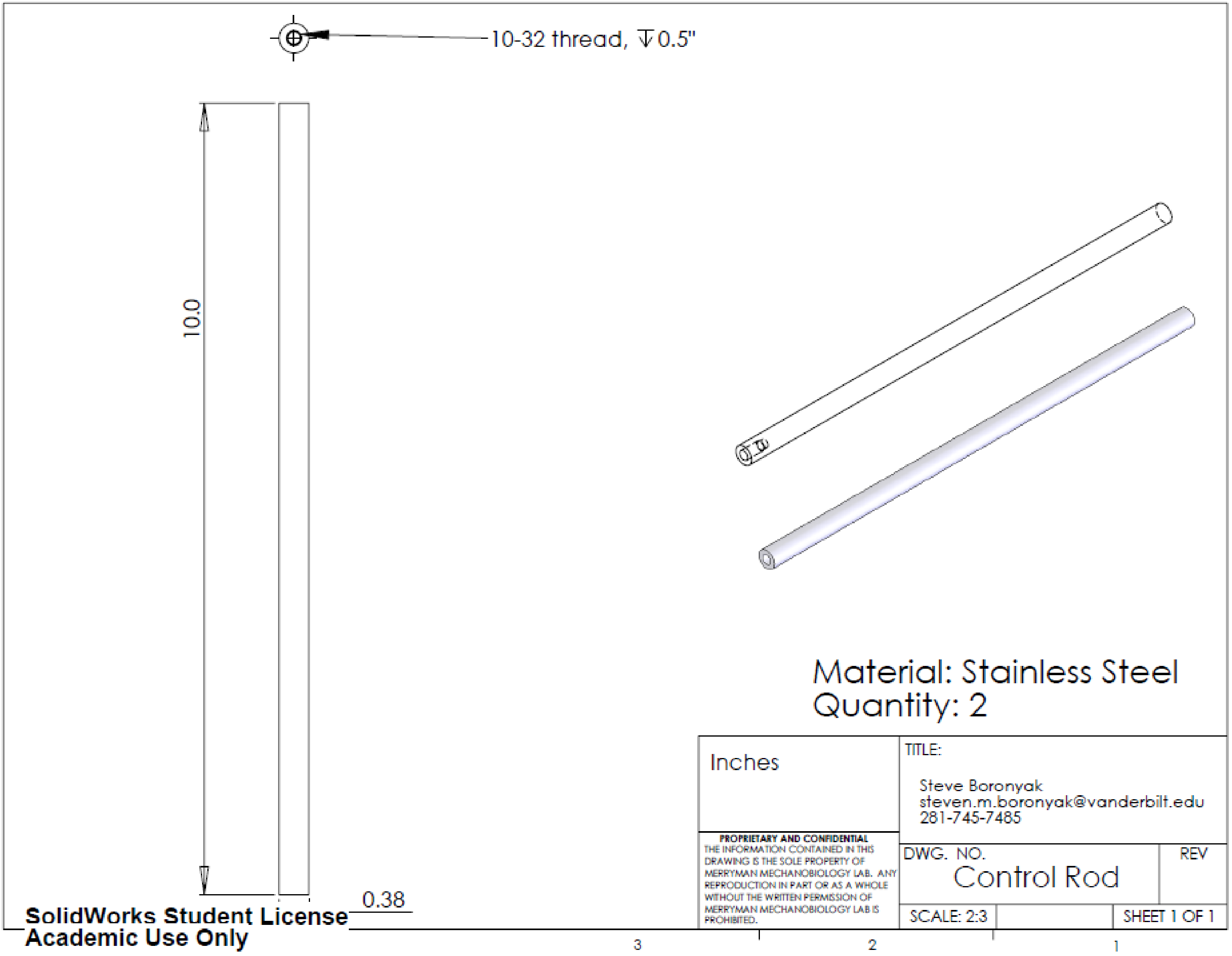

Material: Stainless Steel
Quantity: 2

Inches	TITLE: Steve Boronyak steven.m.boronyak@vanderbilt.edu 281-745-7485
PROPRIETARY AND CONFIDENTIAL THE INFORMATION CONTAINED IN THIS DRAWING IS THE SOLE PROPERTY OF MERRYMAN MECHANOBIOLOGY LAB. ANY REPRODUCTION IN PART OR AS A WHOLE WITHOUT THE WRITTEN PERMISSION OF MERRYMAN MECHANOBIOLOGY LAB IS PROHIBITED.	DWG. NO. Control Rod REV SCALE: 2:3 SHEET 1 OF 1

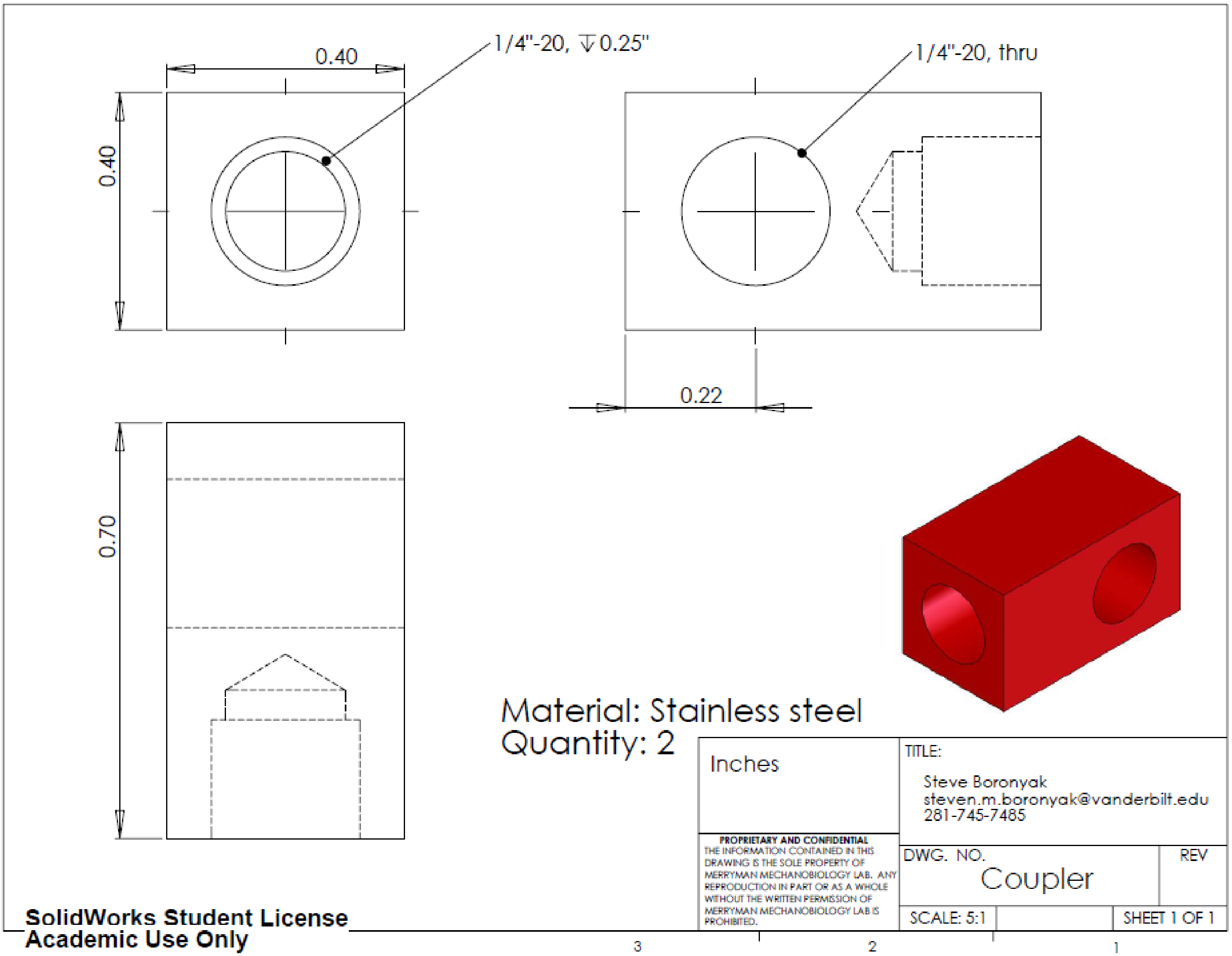
0.40
1/4"-20, ↧0.25"
1/4"-20, thru
0.40
0.22
0.70
Material: Stainless steel
Quantity: 2
Inches
PROPRIETARY AND CONFIDENTIAL
THE INFORMATION CONTAINED IN THIS DRAWING IS THE SOLE PROPERTY OF MERRYMAN MECHANOBIOLOGY LAB. ANY REPRODUCTION IN PART OR AS A WHOLE WITHOUT THE WRITTEN PERMISSION OF MERRYMAN MECHANOBIOLOGY LAB IS PROHIBITED.
TITLE:
Steve Boronyak
steven.m.boronyak@vanderbilt.edu
281-745-7485
DWG. NO.
Coupler
REV
SCALE: 5:1
SHEET 1 OF 1
SolidWorks Student License
Academic Use Only
3
2
1

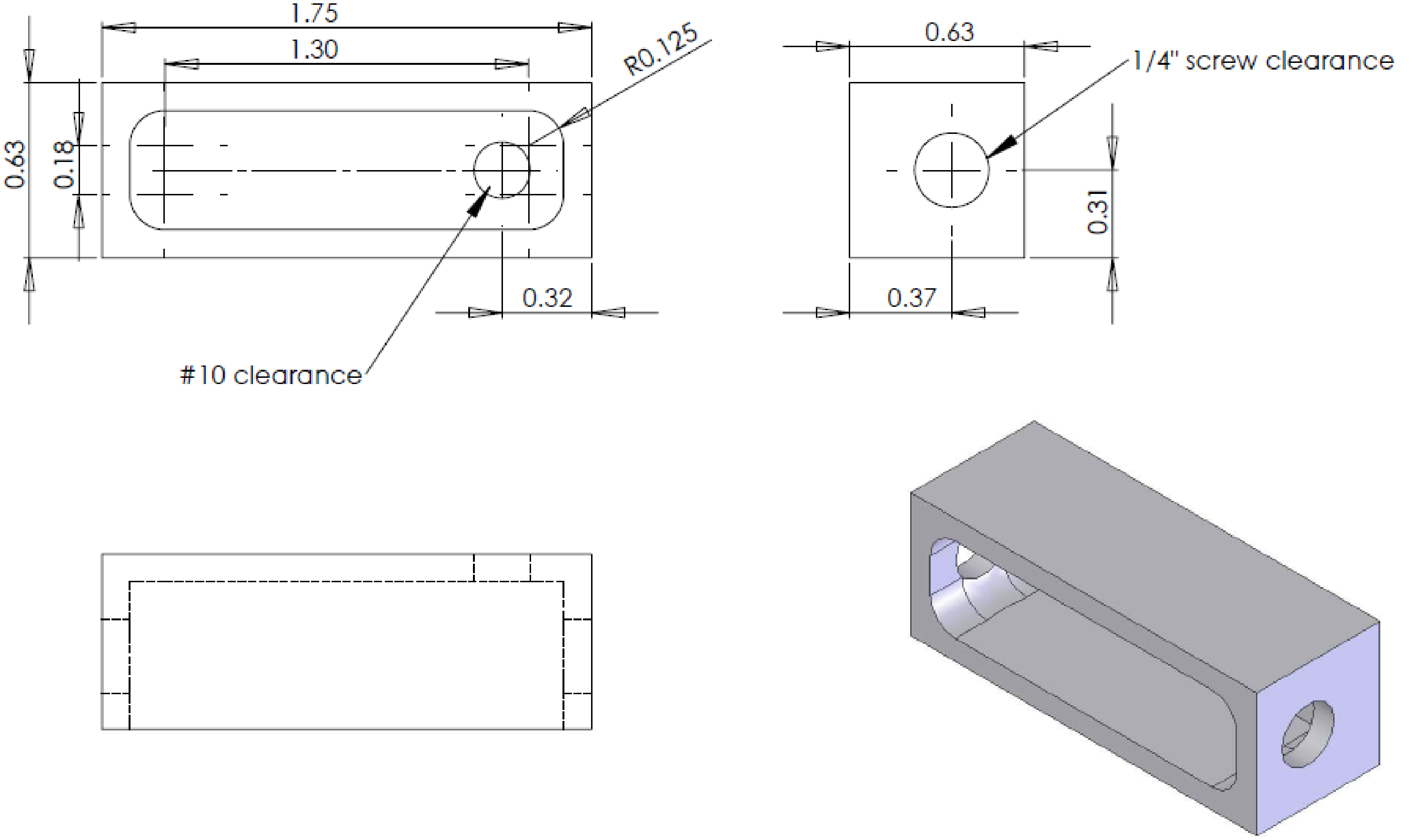

Material: Anodized Aluminum
Quantity: 2

Inches

TITLE:

Steve Boronyak
steven.m.boronyak@vanderbilt.edu
281-745-7485

DWG. NO.
Slide
REV
SCALE: 2:1
SHEET 1 OF 1

3
2
1

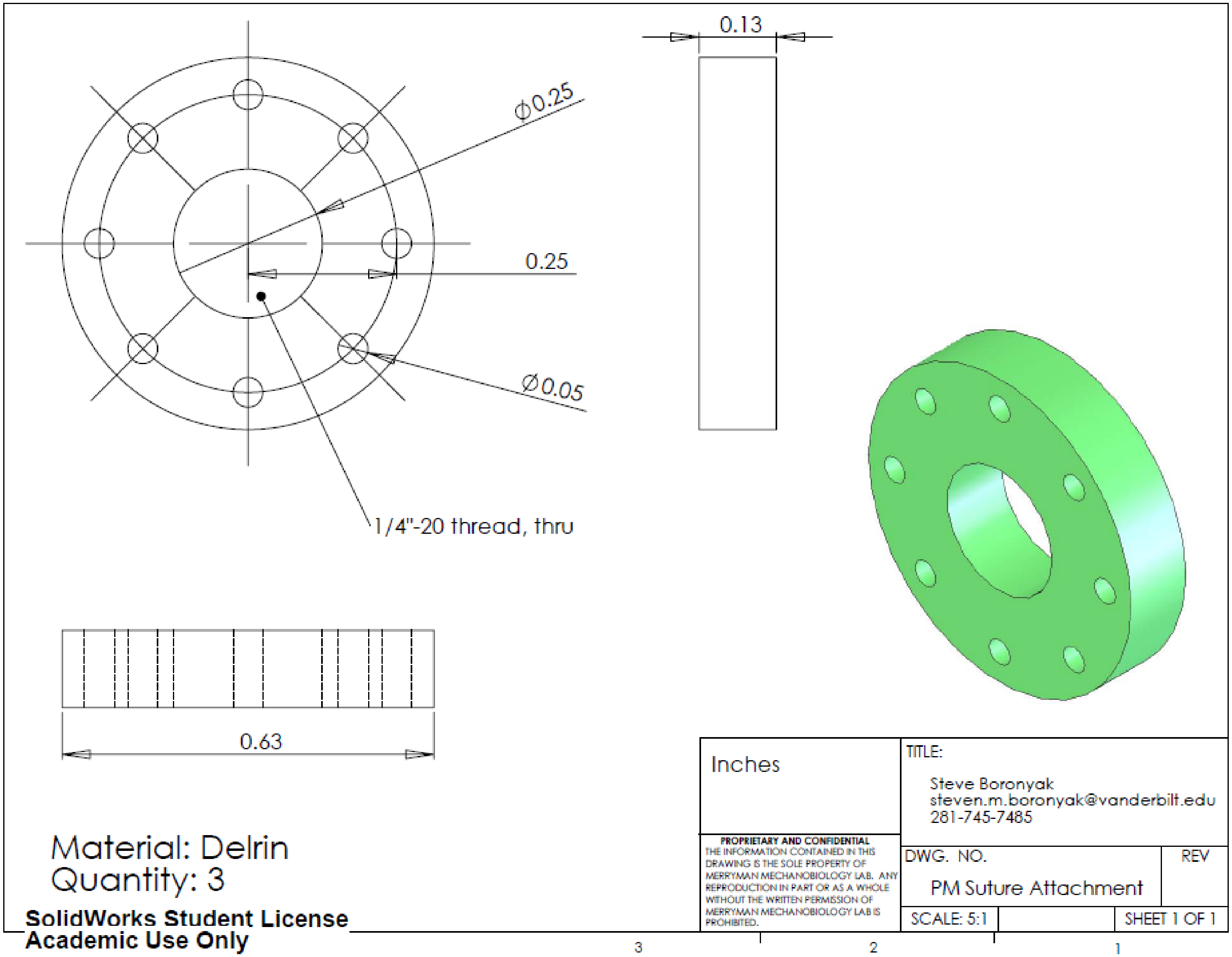

Material: Delrin
Quantity: 3

Inches

TITLE:
Steve Boronyak
steven.m.boronyak@vanderbilt.edu
281-745-7485

DWG. NO.
PM Suture Attachment

REV

SCALE: 5:1

SHEET 1 OF 1

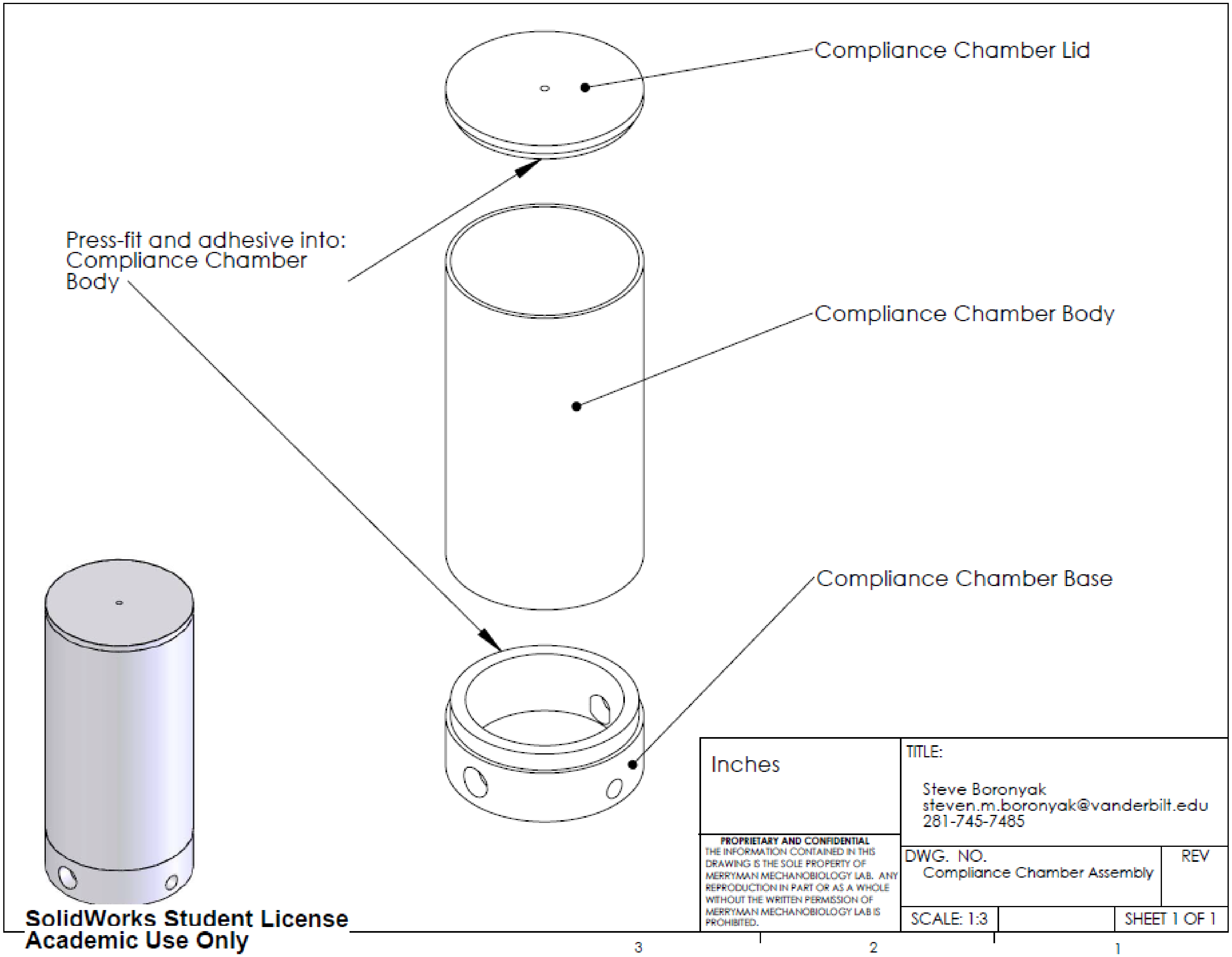
Compliance Chamber Lid
Press-fit and adhesive into: Compliance Chamber Body
Compliance Chamber Body
Compliance Chamber Base
Inches
PROPRIETARY AND CONFIDENTIAL
THE INFORMATION CONTAINED IN THIS DRAWING IS THE SOLE PROPERTY OF MERRYMAN MECHANOBIOLOGY LAB. ANY REPRODUCTION IN PART OR AS A WHOLE WITHOUT THE WRITTEN PERMISSION OF MERRYMAN MECHANOBIOLOGY LAB IS PROHIBITED.
TITLE:
Steve Boronyak
steven.m.boronyak@vanderbilt.edu
281-745-7485
DWG. NO.
Compliance Chamber Assembly
REV
SCALE: 1:3
SHEET 1 OF 1
SolidWorks Student License
Academic Use Only
3
2
1

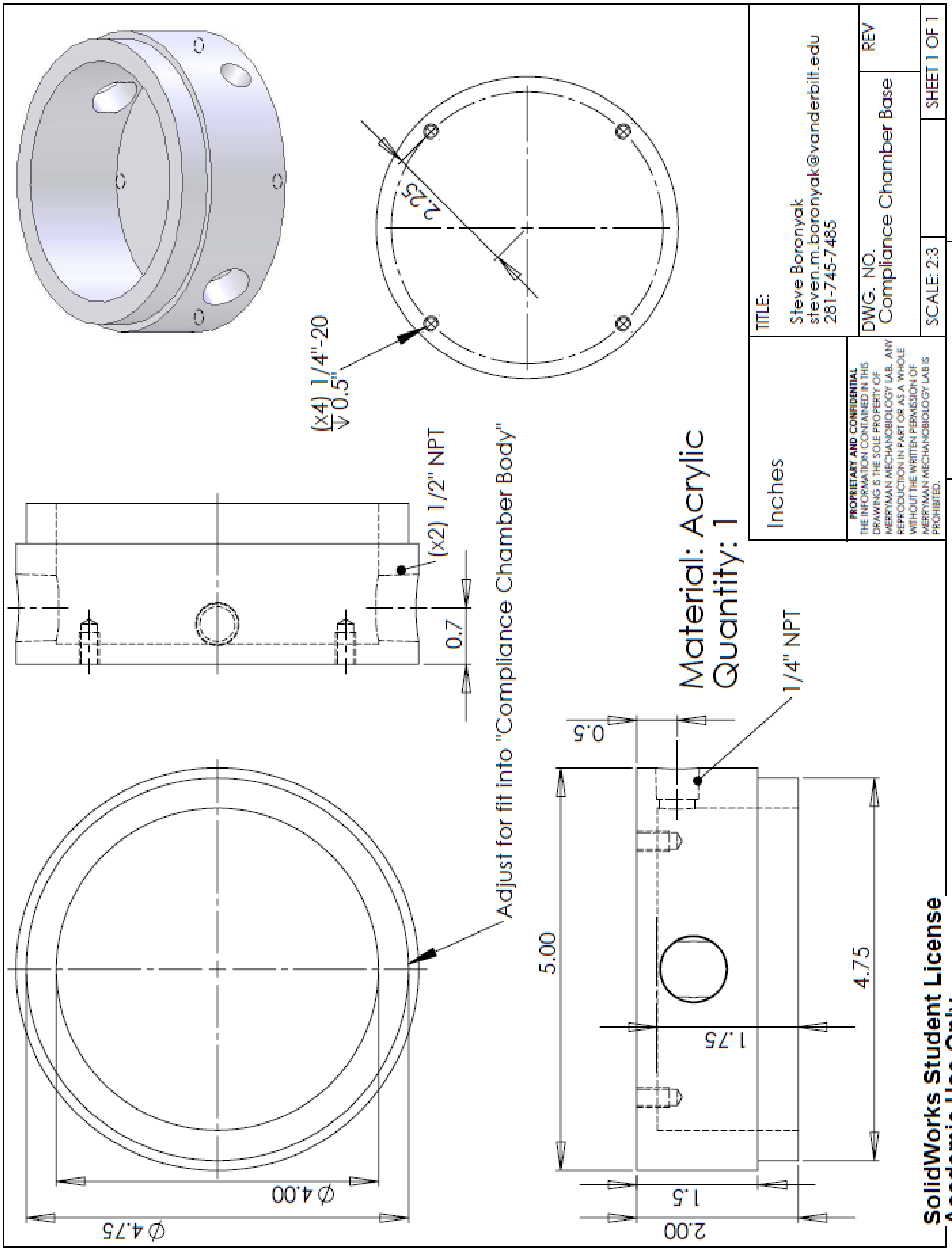TITLE:
Steve Boronyak
steven.m.boronyak@vanderbilt.edu
281-745-7485
DWG. NO.
Compliance Chamber Base
REV
SCALE: 2:3
SHEET 1 OF 1
Inches
PROPRIETARY AND CONFIDENTIAL
THE INFORMATION CONTAINED IN THIS DRAWING IS THE SOLE PROPERTY OF MERRYMAN MECHANOBIOLOGY LAB. ANY REPRODUCTION IN PART OR AS A WHOLE WITHOUT THE WRITTEN PERMISSION OF MERRYMAN MECHANOBIOLOGY LAB IS PROHIBITED.
Material: Acrylic
Quantity: 1
(x4) 1/4"-20
↧ 0.5"
2.25
(x2) 1/2" NPT
0.7
Adjust for fit into "Compliance Chamber Body"
1/4" NPT
0.5
5.00
4.75
1.75
1.5
2.00
Ø4.00
Ø4.75
SolidWorks Student License
Academic Use Only
1
2
3

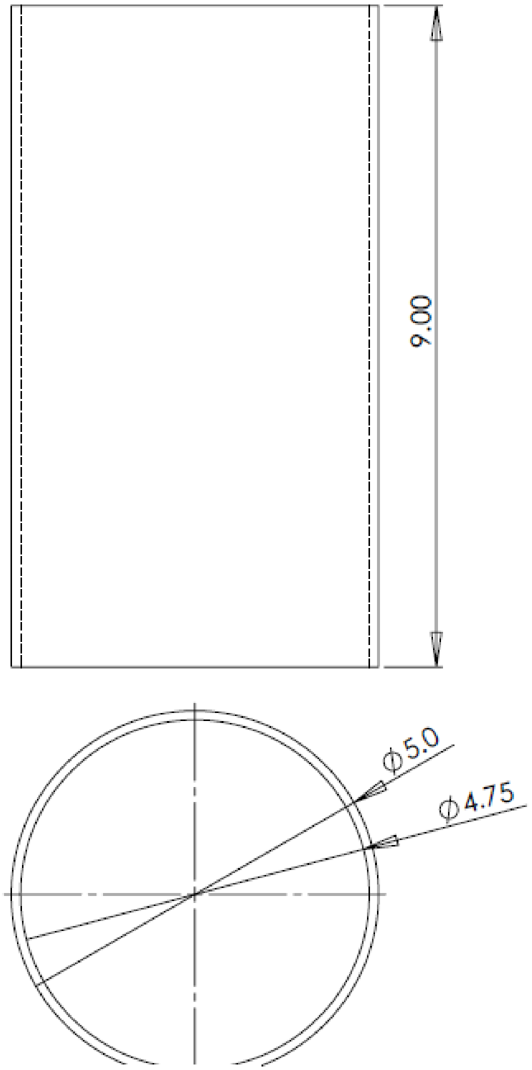

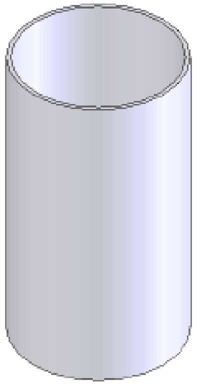

Both "Compliance Chamber Base" and "Compliance Chamber Lid" need to fit into this part

Material: Acrylic
Quantity: 1

Inches

PROPRIETARY AND CONFIDENTIAL
THE INFORMATION CONTAINED IN THIS DRAWING IS THE SOLE PROPERTY OF MERRYMAN MECHANOBIOLOGY LAB. ANY REPRODUCTION IN PART OR AS A WHOLE WITHOUT THE WRITTEN PERMISSION OF MERRYMAN MECHANOBIOLOGY LAB IS PROHIBITED.

TITLE:

Steve Boronyak
steven.m.boronyak@vanderbilt.edu
281-745-7485

DWG. NO.
Compliance Chamber Body

REV

SCALE: 1:2

SHEET 1 OF 1

3 2 1

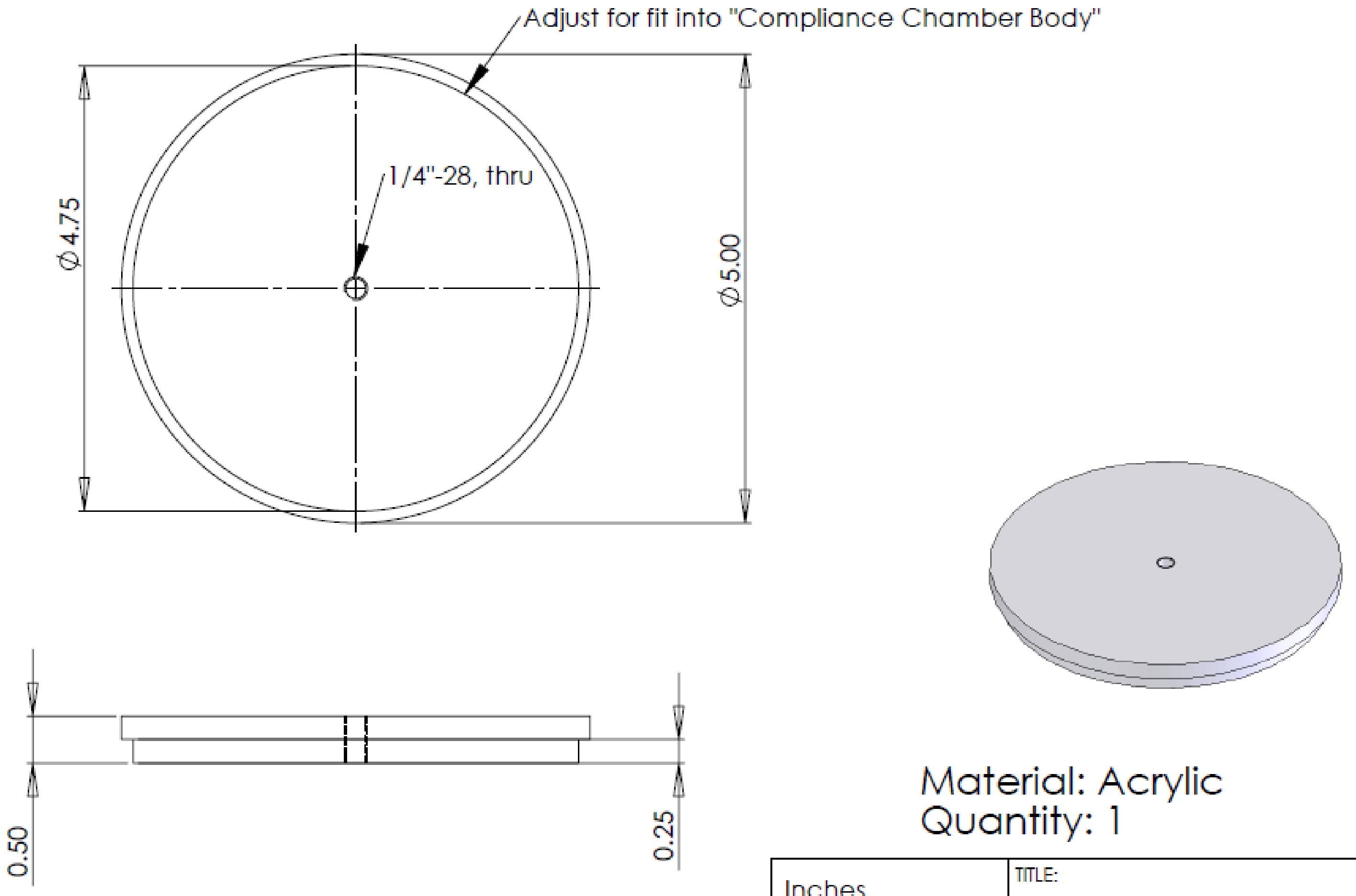

Material: Acrylic
Quantity: 1

Inches	TITLE: Steve Boronyak steven.m.boronyak@vanderbilt.edu 281-745-7485	
PROPRIETARY AND CONFIDENTIAL THE INFORMATION CONTAINED IN THIS DRAWING IS THE SOLE PROPERTY OF MERRYMAN MECHANOBIOLOGY LAB. ANY REPRODUCTION IN PART OR AS A WHOLE WITHOUT THE WRITTEN PERMISSION OF MERRYMAN MECHANOBIOLOGY LAB IS PROHIBITED.	DWG. NO. Compliance Chamber Lid	REV
	SCALE: 2:3	SHEET 1 OF 1

REFERENCES

[1] C. M. Otto, "Clinical practice. Evaluation and management of chronic mitral regurgitation," *N Engl J Med,* vol. 345, pp. 740-6, Sep 6 2001.

[2] E. Rabkin*, et al.*, "Activated interstitial myofibroblasts express catabolic enzymes and mediate matrix remodeling in myxomatous heart valves," *Circulation,* vol. 104, pp. 2525-32, Nov 20 2001.

[3] B. Lung*, et al.*, "A prospective survey of patients with valvular heart disease in Europe: The Euro Heart Survey on Valvular Heart Disease," *European Heart Journal,* vol. 24, pp. 1231-1243, Jul 2003.

[4] M. Mirabel*, et al.*, "What are the characteristics of patients with severe, symptomatic, mitral regurgitation who are denied surgery?," *Eur Heart J,* vol. 28, pp. 1358-65, Jun 2007.

[5] P. T. Chiam and C. E. Ruiz, "Percutaneous transcatheter mitral valve repair: a classification of the technology," *JACC Cardiovasc Interv,* vol. 4, pp. 1-13, Jan 2011.

[6] W. Flameng*, et al.*, "Durability of mitral valve repair in Barlow disease versus fibroelastic deficiency," *J Thorac Cardiovasc Surg,* vol. 135, pp. 274-82, Feb 2008.

[7] T. E. David, "Outcomes of mitral valve repair for mitral regurgitation due to degenerative disease," *Semin Thorac Cardiovasc Surg,* vol. 19, pp. 116-20, Summer 2007.

[8] S. M. Boronyak and W. D. Merryman, "The once and future state of percutaneous mitral valve repair," *Future Cardiol,* vol. 8, pp. 779-93, Sep 2012.

[9] S. Price*, et al.*, "Radiofrequency Ablation Directionally Alters Geometry and Biomechanical Compliance of Mitral Valve Leaflets: Refinement of a Novel Percutaneous Treatment Strategy," *Cardiovascular Engineering and Technology,* vol. 1, pp. 194-201, 2010.

[10] J. L. Williams*, et al.*, "Feasibility of myxomatous mitral valve repair using direct leaflet and chordal radiofrequency ablation," *J Interv Cardiol,* vol. 21, pp. 547-54, Dec 2008.

[11] S. M. Boronyak and W. D. Merryman, "Development of a simultaneous cryo-anchoring and radiofrequency ablation catheter for percutaneous treatment of mitral valve prolapse," *Ann Biomed Eng,* vol. 40, pp. 1971-81, Sep 2012.

[12] V. Fuster and J. W. Hurst, *Hurst's the Heart*, 11th ed. New York: McGraw-Hill, 2004.

[13] M. K. McAfee and H. V. Schaff, "Valve Repair for Mitral Insufficiency," *Cardiology,* vol. 20, pp. 35-43, 1990.

[14] B. H. Trichon*, et al.*, "Relation of frequency and severity of mitral regurgitation to survival among patients with left ventricular systolic dysfunction and heart failure," *Am J Cardiol,* vol. 91, pp. 538-43, Mar 1 2003.

[15] L. A. Freed*, et al.*, "Prevalence and clinical outcome of mitral-valve prolapse," *N Engl J Med,* vol. 341, pp. 1-7, Jul 1 1999.

[16] P. Libby and E. Braunwald, *Braunwald's heart disease : a textbook of cardiovascular medicine*, 8th ed. Philadelphia: Saunders/Elsevier, 2008.

[17] M. De Bonis, *et al.*, "Treatment and management of mitral regurgitation," *Nat Rev Cardiol,* vol. 9, pp. 133-46, Mar 2012.

[18] T. Feldman, *et al.*, "Percutaneous repair or surgery for mitral regurgitation," *N Engl J Med,* vol. 364, pp. 1395-406, Apr 14 2011.

[19] www.bioethics.gov, "The President's Council on Bioethics," p. 309, 2005.

[20] P. W. Fedak, *et al.*, "Evolving concepts and technologies in mitral valve repair," *Circulation,* vol. 117, pp. 963-74, Feb 19 2008.

[21] A. Hulin, *et al.*, "Emerging pathogenic mechanisms in human myxomatous mitral valve: lessons from past and novel data," *Cardiovasc Pathol,* vol. 22, pp. 245-50, Jul-Aug 2013.

[22] A. C. Anyanwu and D. H. Adams, "Etiologic classification of degenerative mitral valve disease: Barlow's disease and fibroelastic deficiency," *Semin Thorac Cardiovasc Surg,* vol. 19, pp. 90-6, Summer 2007.

[23] D. H. Adams, *et al.*, "Degenerative mitral valve regurgitation: best practice revolution," *Eur Heart J,* vol. 31, pp. 1958-66, Aug 2010.

[24] R. O. Bonow, *et al.*, "2008 focused update incorporated into the ACC/AHA 2006 guidelines for the management of patients with valvular heart disease: a report of the American College of Cardiology/American Heart Association Task Force on Practice Guidelines (Writing Committee to revise the 1998 guidelines for the management of patients with valvular heart disease). Endorsed by the Society of Cardiovascular Anesthesiologists, Society for Cardiovascular Angiography and Interventions, and Society of Thoracic Surgeons," *J Am Coll Cardiol,* vol. 52, pp. e1-142, Sep 23 2008.

[25] J. G. Castillo, *et al.*, "[Surgical echocardiography of the mitral valve]," *Rev Esp Cardiol,* vol. 64, pp. 1169-81, Dec 2011.

[26] D. Messika-Zeitoun, *et al.*, "The role of echocardiography in the management of patients with myxomatous disease," *Cardiol Clin,* vol. 31, pp. 217-29, May 2013.

[27] B. D. King, *et al.*, ""Myxomatous" mitral valves: collagen dissolution as the primary defect," *Circulation,* vol. 66, pp. 288-96, Aug 1982.

[28] J. E. Barber, *et al.*, "Mechanical properties of myxomatous mitral valves," *J Thorac Cardiovasc Surg,* vol. 122, pp. 955-62, Nov 2001.

[29] J. E. Barber, *et al.*, "Myxomatous mitral valve chordae. I: Mechanical properties," *J Heart Valve Dis,* vol. 10, pp. 320-4, May 2001.

[30] D. H. Adams and A. C. Anyanwu, "Seeking a higher standard for degenerative mitral valve repair: begin with etiology," *J Thorac Cardiovasc Surg,* vol. 136, pp. 551-6, Sep 2008.

[31] T. Nishida, *et al.*, "Single-institution, 22-year follow-up of 786 CarboMedics mechanical valves used for both primary surgery and reoperation," *J Thorac Cardiovasc Surg,* vol. 147, pp. 1493-8, May 2014.

[32] L. S. De Santo, *et al.*, "Mitral mechanical replacement in young rheumatic women: analysis of long-term survival, valve-related complications, and pregnancy outcomes over a 3707-patient-year follow-up," *J Thorac Cardiovasc Surg,* vol. 130, pp. 13-9, Jul 2005.

[33] M. Ruel, *et al.*, "Very long-term survival implications of heart valve replacement with tissue versus mechanical prostheses in adults <60 years of age," *Circulation,* vol. 116, pp. I294-300, Sep 11 2007.

[34] E. Braunberger, *et al.*, "Very long-term results (more than 20 years) of valve repair with carpentier's techniques in nonrheumatic mitral valve insufficiency," *Circulation,* vol. 104, pp. I8-11, Sep 18 2001.

[35] W. Flameng, *et al.*, "Recurrence of mitral valve regurgitation after mitral valve repair in degenerative valve disease," *Circulation,* vol. 107, pp. 1609-13, Apr 1 2003.

[36] T. E. David, *et al.*, "A comparison of outcomes of mitral valve repair for degenerative disease with posterior, anterior, and bileaflet prolapse," *J Thorac Cardiovasc Surg,* vol. 130, pp. 1242-9, Nov 2005.

[37] D. E. Hansen, *et al.*, "Valvular-ventricular interaction: importance of the mitral apparatus in canine left ventricular systolic performance," *Circulation,* vol. 73, pp. 1310-20, Jun 1986.

[38] K. L. Yun, *et al.*, "Importance of mitral subvalvular apparatus in terms of cardiac energetics and systolic mechanics in the ejecting canine heart," *J Clin Invest,* vol. 87, pp. 247-54, Jan 1991.

[39] M. A. Borger, *et al.*, "Reoperative mitral valve replacement: importance of preservation of the subvalvular apparatus," *Ann Thorac Surg,* vol. 74, pp. 1482-7, Nov 2002.

[40] A. Carpentier, *et al.*, "Reconstructive surgery of mitral valve incompetence: ten-year appraisal," *J Thorac Cardiovasc Surg,* vol. 79, pp. 338-48, Mar 1980.

[41] V. A. Jebara, *et al.*, "Left ventricular outflow tract obstruction after mitral valve repair. Results of the sliding leaflet technique," *Circulation,* vol. 88, pp. II30-4, Nov 1993.

[42] A. Carpentier, "Cardiac valve surgery--the "French correction"," *J Thorac Cardiovasc Surg,* vol. 86, pp. 323-37, Sep 1983.

[43] A. M. Gillinov, *et al.*, "Durability of mitral valve repair for degenerative disease," *J Thorac Cardiovasc Surg,* vol. 116, pp. 734-43, Nov 1998.

[44] N. Kashiyama, *et al.*, "A simple way to treat mitral valve prolapse: chordal replacement using a new mitral leaflet retractor," *Interact Cardiovasc Thorac Surg,* Mar 6 2014.

[45] M. Hata, *et al.*, "Mitral chordae myxoma-chordae replacement with a premeasured gore-tex loop using a minimally invasive video-assisted approach," *J Cardiothorac Surg,* vol. 8, p. 227, 2013.

[46] T. Thom, *et al.*, "Heart disease and stroke statistics--2006 update: a report from the American Heart Association Statistics Committee and Stroke Statistics Subcommittee," *Circulation,* vol. 113, pp. e85-151, Feb 14 2006.

[47] A. C. Galloway, *et al.*, "Evolving techniques for mitral valve reconstruction," *Ann Surg,* vol. 236, pp. 288-93; discussion 293-4, Sep 2002.

[48] P. L. Whitlow, *et al.*, "Acute and 12-month results with catheter-based mitral valve leaflet repair: the EVEREST II (Endovascular Valve Edge-to-Edge Repair) High Risk Study," *J Am Coll Cardiol,* vol. 59, pp. 130-9, Jan 10 2012.

[49] S. K. S. Huang and M. A. Wood, *Catheter Ablation of Cardiac Arrhythmias*, 1st ed. Philadelphia: Elsevier, 2006.

[50] J. S. Grashow, *et al.*, "Biaixal stress-stretch behavior of the mitral valve anterior leaflet at physiologic strain rates," *Ann Biomed Eng,* vol. 34, pp. 315-25, Feb 2006.

[51] O. A. Victal, *et al.*, "Left ventricular volume reduction by radiofrequency heating of chronic myocardial infarction in patients with congestive heart failure," *Circulation,* vol. 105, pp. 1317-22, Mar 19 2002.

[52] M. J. Medvecky, *et al.*, "Thermal capsular shrinkage: Basic science and clinical applications," *Arthroscopy,* vol. 17, pp. 624-35, Jul 2001.

[53] R. R. Heuser, *et al.*, "Percutaneous treatment for mitral regurgitation: the QuantumCor system," *J Interv Cardiol,* vol. 21, pp. 178-82, Apr 2008.

[54] R. Goel, *et al.*, "The QuantumCor device for treating mitral regurgitation: an animal study," *Catheter Cardiovasc Interv,* vol. 74, pp. 43-8, Jul 1 2009.

[55] P. Khairy, *et al.*, "Catheter cryoablation in man: Early clinical experience," *The Canadian Journal of Cardiology,* vol. 15, 1999.

[56] A. C. Skanes, *et al.*, "Cryoablation: potentials and pitfalls," *J Cardiovasc Electrophysiol,* vol. 15, pp. S28-34, Oct 2004.

[57] G. Hindricks, "The Multicentre European Radiofrequency Survey (MERFS): complications of radiofrequency catheter ablation of arrhythmias. The Multicentre European Radiofrequency Survey (MERFS) investigators of the Working Group on Arrhythmias of the European Society of Cardiology," *Eur Heart J,* vol. 14, pp. 1644-53, Dec 1993.

[58] L. Zhou, *et al.*, "Thromboembolic complications of cardiac radiofrequency catheter ablation: a review of the reported incidence, pathogenesis and current research directions," *J Cardiovasc Electrophysiol,* vol. 10, pp. 611-20, Apr 1999.

[59] M. R. Epstein, *et al.*, "Embolic complications associated with radiofrequency catheter ablation. Atakr Investigator Group," *Am J Cardiol,* vol. 77, pp. 655-8, Mar 15 1996.

[60] H. Calkins, *et al.*, "Temperature monitoring during radiofrequency catheter ablation procedures using closed loop control. Atakr Multicenter Investigators Group," *Circulation,* vol. 90, pp. 1279-86, Sep 1994.

[61] S. Nath, *et al.*, "Basic aspects of radiofrequency catheter ablation," *J Cardiovasc Electrophysiol,* vol. 5, pp. 863-76, Oct 1994.

[62] T. Arentz, *et al.*, "Incidence of pulmonary vein stenosis 2 years after radiofrequency catheter ablation of refractory atrial fibrillation," *Eur Heart J,* vol. 24, pp. 963-9, May 2003.

[63] I. Giorgberidze, *et al.*, "Efficacy and safety of radiofrequency catheter ablation of left-sided accessory pathways through the coronary sinus," *Am J Cardiol,* vol. 76, pp. 359-65, Aug 15 1995.

[64] S. K. Huang, *et al.*, "Short- and long-term effects of transcatheter ablation of the coronary sinus by radiofrequency energy," *Circulation,* vol. 78, pp. 416-27, Aug 1988.

[65] S. Ohkawa, *et al.*, "Anatomic effects of cryoablation of the atrioventricular conduction system," *Circulation,* vol. 65, pp. 1155-62, Jun 1982.

[66] J. Neuzner, *et al.*, "[Incidence of intervention-related heart valve lesions after high-frequency catheter ablation of the left-side accessory atrioventricular conduction pathways]," *Z Kardiol,* vol. 84, pp. 1002-8, Dec 1995.

[67] L. A. Pires, *et al.*, "Clinical utility of routine transthoracic echocardiographic studies after uncomplicated radiofrequency catheter ablation: a prospective multicenter study. The Atakr Investigators Group," *Pacing Clin Electrophysiol,* vol. 19, pp. 1502-7, Oct 1996.

[68] A. Olsson, *et al.*, "Frequency and long term follow up of valvar insufficiency caused by retrograde aortic radiofrequency catheter ablation procedures," *Heart,* vol. 81, pp. 292-6, Mar 1999.

[69] T. Ohtsuka, *et al.*, "Surgically repaired delayed mitral regurgitation after radiofrequency catheter ablation for Wolff-Parkinson-White syndrome," *Pacing Clin Electrophysiol,* vol. 25, pp. 1142-3, Jul 2002.

[70] J. G. Penaranda Canal, *et al.*, "Mitral valve injury after radiofrequency ablation for Wolff-Parkinson-White syndrome," *Circulation,* vol. 127, pp. 2551-2, Jun 25 2013.

[71] M. B. Ratcliffe, *et al.*, "Radio frequency heating of chronic ovine infarct leads to sustained infarct area and ventricular volume reduction," *J Thorac Cardiovasc Surg,* vol. 119, pp. 1194-204, Jun 2000.

[72] T. Asai, *et al.*, "Butterfly resection is safe and avoids systolic anterior motion in posterior leaflet prolapse repair," *Ann Thorac Surg,* vol. 92, pp. 2097-102; discussion 2102-3, Dec 2011.

[73] K. L. Franco and E. D. Verrier, *Advanced therapy in cardiac surgery*. Hamilton, Ont. ; Saint Louis: B.C. Decker, 1999.

[74] W. Bothe, *et al.*, "Rigid, complete annuloplasty rings increase anterior mitral leaflet strains in the normal beating ovine heart," *Circulation,* vol. 124, pp. S81-96, Sep 13 2011.

[75] R. Amini, *et al.*, "On the in vivo deformation of the mitral valve anterior leaflet: effects of annular geometry and referential configuration," *Ann Biomed Eng,* vol. 40, pp. 1455-67, Jul 2012.

[76] H. N. Sabbah, *et al.*, "On the mechanism of functional mitral regurgitation," *Am J Cardiol,* vol. 72, pp. 1074-6, Nov 1 1993.

[77] T. Kumanohoso, *et al.*, "Mechanism of higher incidence of ischemic mitral regurgitation in patients with inferior myocardial infarction: quantitative analysis of left ventricular and mitral valve geometry in 103 patients with prior myocardial infarction," *J Thorac Cardiovasc Surg,* vol. 125, pp. 135-43, Jan 2003.

[78] K. Tigen, *et al.*, "The importance of papillary muscle dyssynchrony in predicting the severity of functional mitral regurgitation in patients with non-ischaemic dilated cardiomyopathy: a two-dimensional speckle-tracking echocardiography study," *Eur J Echocardiogr,* vol. 11, pp. 671-6, Sep 2010.

[79] Y. J. Liang, *et al.*, "Incremental value of global systolic dyssynchrony in determining the occurrence of functional mitral regurgitation in patients with left ventricular systolic dysfunction," *Eur Heart J,* May 21 2012.

[80] K. Kalra, *et al.*, "Temporal Changes in Interpapillary Muscle Dynamics as an Active Indicator of Mitral Valve and Left Ventricular Interaction in Ischemic Mitral Regurgitation," *Journal of the American College of Cardiology,* vol. 64, pp. 1867-1879, 2014.

[81] J. Kwan, *et al.*, "Geometric differences of the mitral apparatus between ischemic and dilated cardiomyopathy with significant mitral regurgitation: real-time three-dimensional echocardiography study," *Circulation,* vol. 107, pp. 1135-40, Mar 4 2003.

[82] O. Alfieri, *et al.*, "The double-orifice technique in mitral valve repair: a simple solution for complex problems," *J Thorac Cardiovasc Surg,* vol. 122, pp. 674-81, Oct 2001.

[83] O. Alfieri, *et al.*, ""Edge-to-edge" repair for anterior mitral leaflet prolapse," *Semin Thorac Cardiovasc Surg,* vol. 16, pp. 182-7, Summer 2004.

[84] F. Maisano, *et al.*, "The double-orifice technique as a standardized approach to treat mitral regurgitation due to severe myxomatous disease: surgical technique," *Eur J Cardiothorac Surg,* vol. 17, pp. 201-5, Mar 2000.

[85] R. J. Siegel, *et al.*, "The acute hemodynamic effects of MitraClip therapy," *J Am Coll Cardiol,* vol. 57, pp. 1658-65, Apr 19 2011.

[86] T. Feldman and M. Cilingiroglu, "Percutaneous leaflet repair and annuloplasty for mitral regurgitation," *J Am Coll Cardiol,* vol. 57, pp. 529-37, Feb 1 2011.

[87] F. Maisano, *et al.*, "The evolution from surgery to percutaneous mitral valve interventions: the role of the edge-to-edge technique," *J Am Coll Cardiol,* vol. 58, pp. 2174-82, Nov 15 2011.

[88] S. Baldus, *et al.*, "MitraClip therapy in daily clinical practice: initial results from the German transcatheter mitral valve interventions (TRAMI) registry," *Eur J Heart Fail,* Jun 8 2012.

[89] V. Rudolph, *et al.*, "Echocardiographic and clinical outcomes of MitraClip therapy in patients not amenable to surgery," *J Am Coll Cardiol,* vol. 58, pp. 2190-5, Nov 15 2011.

[90] F. Maisano, *et al.*, "Midterm results of edge-to-edge mitral valve repair without annuloplasty," *J Thorac Cardiovasc Surg,* vol. 126, pp. 1987-97, Dec 2003.

[91] J. H. Jimenez, *et al.*, "Effects of annular size, transmitral pressure, and mitral flow rate on the edge-to-edge repair: an in vitro study," *Ann Thorac Surg,* vol. 82, pp. 1362-8, Oct 2006.

[92] L. R. Croft, *et al.*, "Efficacy of the edge-to-edge repair in the setting of a dilated ventricle: an in vitro study," *Ann Thorac Surg,* vol. 84, pp. 1578-84, Nov 2007.

[93] S. Bhattacharya and Z. He, "Annulus tension of the prolapsed mitral valve corrected by edge-to-edge repair," *J Biomech,* vol. 45, pp. 562-8, Feb 2 2012.

[94] J. Harnek, *et al.*, "Transcatheter implantation of the MONARC coronary sinus device for mitral regurgitation: 1-year results from the EVOLUTION phase I study (Clinical Evaluation of the Edwards Lifesciences Percutaneous Mitral Annuloplasty System for the Treatment of Mitral Regurgitation)," *JACC Cardiovasc Interv,* vol. 4, pp. 115-22, Jan 2011.

[95] J. G. Webb, *et al.*, "Percutaneous transvenous mitral annuloplasty: initial human experience with device implantation in the coronary sinus," *Circulation,* vol. 113, pp. 851-5, Feb 14 2006.

[96] J. Schofer, *et al.*, "Percutaneous mitral annuloplasty for functional mitral regurgitation: results of the CARILLON Mitral Annuloplasty Device European Union Study," *Circulation,* vol. 120, pp. 326-33, Jul 28 2009.

[97] C. V. Maniu, *et al.*, "Acute and chronic reduction of functional mitral regurgitation in experimental heart failure by percutaneous mitral annuloplasty," *J Am Coll Cardiol,* vol. 44, pp. 1652-61, Oct 19 2004.

[98] S. J. Duffy, *et al.*, "Feasibility and short-term efficacy of percutaneous mitral annular reduction for the therapy of functional mitral regurgitation in patients with heart failure," *Catheter Cardiovasc Interv,* vol. 68, pp. 205-10, Aug 2006.

[99] J. H. Kim, *et al.*, "Mitral cerclage annuloplasty, a novel transcatheter treatment for secondary mitral valve regurgitation: initial results in swine," *J Am Coll Cardiol,* vol. 54, pp. 638-51, Aug 11 2009.

[100] E. G. Caiani, *et al.*, "Quantification of mitral annulus dynamic morphology in patients with mitral valve prolapse undergoing repair and annuloplasty during a 6-month follow-up," *Eur J Echocardiogr,* vol. 12, pp. 375-83, May 2011.

[101] R. del Valle-Fernandez, *et al.*, "Insight into the dynamics of the coronary sinus/great cardiac vein and the mitral annulus: implications for percutaneous mitral annuloplasty techniques," *Circ Cardiovasc Interv,* vol. 2, pp. 557-64, Dec 2009.

[102] D. Maselli, *et al.*, "Percutaneous mitral annuloplasty: an anatomic study of human coronary sinus and its relation with mitral valve annulus and coronary arteries," *Circulation,* vol. 114, pp. 377-80, Aug 1 2006.

[103] A. Sorgente, *et al.*, "Influence of left atrial and ventricular volumes on the relation between mitral valve annulus and coronary sinus," *Am J Cardiol,* vol. 102, pp. 890-6, Oct 1 2008.

[104] A. J. Choure, *et al.*, "In vivo analysis of the anatomical relationship of coronary sinus to mitral annulus and left circumflex coronary artery using cardiac multidetector computed tomography: implications for percutaneous coronary sinus mitral annuloplasty," *J Am Coll Cardiol,* vol. 48, pp. 1938-45, Nov 21 2006.

[105] L. F. Tops, *et al.*, "Noninvasive evaluation of coronary sinus anatomy and its relation to the mitral valve annulus: implications for percutaneous mitral annuloplasty," *Circulation,* vol. 115, pp. 1426-32, Mar 20 2007.

[106] S. Rahman, *et al.*, "Remodeling of the mitral valve using radiofrequency energy: review of a new treatment modality for mitral regurgitation," *Cardiovasc Revasc Med,* vol. 11, pp. 249-59, Oct-Dec 2010.

[107] W. Bothe, *et al.*, "How do annuloplasty rings affect mitral leaflet dynamic motion?," *Eur J Cardiothorac Surg,* vol. 38, pp. 340-9, Sep 2010.

[108] M. K. Rausch, *et al.*, "Mitral valve annuloplasty: a quantitative clinical and mechanical comparison of different annuloplasty devices," *Ann Biomed Eng,* vol. 40, pp. 750-61, Mar 2012.

[109] C. E. Eckert, *et al.*, "In vivo dynamic deformation of the mitral valve annulus," *Ann Biomed Eng,* vol. 37, pp. 1757-71, Sep 2009.

[110] M. S. Sacks, *et al.*, "In-vivo dynamic deformation of the mitral valve anterior leaflet," *Ann Thorac Surg,* vol. 82, pp. 1369-77, Oct 2006.

[111] M. Daimon, *et al.*, "Dynamic change in mitral annular area and motion during percutaneous mitral annuloplasty for ischemic mitral regurgitation: preliminary animal study with real-time 3-dimensional echocardiography," *J Am Soc Echocardiogr,* vol. 20, pp. 381-8, Apr 2007.

[112] S. Fukuda, *et al.*, "Maintenance of geometric alterations associated with percutaneous mitral valve repair: real-time three-dimensional echocardiographic assessment in an ovine model," *J Heart Valve Dis,* vol. 17, pp. 276-82, May 2008.

[113] T. Pham and W. Sun, "Characterization of the mechanical properties of the coronary sinus for percutaneous transvenous mitral annuloplasty," *Acta Biomater,* vol. 6, pp. 4336-44, Nov 2010.

[114] T. Pham and W. Sun, "Comparison of biaxial mechanical properties of coronary sinus tissues from porcine, ovine and aged human species," *J Mech Behav Biomed Mater,* vol. 6, pp. 21-9, Feb 2012.

[115] M. S. Sacks, *et al.*, "Surface strains in the anterior leaflet of the functioning mitral valve," *Ann Biomed Eng,* vol. 30, pp. 1281-90, Nov-Dec 2002.

[116] J. S. Grashow, *et al.*, "Planar biaxial creep and stress relaxation of the mitral valve anterior leaflet," *Ann Biomed Eng,* vol. 34, pp. 1509-18, Oct 2006.

[117] J. D. Humphrey, *Cardiovascular Solid Mechanics : Cells, Tissues, and Organs*. New York: Springer, 2002.

[118] M. Wood, *et al.*, "Direct measurement of the lethal isotherm for radiofrequency ablation of myocardial tissue," *Circ Arrhythm Electrophysiol,* vol. 4, pp. 373-8, Jun 1 2011.

[119] C. B. Lim, *et al.*, "In vivo thermography during small bowel fusion using radiofrequency energy," *Surg Endosc,* vol. 24, pp. 2465-74, Oct 2010.

[120] M. J. Lopez, *et al.*, "The effect of radiofrequency energy on the ultrastructure of joint capsular collagen," *Arthroscopy,* vol. 14, pp. 495-501, Jul-Aug 1998.

[121] M. J. Lopez, *et al.*, "The effects of monopolar radiofrequency energy on intact and lacerated ovine menisci," *Arthroscopy,* vol. 17, pp. 613-9, Jul 2001.

[122] G. S. Naseef, 3rd, *et al.*, "The thermal properties of bovine joint capsule. The basic science of laser- and radiofrequency-induced capsular shrinkage," *Am J Sports Med,* vol. 25, pp. 670-4, Sep-Oct 1997.

[123] I. G. Aldous, *et al.*, "Differences in collagen cross-linking between the four valves of the bovine heart: a possible role in adaptation to mechanical fatigue," *American Journal of Physiology-Heart and Circulatory Physiology,* vol. 296, pp. H1898-H1906, Jun 2009.

[124] W. Sun, *et al.*, "Computational modeling of cardiac valve function and intervention," *Annu Rev Biomed Eng,* vol. 16, pp. 53-76, Jul 11 2014.

[125] Q. Wang and W. Sun, "Finite element modeling of mitral valve dynamic deformation using patient-specific multi-slices computed tomography scans," *Ann Biomed Eng,* vol. 41, pp. 142-53, Jan 2013.

[126] P. E. Hammer, *et al.*, "Mass-spring model for simulation of heart valve tissue mechanical behavior," *Ann Biomed Eng,* vol. 39, pp. 1668-79, Jun 2011.

[127] N. A. Tenenholtz, *et al.*, "On the Design of an Interactive, Patient-Specific Surgical Simulator for Mitral Valve Repair," *Rep U S,* vol. 2011, pp. 1327-1332, Dec 31 2011.

[128] P. B. Wells, *et al.*, "Altered mechanical behavior of epicardium under isothermal biaxial loading," *J Biomech Eng,* vol. 126, pp. 492-7, Aug 2004.

[129] J. L. Harris and J. D. Humphrey, "Kinetics of thermal damage to a collagenous membrane under biaxial isotonic loading," *IEEE Trans Biomed Eng,* vol. 51, pp. 371-9, Feb 2004.

[130] J. L. Harris, *et al.*, "Altered mechanical behavior of epicardium due to isothermal heating under biaxial isotonic loads," *J Biomech Eng,* vol. 125, pp. 381-8, Jun 2003.

[131] C. Rossmann, *et al.*, "Dynamics of tissue shrinkage during ablative temperature exposures," *Physiol Meas,* vol. 35, pp. 55-67, Jan 2014.

[132] N. T. Wright and J. D. Humphrey, "Denaturation of collagen via heating: an irreversible rate process," *Annu Rev Biomed Eng,* vol. 4, pp. 109-28, 2002.

[133] M. S. Sacks, "Biaxial mechanical evaluation of planar biological materials," *Journal of Elasticity,* vol. 61, pp. 199-246, 2000.

[134] D. R. Lynch, *Numerical partial differential equations for environmental scientists and engineers : a first practical course*. New York: Springer, 2005.

[135] M. K. Rausch, *et al.*, "Mechanics of the mitral valve : A critical review, an in vivo parameter identification, and the effect of prestrain," *Biomech Model Mechanobiol,* Dec 21 2012.

[136] M. K. Rausch and E. Kuhl, "On the effect of prestrain and residual stress in thin biological membranes," *J Mech Phys Solids,* vol. 61, pp. 1955-1969, Sep 1 2013.

[137] K. May-Newman and F. C. Yin, "A constitutive law for mitral valve tissue," *J Biomech Eng,* vol. 120, pp. 38-47, Feb 1998.

[138] D. K. Hildebrand, *et al.*, "Design and hydrodynamic evaluation of a novel pulsatile bioreactor for biologically active heart valves," *Ann Biomed Eng,* vol. 32, pp. 1039-49, Aug 2004.

[139] J. H. Jimenez, *et al.*, "A saddle-shaped annulus reduces systolic strain on the central region of the mitral valve anterior leaflet," *J Thorac Cardiovasc Surg,* vol. 134, pp. 1562-8, Dec 2007.

[140] M. Padala, *et al.*, "Mitral valve hemodynamics after repair of acute posterior leaflet prolapse: quadrangular resection versus triangular resection versus neochordoplasty," *J Thorac Cardiovasc Surg,* vol. 138, pp. 309-15, Aug 2009.

[141] Y. C. Fung, *Biomechanics: Mechanical Properties of Living Tissues*, 2nd ed. New York: Springer-Verlag, 1993.

[142] F. C. Yin, *et al.*, "Quantification of the mechanical properties of noncontracting canine myocardium under simultaneous biaxial loading," *J Biomech,* vol. 20, pp. 577-89, 1987.

[143] T. F. Coleman and Y. Y. Li, "An interior trust region approach for nonlinear minimization subject to bounds," *Siam Journal on Optimization,* vol. 6, pp. 418-445, May 1996.

[144] L. C. Junqueira, *et al.*, "Picrosirius staining plus polarization microscopy, a specific method for collagen detection in tissue sections," *Histochem J,* vol. 11, pp. 447-55, Jul 1979.

[145] S. Thomsen, *et al.*, "Changes in Birefringence as Markers of Thermal-Damage in Tissues," *Ieee Transactions on Biomedical Engineering,* vol. 36, pp. 1174-1179, Dec 1989.

[146] P. Whittaker, *et al.*, "Quantitative assessment of myocardial collagen with picrosirius red staining and circularly polarized light," *Basic Res Cardiol,* vol. 89, pp. 397-410, Sep-Oct 1994.

[147] M. M. Schulz, *et al.*, "The healing effects on the biomechanical properties of joint capsular tissue treated with Ho:YAG laser: An in vivo rabbit study," *Arthroscopy,* vol. 17, pp. 342-7, Apr 2001.

[148] S. L. Schaefer, *et al.*, "Tissue shrinkage with the holmium:yttrium aluminum garnet laser. A postoperative assessment of tissue length, stiffness, and structure," *Am J Sports Med,* vol. 25, pp. 841-8, Nov-Dec 1997.

[149] S. M. Boronyak and W. D. Merryman, "In vitro assessment of a combined radiofrequency ablation and cryo-anchoring catheter for treatment of mitral valve prolapse," *J Biomech,* vol. 47, pp. 973-80, Mar 21 2014.

[150] J. P. Rabbah, *et al.*, "Effects of targeted papillary muscle relocation on mitral leaflet tenting and coaptation," *Ann Thorac Surg,* vol. 95, pp. 621-8, Feb 2013.

[151] H. Nakagawa, *et al.*, "Locations of high contact force during left atrial mapping in atrial fibrillation patients: electrogram amplitude and impedance are poor predictors of electrode-tissue contact force for ablation of atrial fibrillation," *Circ Arrhythm Electrophysiol,* vol. 6, pp. 746-53, Aug 2013.

[152] H. C. Herrmann, *et al.*, "Mitral valve hemodynamic effects of percutaneous edge-to-edge repair with the MitraClip device for mitral regurgitation," *Catheter Cardiovasc Interv,* vol. 68, pp. 821-8, Dec 2006.